Supramolecular cyclic peptide-polymer nanotubes as drug delivery vectors

Sophie Clara Larnaudie

A thesis submitted in partial fulfilment of the requirements for the degree of

Doctor of Philosophy in Chemistry

Department of Chemistry

University of Warwick

July 2017

Ever tried. Ever failed. No matter. Try again. Fail again. Fail better.

- Samuel Beckett

La science, mon garçon, est faite d'erreurs, mais d'erreurs qu'il est bon de commettre, car elles mènent peu à peu à la vérité.

- Jules Verne

Table of contents

Chapter 2:

Cyclic peptide-polymer conjugates: grafting-to *vs* grafting-from 19

List of Figures

Chapter 1:

List of Tables

Chapter 2:

Chapter 3:

List of Schemes

Abbreviations

5-FU	5-fluorouracil
AA	Acrylic acid
ACVA	4,4′-Azobis(4-cyanovaleric acid)
AFM	Atomic force microscopy
ATRP	Atom transfer radical polymerisation
AUC	Area under the curve
BA	Butyl acrylate
$CDCl_3$	Deuterated chloroform
CDI	Carbonyldiimidazole
CEMA	2-Chloroethyl methacrylate
Cl	Clearance
CP	Cyclic peptide
Cp*	Pentamethylcyclopentadienyl
Cp^{xph}	Phenyltetramethylcyclopentadienyl
CPAETC	(4-Cyano pentanoic acid)yl ethyl trithiocarbonate
$CP(CPAETC)_2$	Cyclic peptide (4-cyano pentanoic acid)yl ethyl trithiocarbonate
$CP(PABTC)_2$	Cyclic peptide (propanoic acid)yl butyl trithiocarbonate
CPNT	Cyclic peptide nanotube
CTA	Chain transfer agent

CuAAC	Copper catalysed azide-alkyne cycloaddition
DCM	Dichloromethane
DIPEA	*N*,*N*-Diisopropylethylamine
DLS	Dynamic light scattering
DMAEA	2-(Dimethylamino)ethyl acrylate
DMAEMA	2-(Dimethylamino)ethyl methacrylate
DMAP	Dimethylamino pyridine
DMF	Dimethyl formamide
DMSO	Dimethyl sulfoxide
DMTMM	4-(4,6-Dimethoxy-1,3,5-triazin-2-yl)-4-methylmorpholinium
DOX	Doxorubicin
DP	Degree of polymerisation
DPA	2-(Diisopropylamino)ethyl methacrylate
DSC	Differencial scanning calorimetry
$E(CPAETC)_2$	Ethyl((4-cyano pentanoic acid)yl ethyl trithiocarbonate)
EDC	1-Ethyl-3-(3-dimethylaminopropyl)carbodiimide
ESI ToF	Electrospray Ionisation Time of Flight
FTIR	Fourier transform infrared spectroscopy
GF	Grafting-from
GFP	Green fluorescent protein
GT	Grafting-to

HBTU	*O*-(Benzotriazole-1-yl)-*N,N,N',N'*-tetramethyluronium hexafluorophosphate
HEA	Hydroxyethyl acrylate
HFIP	Hexafluoro-2-propanol
HPMA	2-Hydroxypropyl methacrylamide
ICP-MS/OES	Inductively coupled plasma mass spectrometry/optical emission spectrophotometry
IEMA	2-Isocyanatoethyl methacrylate
IU	International Units
IV	Intravenous
$k_{p,app}$	Apparent rate constant of propagation
L_c	Distance between adjacent cyclic peptides
Leu	Leucine
LUVs	Large unilamellar vesicles
Lys	Lysine
M	Monomer
MHz	Megahertz
MMA	Methyl methacrylate
MW	molecular weight
n	Refractive index
N_a	Avogadro's number
N_{agg}	Number of aggregation

NAM	*N*-acryloyl morpholine
NHS	*N*-hydroxysuccinimide
NHS-PABTC	*N*-hydroxysuccinimide-(propanoic acid)yl butyl trithiocarbonate
NHS-CPAETC	*N*-hydroxysuccinimide-(4-cyano pentanoic acid)yl ethyl trithiocarbonate
NIPAM	*N*-isopropyl acrylamide
NMM	*N*-methyl morpholine
NMP	Nitroxide mediated polymerisation
NMR	Nuclear magnetic resonance
NOESY	Nuclear Overhauser effet spectroscopy
NT	Nanotube
pAA	Poly(acrylic acid)
PABTC	(Propanoic acid)yl butyl trithiocarbonate
pBA	Poly(butyl acrylate)
PBS	Phosphate buffered saline
pDMAEMA	Poly(2-(dimethylamino)ethyl methacrylate)
pDPA	Poly(2-(diisopropylamino)ethyl methacrylate)
PEI	Poly(ethylene imine)
PEG	Polyethylene glycol
PEGA	Poly(ethylene glygol) methyl ether acrylate
p(EtOx)	Poly(2-ethyl-2-oxazoline)

PFP	Pentaflurophenol
pHEA	Poly(hydroxyethyl acrylate)
pHPMA	Poly(2-hydroxypropyl methacrylamide)
phpy	*C,N*-chelated phenylpyridine
pNIPAM	Poly(N-isopropyl acrylamide)
PUEMA	2-(3-(Pyridin-4-ylmethyl)ureido)ethyl)methacrylate
q	Wave vector
R_θ	Rayleigh ratio
RAFT	Reversible addition fragmentation chain transfer
RDRP	Reversible-deactivation radical polymerisation
R_g	Radius of gyration
SANS	Small angle neutron scattering
SD	Standard deviation
SEC	Size exclusion chromatography
SLS	Static light scattering
SPPS	Solid phase peptide synthesis
$t_{1/2}$	Half-life
TEM	Transmission electron microscopy
TIPS	Triisopropylsilane
TFA	Trifluoroacetic acid
Trp	Tryptophan

UV-Vis	Ultra violet-visible
V_c	Volume of the central compartment
V_d	Volume of distribution
$V_{d,\beta}$	Terminal volume of distribution

Acknowledgements

This is where I'll try to thank all the people who helped me one way or another over the course of this PhD, and I'll do my best to not forget anyone.

First of all, I'll thank my supervisor, Pr. Sébastien Perrier, for giving me the fantastic opportunity to work here. Seb, thanks for your continuous guidance and for being accessible, I really appreciated being able to tell you my point of view in all circumstances, and knowing it will be taken into account. Also, thanks for the encouragements and for considering me like a normal human being even during my occasional tearful freak-outs.

Before I move on to the PhD time itself, I'd like to thank Dr. Sam Verbrugghe from Agfa in Belgium, as well as Dr. Peter Duggan and Dr. Oliver Hutt from CSIRO in Australia, for being amazing supervisors during my Masters projects. Thanks for caring, and for your patience, time and dedication. Working with you definitely convinced me to do a PhD. I would also like to thank Pr. Steve Howdle for his kindness in suggesting I applied with Seb, even when knowing I might bail on the project he was offering me.

The very beginning of my PhD, and especially the transition from life in bustling Melbourne and dream travels in Australia to, well, Coventry, was a bit of a tough one, but a few people made it a lot less depressing. Dr. Guillaume Gody, in addition to teaching me more about RAFT in one day than anyone at CSIRO in 6 months, was life-saving company during the lonely first few weeks of the history of the Perrier group in Warwick, when there were only 2 or 3 of us in the office. He carried on being a great inspiration, and a good friend, on top of being an exceptional chemist. Massiiive thanks for all the help, and the interesting discussions. Thanks to Antonin, for inviting me to Oxford when I needed to escape Coventry, and for all the good times, especially the Irish escapade. Corentin, thanks for the Cambridge weekends, it was great to get a glimpse of the life in the bubble. It was not the same being in the UK after you guys left. Thanks to Olivier and Charly for the Scotland trip, and for meeting with me in Paris even when I was just passing through. Thanks to Sonia for taking me to London parties, and to Beni and Heidi for the much needed crazy holidays. Thanks to Laure and Patricia for the Paris weekends and the amazing Polish New Year. Special thanks to Corentin and Beni for visiting me in the Midlands, that's dedication.

Back in Warwick, the people who joined the group during my first year had a huge impact on everything, especially my social life. Our little family has shrunk with the departures of a

lot of you, but you'll always occupy a special place in my memories. I'll be forever grateful to the other 1st generation PhD students, mainly Liam and Tammie, for sharing all of the struggles, but also all of the good times, of PhDying and of house sharing. Tammie, thanks for being the other girl in this very manly environment, and Liam, thanks for making me one of the lads, even if I'm not funny. Both, thanks for providing means of locomotion, for putting up with me for so long and for teaching me weird words that apparently belong to the English language. Massive thank you to Dr. Johannes Brendel for being a great post-doc and a fantastic friend. Thanks for all the ideas, the beers, the freak-out management, the help, the conversations, and generally being a good person. Ming, thanks for teaching me about "cyclic peptides made of alternating D and L amino acids", for always being in a good mood, and for suggesting pub nights with unwavering regularity and enthusiasm. I'd also like to thank Cookie, for a lot of things but mostly for being the no-fuss guy in this sometimes manic environment, and for being yourself; your occasional outbursts are always a great entertainment. Agnes, thanks for being a constant bubble of happiness, for the endless hours of talking, and for putting up with grumpy me when running. Thanks to Julia for all the baking discussions, and the positive attitude. Sylvain, thanks for helping me deciphering SANS. Also, you introduced wrestling and naps to the office, and for this you'll never be forgotten. Matthias, thanks for having us at your house for various food-related events, and for giving us access to baby cuddles. Raoul, thanks for your help in bio. You were a quite late addition to the group but definitely one of the best ones, such good professional skills combined with so much hilarious randomness is a rare thing. All of you, thanks for the parties and for the amazing hiking trips to various rainy parts of the UK (just joking, the weather was amazing…sometimes).

I'd also like to thank all the other members of the Perrier group, Junliang (those dumplings!), Pratik, Joji, Majda, Caroline, Guillaume, Andy(s), Sean, Ed (special thanks for the thesis proof-reading!) and all the students who spent a few months with us. My Warwick thank yous need to be extended to the group of Pr. David Haddleton, and especially to Dr. Jamie Godfrey, to the "alrighty" team (namely Athina, Vasiliki, Gabit and the others), to Dr. Kristian Kempe, Dr Chongyu Zhu, Dr Paul Wilson and of course to Alex, but I'll get back to that. Special mention to my only non-chemistry friend, soon to be Dr. Irina Schumski, for helping me keep my sanity, and making me realise that even if I don't understand anything about your field, we're all in the same boat when it comes to doing a PhD!

Next, I'll thank Pr. Peter Sadler for the collaboration, and the members of his group who helped me a lot with all things Iridium-related. Thanks to Abraha for being my drug dealer,

to James for running so many ICP experiments, and to Isolda and Carlos for all the cell work.

During the course of my PhD I was lucky enough to go to Monash University in Melbourne for a few months, and for this I need to thank Seb again. I'll also thank Pr. Tom Davis for hosting me in his group and Pr. Chris Porter for giving me access to his labs. I'd like to thank Dr. Tri-Hung Nguyen for his patience in teaching me how to operate on rats and what all these pharmacokinetic parameters mean. Still in the animal lab, huge thanks to Ian, Gracia and Given for being so nice while answering all of my stupid questions. Also, thanks to Nadine, May, Emily, Tobi, Stefan, Joanne and all the others for the social aspects. Last but not least, I would like to thank Dr. Joaquin "Ximo" Sanchis. Thanks for arranging everything to make my start in Monash so smooth, for being the most generous host I could have dreamed of, for collecting organs for me while I was handing you vials trying not to listen to the sound of bones cracking, for staying late doing confocal with me, for remeasuring all of my 700 samples after I was gone, and more generally for all the conversations, for managing my panicky moments and for asking the right questions to help me figure things out.

To my dear friends Marion, Pauline and Agathe, thanks for remaining so close while being so far, and for always being supportive.

Alex, after being "just" an amazing friend, you've been my rock for these past two years, thank you so much for all the good times, and for the constant support, for always listening to me, even when I'm ranting, for making me smile in all circumstances and for telling me it's all going to be OK. Sorry for freaking out so often, and thanks for being so understanding. I could keep going, but this thesis is about curing cancer, not about how much you mean to me, so I'll stop here.

The last bit will have to be in French, I'd like to finish by thanking my family, who has always been there for me.

Je vais commencer par remercier mes parents pour avoir fait de moi qui je suis, et m'avoir toujours donné les moyens d'atteindre mes objectifs. Merci du fond du cœur pour votre éternel soutien. Je voudrais aussi remercier ma sœur Céline et ma tribu de cousins. J'vous aime ! Merci aussi à mes oncles et tantes, en particulier tonton/parrain Raymond, et à Nanny. Enfin, merci à Oma, pour être un modèle à tellement de niveaux. Ta force, ta gentillesse et ton amour inconditionnels m'aident à franchir tous les obstacles.

Declaration

Experimental work contained in this thesis is original research carried out by the author, unless stated otherwise, in the Department of Chemistry at the University of Warwick, and in the Department of Drug Delivery, Disposition and Dynamics at Monash Institute of Pharmaceutical Sciences, Monash University, between October 2013 and July 2017. No material contained here has been submitted for any other degree, or at any other institution.

Results from other authors are referenced throughout the text in the usual manner.

Date: _____ _____

Sophie Larnaudie

Abstract

The objective of this thesis is to develop a range of polymeric nanotubes based on self-assembling cyclic peptides suitable to be used as drug delivery systems, and to investigate their behaviour *in vitro* and *in vivo*.

The interest for cylindrical structures in a drug delivery context arises from their reported longer circulation times, and enhanced tumour accumulation *in vivo* compared to spherical nanoparticles. Moreover, supramolecular systems have attracted a lot of attention thanks to their versatility and potential ability to facilitate clearance.

The design of polymeric nanotubes constructed around a cyclic peptide scaffold is described, and various systems are developed. Firstly, the two main synthetic routes (grafting-to and grafting-from) yielding peptide-polymer conjugates are compared in a systematic study, which shows that the two approaches present distinct advantages, and are complementary in nature. This information is then used to design cyclic peptide conjugates specifically directed to drug delivery, using a polymer that combines biocompatible properties and functional handles. Analysis of their self-assembly in solution confirms the cylindrical shape of the obtained supramolecular structures, and a study of their behaviour *in vitro* and *in vivo* establishes their potential as delivery systems. Subsequently, the complexation of a highly potent organometallic anticancer agent is described. *In vitro* studies determined that the use of the nanotubes leads to higher potency and enhanced selectivity towards cancer cells. Finally, a core-shell system designed for drug encapsulation and subsequent pH-triggered release is presented. This approach relies on the use of an amphiphilic and pH responsive system, which in addition confers more stability to the obtained nanotubes.

The work presented in this thesis provides a bottom-up approach in the design of novel self-assembled cyclic peptide nanotubes highly tuned for drug delivery applications.

Chapter 1

Therapeutic uses of nanotubes made of self-assembling cyclic peptides

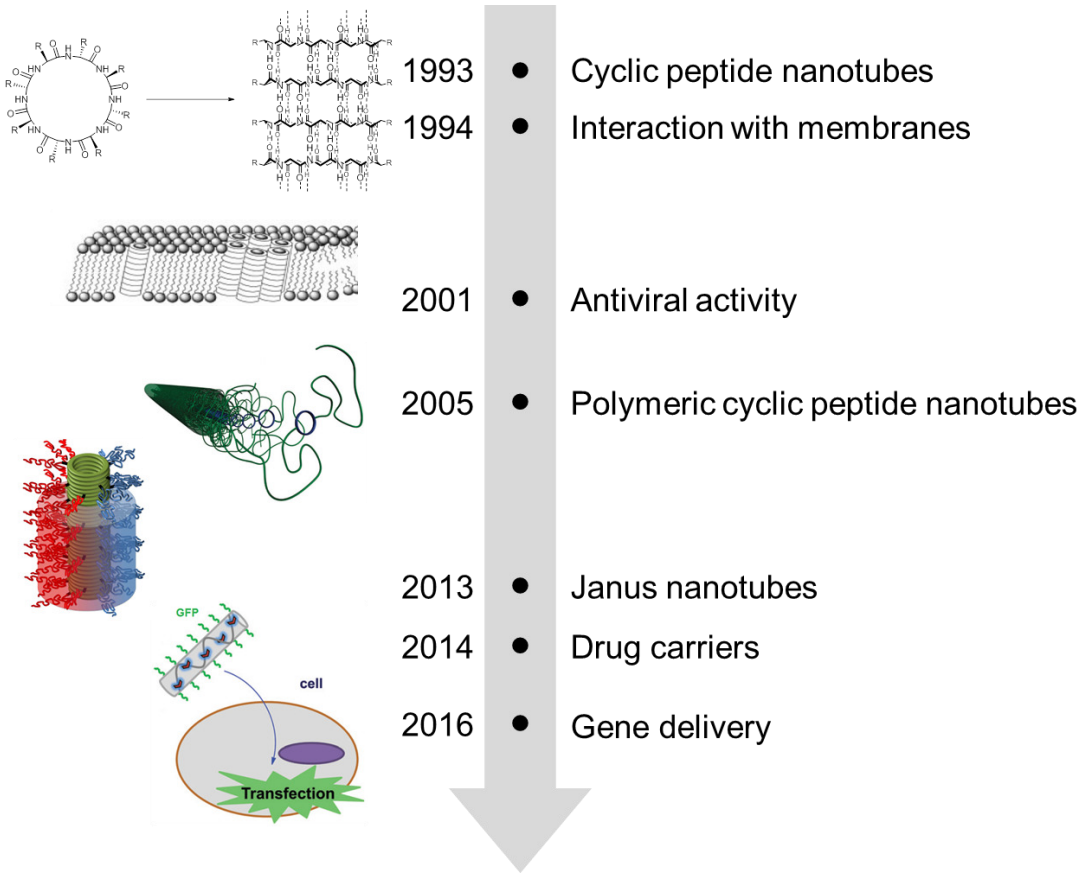

1.1 Introduction

Despite several decades of research, the effective and directed transport of pharmaceutical active materials into desired compartments of the body or cells still remains a challenge faced by material scientists or researchers in life sciences. Nevertheless this continuous effort has revealed several critical factors for the design of transport vectors which considerably alter the effectiveness of the delivery of active drugs.[1,2] Among all the various properties which can be modified, the variation of the shape certainly attracted considerable attention in research.[3-5] Studies have for example demonstrated that cylindrical systems may offer increased circulation time *in vivo*[6-9] or higher tumour targeting capacity than spherical ones.[10-12] Different types of cylindrical structures have been used as therapeutics, including inorganic (silica,[7] gold,[13] quantum dots[14]) and organic (polymeric,[6,15,16] carbon nanotubes,[17] or virus-based nanoparticles[8]). In addition to the mentioned materials, hollow nanotubes have substantial potential as therapeutics: guest molecules can be loaded in the inside cavity, they can form channels (for example across membranes), and their aspect ratio can be interesting for drug delivery.[18] Most commonly organic nanotubes are related to single and multi-walled carbon nanotubes,[19] however when considering biomedical applications supramolecular chemistry represents an interesting tool for designing nanotubes as this chemistry constitutes one of the major driving forces for structure formation in nature.[20] The self-assembly of molecules into larger nanotubular structures allows for a bottom-up approach that permits high levels of control over numerous structural properties, including the internal diameter. From a drug delivery perspective, the non-covalent aspect of such materials can be highly beneficial in various ways. First of all, due to the reversibility of the intermolecular bonds that hold the structure together, it can be hypothesised that they will ultimately break down into the starting building blocks that can be cleared out easily, thereby avoiding organ accumulation *in vivo*. Moreover, the supramolecular approach could potentially allow for a modular "mix and match" strategy to be applied whereby unimers bearing drugs, targeting moieties and fluorescent dyes can be synthesised separately and assembled to afford highly functional materials from simpler building blocks. With the above design parameters in mind, nanotubes made of self-assembling cyclic peptides appear to be relevant candidates for the fabrication of drug delivery vehicles. In this chapter, these materials will be described, and their existing applications as therapeutics will be briefly reviewed. Subsequently, the rationale behind their functionalisation with polymers will be

explained. The syntheses of polymeric nanotubes using a cyclic peptide scaffold will be detailed, and the efforts to use these materials in a therapeutic context will be highlighted.

1.2 Self-assembling cyclic peptides

1.2.1 Design and synthesis

Cyclic peptides presenting an even number of α-amino acids of alternating D and L chirality (cyclic D,L-α-peptides) were first predicted to form nanotubes by De Santis *et al.* in 1974,[21] but it was not until 1993 that Ghadiri *et al.* were able to demonstrate this experimentally.[22]

The alternating chirality provides these peptides with a flat conformation in which the hydrogen bonding-prone amide groups lie perpendicular to the plane, enabling them to stack on top of each other through antiparallel β-sheet formation, thereby forming supramolecular tubes (Figure 1.1).

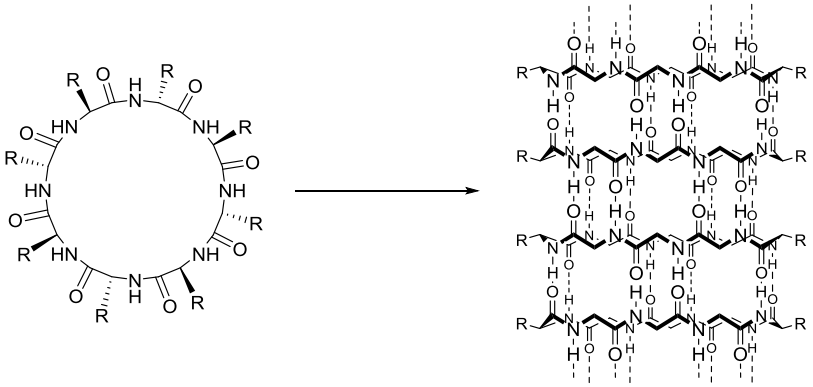

Figure 1.1: Example of self-assembling cyclic D,L-α-peptides, here containing eight amino acids.

Such peptides are generally accessed *via* a combination of solid phase peptide synthesis (SPPS) and cyclisation (either in dilute solution or on resin).[23] This synthetic route allows for the precise tailoring of the materials through modification of various design elements (Figure 1.2).[23,24]

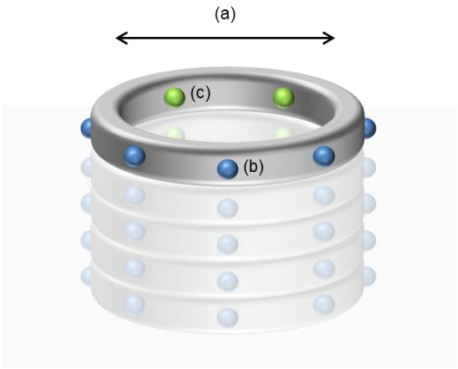

Figure 1.2: Various design elements of cyclic peptide nanotubes: (a) internal diameter, (b) external functionality, (c) internal functionality.

The number of amino acids allows for the control of the internal diameter (see (a) in Figure 1.2). Cyclic D,L-α-peptides comprising four,[25] six,[26-28] eight,[22,26,29-33] ten,[34] or twelve[35] amino acids have been reported, with diameters ranging from 2 to 13 Å, as determined by X-ray crystallography, electron diffraction measurements or molecular modelling.

Moreover, the amino acids side chains are projected pseudo-equatorially, which enables control of the external functionality (see (b) in Figure 1.2). The vast library of commercially available amino acids allows for the introduction of for example, hydrophilic, hydrophobic, basic or acidic residues.

Designs can be further expanded by the introduction of other types of amino acids. For example, nanotube formation has been reported for cyclic peptides containing β-amino acids,[36,37] as well as α-ε[38] and α-γ[31,39,40] hybrids using cyclic γ-amino acids. Through these, alteration of the internal chemistry of the tubes is possible (see (c) in Figure 1.2). Reports showed that the introduction of cyclic alkanes[39] or methyl groups[31] increases the hydrophobicity of the inside cavity, while the sequencing of a hydroxytetrahydrofuran-containing amino acid allows the introduction of a hydroxyl group into the core.[41]

By taking all the above parameters into consideration, it is possible to design bespoke materials, highly tuneable for the desired application.

1.2.2 Applications as therapeutics

With the multiple options to modify the properties of these materials, it is not surprising that cyclic peptide nanotubes have been tested in a variety of applications, such as ion sensors,[42,43] electronic devices[44-46] and as photoresponsive materials.[47,48] The most useful feature, however, is certainly their ability to interact with phospholipid bilayers.[32,49]

Typically, hydrophobic peptides form transmembrane channels made of single tubes, which result in applications as ion channels.[32,34,50] On the other hand, nanotubes made of amphipathic peptides (that present both a hydrophilic and a hydrophobic domain) tend to form either barrel-stave pores with hydrophilic residues oriented towards the interior of the nanotube bundle, or to lie parallel to the membrane, with hydrophobic residues inserted within the lipid bilayer and hydrophilic residues exposed on the surface (Figure 1.3).[51] This specificity is not limited to artificial membranes and has been also demonstrated in biological membranes, thereby suggesting they have potential as therapeutics, from antibacterial materials to drug delivery vehicles.

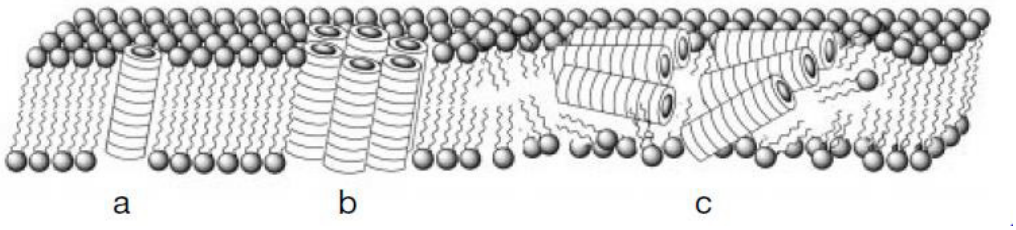

Figure 1.3: Different modes of cyclic peptide self-assembly in membranes: a) intramolecular pore, b) barrel stave and c) carpet-like. Adapted from Fernandez-Lopez *et al*.[26]

1.2.2.1 Antimicrobials

A library of amphipathic cyclic D,L-α-peptides comprising 6 or 8 residues was first tested for antibacterial activity by Fernandez-Lopez *et al.* in 2001.[26] These peptides were found to be selective towards bacterial membranes and to exhibit remarkable activity against various bacterial strains such as *Staphylococcus aureus* (*S. aureus*) and *Escherichia coli* (*E. coli*). The authors found that the nature of the amino acids present in the peptide sequence has a tremendous impact on the activity and selectivity of the tested antibacterial compounds (2 orders of magnitude in some cases). Their mode of action was investigated and it was determined to rely on the peptides assembling within the membrane in a carpet-like fashion, avoiding receptor interactions, which leads to rapid cell death and interestingly helps preventing resistance. Insights into the mechanism of interaction between one of these peptides and lipid bilayers were provided by coarse-grained molecular dynamics simulations, which confirmed the carpet-like arrangement of amphipathic peptides within the membrane and showed that high concentrations of peptide deeply disturbed the mechanical properties of the bilayer.[52] Additional *in vivo* studies in mice infection models showed that intravenous injection of the peptide drastically reduced the bacterial load at the

infection site.[53] Further to this, Motiei *et al.* explored the performance of cyclic D,L-α-glycopeptides containing various glycosyl amino acids derivatives.[54] Depending on the selected sugar and its position within the peptide sequence, higher selectivity towards bacteria could be achieved when compared with activity against human and murine red blood cells or mouse fibroblasts, with the toxicity against mammalian cells reduced 5-fold in some cases.

The antimicrobial potential of cyclic peptides was also assessed against other biological organisms. Fletcher *et al.* used a combinatorial approach to identify 6-residue cyclic D,L-α-peptides potentially active against two eukaryotic marine algae: *Ulva linza* and *Navicula perminuta*.[27] Their study demonstrated that selectivity can be tuned through precise choice of the peptide sequence, with some candidates exhibiting broad-spectrum activity while others were highly selective (100-fold) towards *U. linza*.

In addition, Horne *et al.* have established the potential of this class of materials as antiviral agents, using adenovirus and influenza virus models.[29] They have shown that in the presence of an 8-residue cyclic D,L-α-peptide selected from a library of 400 compounds, the virus is unable to escape the endosome. They hypothesised that the peptides self-assemble into the endosome membranes, inducing membrane permeation, thereby preventing the acidification of the endosomes and ultimately stopping the virus from being released into the cytoplasm (Figure 1.4).

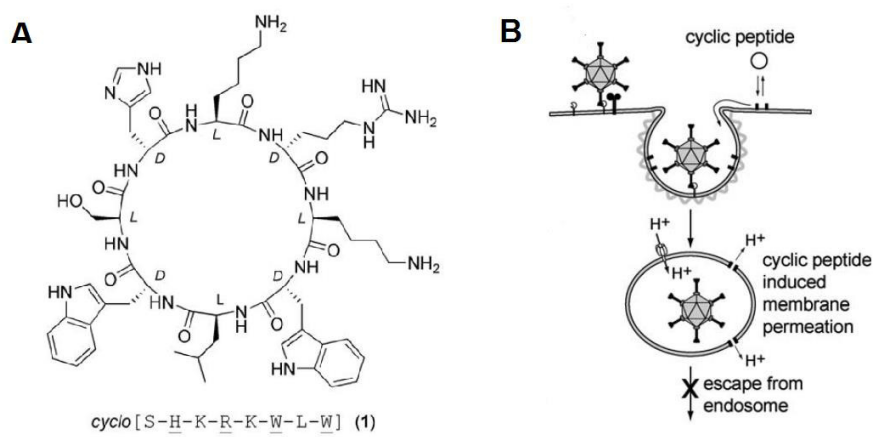

Figure 1.4: A) Structure of peptide identified as adenovirus delivery inhibitor. B) Suggested mechanism for cyclic peptide-mediated prevention of virus endosomal release. Adapted from Horne *et al.*[29]

1.2.2.2 Drug and gene delivery

The membrane-interacting potential of cyclic D,L-α-peptides was also exploited for drug and gene delivery. Liu *et al.* studied a highly hydrophobic 10-residue peptide which forms transmembrane nanotubes with an internal diameter of 1 nm, sufficient to serve as a channel for the small anticancer drug 5-fluorouracil (5-FU, 0.44 nm).[55] They experimentally showed that the presence of the cyclic peptide considerably increases the release of 5-FU from liposomes (from 5% to 70%). Molecular dynamics simulations further confirmed the transport of 5-FU within channels formed by the cyclic peptide within lipid bilayers, and that it occurred by hopping the drug along the nanotube between different energy minima. The same group later extended their study to other drugs and showed that the transport of 5-FU as well as other small anticancer agents across membranes increased with increasing concentrations of cyclic peptide. Moreover, they showed that the release of cytarabine, a drug that is bigger than the pore size (1.11 nm), was not enhanced by the presence of cyclic peptide, confirming that escape happens through channel formation (Figure 1.5).[56] *In vitro* cell viability tests demonstrated that despite having only a very weak anticancer activity, cyclic peptides could enhance the efficacy of 5-FU and, in some cell lines, in a synergistic manner. The combination of 5-FU and cyclic peptides also inhibited tumour growth in mouse models, further indicating the therapeutic potential of these materials.

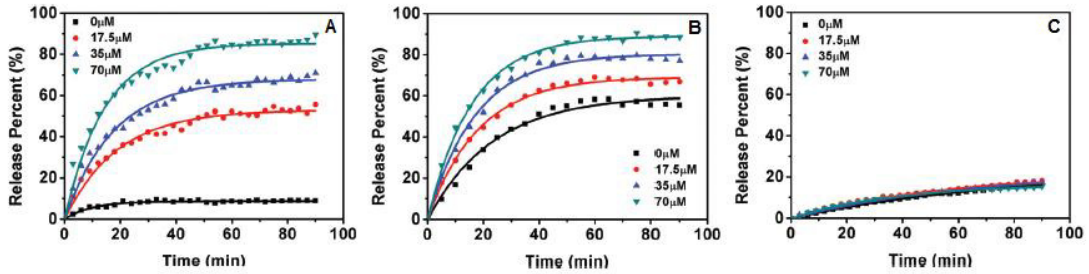

Figure 1.5: Cyclic peptide-mediated transmembrane transport of A) 5-FU, B) cisplatin and C) cytarabine. Increasing concentrations of peptide lead to enhancement of the transport for 5-FU and cisplatin but has no effect on the transport of cytarabine. Adapted from Chen *et al.*[56]

Recent research by Li *et al.* demonstrated the first example of gene delivery using self-assembling cyclic D,L-α-peptides.[57] They reported the design of a specific cationic octapeptide and its assembly into charged nanofibres able to complex green fluorescent protein (GFP) plasmid without altering their structure. The transfection efficacy of the complexes in HeLa cells was comparable to that of commonly used polyethyleneimine (PEI), and in contrast to PEI, the transfection was not inhibited in the presence of

bafilomycin, which suppresses endosomal escape. The authors admit that further studies are necessary to precisely elucidate the mechanism of transfection, but these results suggest a non-endocytic mechanism which could be explained by the formation of a peptide channel, either directly across the cellular membrane or through an effect of endosomal membrane permeation as previously observed by Horne *et al.*[29] (see above).

1.3 Cyclic peptide-polymer conjugates

1.3.1 Incentive and synthesis

The major drawback of cyclic peptide nanotubes is their propensity to uncontrollably aggregate into micrometre-long bundles, which greatly limits their solubility, hence their possible areas of application. The main strategy used to circumvent this limitation is to conjugate (macro)molecules to the side chains of the peptides. This approach helps to prevent lateral aggregation, and, depending on the bulkiness of the attached molecule, can also participate in the control of the length of the resulting nanotubes. As such, in particular, polymeric cyclic peptide nanotubes have attracted growing interest in recent years.[58-60] The use of polymers allows for the introduction of a multitude of functionalities as well as functionalisation sites, which is especially attractive with therapeutic applications in mind.

Reversible-deactivation radical polymerisation (RDRP) techniques such as reversible addition-fragmentation chain transfer polymerisation (RAFT),[61,62] atom transfer radical polymerisation (ATRP)[63-66] or nitroxide mediated polymerisation (NMP)[67,68] are valuable tools when preparing well defined and highly functional polymeric cyclic peptide nanotubes and have been used in a variety of examples. The two main synthetic routes yielding peptide-polymer conjugates are “grafting-to”, in which a pre-formed polymer chain is attached to the peptide through a highly efficient ligation technique, and “grafting-from”, in which the polymer chain is grown from the peptide (see Chapter 2).[69-71]

The first report of polymeric cyclic peptide nanotubes was given by Biesalski and co-workers,[59] who used an octapeptide containing three residues functionalised with ATRP initiators to grow poly(*N*-isopropylacrylamide) (pNIPAM) chains (Figure 1.6). The formation of polymer-coated nanotubes was confirmed by atomic force microscopy (AFM) and the β-sheet arrangement of the peptides was verified using Fourier Transform Infrared spectroscopy (FTIR). The same group later described the effect of different degrees of

polymerisation on the length of the nanotubes, corroborating the hypothesis that steric hindrance caused by the polymer chains helps to reduce the size of the aggregates.[72]

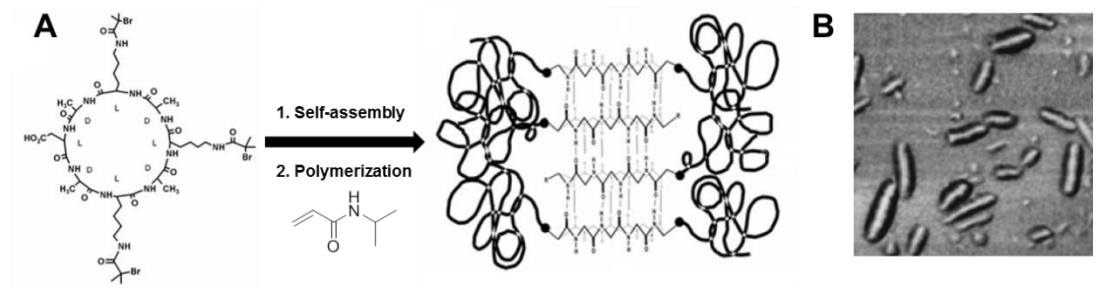

Figure 1.6: A) Grafting-from synthesis of cyclic peptide-pNIPAM nanotubes. B) AFM phase image of the nanotubes adsorbed on a silicon wafer (scale 0.8 μm). Adapted from Couet *et al.*[59]

Börner and co-workers also described the conjugation of carboxylated poly(butyl acrylate) (pBA) chains (synthesised by ATRP prior to ligation) to the two lysine residues of another octapeptide, using a carbodiimide coupling agent.[58] Infrared spectroscopy and electron diffraction measurements confirmed the arrangement of the peptides in a β-sheet structure, and the tubular shape of the assemblies was demonstrated by AFM. In this example, the use of the condensation reaction necessitated an excess of polymer, which led to tedious purification steps. Chapman *et al.* pioneered the use of the highly efficient copper catalysed azide-alkyne cycloaddition (CuAAC) to synthesise cyclic peptide-polymer conjugates. Through the simple modification of the RAFT chain transfer agent (CTA) with an alkyne group and the sequencing of an azide-modified lysine residue in the cyclic peptide, conjugation of two polymer arms to a cyclic D,L-α-peptide was achieved in nearly stoichiometric conditions, enabling characterisation of the self-assemblies in solution without the need for purification.[60,73,74] These first studies focused on investigating the limits of the reaction and optimising the conditions using conventional monomers such as BA, hydroxyethyl acrylate (HEA), styrene, acrylic acid (AA) and dimethylaminoethyl acrylate (DMAEA) (Figure 1.7). One of the main improvements was to switch from conventional heating to microwave irradiation, which allowed the reaction times to be reduced from 3 days to 15 minutes.[74] The self-assembly was initially confirmed by a combination of FTIR, transmission electron microscopy (TEM) and dynamic light scattering (DLS). Later, the assembly of pBA conjugates of varying degrees of polymerisation (DPs) was thoroughly studied by small angle neutron scattering (SANS), a technique which allows for much more precise understanding of the morphology in solution.[75]

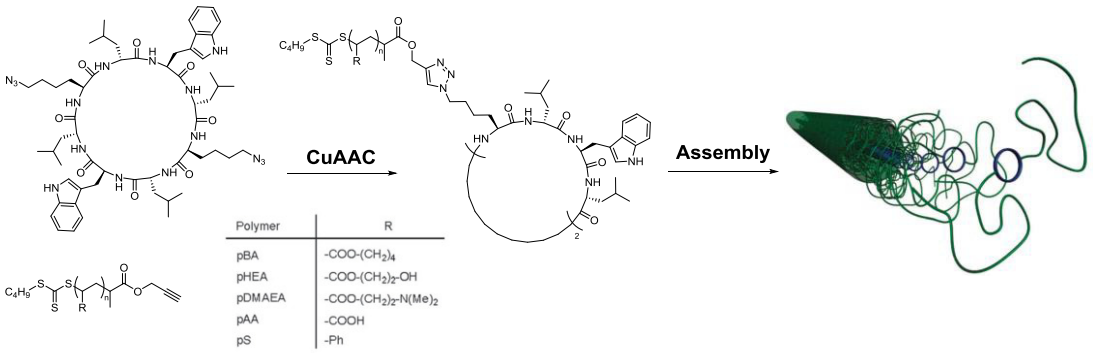

Figure 1.7: Cyclic peptide-polymer conjugates *via* a grafting-to method using CuAAC. Adapted from Chapman *et al.*[74]

After these initial fundamental studies, increasing attention was paid to the synthesis of more functional materials. In one of the first examples, a conjugate made with diblock copolymers of isoprene and acrylic acid was synthesised (Figure 1.8). After characterising its assembly into multishell nanotubes, hollow tubes with a tuneable pore size could be created by crosslinking of the acrylic acid shell and subsequent ozonolysis of the isoprene core. Additionally, this method of degradation leads to the presence of aldehydes moieties on the inside of the pore, which constitute a handle for potential further modification.[76]

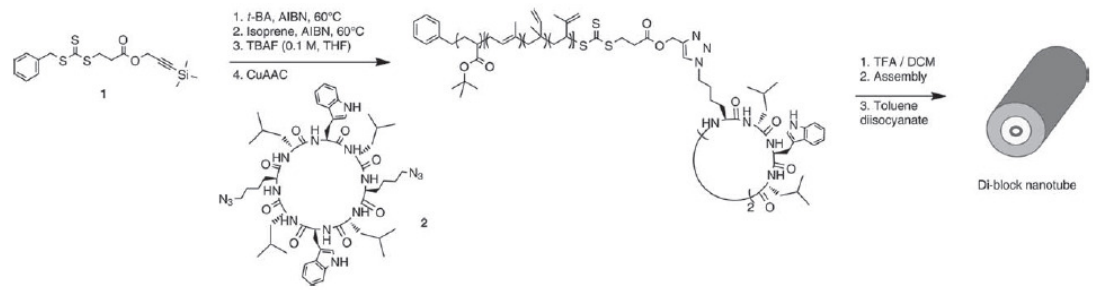

Figure 1.8: Synthesis of multishell cyclic peptide-polymer nanotubes. Adapted from Chapman *et al.*[76]

Thermoresponsive nanotubes made with poly(2-ethyl-2-oxazoline) (pEtOx) arms were also synthesised and found to reversibly aggregate into micrometre-sized particles above their cloud point temperature.[77] Finally, cyclic peptide-polymer conjugates were obtained using pHEA and pAA polymers. These materials were found to form nanotubes in polar solvents, including water, indicating that the polymer shell provides sufficient shielding of the cyclic peptide assembled core to avoid disruption of the hydrogen bonds.[78] The pAA-containing nanotubes were also shown to be pH-responsive; whereby the assembly was shorter at higher pH, when the deprotonation of the acrylic acid units creates electrostatic repulsion

between the polymer chains. More recently, Catrouillet *et al.* showed how the use of pH-responsive poly(2-(dimethylamino)ethyl methacrylate) (pDMAEMA) allowed for precise tuning of the length of the nanotubes in water at different pHs through modification of the degree of ionisation.[79]

1.3.2 Towards therapeutic applications

1.3.2.1 Membrane interactions

Although non-modified cyclic peptides were shown to assemble inside lipid bilayers by Ghadiri and co-workers as early as 1994,[32] it is only recently that the ability of polymer-modified cyclic peptides to form transmembrane channels was investigated.[80,81] Danial *et al.* described various systems able to form either barrel-stave or single channel pores within artificial lipid bilayers. Initially, Janus cyclic peptide-polymer nanotubes were introduced (Figure 1.9).

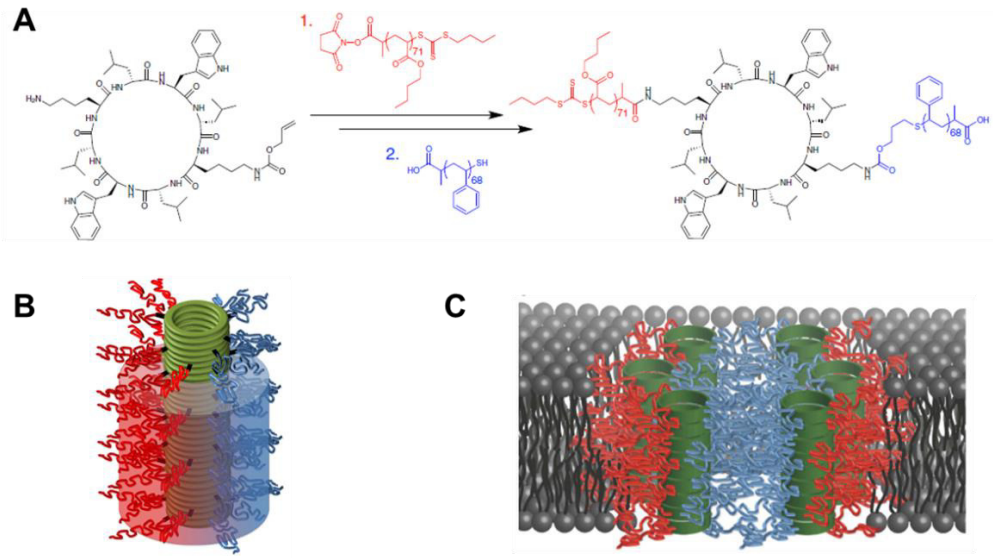

Figure 1.9: A) Synthesis of the Janus conjugates. B) Representation of the polymer microphase separation leading to Janus nanotubes. C) Schematic representation of the Janus nanotubes insertion in lipid bilayers, forming a micropore. Adapted from Danial *et al.*[80]

Two different polymers, known to undergo microphase separation, were attached to opposite sides of a cyclic D,L-α-octapeptide, using a synthetic route relying on orthogonal coupling reactions. Thorough characterisation of the assemblies based on 2D ^{1}H-^{1}H nuclear Overhauser effect spectroscopy (NOESY) nuclear magnetic resonance (NMR) and differential scanning calorimetry (DSC) measurements confirmed the demixing of the two

polymers, hence the formation of Janus-type tubes. A fluorescence-based assay using calcein encapsulated into large unilamellar vesicles (LUVs) determined that the presence of the Janus tubes led to calcein leakage from the LUVs. Given the fact that calcein is larger than the lumen of the cyclic peptide, the authors concluded that pores were formed in a barrel-stave manner. This observation is coherent with the immiscibility of one of the polymer arms with the lipids forming the membrane, resulting in its segregation on the inside of the formed macropore.

A subsequent study described the membrane interaction of a library of symmetrical conjugates exhibiting various degrees of hydrophobicity and hydrophilicity.[81] When using these conjugates, pore formation occurred in a single channel manner, as supported by the results of a fluorescence assay. The partitioning activity of the different conjugates could be related to their lipophilicity, with the more hydrophobic conjugates enabling much more transmembrane ion transport than the less hydrophobic, and the hydrophilic conjugates. Interestingly, using a pNIPAM conjugate, pore formation could also be triggered by temperature: limited transport was observed at room temperature but heating up the sample above its cloud point led to a notable increase in ion transport across the membrane. These examples provide an excellent bench-mark in the future design of novel membrane-channel structures.

1.3.2.2 Drug delivery

Aside from their interesting ability to interact with biologically relevant membranes, self-assembling cyclic peptides represent a versatile scaffold for the design of tubular drug carriers. Decoration with polymers can help to enhance their solubility and provide stealth to the carrier, and allows for its extensive functionalisation, facilitating the introduction of, for example, drugs, targeting moieties or fluorescent dyes.

Despite these possible advantages, the use of polymer-coated cyclic peptide nanotubes as drug delivery systems is currently limited to a couple of examples. Wang *et al*. reported a system which consisted of PEGylated bundles of nanotubes for the delivery of the anticancer drug doxorubicin (DOX) (Figure 1.10).[82] A cyclic D,L-α-octapeptide containing a glutamic acid and a cysteine residue was mixed with DOX, leading to the formation of ion-pair complexes which were subsequently assembled into bundles of nanotubes. In order to disperse these bundles, the cysteine residues present on the surface of the bundles were used as an anchorage point to attach polyethylene glycol (PEG) chains. The obtained PEG-modified, DOX-loaded cyclic peptide nanotube (PEG-CPNT/DOX) bundles were tested *in*

vitro on both human breast cancer MCF-7 cells and their multidrug resistant counterpart MCF-7/ADR. Interestingly, the DOX-loaded bundles were found to be ca. 5 times more potent than free DOX against the resistant cell line, while the drug free bundles used as a control were non-toxic. In addition, flow cytometry analysis and confocal imaging experiments showed that the peptides increased DOX uptake. In contrast to the free drug, which diffuses passively into the cytoplasm, the bundles seemed to undergo an endocytic mechanism of cellular entry.

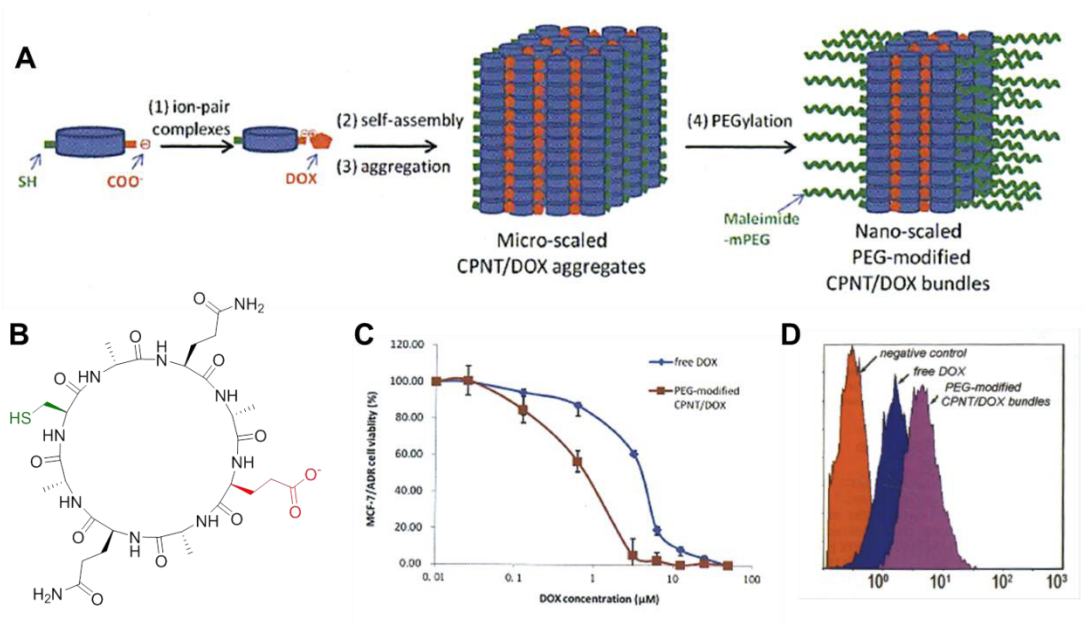

Figure 1.10: Preparation of PEG-CPNT/DOX bundles. B) Structure of the cyclic peptide. C) Cytotoxicity of the PEG-CPNT/DOX bundles against MCF-7/ADR. D) Flow cytometry analysis for the cellular uptake of PEG-CPNT/DOX bundles in MCF-7/ADR. Adapted from Wang *et al*.[82]

Additionally, Blunden *et al*. reported the use of cyclic peptide-polymer conjugates for the delivery of RAPTA-C, a ruthenium anticancer drug (Figure 1.11).[83] Through CuAAC coupling, a cyclic D,L-α-octapeptide was decorated with a hydrophilic copolymer made of HEA and 2-chloroethyl methacrylate (CEMA). This functional monomer was introduced to provide a handle for the subsequent ligation of RAPTA-C. The resulting conjugates were self-assembled and their nanotubular structure was confirmed by static and dynamic light scattering (S(D)LS), and TEM. The efficacy of the drug loaded nanotubes against ovarian A2780 and cisplatin-resistant ovarian A2780cis cancer cells was then determined and compared to that of the free drug. The complexation of the drug to the nanotubes was found to increase its potency by more than an order or magnitude in both cases (18 times more in A2780 and 12 in A2780cis, respectively).

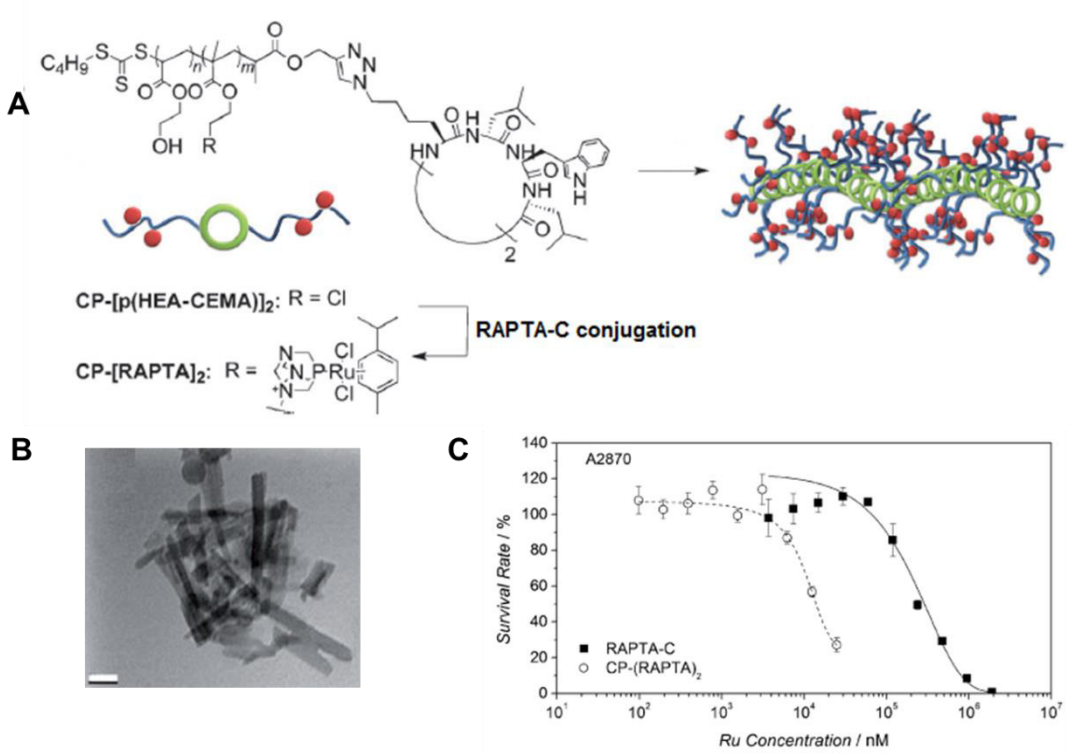

Figure 1.11: A) Cyclic peptide-polymer nanotube functionalised with RAPTA-C. B) TEM image of a crosslinked nanotube (scale bar 50 nm). C) Cytotoxicity of the drug-loaded nanotubes against A2780 cells. Adapted from Blunden *et al*.[83]

1.4 Motivation for this work

The variety of design features and the ease of synthesis of polymeric cyclic peptide nanotubes highlight the tremendous potential of these materials as drug delivery vehicles. However, so far only two very preliminary studies have explored their performance as drug carriers. Attention needs to be paid to the choice of the starting materials such as monomers that are widely recognised as suitable building blocks for drug delivery systems and highly potent drugs. Another critical aspect is the precise characterisation of the self-assembled structures in solution, which has so far been partially overlooked. A better understanding of the behaviour of such materials *in vitro* is also highly desirable. For instance, the mode of cellular entry of the carrier (with or without a drug) could be studied in more details. In addition, there is currently no report concerning the performance of cyclic peptide-polymer nanotubes *in vivo*.

The present work proposes to address some of these limitations, focusing on several aspects. Initially, the two main synthetic routes leading cyclic peptide-polymer conjugates will be

explored in a systematic comparison between the grafting-to (convergent) and grafting-from (divergent) approaches. Subsequently, particular attention will be paid to the more robust design of cyclic peptide conjugates specifically directed to drug delivery, using a well-studied biocompatible monomer and a functional handle able to complex anticancer drugs. Following on, the self-assembled system will be thoroughly characterised in solution, by combining appropriate scattering techniques such as SANS and SLS. A novel study looking at the *in vitro* and *in vivo* behaviour of a cyclic peptide-polymer nanotube will be undertaken with particular focus on the quantification and the mode of cellular entry of the carrier. For the first time, *in vivo* studies will provide insight on the hypothesis that these systems might avoid organ accumulation thanks to their supramolecular nature. The possibility of attaching a highly potent organometallic anticancer agent to these polymeric cyclic peptide nanotubes will then be explored, and the *in vitro* behaviour of the drug-loaded nanotubes will be studied, including investigations on their mode of action. Finally, a more advanced system designed for drug encapsulation and subsequent pH-triggered release will be presented.

As a whole, this thesis will describe a thorough design strategy for the synthesis of cyclic peptide-polymer nanotubes suitable to be used as drug delivery systems, and provide insights regarding their behaviour both *in vitro* and *in vivo*.

1.5 References

1. L. Y. T. Chou, K. Ming, W. C. W. Chan, *Chem. Soc. Rev.* **2011,** *40* (1), 233-245.
2. R. A. Petros, J. M. DeSimone, *Nat. Rev. Drug Discov.* **2010,** *9* (8), 615-627.
3. N. P. Truong, M. R. Whittaker, C. W. Mak, T. P. Davis, *Expert Opin. Drug Delivery* **2015,** *12* (1), 129-142.
4. S. Venkataraman, J. L. Hedrick, Z. Y. Ong, C. Yang, P. L. R. Ee, P. T. Hammond, Y. Y. Yang, *Adv. Drug Delivery Rev.* **2011,** *63* (14–15), 1228-1246.
5. J. A. Champion, Y. K. Katare, S. Mitragotri, *J. Controlled Release* **2007,** *121* (1-2), 3-9.
6. Y. Geng, P. Dalhaimer, S. S. Cai, R. Tsai, M. Tewari, T. Minko, D. E. Discher, *Nat. Nanotechnol.* **2007,** *2* (4), 249-255.
7. X. Huang, L. Li, T. Liu, N. Hao, H. Liu, D. Chen, F. Tang, *ACS Nano* **2011,** *5* (7), 5390-5399.
8. M. A. Bruckman, L. N. Randolph, A. VanMeter, S. Hern, A. J. Shoffstall, R. E. Taurog, N. F. Steinmetz, *Virology* **2014,** *449*, 163-173.
9. M. Janát-Amsbury, A. Ray, C. Peterson, H. Ghandehari, *Eur. J. Pharm. Biopharm.* **2011,** *77* (3), 417-423.
10. D. A. Christian, S. Cai, O. B. Garbuzenko, T. Harada, A. L. Zajac, T. Minko, D. E. Discher, *Mol. Pharmaceutics* **2009,** *6* (5), 1343-1352.
11. J.-H. Park, G. von Maltzahn, L. Zhang, A. M. Derfus, D. Simberg, T. J. Harris, E. Ruoslahti, S. N. Bhatia, M. J. Sailor, *Small* **2009,** *5* (6), 694-700.

12. K. C. L. Black, Y. Wang, H. P. Luehmann, X. Cai, W. Xing, B. Pang, Y. Zhao, C. S. Cutler, L. V. Wang, Y. Liu, Y. Xia, *ACS Nano* **2014,** *8* (5), 4385-4394.
13. Y. Qiu, Y. Liu, L. Wang, L. Xu, R. Bai, Y. Ji, X. Wu, Y. Zhao, Y. Li, C. Chen, *Biomaterials* **2010,** *31* (30), 7606-7619.
14. V. P. Chauhan, Z. Popović, O. Chen, J. Cui, D. Fukumura, M. G. Bawendi, R. K. Jain, *Angew. Chem. Int. Ed.* **2011,** *50* (48), 11417-11420.
15. S. Barua, J.-W. Yoo, P. Kolhar, A. Wakankar, Y. R. Gokarn, S. Mitragotri, *PNAS* **2013,** *110* (9), 3270-3275.
16. M. Elsabahy, K. L. Wooley, *Chem. Soc. Rev.* **2012,** *41* (7), 2545-2561.
17. Z. Liu, W. Cai, L. He, N. Nakayama, K. Chen, X. Sun, X. Chen, H. Dai, *Nat Nano* **2007,** *2* (1), 47-52.
18. C. R. Martin, P. Kohli, *Nat. Rev. Drug Discovery* **2003,** *2* (1), 29-37.
19. D. Tasis, N. Tagmatarchis, A. Bianco, M. Prato, *Chem. Rev.* **2006,** *106* (3), 1105-1136.
20. E. Krieg, M. M. C. Bastings, P. Besenius, B. Rybtchinski, *Chem. Rev.* **2016,** *116* (4), 2414-2477.
21. P. De Santis, S. Morosetti, R. Rizzo, *Macromolecules* **1974,** *7* (1), 52-58.
22. M. R. Ghadiri, J. R. Granja, R. A. Milligan, D. E. McRee, N. Khazanovich, *Nature* **1993,** *366* (6453), 324-327.
23. R. Chapman, M. Danial, M. L. Koh, K. A. Jolliffe, S. Perrier, *Chem. Soc. Rev.* **2012,** *41* (18), 6023-6041.
24. R. J. Brea, C. Reiriz, J. R. Granja, *Chem. Soc. Rev.* **2010,** *39* (5), 1448-1456.
25. T. Suga, S. Osada, H. Kodama, *Bioorg. Med. Chem.* **2012,** *20* (1), 42-46.
26. S. Fernandez-Lopez, H. S. Kim, E. C. Choi, M. Delgado, J. R. Granja, A. Khasanov, K. Kraehenbuehl, G. Long, D. A. Weinberger, K. M. Wilcoxen, M. R. Ghadiri, *Nature* **2001,** *412* (6845), 452-455.
27. J. T. Fletcher, J. A. Finlay, M. E. Callow, J. A. Callow, M. R. Ghadiri, *Chem. Eur. J.* **2007,** *13* (14), 4008-4013.
28. X. Sun, G. P. Lorenzi, *Helv. Chim. Acta* **1994,** *77* (6), 1520-1526.
29. W. S. Horne, C. M. Wiethoff, C. L. Cui, K. M. Wilcoxen, M. Amorin, M. R. Ghadiri, G. R. Nemerow, *Bioorg. Med. Chem.* **2005,** *13* (17), 5145-5153.
30. M. E. Polaskova, N. J. Ede, J. N. Lambert, *Aust. J. Chem.* **1998,** *51* (7), 535-540.
31. R. Hourani, C. Zhang, R. van der Weegen, L. Ruiz, C. Y. Li, S. Keten, B. A. Helms, T. Xu, *J. Am. Chem. Soc.* **2011,** *133* (39), 15296-15299.
32. M. R. Ghadiri, J. R. Granja, L. K. Buehler, *Nature* **1994,** *369* (6478), 301-304.
33. M. Engels, D. Bashford, M. R. Ghadiri, *J. Am. Chem. Soc.* **1995,** *117* (36), 9151-9158.
34. J. R. Granja, M. R. Ghadiri, *J. Am. Chem. Soc.* **1994,** *116* (23), 10785-10786.
35. N. Khazanovich, J. R. Granja, D. E. McRee, R. A. Milligan, M. R. Ghadiri, *J. Am. Chem. Soc.* **1994,** *116* (13), 6011-6012.
36. D. Seebach, J. L. Matthews, A. Meden, T. Wessels, C. Baerlocher, L. B. McCusker, *Helv. Chim. Acta* **1997,** *80* (1), 173-182.
37. F. Fujimura, Y. Horikawa, T. Morita, J. Sugiyama, S. Kimura, *Biomacromolecules* **2007,** *8* (2), 611-616.
38. J. H. van Maarseveen, W. S. Horne, M. R. Ghadiri, *Org. Lett.* **2005,** *7* (20), 4503-4506.
39. M. Amorín, L. Castedo, J. R. Granja, *J. Am. Chem. Soc.* **2003,** *125* (10), 2844-2845.
40. R. J. Brea, M. Amorín, L. Castedo, J. R. Granja, *Angew. Chem. Int. Ed.* **2005,** *44* (35), 5710-5713.
41. C. Reiriz, M. Amorin, R. Garcia-Fandino, L. Castedo, J. R. Granja, *Organic & Biomolecular Chemistry* **2009,** *7* (21), 4358-4361.
42. K. Motesharei, M. R. Ghadiri, *J. Am. Chem. Soc.* **1997,** *119* (46), 11306-11312.

43. J. Sánchez-Quesada, M. R. Ghadiri, H. Bayley, O. Braha, *J. Am. Chem. Soc.* **2000,** *122* (48), 11757-11766.
44. F. Fujimura, S. Kimura, *Org. Lett.* **2007,** *9* (5), 793-796.
45. C. Reiriz, R. J. Brea, R. Arranz, J. L. Carrascosa, A. Garibotti, B. Manning, J. M. Valpuesta, R. Eritja, L. Castedo, J. R. Granja, *J. Am. Chem. Soc.* **2009,** *131* (32), 11335-11337.
46. N. Ashkenasy, W. S. Horne, M. R. Ghadiri, *Small* **2006,** *2* (1), 99-102.
47. M. S. Vollmer, T. D. Clark, C. Steinem, M. R. Ghadiri, *Angew. Chem. Int. Ed.* **1999,** *38* (11), 1598-1601.
48. C. Steinem, A. Janshoff, M. S. Vollmer, M. R. Ghadiri, *Langmuir* **1999,** *15* (11), 3956-3964.
49. M. Danial, S. Perrier, K. A. Jolliffe, *Organic & Biomolecular Chemistry* **2015,** *13* (8), 2464-2473.
50. J. Sánchez-Quesada, H. Sun Kim, M. R. Ghadiri, *Angew. Chem. Int. Ed.* **2001,** *40* (13), 2503-2506.
51. H. S. Kim, J. D. Hartgerink, M. R. Ghadiri, *J. Am. Chem. Soc.* **1998,** *120* (18), 4417-4424.
52. A. Khalfa, M. Tarek, *J. Phys. Chem. B* **2010,** *114* (8), 2676-2684.
53. V. Dartois, J. Sanchez-Quesada, E. Cabezas, E. Chi, C. Dubbelde, C. Dunn, J. Granja, C. Gritzen, D. Weinberger, M. R. Ghadiri, *Antimicrob. Agents Chemother.* **2005,** *49* (8), 3302-3310.
54. L. Motiei, S. Rahimipour, D. A. Thayer, C.-H. Wong, M. R. Ghadiri, *Chem. Commun.* **2009,** (25), 3693-3695.
55. H. Liu, J. Chen, Q. Shen, W. Fu, W. Wu, *Mol. Pharmaceutics* **2010,** *7* (6), 1985-1994.
56. J. Chen, B. Zhang, F. Xia, Y. Xie, S. Jiang, R. Su, Y. Lu, W. Wu, *Nanoscale* **2016,** *8* (13), 7127-7136.
57. M. Li, M. Ehlers, S. Schlesiger, E. Zellermann, S. K. Knauer, C. Schmuck, *Angew. Chem. Int. Ed.* **2016,** *128* (2), 608-611.
58. M. G. J. ten Cate, N. Severin, H. G. Börner, *Macromolecules* **2006,** *39* (23), 7831-7838.
59. J. Couet, J. D. Jeyaprakash, S. Samuel, A. Kopyshev, S. Santer, M. Biesalski, *Angew. Chem. Int. Ed.* **2005,** *44* (21), 3297-3301.
60. R. Chapman, K. A. Jolliffe, S. Perrier, *Aust. J. Chem.* **2010,** *63* (8), 1169-1172.
61. G. Moad, E. Rizzardo, S. H. Thang, *Aust. J. Chem.* **2012,** *65* (8), 985-1076.
62. J. Chiefari, Y. K. Chong, F. Ercole, J. Krstina, J. Jeffery, T. P. T. Le, R. T. A. Mayadunne, G. F. Meijs, C. L. Moad, G. Moad, E. Rizzardo, S. H. Thang, *Macromolecules* **1998,** *31* (16), 5559-5562.
63. K. Matyjaszewski, *Macromolecules* **2012,** *45* (10), 4015-4039.
64. M. Kato, M. Kamigaito, M. Sawamoto, T. Higashimura, *Macromolecules* **1995,** *28* (5), 1721-1723.
65. C. Boyer, N. A. Corrigan, K. Jung, D. Nguyen, T.-K. Nguyen, N. N. M. Adnan, S. Oliver, S. Shanmugam, J. Yeow, *Chem. Rev.* **2016,** *116* (4), 1803-1949.
66. J.-S. Wang, K. Matyjaszewski, *J. Am. Chem. Soc.* **1995,** *117* (20), 5614-5615.
67. D. H. Solomon, E. Rizzardo, P. Cacioli, Polymerization process and polymers produced thereby. USPatent, 4581429 A, 1986.
68. J. Nicolas, Y. Guillaneuf, C. Lefay, D. Bertin, D. Gigmes, B. Charleux, *Prog. Polym. Sci.* **2013,** *38* (1), 63-235.
69. S. Dehn, R. Chapman, K. A. Jolliffe, S. Perrier, *Polym. Rev.* **2011,** *51* (2), 214-234.
70. S. C. Larnaudie, J. C. Brendel, K. A. Jolliffe, S. Perrier, *J. Polym. Sci., Part A: Polym. Chem.* **2016,** *54* (7), 1003-1011.
71. M. A. Gauthier, H. A. Klok, *Chem. Commun.* **2008,** (23), 2591-2611.

72. J. Couet, M. Biesalski, *Small* **2008,** *4* (7), 1008-1016.
73. C. K. Poon, R. Chapman, K. A. Jolliffe, S. Perrier, *Polym. Chem.* **2012,** *3* (7), 1820-1826.
74. R. Chapman, K. A. Jolliffe, S. Perrier, *Polym. Chem.* **2011,** *2* (9), 1956-1963.
75. R. Chapman, M. L. Koh, G. G. Warr, K. A. Jolliffe, S. Perrier, *Chem. Sci.* **2013,** *4* (6), 2581-2589.
76. R. Chapman, K. A. Jolliffe, S. Perrier, *Adv. Mater.* **2013,** *25* (8), 1170-1172.
77. R. Chapman, P. J. M. Bouten, R. Hoogenboom, K. A. Jolliffe, S. Perrier, *Chem. Commun.* **2013,** *49* (58), 6522-6524.
78. R. Chapman, G. G. Warr, S. Perrier, K. A. Jolliffe, *Chem. Eur. J.* **2013,** *19* (6), 1955-1961.
79. S. Catrouillet, J. C. Brendel, S. Larnaudie, T. Barlow, K. A. Jolliffe, S. Perrier, *ACS Macro Letters* **2016,** *5* (10), 1119-1123.
80. M. Danial, C. M. N. Tran, P. G. Young, S. Perrier, K. A. Jolliffe, *Nat. Commun.* **2013,** *4*, 2780.
81. M. Danial, C. M. N. Tran, K. A. Jolliffe, S. Perrier, *J. Am. Chem. Soc.* **2014,** *136* (22), 8018-8026.
82. Y. Wang, S. Yi, L. Sun, Y. Huang, S. C. Lenaghan, M. Zhang, *J. Biomed. Nanotechnol.* **2014,** *10* (3), 445-454.
83. B. M. Blunden, R. Chapman, M. Danial, H. X. Lu, K. A. Jolliffe, S. Perrier, M. H. Stenzel, *Chem. Eur. J.* **2014,** *20* (40), 12745-12749.

Chapter 2

Cyclic peptide-polymer conjugates: grafting-to *vs* grafting-from

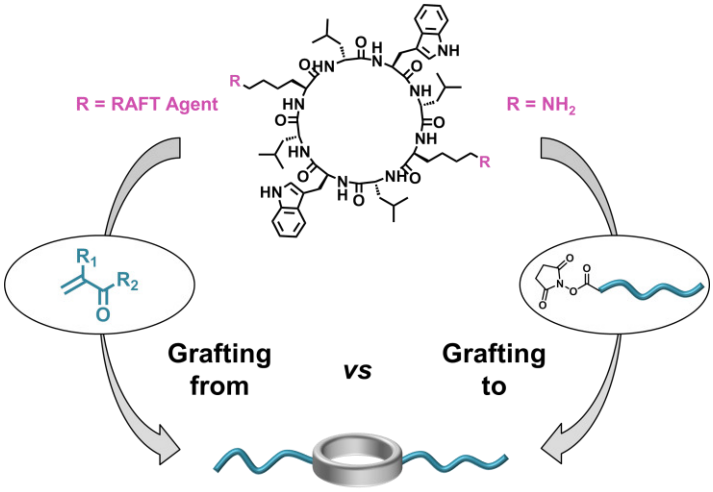

This chapter describes a systematic comparison between the grafting-to (convergent) and grafting-from (divergent) synthetic routes leading to cyclic peptide-polymer conjugates. The RAFT (reversible addition-fragmentation chain transfer) process was used to control the polymerisations and the couplings between cyclic peptide and polymer or RAFT agent were performed using N-hydroxysuccinimide (NHS) active ester ligation. The kinetics of polymerisation and polymer conjugation to cyclic peptides were studied using both grafting-to and grafting-from strategies, using N-acryloyl morpholine as a model monomer. The cyclic peptide chain transfer agent was able to mediate polymerisation as efficiently as a traditional RAFT agent, reaching high conversion in the same time scale whilst maintaining excellent control over the molecular weight distribution. The conjugation of polymers to cyclic peptides proceeded to high conversion, and the nature of the carbon at the α-position to the NHS group was found to play a crucial role in the reaction kinetics. The study was extended to a wider range of monomers, including hydrophilic/temperature responsive acrylamides, hydrophilic/hydrophobic acrylates, and hydrophobic/pH responsive methacrylates. Both approaches lead to similar peptide-polymer conjugates in most cases, while some exceptions highlight the advantages of one or the other method, indicating their complementarity.

2.1 Introduction

The study of hybrid materials composed of synthetic polymers and biomolecules has become an extremely prolific field of research since the concept was first introduced by Ringsdorf in 1975.[1] Such materials achieve remarkable properties by combining the precise structure and function of biomolecules with the tuneable nature of polymers.[2,3] Peptide-polymer conjugates are of particular interest as they have applications in a wide range of fields, including therapeutics[4] and separation technologies.[5]

Typically, such conjugates are synthesised by a grafting-from (divergent) or grafting-to (convergent) approach.[6,7] In the grafting-from approach,[8,9] the polymer chains are grown from the peptide using a wide range of polymerisation techniques[10-14] while in the grafting-to approach the polymers are synthesised separately and then grafted to the peptide.[15-17] Fortunately, progress in conjugation chemistry has resulted in a variety of efficient reactions that are particularly useful for the functionalisation of polymers,[18,19] including the well-established copper(I)-catalysed alkyne-azide cycloaddition (CuAAC),[20-22] or more traditional activated ester-mediated ligations.[23-25] However, despite the use of these highly efficient reactions, the grafting-to approach often requires an excess of polymer and subsequent purification steps to remove unreacted polymers.[26,27] The grafting-from synthetic strategy enables the use of a wider range of monomers, as it is not limited by monomer side chain functionalities that are orthogonal with the chain end group used for the conjugation reaction, as in the grafting-to route. On the other hand, the grafting-to strategy allows for better characterisation as the peptide and polymer chains can be fully analysed prior to the ligation step. Additionally, possible competitive reactions arising from the amino acid functional groups which could occur during the polymerisation process[28,29] can also be circumvented when preparing the polymer separately. Finally, the grafting-to approach allows the use of a more versatile peptide, which does not bear initiating groups required for polymerisation, and therefore allows for the coupling of polymers accessed by a variety of polymerisation methods.

The functionalisation of β-sheet forming self-assembling cyclic peptides (CP)[30] by polymeric chains has opened the path to the design of polymeric nanotubes,[31-33] which have diverse potential applications in drug delivery[34] and materials science.[35] Moreover, by changing the nature of the polymers, various properties can be introduced, such as solubility in water and pH responsiveness.[36] Temperature responsive[37] and multishell[38] cyclic peptide-

polymer conjugate nanotubes (CPNTs) were also synthesised, the latter presenting a hydrophobic internal shell and a hydrophilic external shell.

The synthesis of CP-polymer conjugates has been reported using both the grafting-to and the grafting-from methods. Couet *et al*. were the first to grow polymer chains from self-assembling cyclic peptides: CPs modified with ATRP initiators were used to access poly(*N*-isopropyl acrylamide)[31] and poly(butyl acrylate)[39] conjugates. Ten Cate *et al*. reported the first grafting-to synthesis of poly(butyl acrylate) conjugates by carboxylic acid attachment to the lysine residues present on the CP.[32] Later, copper mediated azide alkyne cycloaddition was used, with numerous examples reported in the literature.[33,35-38,40] More recently, Danial *et al*. have reported alternative efficient coupling strategies that avoid the use of copper, whereby polymers were coupled to cyclic peptides using both thiol-ene reactions and active ester chemistry.[41]

Despite the numerous individual approaches to create CP-polymer conjugates, no comprehensive comparison between the grafting-from and the grafting-to approaches has been reported. Therefore we designed this systematic study comparing the two synthetic routes to clearly determine the advantages and disadvantages of each strategy. A schematic overview of this study is displayed in Scheme 2.1.

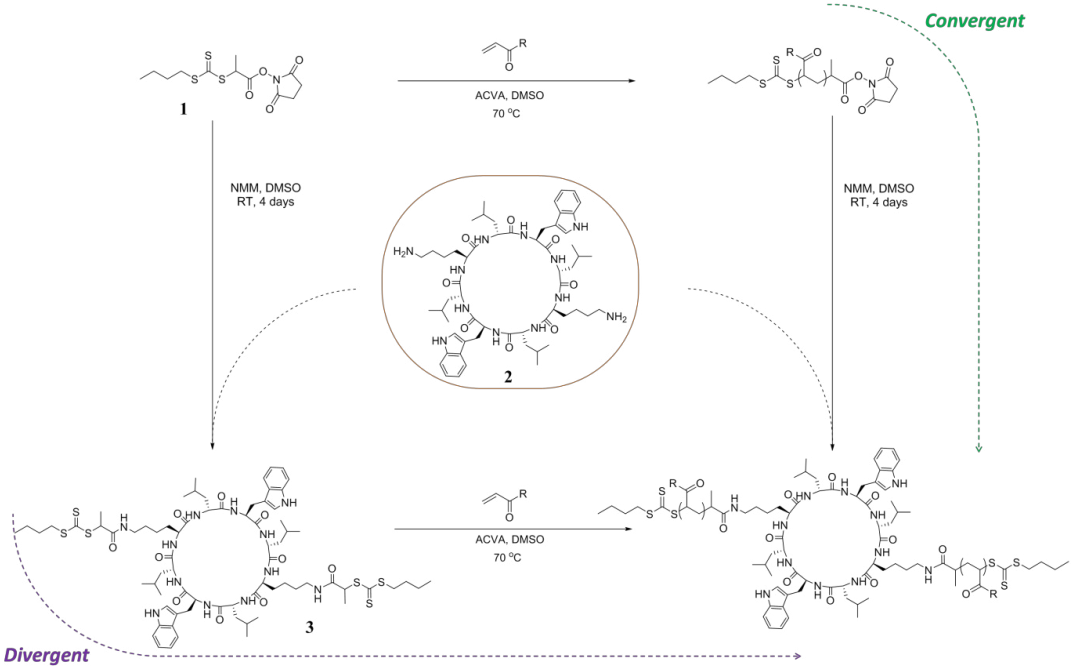

Scheme 2.1: Grafting-to and grafting-from synthetic routes to a cyclic peptide-polymer conjugate.

In both the grafting-from and the grafting-to syntheses, the RAFT (reversible addition-fragmentation chain transfer) process is used to control the polymerisation. The comparison

relies on the analysis of the reactions kinetics, the impact of the molecular weight and, finally, the investigation of conjugates built from different monomers using both routes.

2.2 Results and discussion

2.2.1 Synthesis of the cyclic peptide chain transfer agent

The initial cyclic peptide (CP) **2** (sequence of amino acids: L-Lys(Boc)-D-Leu-L-Trp(Boc)-D-Leu-L-Lys(Boc)-D-Leu-L-Trp(Boc)-D-Leu) and the chain transfer agent (CTA) *N*-hydroxysuccinimide (propanoic acid)yl butyl trithiocarbonate (NHS-PABTC, **1**) were synthesised according to previously reported procedures (see experimental section 2.4).[41] The desired cyclic peptide chain transfer agent $CP(PABTC)_2$ **3** was then obtained by coupling the chain transfer agent **1** to the lysine residues of CP **2** (Scheme 2.1). The fragmenting group of the CTA (so called R-group) was used for conjugation, allowing for the polymer to be grown directly from the peptide. In a Z-group approach, the polymer is capped by the peptide, which can be more sterically demanding and lead to termination events. The coupling reaction was monitored by mass spectrometry, which showed appearance of the mono-functionalised peptide after 1 h, and of the desired product after 4 h. The coupling reaction was quantitative, as no residual CP or mono-functionalised product was detected after 24 h, affording $CP(PABTC)_2$ (**3**) in high yield. Although aminolysis of the trithiocarbonate by the lysine residues is a potential side reaction, no evidence of the corresponding dithiocarbamates was found (Figure 2.1).

Species	$[CP\ 2 + 2H]^{2+}$	$[CP\ 2 + CTA + H]^{+}$	$[CP\ 2 + 2CTA + Na]^{+}$	$[CP\ 2 + 2CTA + NMM]^{+}$
Calculated exact mass	541.3503 ■	1301.6971 ▲	1543.6846 ●	1622.7862

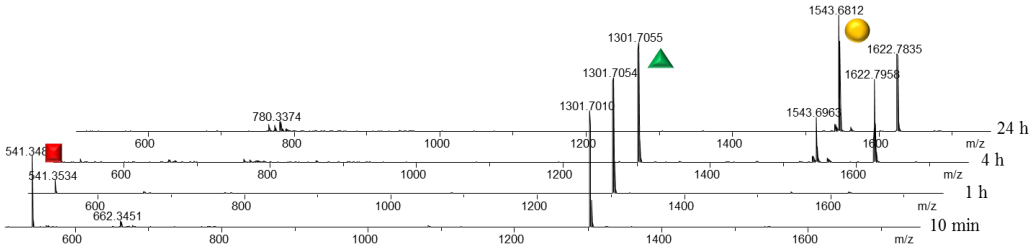

Figure 2.1: Mass spectrometry monitoring of the synthesis of cyclic peptide (propanoic acid)yl butyl trithiocarbonate ($CP(PABTC)_2$).

The ^{1}H NMR of **3** confirmed its structure, as it includes all the signals corresponding to the added CTA (Figure 2.2).

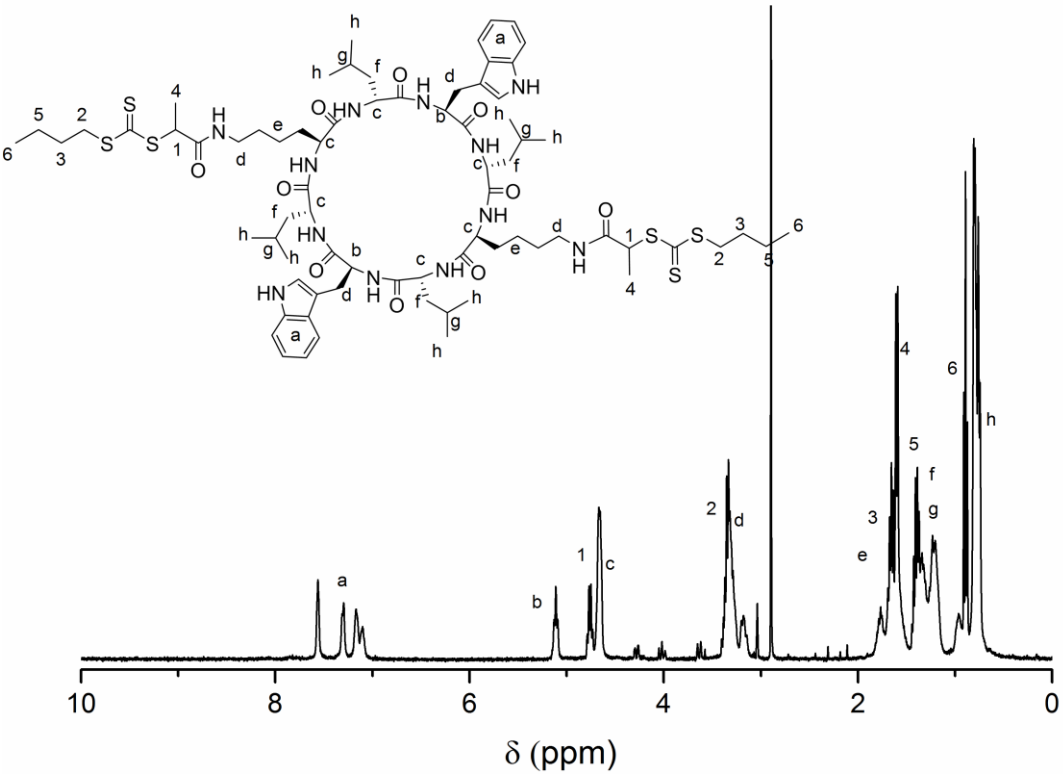

Figure 2.2: ^{1}H-NMR spectrum (TFA-*d*, 400 MHz) of CP(PABTC)$_2$.

2.2.2 Study of polymerisation kinetics using *N*-acryloyl morpholine

An initial study was undertaken to establish optimal polymerisation conditions for the reactions mediated by NHS-PABTC **1** (grafting-to approach) and $CP(PABTC)_2$ **3** (grafting-from approach), using *N*-acryloyl morpholine (NAM) as a model monomer in both cases (Figure 2.3).

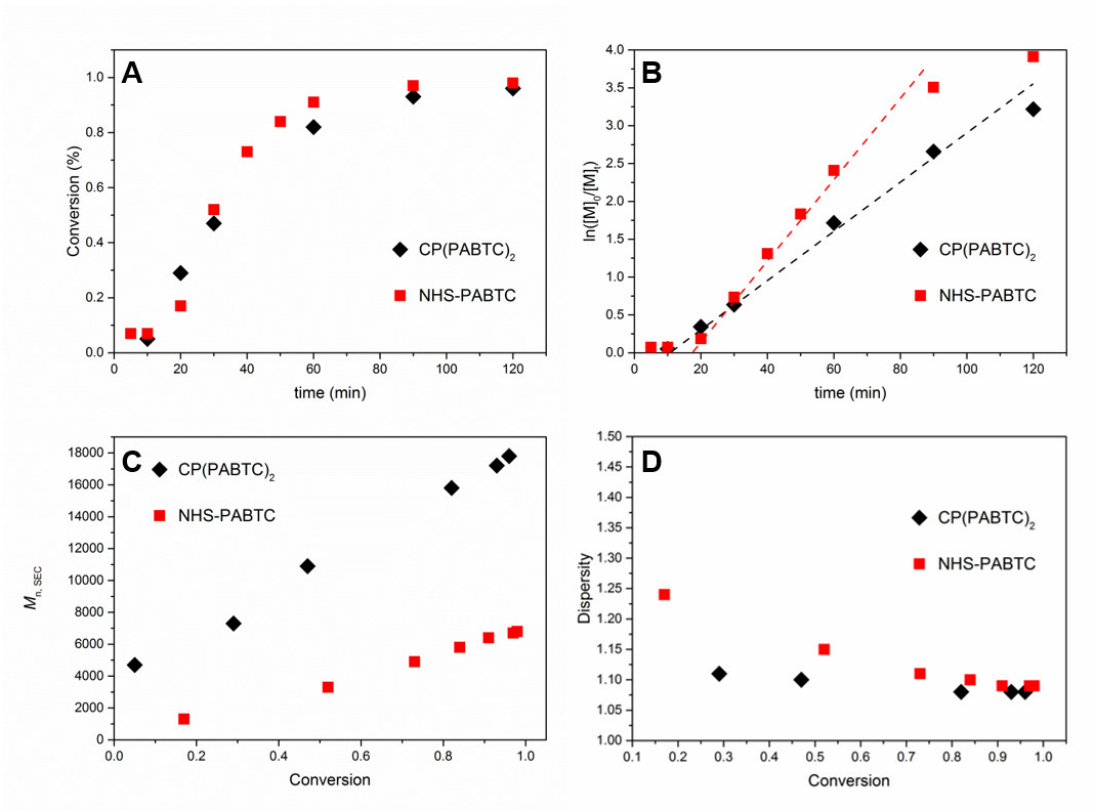

Figure 2.3: Kinetic plots of the polymerisation of NAM mediated by NHS-PABTC (red squares) and $CP(PABTC)_2$ (black diamonds). The dashed lines serves as guide to the eye to highlight the linear region in the plot of $\ln([M]_0/[M]_t)$ *vs* time.

A degree of polymerisation (DP) of 50 per trithiocarbonate group was targeted (corresponding to a total DP of 100 for the bifunctional $CP(PABTC)_2$ **3**, see Table 2.1, runs 3 and 4). Both polymerisations were found to proceed to high conversion (> 95%) in 2 hours, despite a short induction period (10 to 20 min), attributed to initialisation (Figure 2.3 A).[42] The linear behaviour of the $\ln([M]_0/[M]_t)$ *vs* time plot suggests a relatively constant concentration of radicals throughout the polymerisation in both cases (Figure 2.3 B). The apparent rate constant of propagation $k_{p,app}$ appeared slightly lower in the case of the $CP(PABTC)_2$ mediated polymerisation. A linear evolution of molecular weight (Figure 2.3

C) as well as low dispersity values ($Đ$ < 1.1, Figure 2.3 D) were observed for both reactions, suggesting good control over the polymerisation. As was expected, the materials obtained by CP(PABTC)$_2$ **3**, which carries two propagating radicals per CTA, have a higher molecular weight than those obtained from PABTC. When using SEC, the differences in hydrodynamic volume between the samples and the calibration standards make it difficult to clearly correlate the difference in molecular weights. In addition, the presence of the cyclic peptide results in a different architecture, which can at least partially explain the observed results.

Table 2.1: Polymerisations of NAM mediated by NHS-PABTC **1** and CP(PABTC)$_2$ **3**. Reactions were carried out in DMSO at 70°C for 2 hours, using ACVA as initiator, with $[M]_0$ = 2 M.

[M]:[CTA][a]	[CTA]:[I][a,b]	CTA	Monomer conversion[c]	$M_{n,th}$[c] (g.mol^{-1})	$M_{n,SEC}$[d] (g.mol^{-1})	$Đ$
50	20	CP(PABTC)$_2$	86%	7600	11200	1.10
25	40	NHS-PABTC	90%	3400	2900	1.12
100	10	CP(PABTC)$_2$	96%	15100	17800	1.08
50	20	NHS-PABTC	98%	7200	6800	1.09
200	10	CP(PABTC)$_2$	96%	28600	28300	1.09
100	10	NHS-PABTC	99%	14400	11700	1.09

[a] The denomination "CTA" refers to the whole molecule, which is bifunctional in the case of CP(PABTC)$_2$. [b] I: ACVA. [c] Determined by ^{1}H NMR. [d] Determined by SEC using DMF (0.1% LiBr) as eluent, calibrated with pMMA standards.

In order to demonstrate chain end fidelity, chain extension was performed on the conjugate made with **3** by further addition of monomer. A clear shift in the molecular weight distribution was observed (from $M_{n,GPC}$ = 15700, $Đ$ = 1.11 for CP-(pNAM$_{48}$)$_2$ to $M_{n,GPC}$ = 31900, $Đ$ = 1.11 for CP-(pNAM$_{48}$-*b*-pNAM$_{90}$)$_2$) illustrating good chain end group retention (Figure 2.4).

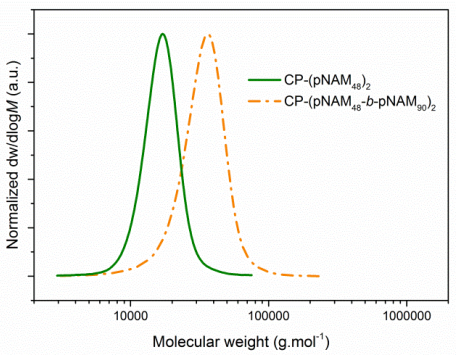

Figure 2.4: Size exclusion chromatograms of the block extension by grafting-from.

2.2.3 Kinetics of polymer conjugation to cyclic peptide

In addition to the polymerisation, or grafting-from, kinetics, the speed and yield of the grafting-to conjugation of $pNAM_{50}$ to the CP **2** were investigated, using two different NHS-functionalised end groups (Scheme 2.2), and the optimised conditions previously determined.[26]

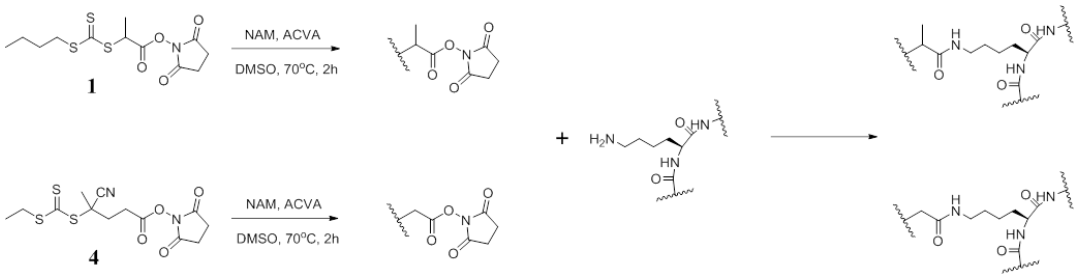

Scheme 2.2: Polymers used in the determination of kinetics of the conjugation to CP **1**.

The grafting efficiency at different time points was calculated in terms of percentage of polymer chains grafted relative to the theoretical maximum, which was measured by deconvoluting the molecular weight distribution (number distribution) of the polymers assuming Gaussian distributions.[43,44]

Although Poisson distributions are accepted models of molecular weight distributions for polymers obtained by living polymerisation, they are typically limited to very narrow dispersities ($Đ$ < 1.05). For controlled radical polymerisation techniques, Gaussian distributions are generally accepted as suitable models to take into account the broadening of the molecular weight distribution due to side reactions of irreversible transfer and termination. In order to quantify the efficiency of the coupling reactions, the number distribution obtained by SEC was deconvoluted using Gaussian curves (Figure 2.5).

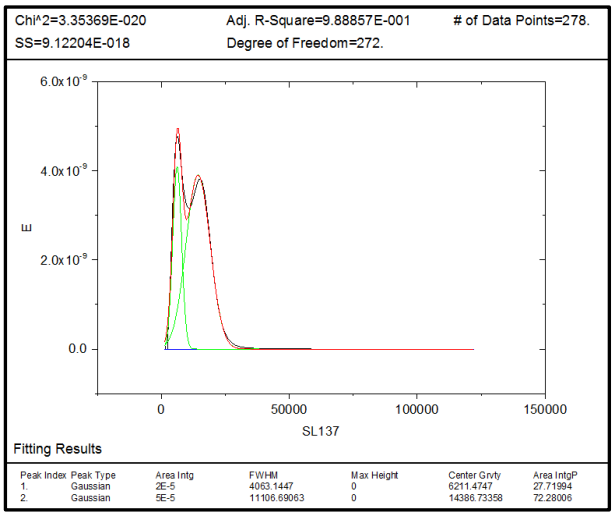

Figure 2.5: Deconvolution of the SEC number distribution for coupling of NHS-pNAM$_{50}$ made with **1** to CP(PABTC)$_2$.

The percentage of conjugated chains was determined using equation 1:

$$\%\ conjugated\ polymer\ chains = \frac{\%\ Area\ conjugate * 2}{\%\ Area\ conjugate * 2 + \%\ Area\ free\ polymer} \quad (1)$$

The polymer was used in slight excess, so the theoretical maximum conjugation is 2/2.2 x100 = 91%.

Conjugation efficiency was calculated as a percentage relative to this maximum value, using equation 2:

$$Conjugation\ efficiency = \frac{\%\ conjugated\ polymer\ chains}{\%\ theoretical\ maximum\ conjugation} \quad (2)$$

The conjugation was found to proceed to its maximum conversion within 96 hours when using NHS-PABTC **1**, while it was completed in under 24 hours with *N*-hydroxysuccinimide-(4-cyano pentanoic acid)yl ethyl trithiocarbonate (NHS-CPAETC, **4**) (Figure 2.6). This difference is most likely due to the nature of the carbon in the α-position of the activated ester functionality, at the α-chain end of the polymer. In the case of NHS-CPAETC, this carbon is secondary, whilst the same carbon atom is tertiary in NHS-PABTC. The reduced steric hindrance facilitates the attack of the amine-bearing lysine residues.[45,46] The lower final conversion observed in the case of NHS-PABTC is likely related to the slow hydrolysis of the active ester group over the extended reaction time.

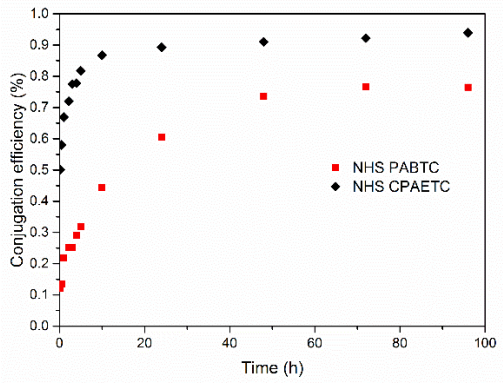

Figure 2.6: Conjugation kinetics of $pNAM_{50}$ to CP **2** using NHS-PABTC **1** (red squares) and NHS-CPAETC **4** (black diamonds) (note: the first sample was taken after 10 minutes).

In the further study NHS-PABTC **1** was used, since it is a more appropriate CTA for the polymerisation of acrylates and acrylamides.[47] However, it should be noted that although the use of activated and α-unsubstituted carboxylic acid end-groups is desirable for efficient and fast conjugation, the influence of the degree of substitution on the stability of the activated ester is still under investigation.

2.2.4 Variation of molecular weight

In extension to the previous kinetic studies, we targeted various DPs in the polymerisation of NAM, to establish whether the length of the polymer chain has an influence on the monomer conversion (Table 2.1), and on the grafting efficiency (Figure 2.7). All polymerisations reached high conversion (> 95% for DP 100, > 85% for DP 25), and the obtained polymers had low dispersities ($Đ$ < 1.12). The slightly lower conversion in the case of a targeted DP of 25 is likely due to the initialisation phenomenon mentioned previously, as lower DPs require larger amounts of CTAs.

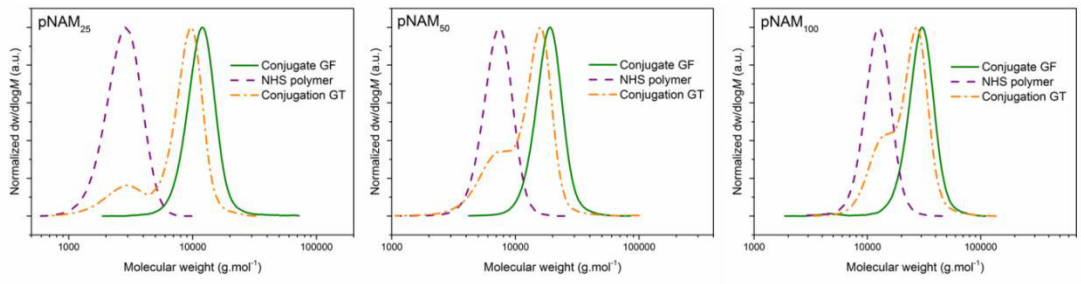

Figure 2.7: SEC chromatograms of NHS-functionalised pNAM (purple dashed lines), CP-pNAM conjugates made by the grafting-from (GF) method (solid green lines) and conjugation of NHS-pNAM to the CP **2** by the grafting-to (GT) strategy (orange dashed lines)..

In order to compare the conjugates obtained by the grafting-from and grafting-to methods, the polymers made with NHS-PABTC **1** were grafted to CP **2** (Scheme 2.1). In all three cases, the conjugates obtained by the grafting-to method are similar to the one obtained by the grafting-from strategy (Figure 2.7).

The small difference in molecular weight observed between the two types of conjugates can be attributed to errors arising from accurately weighing the very small amounts of cyclic peptide CTA required to mediate polymerisation in the case of the grafting-from strategy. The grafting efficiency was calculated as a percentage of polymer chains grafted relative to the theoretical maximum, obtained by deconvoluting the molecular weight distribution (number distribution) of the polymers assuming Gaussian distributions (Table 2.2).[43,44]

Table 2.2: Conjugation efficiencies calculated by deconvolution.

Polymer	% Area polymer	% Area conjugate	% Conjugated polymer chains	Conjugation efficiency
$pNAM_{25}$	41	59	74%	82%
$pNAM_{50}$	46	54	70%	77%
$pNAM_{100}$	35	65	79%	87%
pBA_{50}	50	50	67%	73%
$pNIPAM_{50}$	52	48	65%	71%
$pHEA_{50}$	28	72	84%	92%
$pPEGA_{50}$	46	54	70%	77%
$pMMA_{50}$	21	79	88%	97%

There was no clear trend in the grafting efficiency related to the length of the polymer chains (82% for $pNAM_{25}$, 77% for $pNAM_{50}$, 87% for $pNAM_{100}$), which suggests that steric hindrance related to the length of the polymer chain does not affect the grafting reaction within the tested range of DPs.

2.2.5 Influence of monomers

In order to examine how the nature of the polymer influences the conjugation, a wider range of monomers, namely hydrophobic (butyl acrylate, BA), temperature responsive (*N*-isopropylacrylamide, NIPAM) and hydrophilic (hydroxyethyl acrylate, HEA, (polyethylene glycol) acrylate methyl ether 480, PEGA) acrylic monomers, hydrophobic (methyl methacrylate, MMA) and pH responsive (dimethylaminoethyl methacrylate, DMAEMA) methacrylic monomers, was studied.

In the polymerisation of acrylic monomers (Table 2.3), excellent control ($Đ$ < 1.16) was obtained with NHS-PABTC **1** (Figure 2.8, dashed lines). However, when using the peptide based CP(PABTC)$_2$ **3** (Figure 2.8, solid lines), only the polymerisation of NIPAM was found to be similarly well controlled ($Đ$ = 1.09). The dispersity was slightly higher for BA and HEA, but remains below 1.3, which still conforms to a high degree of control. However, the polymerisation of PEGA lead to a considerably broader distribution ($Đ$ = 3.75). This is likely caused by the sterically demanding size of the monomer. Keeping in mind that the cyclic peptides assemble into nanotubes, the addition of a new monomer to the active chain-end may be hindered, and the necessary equal probability of chain growth will be lost.

Table 2.3: Polymerisation of acrylate and acrylamide monomers mediated by NHS-PABTC **1** and CP(PABTC)$_2$ **3**. Unless otherwise stated, reactions were carried out in DMSO at 70°C, using ACVA as initiator, with $[M]_0$ = 2 M and targeting a DP 50.

Monomer	Reaction time (h)	CTA	Monomer conversion[a]	$M_{n,th}$[a] (g.mol^{-1})	$M_{n,SEC}$[b] (g.mol^{-1})	$Đ$
BA[c]	2	CP(PABTC)$_2$	70%	10500	12800	1.24
BA[c]	2	NHS-PABTC	75%	5100	6000	1.13
NIPAM	2	CP(PABTC)$_2$	74%	9900	17600	1.09
NIPAM[d]	2	NHS-PABTC	82%	4900	6800	1.09
HEA	1.5	CP(PABTC)$_2$	76%	10800	21700	1.29
HEA	1.5	NHS-PABTC	83%	4900	9100	1.10
PEGA[e]	3	CP(PABTC)$_2$	92%	45700	34600	3.75
PEGA[e]	3	NHS-PABTC	82%	20000	16600	1.16

[a] Determined by ^{1}H NMR. [b]Determined by SEC using DMF (0.1% LiBr) as eluent, calibrated with pMMA standards. [c] Solvent: DMF. [d] Solvent: dioxane. [e] $[M]_0$ = 1 M.

Conjugations of the polymers made with NHS-PABTC **1** to the CP **2** were found to yield conjugates comparable to those made by the grafting-from approach (except in the case of PEGA). The conjugation of pHEA was the most efficient (92%), while conjugation of

pNIPAM and pBA proceeded to 70% efficiency (Table 2.2). Due to insolubility of pBA in DMSO, these reactions were conducted in DMF. It is noteworthy to mention that the grafting-to approach enables access to well-defined pPEGA conjugates (with efficiency > 75%), suggesting a greater flexibility of the grafting-to method with regards to sterically demanding monomers.

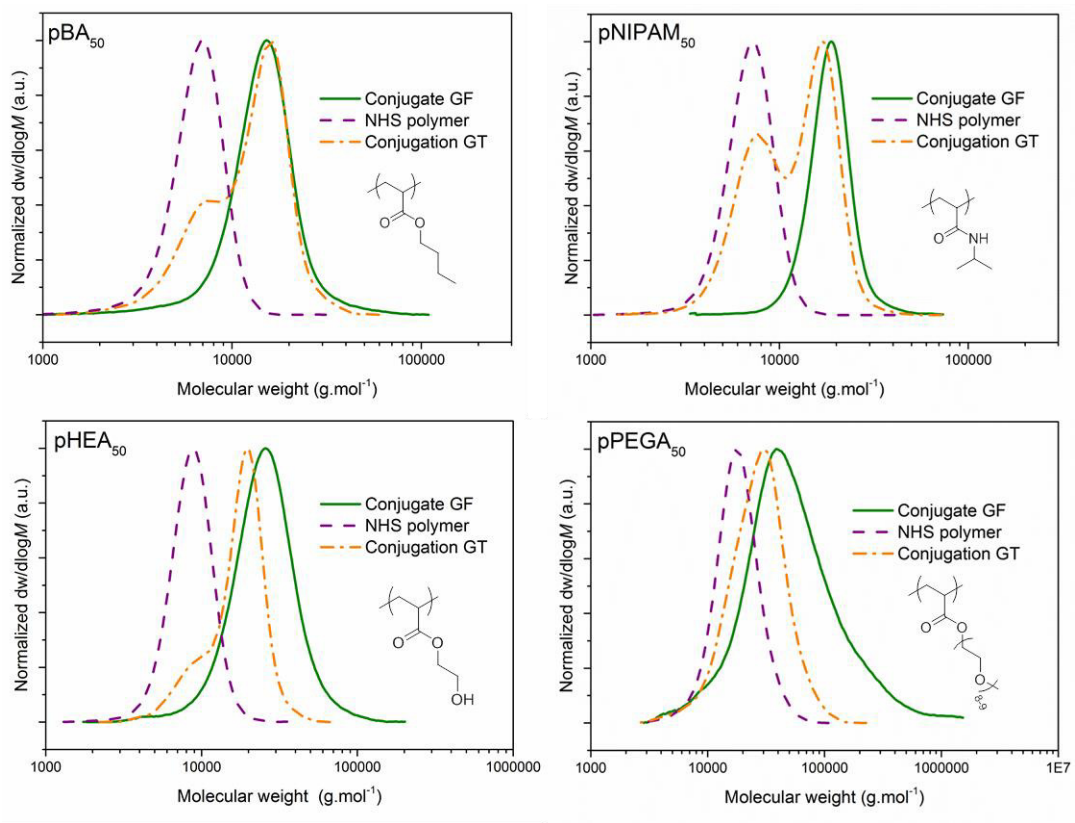

Figure 2.8: SEC chromatograms of NHS-functionalised polymers (purple dashed lines), CP-polymer conjugates made by the grafting-from (GF) method (plain green lines) and conjugation of NHS polymers to the CP **2** by the grafting-to (GT) strategy (orange dashed lines).

Taking this study a step further, methacrylate-based polymers were studied. Controlled polymerisation of methacrylates is not possible using a PABTC-based RAFT agent, due to the secondary nature of the R-group reinitiating radical.[48] Hence, CP(CPAETC)$_2$ **5** (Scheme 2.3) was synthesised from CP **2** and an active ester functionalised CPAETC-based CTA, following a similar protocol to that used in the synthesis of CP(PABTC)$_2$ **3**.

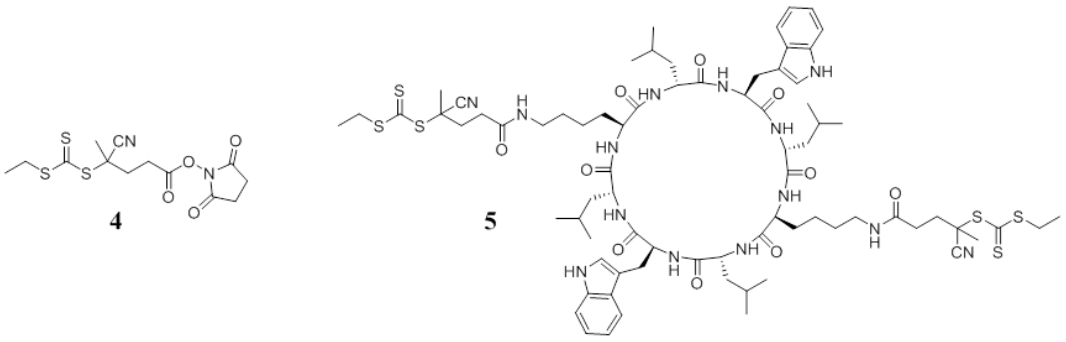

Scheme 2.3: Chain transfer agents used to mediate the polymerisation of methacrylates.

As with the previous examples, the polymerisations of the hydrophobic methyl methacrylate (MMA) and hydrophilic and pH responsive dimethylaminoethyl methacrylate (DMAEMA) were performed using both NHS-CPAETC **4** and the peptide attached analogue CP(CPAETC)$_2$ **5** for comparison (Table 2.4). The polymerisation times were increased to 12h to compensate for the lower rate constant of propagation (k_p) of methacrylate monomers. This longer reaction time allowed for conversion values > 80%, while the obtained polymers still had well controlled molecular weight distributions ($Đ$ < 1.2).

Table 2.4: Polymerisation of methacrylate monomers mediated by NHS-CPAETC **4** and CP(CPAETC)$_2$ **5**. Reactions were carried out in DMSO at 70°C, using ACVA as initiator, with $[M]_0$ = 2 M and targeting a DP 50.

Monomer	Reaction time (h)	CTA	Monomer conversion[a]	$M_{n,th}$[a] (g.mol^{-1})	$M_{n,SEC}$[b] (g.mol^{-1})	$Đ$
MMA	12	CP(CPAETC)$_2$	91%	11800	15900	1.11
MMA	12	NHS-CPAETC	80%	4400	4800	1.13
DMAEMA	12	CP(CPAETC)$_2$	89%	15600	22700	1.19
DMAEMA	12	NHS-CPAETC	95%	7800	13000	1.11

[a] Determined by ^{1}H NMR. [b]Determined by SEC using DMF (0.1% LiBr) as eluent, calibrated with pMMA standards.

The NHS-functionalised polymers were further conjugated to CP **2** (Figure 2.9,Table 2.2). In the case of pMMA, an excellent grafting efficiency was observed (97%). However, no product was obtained when attempting the conjugation of pDMAEMA to CP **2**. It is likely that the chain end functionality of the pDMAEMA is lost during polymerisation, due to the basic nature of the monomer, which could catalyse the hydrolysis of the activated ester end-group. This particular case highlights the advantages of the grafting-from method.

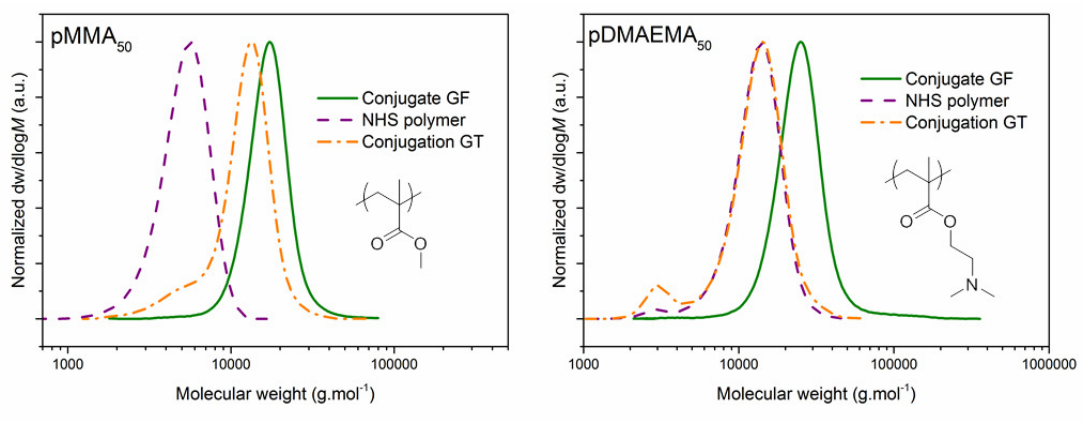

Figure 2.9: SEC chromatograms of NHS-functionalised polymers (purple dashed lines), CP-polymer conjugates made by the grafting-from (GF) method (plain green lines) and conjugation of NHS polymers to the CP **2** by the grafting-to (GT) strategy (orange dashed lines).

2.3 Conclusions

Two synthetic pathways leading to cyclic peptide-polymer conjugates were explored and compared. A range of functional monomers was polymerised from, and grafted to, a cyclic peptide, using an active ester ligation strategy. Initial kinetic studies using a cyclic peptide modified with CTA groups clearly revealed an excellent control of the polymerisation without the appearance of any detectable termination reaction. With the exception of PEGA, where polymerisation from the peptide was not controlled due to steric hindrance, all tested monomers led to well defined grafting-from conjugates ($Đ$ = 1.29 for HEA, $Đ$ < 1.25 in all other cases) within two hours. The grafting-to counterparts of these conjugates were obtained after polymerisation using an NHS-functionalised CTA, followed by an active ester coupling to the cyclic peptide. Comparing two different CTAs, NHS-PABTC **1** and NHS-CPAETC **4**, which bear an α-methylated and an α-unsubstituted ester function, respectively, we observed a considerably enhanced speed of conjugation for the latter, less hindered RAFT agent. Varying the type of monomer, conjugation efficiency was found to be best for MMA and HEA (97% and 92% grafting, respectively), but lower for NIPAM and PEGA (71% and 77%, respectively). In the case of DMAEMA, grafting-to gave no product and, thus, the implementation of the grafting-from method allowed for the preparation of conjugates otherwise unreachable by an active ester grafting-to pathway.

Generally comparing the two investigated synthetic routes, the grafting-from approach permits pure conjugate synthesis (no unreacted polymeric chains remain in the sample) to be

achieved in faster reaction times. This approach is, however, dependent on the availability of a solvent that can solubilise the peptide, the monomer and the resulting conjugate. It is also unfavourable when attempting to control the polymerisation of bulky monomers such as PEGA. On the other hand, the grafting-to strategy remains more flexible in terms of choice of solvent and scalability, and also enables a modular approach to design peptide conjugates, using different combinations of peptides and polymers. Nevertheless, purification to remove excess or unreacted polymer remains a challenge, and the reactivity of some monomers can be an obstacle for an efficient conjugation. In summary, this work demonstrates that both techniques carry advantages and disadvantages, but are complementary in nature, and their combination gives access to a large variety of well-defined cyclic peptide-polymer conjugates.

2.4 Experimental

2.4.1 Materials

Bromo-propionic acid (>99%), 1-butanethiol (99%), carbon disulfide (>99%), ethanethiol (97%), 2-hydroxyethyl acrylate (96 %), *N*-acryloylmorpholine (NAM, 97 %), poly(ethylene glygol) methyl ether acrylate 480, *N*-isopropyl acrylamide (97 %), butyl acrylate, methyl methacrylate, 2-(dimethylamino)ethyl methacrylate, *N*-hydroxysuccinimide (98 %), 4-dimethylaminopyridine (DMAP, 99 %), pentafluorophenol (PFP, >99%), triisopropylsilane (TIPS, 99 %), deuterated solvents for NMR and aluminum oxide were purchased from Sigma-Aldrich. 1,1,1,3,3,3-Hexafluoroisopropanol (HFIP, 99 %) and iodine were purchased from Acros Organics. *N*-methylmorpholine (NMM, 99 %) and piperidine were purchased from Alfa Aesar. Sodium hydroxide pellets, sodium thiosulfate pentahydrate and anhydrous magnesium sulfate ($MgSO_4$) were purchased from Fisher Scientific. *N,N*-diisopropylethylamine (DIPEA, 99 %), was purchased from Merck. 4,4′-Azobis(4-cyanovaleric acid) (ACVA) was purchased from MP Biomedicals. Fmoc-D-Leu-OH, Fmoc-L-Lys-OH, Fmoc-L-Trp(Boc)-OH, *O*-(benzotriazole-1-yl)-*N,N,N',N'*-tetramethyluronium hexafluorophosphate (HBTU), 2-chlorotrityl chloride resin (100-200 mesh) and 1-ethyl-3-(3-dimethylaminopropyl)carbodiimide (EDC) were purchased from Iris Biotech and used as received. All solvents were bought from commercial sources and used as received. The cyclisation coupling agent DMTMM·BF_4 was synthesised according to an established literature method.[49]

2.4.2 Characterisation

NMR spectra were recorded on Bruker DPX-300, DPX-400 and HD-500 instruments. Mass spectrometry measurements were performed on a Bruker MicroToF for ESI ToF and on an Agilent 6130B Single Quad for ESI. Molecular weight distributions and dispersities were assessed by size exclusion chromatography (SEC) on an Agilent PL50 instrument equipped with differential refractive index (DRI) and UV detectors. The system was equipped with 2 x PolarGel M columns (300 x 7.5 mm) and a PolarGel 5 µm guard column. The eluent is DMF with 0.1 % LiBr additive. Samples were run at 1 mL/min at 50'C. Poly(methyl methacrylate) standards (Agilent EasyVials) were used for calibration. Analyte samples were filtered through a nylon membrane with 0.22 µm pore size before injection. Respectively, experimental molar mass (M_n) and dispersity ($Đ$) values of synthesized polymers were determined by conventional calibration using Agilent GPC/SEC software.

2.4.3 Synthesis

Please refer to Appendix A for NMR spectra.

2.4.3.1 Synthesis of (propanoic acid)yl butyl trithiocarbonate (PABTC)

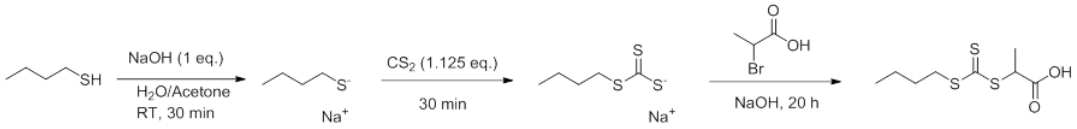

A 50% w/w aqueous sodium hydroxide solution (4.4 g, 2.2 g NaOH, 55 mmol) was added to a stirred mixture of butanethiol (5 g, 5.9 mL, 55 mmol) and water (8.5 mL). Acetone (2.8 mL) was then added, and the resulting clear solution was stirred for 30 min at room temperature. Carbon disulfide (4.75 g, 1.125 eq., 62.4 mmol) was added and the resulting orange solution was stirred for 30 min, then cooled to < 10 °C. 2- Bromopropionic acid (8.69g, 1.025 eq., 56.8 mmol) was slowly added under temperature supervision, followed by the slow addition of a 50% w/w aqueous NaOH solution (4.5 g, 2.25 g NaOH, 57 mmol). When the exotherm stopped, water (8 mL) was added and the reaction was left to stir at RT for 20 hours. More water (15 mL) was then added to the reaction mixture, which was cooled below 10 °C. A 10 M solution of HCl was slowly added, keeping the temperature below 10 °C and stopping when pH reached 3. The orange solid separated, crystallised and was recovered by filtration under reduced pressure. Yield: 55% (7.2 g, 30.3 mmol). ^{1}H-NMR ($CDCl_3$, 300 MHz, pm): δ = 4.88 (q, 1H, J = 9 Hz, CH(CH_3)), 3.39 (t, 2H, J = 9 Hz, S-CH_2-CH_2), 1.70 (m, 2H, S-CH_2-CH_2-CH_2), 1.64 (d, 3H, J = 9 Hz, CH(CH_3)), 1.44 (m, 2H, CH_2-CH_2-CH_3), 0.94 (t, 3H, J = 9 Hz, CH_2-CH_3). ^{13}C-NMR ($CDCl_3$, 125 MHz, ppm): δ = 221.5,

177.5, 47.5, 37.0, 29.8, 22.0, 16.5, 13.5. MS (ESI): $[M+H]^+$ calculated: 261.0, found: 260.9. MP: 53-55ºC.

2.4.3.2 Synthesis of *N*-hydroxysuccinimide-(propanoic acid)yl butyl trithiocarbonate (NHS-PABTC)

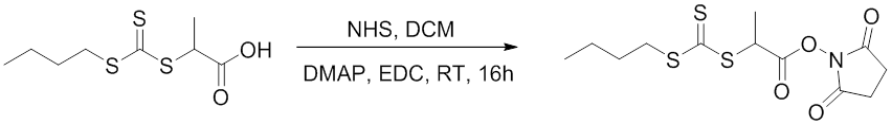

PABTC (1.016 g, 4.27 mmol), *N*-hydroxysuccinimide (1.2 eq., 0.59 g, 5.12 mmol) and DMAP (0.1 eq., 52 mg, 0.43 mmol) were dissolved in DCM (20 mL) and stirred. In a separate vessel EDC (1.2 eq., 0.982 g, 5.12 mmol) was dissolved in DCM (50 mL) and this solution was added dropwise over 15 minutes to the solution containing the chain transfer agent. The mixture was stirred for 16 hours at room temperature. Subsequently, the DCM was evaporated and the crude product redissolved in diethyl ether. The orange mixture was washed with a saturated solution of $NaHCO_3$ (2 x 40 mL) and water (2 x 40 mL). The oraganic phases were collected and dried with $MgSO_4$. The volume was reduced *via* rotary evaporation after which silica flash chromatography was performed in hexane:ethyl acetate, with the content of ethyl acetate varying from 20% to 80% over 30 min. The purified NHS-PABTC chain transfer agent was isolated as a yellow oil. Yield: 49% g (0.7 g, 2.07 mmol). ^{1}H-NMR ($CDCl_3$, 300 MHz, ppm): δ = 5.15 (q, 1H, *J* = 9 Hz, C*H*(-CH_3)), 3.39 (t, 2H, *J* = 9 Hz, S-C*H*$_2$-CH_2), 2.83 (s, 4H, succinimidyl C*H*$_2$-C*H*$_2$), 1.75 (d, 3H, *J* = 9 Hz, CH(C*H*$_3$)), 1.70 (m, 2H, CH_2-C*H*$_2$-CH_2), 1.44 (m, 2H, CH_2-C*H*$_2$-CH_3), 0.94 (t, 3H, *J* = 9 Hz, CH_2-C*H*$_3$). ^{13}C-NMR ($CDCl_3$, 125 MHz, ppm): δ = 220.2, 168.6, 167.2, 45.0, 37.2, 29.8, 25.5, 22.0, 16.6, 13.5. MS (ESI): $[M+H]^+$ calculated: 335.03, found: 334.9.

2.4.3.3 Synthesis of bis-(ethylsulfanylthiocarbonyl) disulfide

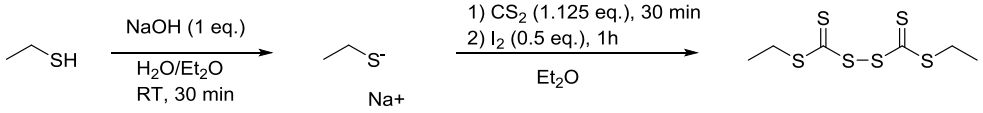

To a solution of ethanethiol (5 mL, 67.5 mmol) in diethyl ether (145 mL) under strong stirring was added an aqueous solution of sodium hydroxide (8 mL containing 2.70 g, 67.5 mmol of NaOH). The clear, colourless solution was stirred for 30 min, then treated with carbon disulfide (1.125 eq., 4.6 mL, 75.9 mmol) to yield an orange solution. After a further 30 min of stirring, the mixture was further reacted by slow addition of iodine (0.5 eq., 8.57 g, 33.75 mmol). After one hour, the ether phase was washed two times with an aqueous

sodium thiosulfate solution and once with water, dried on $MgSO_4$ and concentrated under reduced pressure. The crude product was used in the next step without purification.

2.4.3.4 Synthesis of (4-cyano pentanoic acid)yl ethyl trithiocarbonate (CPAETC)

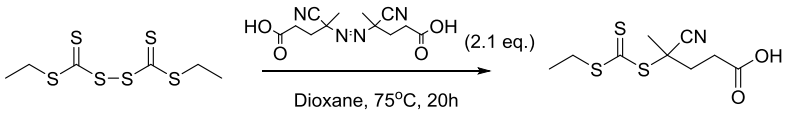

To a solution of bis-(ethylsulfanylthiocarbonyl) disulfide (8.01 g, 29.2 mmol) in dioxane (200 mL), 4,4'-azobis(4-cyanovaleric acid) (17.17 g, 2.1 eq., 61.26 mmol) was added and the mixture was stirred for 20 hours at 75 °C. After removal of the solvent under reduced pressure, a silica flash chromatography was performed in hexane:ethyl acetate with content of ethyl acetate varying from 0% to 80% over 30 min. After drying under vacuum, an orange powder was obtained. ^{1}H-NMR ($CDCl_3$, 300 MHz, ppm): δ = 3.35 (q, 2H, *J* = 9 Hz, S-C*H*$_2$-CH_3), 2.8-2.3 (m, 4H, C(O)-C*H*$_2$-C*H*$_2$-), 1.89 (s, 3H, C(CN)(C*H*$_3$)), 1.36 (t, 3H, *J* = 9 Hz, CH_2-C*H*$_3$). ^{13}C-NMR ($CDCl_3$, 125 MHz, ppm): δ = 216.9, 177.3, 118.9, 46.2, 33.4, 31.4, 29.5, 24.8, 12.7. MS (ESI): $[M+Na]^+$ calculated: 286.0, found: 285.9. MP: 62-64 ºC.

2.4.3.5 Synthesis of *N*-hydroxysuccinimide-(4-cyano pentanoic acid)yl ethyl trithiocarbonate (NHS-CPAETC)

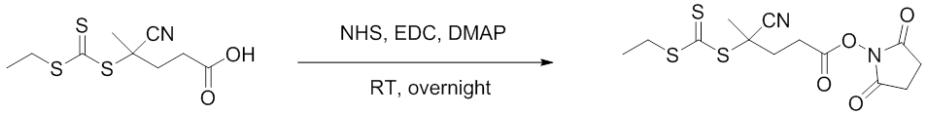

CPAETC (1 g, 3.80 mmol) was dissolved in DCM (20 mL). *N*-hydroxysuccinimide (0.52 g, 1.2 eq., 4.56 mmol) and DMAP (46 mg, 0.1 eq., 0.38 mmol) were added to the stirring mixture. In a separate vial, EDC (0.87 g, 1.2 eq., 4.56 mmol) was dissolved in DCM (10 mL) and slowly added to the previous one. The resulting mixture was stirred at room temperature for 16 hours, and washed with water (2 x 75 mL) and brine (2 x 75 mL). The organic phases were combined, dried on $MgSO_4$ and the solvent evaporated under reduced pressure. Silica flash chromatography was performed in hexane:ethyl acetate with content of ethyl acetate varying from 20% to 80% over 30 min. The purified NHS-CPAETC was isolated as a yellow powder. Yield: 81% (1.11g, 3.07 mmol). ^{1}H-NMR ($CDCl_3$, 300 MHz, ppm): δ = 3.35 (q, 2H, *J* = 9 Hz, S-C*H*$_2$-CH_3), 2.94 (t, 2H, *J* = 9 Hz, C(O)-C*H*$_2$-CH_2), 2.86 (s, 4H, *J* = 9 Hz, succinimidyl C*H*$_2$-C*H*$_2$), 2.76-2.46 (m, 2H, C(O)-CH_2-C*H*$_2$), 1.89 (s, 3H, C(CN)(C*H*$_3$)), 1.37 (t, 3H, *J* = 9 Hz, CH_2-C*H*$_3$). ^{13}C-NMR ($CDCl_3$, 125 MHz, ppm): δ =

216.3, 168.8, 167.0, 118.6, 45.9, 33.1, 31.4, 26.8, 25.5, 24.7, 12.7. MS (ESI): $[M+Na]^+$ calculated: 383.0, found: 382.9. MP: 122-126 ºC.

2.4.3.6 Synthesis of pentafluorophenol-(4-cyano pentanoic acid)yl ethyl trithiocarbonate (PFP-CPAETC)

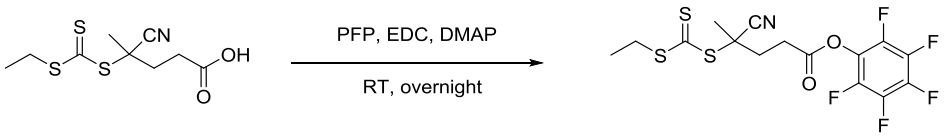

CPAETC (2 g, 7.59 mmol) was dissolved in DCM (25 mL). Pentafluorophenol (1.68 g, 1.2 eq., 9.11 mmol) and DMAP (93 mg, 0.1 eq., 0.76 mmol) were added to the stirring mixture, then a solution of EDC (1.75 g, 1.2 eq., 9.11 mmol) in DCM (15 mL) was slowly added. The resulting mixture was stirred at room temperature for 16 hours, washed with a saturated $NaHCO_3$ solution (2 x 40 mL) and with water (2 x 40 mL). The aqueous phases were re-extracted with 40 mL DCM. The organic phases were combined, dried on $MgSO_4$ and the solvent was evaporated under reduced pressure. A silica flash chromatography was performed in hexane:ethyl acetate with content of ethyl acetate varying from 0% to 10% over 30 min. The purified PFP-CPAETC was isolated as an orange powder/oil (melting point around RT). Yield: 45% (1.45g, 3.4 mmol). ^{1}H-NMR ($CDCl_3$, 300 MHz, ppm): δ = 3.37 (q, 2H, *J* = 9 Hz, S-C*H*$_2$-CH$_3$), 3.02 (t, 2H, *J* = 9 Hz, C(O)-C*H*$_2$-CH$_2$), 2.77-2.46 (m, 2H, C(O)-CH$_2$-C*H*$_2$), 1.94 (s, 3H, C(CN)(C*H*$_3$)), 1.38 (t, 3H, *J* = 9 Hz, CH$_2$-C*H*$_3$). ^{13}C-NMR ($CDCl_3$, 125 MHz, ppm): δ = 216.3, 167.7, 142.1, 140.7, 139.9, 138.6, 136.9, 118.7, 46.0, 33.4, 31.4, 29.0, 24.9, 12.7. ^{19}F-NMR ($CDCl_3$, 300 MHz, ppm): δ = -153 (d, *J* = 18 Hz, 2F), -158 (t, *J* = 22 Hz, 1F), -162 (dd, J_1 = 18 Hz, J_2 = 22 Hz, 2F). MS (ESI ToF): $[M+Na]^+$ calculated: 451.9848, found: 451.9870.

2.4.3.7 Synthesis of linear peptide

Solid phase synthesis of linear peptide H_2N-L-Lys(Boc)-D-Leu-L-Trp(Boc)-D-Leu-L-Lys(Boc)-D-Leu-L-Trp(Boc)-D-Leu-COOH was performed on a 2-chlorotrityl resin (0.50 g, resin loading 1.1 mmol·g^{-1}) in a 10 mL sinter-fitted syringe. The resin was allowed to swell for 30 minutes using anhydrous dichloromethane (DCM, 4 mL). After draining the DCM, a solution containing Fmoc-D-Leu-OH (2 eq., 0.39 g, 1.1 mmol) and DIPEA (4 eq./amino acid, 0.57 g, 4.4 mmol) in DCM (2 mL) was bubbled with N_2 for 15 min then added to the resin and agitated for 2 hours at room temperature. Following draining of the solution, the resin was washed with a mixture of DCM / DIPEA / methanol (17:1:2, 3 x 4 mL) to cap any unreacted sites on the resin, then washed with DCM (3 x 4 mL), DMF (3 x 4 mL) and DCM

(3 x 4 mL) once more, after which the resin was dried under reduced pressure. Loading content was determined by deprotecting a sample of the dried resin (5.7 mg) by agitating in 20 % piperidine in DMF (1 mL, 25 min). The resulting solution was diluted by a factor of 100 with DMF and UV-Vis was used to correlate molarity with the absorption of the Fmoc group at λ = 301 nm (ε = 7800 $M^{-1} \cdot cm^{-1}$). The loaded resin (0.30 g, 0.218 mmol) was transferred to a sintered syringe, and swollen in DCM for 30 min. Following the draining of the DCM, the resin was washed with DMF, and the Fmoc groups were removed by addition of 20% piperidine in DMF (2 x 10 mL; 5 min each). After removal of the deprotecting solution, the resin was washed with DMF (3 x 4 mL), DCM (3 x 4 mL) and further DMF (3 x 4 mL). For subsequent coupling reactions, solutions containing the Fmoc-amino acid (3 eq., 0.653 mmol), HBTU (3.1 eq., 0.675 mmol) and DIPEA (6 eq., 1.307 mmol) in DMF (2 mL) were prepared, bubbled with N_2 for 15 min and added to the resin. The coupling reaction was allowed to proceed at ambient temperature for 3 hours. Deprotection and addition steps were repeated to obtain the desired octapeptide. After completion of the amino acid coupling reactions and removal of the final Fmoc protecting group using 20 % piperidine in DMF, the peptide was cleaved from the resin using a solution of 20% HFIP in DCM (3 x 8 mL; 10 min each). The resin was washed with DCM (3 x 4 mL) and the filtrate was concentrated under reduced pressure to yield the linear peptide as an off-white solid. Yield 0.40 g (quantitative). ^{1}H-NMR (400 MHz, TFA-*d*, ppm): δ = 8.07 (m, 2H, Trp), 7.54-7.22 (m, 8H, Trp), 5.11 (m, 2H, H_α Trp), 4.68-4.48 (m, 5H, H_α Leu and H_α Lys), 4.21 (m, 1H, H_α Lys N-end), 3.32-3.03 (m, 8H, CH_2 Trp and CH_2-NH Lys), 2.07-0.86 (m, 60H, CH_2-CH_2-CH_2 Lys, CH_2-CH Leu, $C(CH_3)_3$ Boc), 0.85-0.58 (m, 24H, CH_3 Leu), NH signals not observed. MS (ESI): $[M+H]^+$ calculated: 1498.9, found 1498.9.

2.4.3.8 Cyclisation of linear peptide

Linear peptide (200 mg, 0.127 mmol) was dissolved in DMF (20 mL) and N_2 was bubbled through the solution for 20 min. DMTMM·BF_4 (1.2 eq., 51 mg, 0.152 mmol) was dissolved in DMF (5 mL) with N_2 bubbled through the solution for 20 min, and was then added dropwise to the linear peptide solution. The mixture was stirred under an atmosphere of N_2 for 5 days. The DMF solution was reduced to a volume of ~ 1 mL under reduced pressure, and methanol (20 mL) was added. Aliquots of the suspension were distributed into 2 mL Eppendorf tubes and centrifuged at 10000 rpm for 4 minutes using a benchtop centrifuge. After discarding the supernatant, the pellets were resuspended in methanol. The Eppendorf tubes were centrifuged once more and the supernatant discarded. The pellets were resuspended in methanol and the solvent was evaporated under reduced pressure to yield the

Boc-protected cyclic peptide in the form of a white powder. Yield 73 % (138 mg, 0.093 mmol). ^{1}H-NMR (400 MHz, TFA-*d*, ppm): δ = 8.07 (m, 2H, Trp), 7.54-7.22 (m, 8H, Trp), 5.15 (m, 2H, H_α Trp), 4.79-4.52 (m, 6H, H_α Leu and H_α Lys), 3.29-2.96 (m, 8H, CH_2 Trp and C*H*$_2$-NH Lys), 2.07-0.86 (m, 60H, CH_2-CH_2-CH_2 Lys, CH_2-CH Leu, $C(CH_3)_3$ Boc), 0.85-0.58 (m, 24H, CH_3 Leu), NH signals not observed. MS (ESI) $[M+Na]^+$ calculated: 1503.89, found: 1503.8.

2.4.3.9 Deprotection of cyclic peptide

Boc-protected cyclic peptide was treated with a cleavage cocktail consisting of TFA:triisopropylsilane:water (18:1:1 v/v/v, 5 mL) for 2 hours. The Boc-deprotected cyclic peptide was isolated from the cleavage cocktail by precipitation in ice-cold diethyl ether. The suspended precipitate was distributed into 2 mL Eppendorf tubes and isolated *via* centrifugation at 1000 rpm. The supernatant was discarded and the pellet was washed with diethyl ether and centrifuged 2-fold after which the solvent was evaporated under reduced pressure to yield a white powder. Yield: 124 mg (quantitative). ^{1}H-NMR (400 MHz, TFA-*d*, ppm): δ = 7.64-6.60 (m, 10H, Trp), 5.16 (m, 2H, H_α Trp), 4.73 (m, 6H, H_α Leu and H_α Lys), 3.29-2.96 (m, 8H, CH_2 Trp and C*H*$_2$-NH Lys), 2.07-0.86 (m, 24H, CH_2-CH_2-CH_2 Lys, CH_2-CH Leu,), 0.85-0.58 (m, 24H, CH_3 Leu), NH signals not observed. MS (ESI) $[M+Na]^+$ calculated: 1103.67, found: 1103.5.

2.4.3.10 Cyclic peptide (propanoic acid)yl butyl trithiocarbonate (CP(PABTC)$_2$)

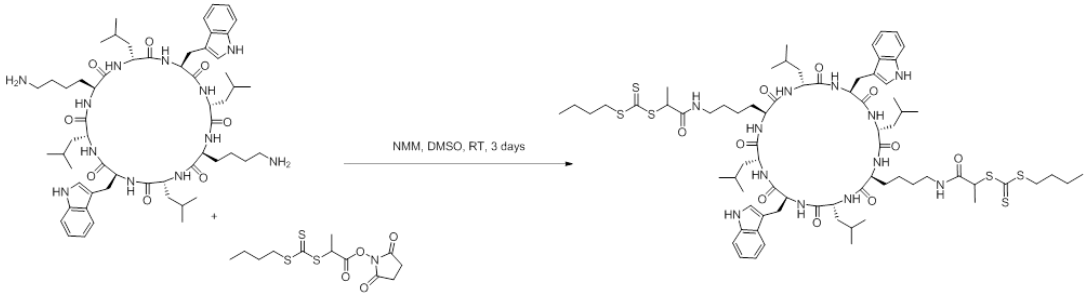

Succinimidyl ester conjugation of chain transfer agent to the cyclic peptide **2** (60 mg, 0.046 mmol) was achieved in DMSO (6 mL) with NHS-PABTC **1** (30.7 mg, 2 eq., 0.092 mmol). NMM (28 mg, 6 eq., 0.28 mmol) was added to the reaction mixture and was left to stir at room temperature for 3 days. The reaction was monitored by mass spectrometry (ESI ToF). After the reaction, DMSO was removed using a stream of N_2 and the modified cyclic peptide

was precipitated into ice cold ethyl acetate. The suspended precipitate was distributed into 2 mL Eppendorf tubes and isolated *via* centrifugation at 1000 rpm. The supernatant was discarded and the pellets were washed with ethyl acetate and centrifuged 2-fold after which the solvent was evaporated under reduced pressure to yield $CP(PABTC)_2$ **3** as a yellow powder. ^{1}H-NMR (400 MHz, TFA-*d*, ppm): δ = 7.66-6.96 (m, 10H, Trp), 5.11 (m, 2H, H_α Trp), 4.73 (m, $6H_{peptide}$ + $2H_{PABTC}$ = 8H, H_α Leu, H_α Lys and CH PABTC), 3.43-3.08 (m, $8H_{peptide}$ + $4H_{PABTC}$ = 12H, CH_2 Trp, CH_2-NH Lys and CH_2 PABTC), 1.92-1.11 (m, $24H_{peptide}$ + $14H_{PABTC}$ = 38H, CH_2-CH_2-CH_2 Lys, CH_2-CH Leu, CH_2-CH_2 and CH_3-CH from PABTC), 0.95-0.57 (m, $24H_{peptide}$ + $6H_{PABTC}$ = 30H, CH_3 Leu and CH_3-CH_2 from PABTC), NH signals not observed. MS (ESI ToF): $[M+Na]^+$ calculated: 1543.6846, found: 1543.6738.

2.4.3.11 Cyclic peptide (cyano pentanoic acid)yl ethyl trithiocarbonate ($CP(CPAETC)_2$)

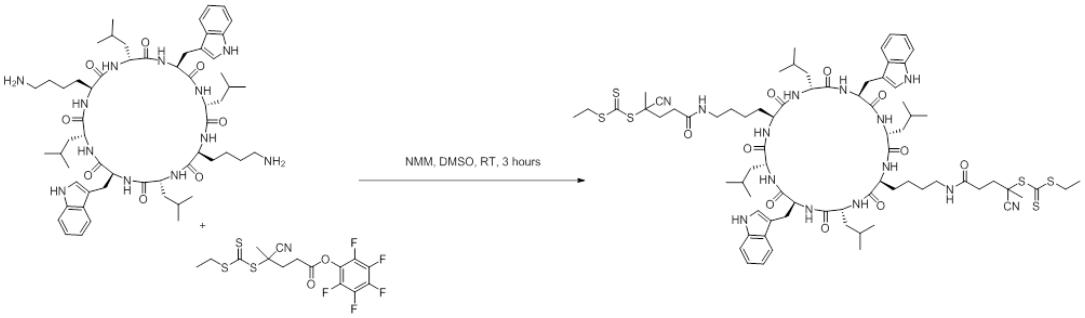

Pentafluorophenol ester conjugation of chain transfer agent to the cyclic peptide (67 mg, $5.12.10^{-5}$ mol) was achieved in DMSO (6 mL) with PFP-CPAETC (46 mg, 2.1 eq., $1.07.10^{-4}$ mol). NMM (31 mg, 6 eq., $3.07.10^{-4}$ mol) was added to the reaction mixture and it was left to stir at room temperature for 3 hours. After the reaction, DMSO was removed using a stream of N_2 and the modified cyclic peptide was precipitated into ice cold ethyl acetate. The suspended precipitate was distributed into 2 mL Eppendorf tubes and isolated *via* centrifugation at 1000 rpm. The supernatant was discarded and the pellets were washed with ethyl acetate and centrifuged 2-fold after which the solvent was evaporated under reduced pressure to yield $CP(CPAETC)_2$ as a yellow powder. Yield: 74% (60 mg, $3.82.10^{-5}$ mol). ^{1}H-NMR (400 MHz, TFA-*d*, ppm): δ = 7.69-7.07 (m, 10H, Trp), 5.11 (m, 2H, H_α Trp), 4.67 (m, $6H_{peptide}$, H_α Leu and H_α Lys), 3.66 (m, 4H, CH_2-CH_3 CPAETC), 3.43-3.08 (m, 8H, CH_2 Trp and CH_2-NH Lys), 2.70 (m, 8H, CH_2-CH_2 CPAETC), 1.99 (m, 6H, C(CN)(CH_3) CPAETC), 1.86-1.50 (m, 12H, CH_2-CH_2-CH_2 Lys), 1.49-1.10 (m, 12H, CH_2-CH Leu), 0.99-0.57 (m, 30H, CH_3 Leu and CH_2-CH_3 CPAETC), NH signals not observed. MS (ESI ToF): $[M+Na]^+$ calculated: 1593.7, found: 1593.7.

2.4.3.12 Polymerisations

Typical protocol: chain transfer agent (CTA), monomer, initiator (ACVA) and solvent were introduced in a flask equipped with a magnetic stirrer and sealed with a rubber septum. Nitrogen was bubbled through the solution for 15 min, and the flask was then put in a thermostated oil bath set at 70 °C. The polymerisations were stopped by cooling the flask and opening it to air. Conditions specific to each polymerisation are detailed in Table 2.5. Conversions were determined by ^{1}H-NMR using one of the following two methods:

- Comparison of the integration of the vinyl protons corresponding to the remaining monomer with the integration of polymer side chains signals;
- Comparison of the integration of one of the CTA signals with the vinyl protons before and after polymerisation.

Table 2.5: Summary of experimental conditions for the polymerisations.

Monomer	Solvent	CTA	$[M]_0$ ($g.mol^{-1}$)	$[M]_0$:$[CTA]_0$	$[CTA]_0$:$[ACVA]_0$	Time (h)
NAM	DMSO	NHS-PABTC	2	25	40	2
NAM	DMSO	NHS-PABTC	2	50	20	2
NAM	DMSO	NHS-PABTC	2	100	10	2
NAM	DMSO	$CP(PABTC)_2$	2	50	20	2
NAM	DMSO	$CP(PABTC)_2$	2	100	10	2
NAM	DMSO	$CP(PABTC)_2$	2	200	10	2
BA	DMF	NHS-PABTC	2	50	20	2
BA	DMF	$CP(PABTC)_2$	2	100	10	2
NIPAM	Dioxane	NHS-PABTC	2	50	20	2
NIPAM	DMSO	$CP(PABTC)_2$	2	100	10	2
HEA	DMSO	NHS-PABTC	2	50	20	1.5
HEA	DMSO	$CP(PABTC)_2$	2	100	10	1.5
PEGA	DMSO	NHS-PABTC	1	50	20	3
PEGA	DMSO	$CP(PABTC)_2$	1	100	10	3
MMA	DMSO	NHS-CPAETC	2	50	20	12
MMA	DMSO	$CP(CPAETC)_2$	2	100	10	12
DMAEMA	DMSO	NHS-CPAETC	2	50	20	12
DMAEMA	DMSO	$CP(CPAETC)_2$	2	100	10	12

Protocol for chain extension: CP-(pNAM$_{48}$)$_2$ made by grafting-from (Table 2.5, run 5) was extended by addition of further monomer ([M]$_0$:[CTA]$_0$ = 180, corresponding to a DP 90 on each arm of the conjugate) and ACVA (from a stock solution in DMSO). The vial was sealed once again with a rubber septum, nitrogen was bubbled through the mixture for 15 min, and the flask was put in a thermostated oil bath set at 70 °C. The polymerisation was stopped after 2 hours. Conversion was determined by ^{1}H NMR and found to be > 99 %. The composition of the diblock is therefore CP-(pNAM$_{48}$-*b*-pNAM$_{90}$)$_2$.

2.4.3.13 Conjugation of polymers to CP

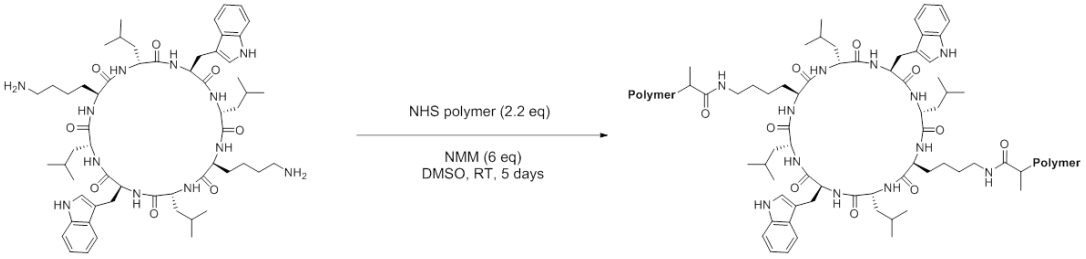

Succinimidyl ester conjugation of polymers to the cyclic peptide **2** was achieved in DMSO (DMF in the case of poly(butyl acrylate) conjugation) with polymer (2.2 eq.; 1.1 per conjugation site) and NMM (6 eq.). The mixture was stirred at room temperature for 5 days and samples for SEC analysis were taken at regular intervals.

2.5 References

1. H. Ringsdorf, *J. Polym. Sci. Polym. Symp.* **1975,** *51* (1), 135-153.
2. I. Cobo, M. Li, B. S. Sumerlin, S. Perrier, *Nat. Mater.* **2015,** *14* (2), 143-159.
3. E. M. Pelegri-O'Day, E. W. Lin, H. D. Maynard, *J. Am. Chem. Soc.* **2014,** *136* (41), 14323-14332.
4. L. A. Canalle, D. Lowik, J. C. M. van Hest, *Chem. Soc. Rev.* **2010,** *39* (1), 329-353.
5. J. Y. Shu, B. Panganiban, T. Xu, *Annu. Rev. Phys. Chem.* **2013,** *64*, 631-657.
6. S. Dehn, R. Chapman, K. A. Jolliffe, S. Perrier, *Polym. Rev.* **2011,** *51* (2), 214-234.
7. M. A. Gauthier, H. A. Klok, *Chem. Commun.* **2008,** (23), 2591-2611.
8. B. S. Sumerlin, *ACS Macro Letters* **2012,** *1* (1), 141-145.
9. J. D. Wallat, K. A. Rose, J. K. Pokorski, *Polym. Chem.* **2014,** *5* (5), 1545-1558.
10. P. De, M. Li, S. R. Gondi, B. S. Sumerlin, *J. Am. Chem. Soc.* **2008,** *130* (34), 11288-11289.
11. H. Li, M. Li, X. Yu, A. P. Bapat, B. S. Sumerlin, *Polym. Chem.* **2011,** *2* (7), 1531-1535.
12. M. Li, H. Li, P. De, B. S. Sumerlin, *Macromol. Rapid Commun.* **2011,** *32* (4), 354-359.
13. K. L. Heredia, D. Bontempo, T. Ly, J. T. Byers, S. Halstenberg, H. D. Maynard, *J. Am. Chem. Soc.* **2005,** *127* (48), 16955-16960.
14. B. S. Lele, H. Murata, K. Matyjaszewski, A. J. Russell, *Biomacromolecules* **2005,** *6* (6), 3380-3387.

15. M. P. Robin, P. Wilson, A. B. Mabire, J. K. Kiviaho, J. E. Raymond, D. M. Haddleton, R. K. O'Reilly, *J. Am. Chem. Soc.* **2013,** *135* (8), 2875-2878.
16. R. M. Broyer, G. N. Grover, H. D. Maynard, *Chem. Commun.* **2011,** *47* (8), 2212-2226.
17. D. E. Borchmann, T. P. Carberry, M. Weck, *Macromol. Rapid Commun.* **2014,** *35* (1), 27-43.
18. A. S. Goldmann, M. Glassner, A. J. Inglis, C. Barner-Kowollik, *Macromol. Rapid Commun.* **2013,** *34* (10), 810-849.
19. G. Gody, C. Rossner, J. Moraes, P. Vana, T. Maschmeyer, S. Perrier, *J. Am. Chem. Soc.* **2012,** *134* (30), 12596-12603.
20. V. V. Rostovtsev, L. G. Green, V. V. Fokin, K. B. Sharpless, *Angew. Chem. Int. Ed.* **2002,** *114* (14), 2708-2711.
21. M. Meldal, C. W. Tornøe, *Chem. Rev.* **2008,** *108* (8), 2952-3015.
22. J. C. Brendel, F. Liu, A. S. Lang, T. P. Russell, M. Thelakkat, *ACS Nano* **2013,** *7* (7), 6069-6078.
23. G. W. Anderson, J. E. Zimmerman, F. M. Callahan, *J. Am. Chem. Soc.* **1964,** *86* (9), 1839-1842.
24. N. Vanparijs, S. Maji, B. Louage, L. Voorhaar, D. Laplace, Q. Zhang, Y. Shi, W. E. Hennink, R. Hoogenboom, B. G. De Geest, *Polym. Chem.* **2015**.
25. P. J. Roth, K. T. Wiss, R. Zentel, P. Theato, *Macromolecules* **2008,** *41* (22), 8513-8519.
26. M. Danial, C. M. N. Tran, K. A. Jolliffe, S. Perrier, *J. Am. Chem. Soc.* **2014,** *136* (22), 8018-8026.
27. C. K. Poon, R. Chapman, K. A. Jolliffe, S. Perrier, *Polym. Chem.* **2012,** *3* (7), 1820-1826.
28. G. Moad, Y. K. Chong, A. Postma, E. Rizzardo, S. H. Thang, *Polymer* **2005,** *46* (19), 8458-8468.
29. C. Henríquez, C. Bueno, E. A. Lissi, M. V. Encinas, *Polymer* **2003,** *44* (19), 5559-5561.
30. M. R. Ghadiri, J. R. Granja, R. A. Milligan, D. E. McRee, N. Khazanovich, *Nature* **1993,** *366* (6453), 324-327.
31. J. Couet, J. D. Jeyaprakash, S. Samuel, A. Kopyshev, S. Santer, M. Biesalski, *Angew. Chem. Int. Ed.* **2005,** *44* (21), 3297-3301.
32. M. G. J. ten Cate, N. Severin, H. G. Börner, *Macromolecules* **2006,** *39* (23), 7831-7838.
33. R. Chapman, K. A. Jolliffe, S. Perrier, *Polym. Chem.* **2011,** *2* (9), 1956-1963.
34. B. M. Blunden, R. Chapman, M. Danial, H. X. Lu, K. A. Jolliffe, S. Perrier, M. H. Stenzel, *Chem. Eur. J.* **2014,** *20* (40), 12745-12749.
35. T. Xu, N. N. Zhao, F. Ren, R. Hourani, M. T. Lee, J. Y. Shu, S. Mao, B. A. Helms, *ACS Nano* **2011,** *5* (2), 1376-1384.
36. R. Chapman, G. G. Warr, S. Perrier, K. A. Jolliffe, *Chem. Eur. J.* **2013,** *19* (6), 1955-1961.
37. R. Chapman, P. J. M. Bouten, R. Hoogenboom, K. A. Jolliffe, S. Perrier, *Chem. Commun.* **2013,** *49* (58), 6522-6524.
38. R. Chapman, K. A. Jolliffe, S. Perrier, *Adv. Mater.* **2013,** *25* (8), 1170-1172.
39. S. Loschonsky, J. Couet, M. Biesalski, *Macromol. Rapid Commun.* **2008,** *29* (4), 309-315.
40. R. Chapman, K. A. Jolliffe, S. Perrier, *Aust. J. Chem.* **2010,** *63* (8), 1169-1172.
41. M. Danial, C. M. N. Tran, P. G. Young, S. Perrier, K. A. Jolliffe, *Nat. Commun.* **2013,** *4*, 2780.
42. G. Moad, E. Rizzardo, S. H. Thang, *Aust. J. Chem.* **2005,** *58* (6), 379-410.
43. M. J. Monteiro, *Eur. Polym. J.* **2015,** *65* (0), 197-201.

44. A. M. Striegel, *Modern size-exclusion liquid chromatography: practice of gel permeation and gel filtration chromatography*. 2nd ed.; Hoboken, N.J. : Wiley, c2009: 1967.
45. M. J. Roberts, M. D. Bentley, J. M. Harris, *Adv. Drug Delivery Rev.* **2002,** *54* (4), 459-476.
46. F. Lecolley, L. Tao, G. Mantovani, I. Durkin, S. Lautru, D. M. Haddleton, *Chem. Commun.* **2004,** (18), 2026-2027.
47. G. Moad, E. Rizzardo, S. H. Thang, *Aust. J. Chem.* **2012,** *65* (8), 985-1076.
48. D. J. Keddie, G. Moad, E. Rizzardo, S. H. Thang, *Macromolecules* **2012,** *45* (13), 5321-5342.
49. S. A. Raw, *Tetrahedron Lett.* **2009,** *50* (8), 946-948.

Chapter 3

Cyclic peptide-poly(HPMA) nanotubes as drug delivery vectors: *in vitro* assessment, pharmacokinetics and biodistribution.

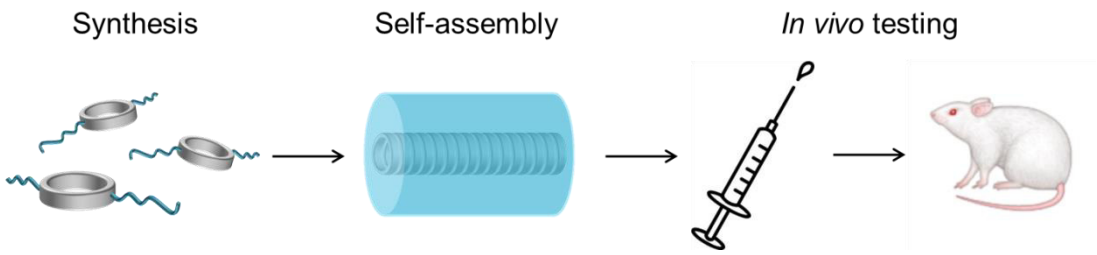

Size and shape have progressively appeared as some of the key factors influencing the properties of drug delivery systems, both in vitro and in vivo. In particular, elongated materials are thought to interact differently with cells and exhibit longer circulation times than spherical structures. A challenge, however, remains the creation of stable self-assembled materials with anisotropic shape for delivery applications that still feature the ability to disassemble, avoiding organ accumulation and facilitating their clearance from the system. In this chapter, self-assembled cyclic peptide-polymer conjugates were synthesised, and their behaviour in solution was characterised, confirming the formation of supramolecular nanotubes. In vitro they were found to be non-toxic and cell uptake studies revealed that the pathway of entry was energy dependent. Moreover, the nanotubes entered the cells significantly more than a non self-assembled polymeric counterpart. Pharmacokinetic studies in rats, following intravenous injection of the peptide-polymer conjugates and the non-assembled control polymer, showed that the increased size of the nanotubes enabled increased exposure in comparison to the polymer. Nevertheless, the ability of the nanotubes to slowly disassemble into smaller units still allows for almost complete clearance and circumvents organ accumulation, making these materials an excellent candidate in the search for high performing drug carriers.

3.1 Introduction

Nanomedicine and the use of nanoscale delivery vectors in particular, has completely reshaped the way small molecular drugs are administered and has shown to dramatically improve their *in vivo* therapeutic performance over the past two decades.[1,2] Regardless of particle composition, the carrier's large size permits longer circulation times by avoiding immediate renal filtration, and enables passive targeting to take place through the enhanced permeability and retention (EPR) effect.[3,4] Delivery systems also provide protection of the drug,[5] and allow for the introduction of targeting moieties,[6-8] thus reducing side effects and generally enhancing drug delivery efficiency. A multitude of drug delivery vectors have been thoroughly studied in the past decades, including inorganic (gold[9] and silica[10] nanoparticles, as well as quantum dots[11]) and organic (viral nanoparticles,[12] carbon nanotubes[13] or polymer-based structures[14]) carriers. Shape has progressively appeared as one of the features that have a major influence on the *in vivo* behaviour of carriers, with cylindrical structures attracting a lot of attention.[15] It has been shown that because of their increased aspect ratio, elongated nanoparticles exhibit longer circulation times and can enhance cellular uptake and tumour accumulation *in vivo*.[16] Filomicelles,[17] polymer brushes[18] and PEGylated tobacco mosaic viruses[19,20] are among organic tubular structures that have already been studied *in vivo* and show promising results. Discher *et al.* have, for example, studied filomicelles and compared their behaviour to that of their spherical counterparts *in vivo*.[21] They have shown that the cylindrical structures not only circulate in the blood for a considerable amount of time and manage to reach and enter tumour tissues, but also enable for a much higher loading of the anticancer agent Paclitaxel in comparison with spherical particles, whilst still maintaining similar survival rates in mice; clearly demonstrating an enhanced therapeutic efficiency. Additionally, Müllner *et al.* studied the pharmacokinetics of unimolecular cylindrical polymer brushes in rats, showing that they exhibit long term blood circulation, and that the aspect ratio of the brushes has a considerable impact on their pharmacokinetic parameters.[22] They further studied this system in mouse xenografts, demonstrating that the brushes undergo EPR effect and tend to passively target tumour tissues.[23] The main limitation of such large stable objects is their relatively poor clearance from the system, usually ascribed to their recognition by the mononuclear phagocytic system (MPS) leading to high accumulation in organs such as the spleen and the liver.[24]

One way to circumvent this issue is to explore the use of materials which undergo supramolecular self-assembly, for example by directed hydrogen bonds.[25] Supramolecular polymers,[26] especially those who self-assemble in aqueous media,[27] have started to gain considerable attention in the field of nanomedicine. They allow for a bottom-up design strategy that enables extensive functionalisation of the building blocks, resulting in large libraries of materials. Examples of such systems include those based on host-guest interactions,[28] or on the *in situ* assembly of peptide amphiphiles into long fibres.[29-31] One of the major advantages over other nano-systems is their supramolecular nature which not only provides considerable stability, but also allows them to eventually break up into unimeric entities, small enough to be readily cleared from the body, avoiding undesired organ accumulation.

An emerging class of elongated drug carriers, which feature such a supramolecular assembly process, are nanotubes formed of cyclic peptide-polymer conjugates.[32] As detailed in Chapter 1, cyclic peptides formed of an even number of alternating D- and L- amino acids have been shown to adopt a flat conformation leading to self-assembly into nanotubes through antiparallel β-sheet formation.[33] Conjugation of water-soluble polymers to these peptides enables control over the size and the functionality of the nanotubes. To date, few reports look at these systems as drug carriers, and they have demonstrated promising results in experiments on cell systems,[34,35] but their *in vivo* behaviour has yet to be explored.

In this chapter, poly(2-hydroxypropyl methacrylamide) (pHPMA)-based cyclic peptide-polymer conjugates were synthesised, and their ability to self-assemble into nanotubes was studied. After selection of the most promising candidate, a non-assembling polymer which does not contain the peptide core was also synthesised as a control. The *in vitro* behaviour of both conjugate and control polymer, as well as their pharmacokinetics and biodistribution in rats, were studied.

3.2 Results and discussion

3.2.1 Design and synthesis

3.2.1.1 Monomer choice and synthesis

During the past decades, pHPMA has been extensively studied in the context of cancer therapy[36] and several formulations containing this polymer are undergoing different stages of clinical trials.[37,38] In addition, pHPMA can be readily synthesised by radical polymerisation methods, which facilitates the introduction of comonomers and the formation of well-defined end-groups. As such, pHPMA was chosen in this work, as the selection of a polymer which is pharmaceutically relevant is critical when designing a drug delivery vector. In order to provide a binding site for the future ligation of organometallic drugs (see Chapter 4), a pyridine comonomer was introduced. Although commercially available, the use of vinyl pyridine was avoided, since the sterically-demanding environment of the polymer backbone might limit complexation. Consequently, a more flexible monomer bearing a pyridine group was synthesised: 2-(3-(Pyridin-4-ylmethyl)ureido)ethyl)methacrylate (PUEMA) (Scheme 3.1).

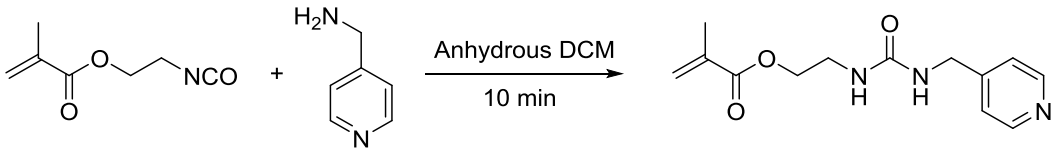

Scheme 3.1: Synthesis of 2-(3-(pyridin-4-ylmethyl)ureido)ethyl)methacrylate (PUEMA).

The chosen synthetic route to make this monomer takes advantage of the efficient reaction which occurs between an isocyanate and an amine group. The commercially available 2-isocyanatoethyl methacrylate (IEMA) was coupled to 4-methylamino pyridine in stoichiometric amounts. The reaction was complete after 10 min, as monitored by Fourier Transformed Infra-Red spectroscopy (FTIR) (Figure 3.1 A), which showed complete disappearance of the isocyanate peak at 2264 cm^{-1}, as well as the appearance of urea peaks at 1585 cm^{-1} and 3313 cm^{-1} for the carbonyl and for the N-H bonds, respectively. After evaporation of the solvent, a pure product was obtained without the need for further purification steps. The structure of the product was confirmed by ^{1}H NMR, ^{13}C NMR (Figure 3.1 B-C) and mass spectrometry.

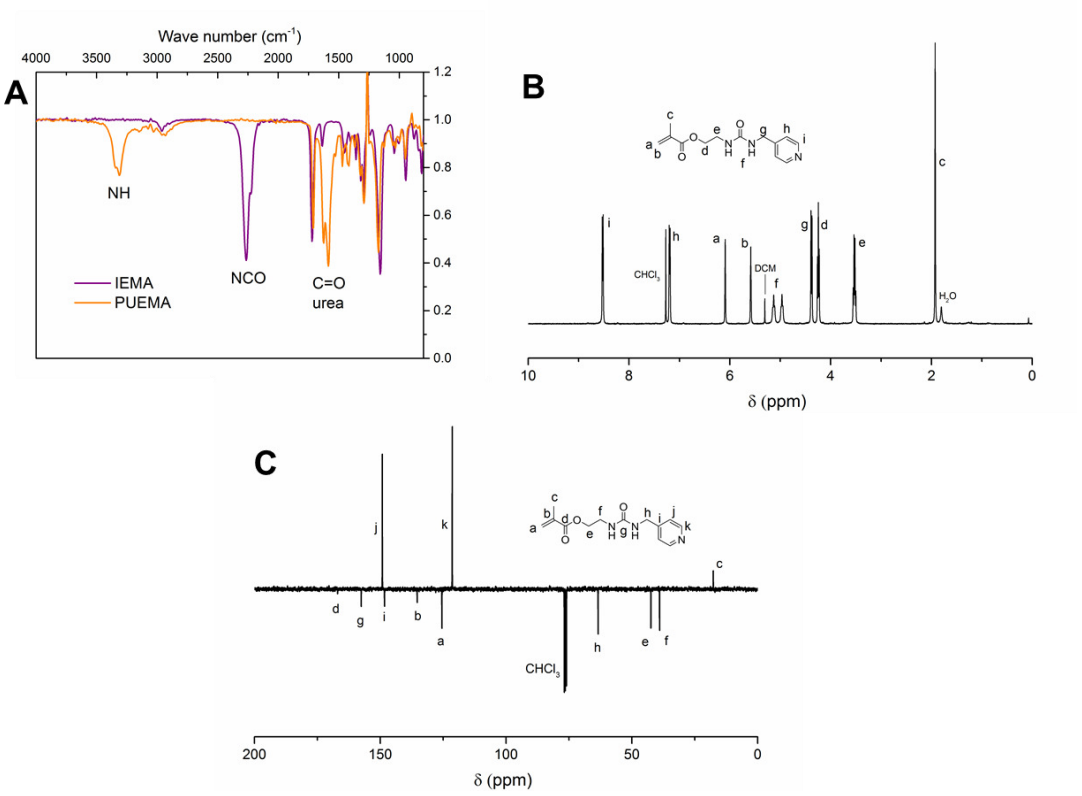

Figure 3.1: A) FTIR spectra indicating the formation of PUEMA. B) ^{1}H NMR spectrum ($CDCl_3$, 300 MHz) of PUEMA. C) ^{13}C-APT NMR spectrum ($CDCl_3$, 75 MHz) of PUEMA.

3.2.1.2 Polymerisations and peptide conjugation

When designing polymeric drug delivery systems, well-defined polymers are required to ensure reproducibility and to establish reliable structure-property relationships. Among others, reversible addition-fragmentation chain transfer (RAFT) polymerisation has demonstrated good potential to provide excellent control of the polymer lengths along with narrow size distributions.[39] In the case of HPMA, a variety of suitable solvents have been reported, but only a few seem to promote high conversion of the monomer, highly desirable in terms of economic scale-up of materials and purification steps. Among the examples of reported strategies for the polymerisation of HPMA to high conversions, aqueous conditions seem to be the most effective in producing well-defined polymers.[40,41]

Here, the RAFT polymerisation of HPMA, as well as the copolymerisation of HPMA and PUEMA (5% of the initial total monomer concentration), were performed in an aqueous acidic buffer/DMSO mixture (Scheme 3.2). The use of an acidic buffer (pH 4) circumvented any risk of hydrolysis of the chain transfer agent (CTA) and helped to achieve high

conversion of HPMA, while maintaining excellent control over the molecular weight distribution.[40]

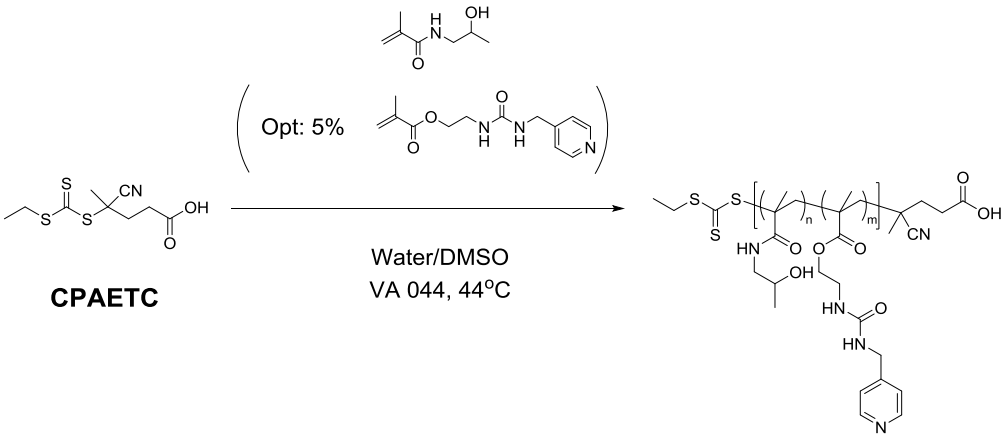

Scheme 3.2: RAFT (co)polymerisation of HPMA.

Kinetic measurements of the homopolymerisation of HPMA, as well as the copolymerisation of HPMA and PUEMA, were performed (Figure 3.2). In both cases, the linear behaviour of the $\ln([M]_0/[M]_t)$ *vs* time plots suggests a constant concentration of radicals throughout the polymerisation (Figure 3.2 B and E). A linear evolution of molecular weight as well as low dispersity values ($Đ < 1.2$) were observed (Figure 3.2 C and F), suggesting good control over the polymerisation. Monitoring the conversion of each monomer during the copolymerisation showed that PUEMA was consumed significantly faster than HPMA, indicating a higher reactivity (Figure 3.2 D). As a consequence, the PUEMA units are on average located towards the α-chain end of the polymer.

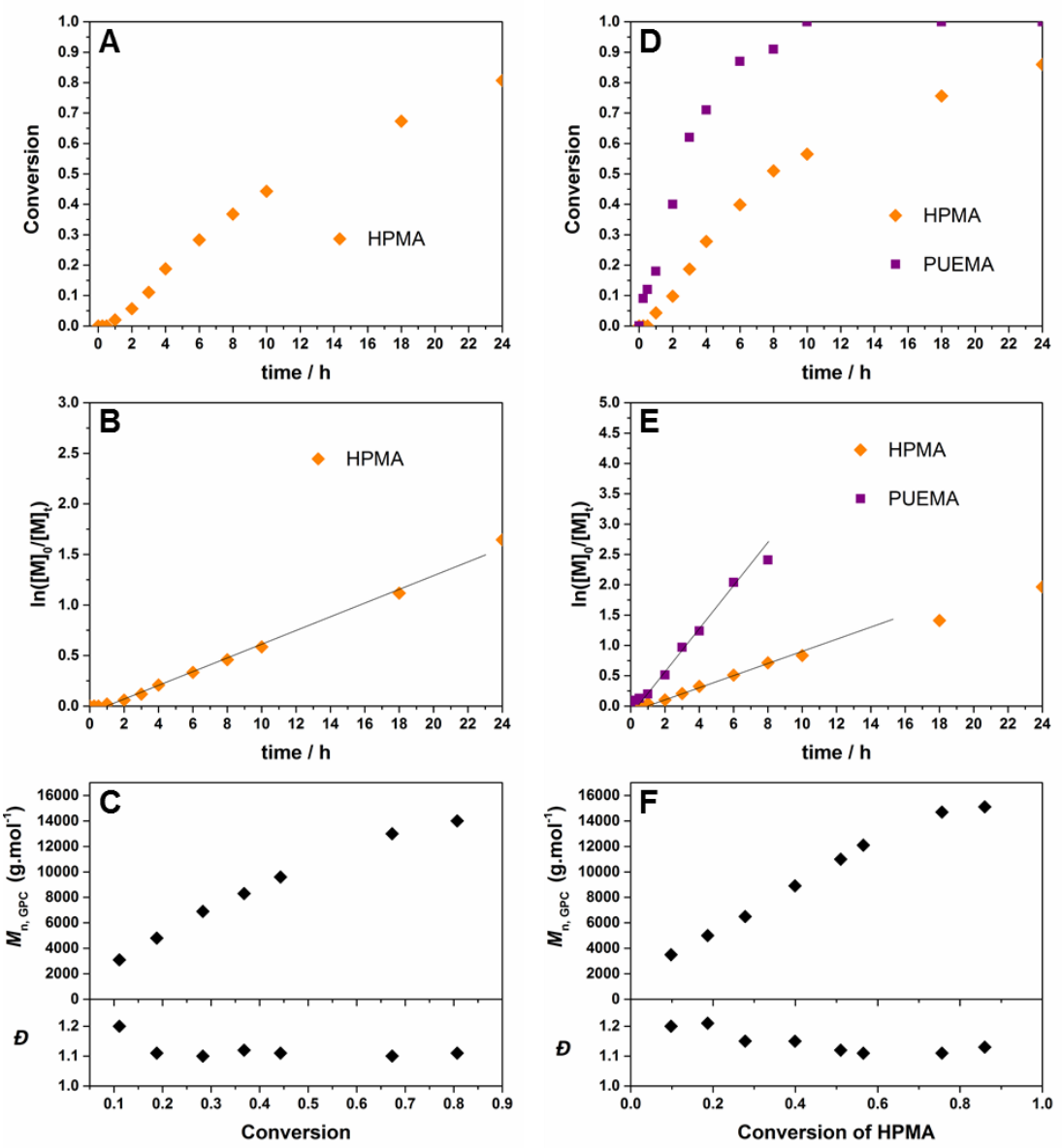

Figure 3.2: Kinetic plots for the RAFT homopolymerisation of HPMA (left) and copolymerisation of HPMA and PUEMA (right) using CPAETC as the CTA: conversion of monomers *vs* time (top), $\ln([M]_0/[M]_t)$ *vs* time (middle) (the lines serve as guides to highlight the linear region.), M_n and $Đ$ determined by DMF SEC *vs* conversion (bottom).

Subsequently, three different polymers were synthesised (Scheme 3.3). Two different degrees of polymerisation (DP) were targeted for HPMA homopolymers (**P1** DP = 25 and **P2** DP = 50). A third polymer (**P3** DP = 50) incorporating a small percentage of PUEMA was also prepared in order to test the influence of functional handles in the system. In addition, a bifunctional CTA ($E(CPAECTC)_2$) was used to provide a non self-assembling polymeric control, **P4,** for subsequent biological testing (see sections 3.2.3 and 3.2.4). All obtained polymers, **P1-4,** were well-defined, with dispersities ≤ 1.12 (Table 3.1). The

observed differences between theoretical and SEC-derived molecular weight can be explained by the fact that pHPMA possesses a different hydrodynamic volume in DMF than the pMMA standards used in the SEC calibration.

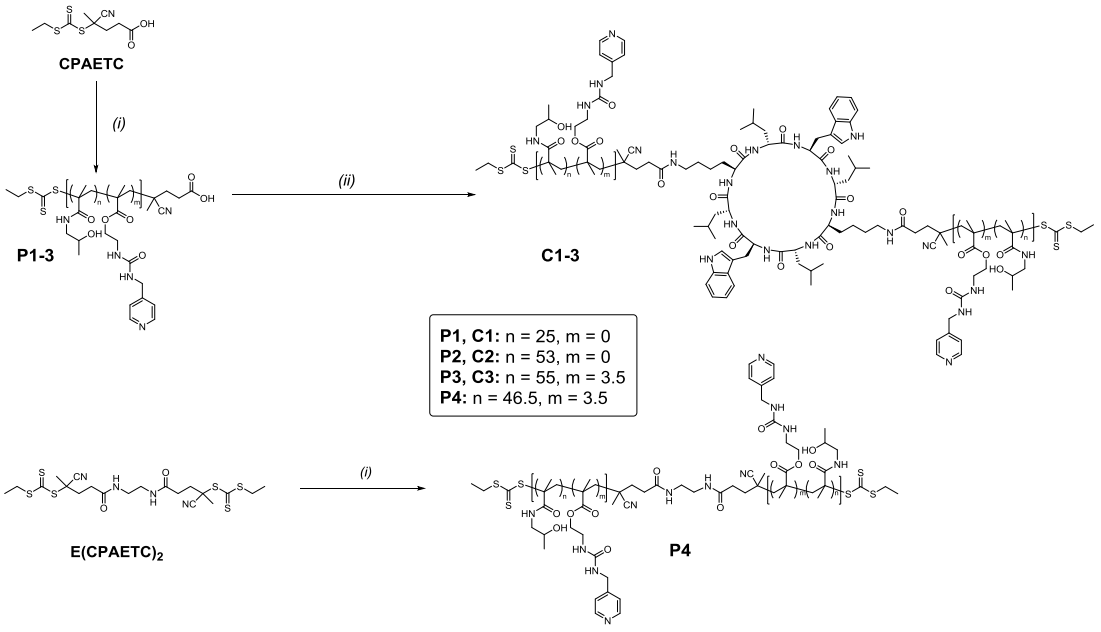

Scheme 3.3: Synthesis of polymers **P1-4** and conjugates **C1-3**. (*i*) HPMA, VA 044, DMSO/H_2O (optional: 5% PUEMA). (*ii*) cyclo(D-Leu-Lys-D-Leu-Trp)$_2$, HBTU, NMM, DMSO.

Table 3.1: Summary of polymers and conjugates used in this work.

Entry	Material	$M_{n,th}$ [a] (g.mol^{-1})	$M_{n,GPC}$ [b] (g.mol^{-1})	$Đ$ [b]
P1	pHPMA$_{25}$	3900	7000	1.10
C1	CP-(pHPMA$_{25}$)$_2$	8800	14200	1.13
P2	pHPMA$_{53}$	7800	11700	1.10
C2	CP-(pHPMA$_{53}$)$_2$	16600	27900	1.12
P3	p(HPMA$_{55}$-*co*-PUEMA$_{3.5}$)	9100	11900	1.10
C3	CP-(p(HPMA$_{55}$-*co*-PUEMA$_{3.5}$))$_2$	19200	24600	1.18
P4	pHPMA$_{93}$-*co*-PUEMA$_7$	15700	21400	1.12

[a] Determined by ^{1}H NMR. [b] Determined by SEC using DMF (0.1% LiBr) as eluent, calibrated with pMMA standards.

The polymers **P1-3** were subsequently attached to cyclo(D-Leu-Lys-D-Leu-Trp)$_2$, *via* amide bond formation between the carboxylic acid chain end of the polymers and the two lysine residues present on the cyclic peptide, using *O*-(benzotriazol-1-yl)-*N,N,N′,N′*-tetramethyluronium hexafluorophosphate (HBTU) as a coupling reagent in the presence of an organic base. This ligation technique follows typical coupling reactions used in solid phase peptide chemistry, and shares the advantages of the active ester conjugation shown in Chapter 2. In addition, it leads to the formation of a stable amide bond, and does not require tedious modification of the chain transfer agent (CTA) or the lysine residue of the cyclic peptide.[42-44]

The reaction was monitored by size exclusion chromatography (SEC) for the attachment of **P3** (Figure 3.3), which showed the rapid appearance of a peak corresponding to the conjugate **C3**, at ca. double the molecular weight of the polymer **P3** (M_n = 11900 and 24600 g.mol^{-1} for the polymer and the conjugate, respectively). The coupling was complete after 1 h and the water-soluble nature of these conjugates enabled straightforward purification by dialysis.

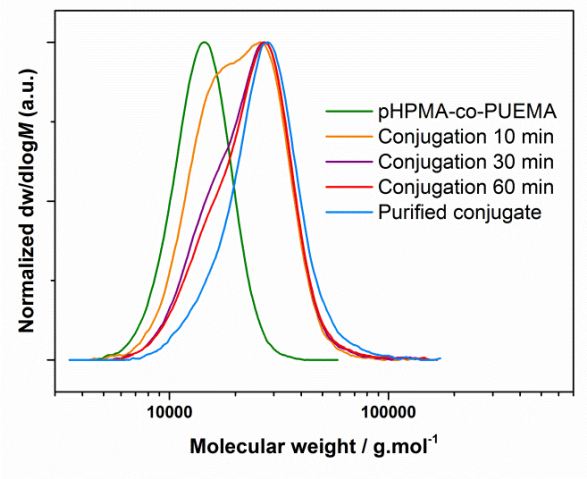

Figure 3.3: Synthesis and purification of **C3** (CP-(p(HPMA-co-PUEMA))$_2$): SEC traces of the polymer prior to reaction (green), the reaction mixture at different time points, and of the pure conjugate isolated by dialysis (blue).

The obtained peptide-polymer conjugates **C1-3** were purified by dialysis and isolated. SEC analysis revealed that low dispersities (≤ 1.20) were maintained (Figure 3.4 and Table 3.1).

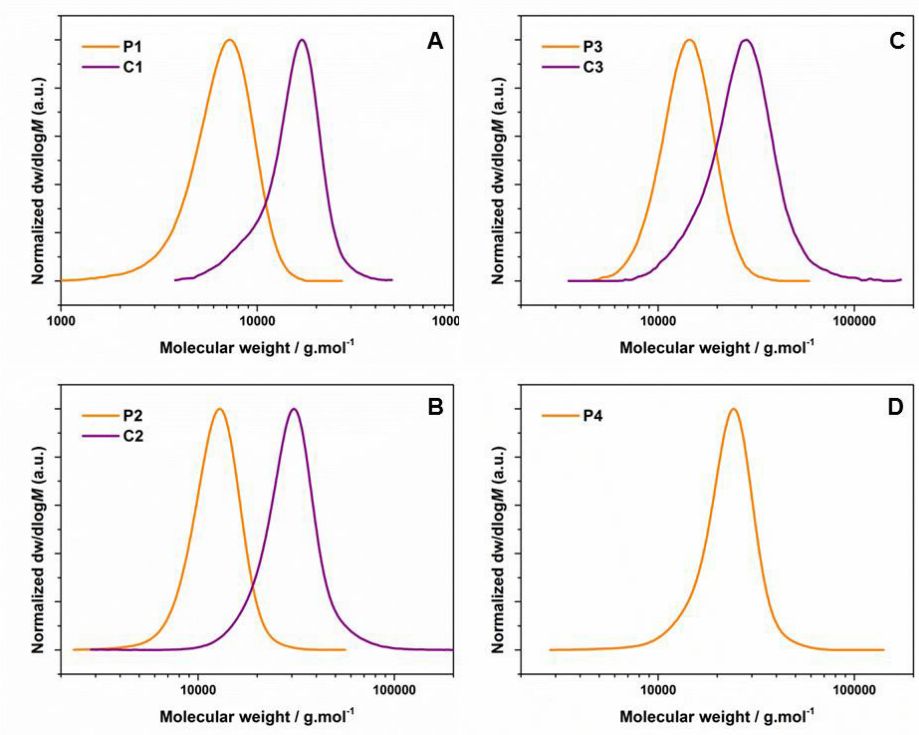

Figure 3.4: SEC chromatograms of A) $pHPMA_{25}$ (**P1**) and CP-$(pHPMA_{25})_2$ (**C1**) B) $pHPMA_{53}$ (**P2**) and CP-$(pHPMA_{53})_2$ (**C2**) C) $pHPMA_{55}$-*co*-$PUEMA_{3.5}$ (**P3**) and CP-$(pHPMA_{55}$-*co*-$PUEMA_{3.5})_2$ (**C3**) D) $pHPMA_{93}$-*co*-$PUEMA_7$ (**P4**).

3.2.2 Characterisation of supramolecular nanotubes in solution using scattering techniques

In contrast to electron microscopy, which requires contrast and often drying on a grid (except if using cryo-TEM), therefore complicates the analysis and presents a risk of disruption of the self-assembly, scattering techniques constitute a powerful tool for the characterisation of supramolecular materials in solution. These techniques, such as small angle neutron scattering (SANS) and static light scattering (SLS), rely on the measurement of the scattered intensity at an angle θ by a particle irradiated with an incident beam at a wavelength λ_0 (Figure 3.5).

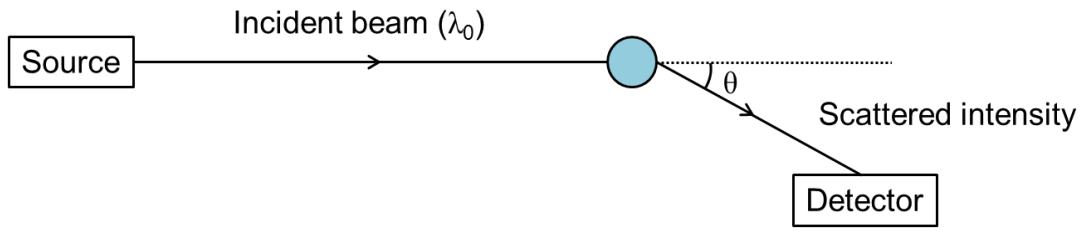

Figure 3.5: Principle of scattering.

The wave vector q can be defined by equation 1, with *n* the refractive index of the solvent:

$$q = \frac{4\pi}{\lambda_0}\sin\frac{\theta}{2} \text{ (SANS)} \qquad \text{or} \qquad q = \frac{4\pi n}{\lambda_0}\sin\frac{\theta}{2} \text{ (SLS)} \tag{1}$$

The inverse of the wave vector, q^{-1}, is proportional to the size of the window of observation. As such, the bigger the wave vector, the smaller the window of observation. By varying the position of the detector (therefore the value of θ) and the wavelength of the incident beam (by using light or neutrons), information can be gained on an extended range of sizes. SANS and SLS are complementary techniques, as shown on Figure 3.6. By using Ultra Small Angle Neutron Scattering (USANS), the q-range obtained with neutrons can be extended towards lower q-range, however resolution is decreased and high q values cannot be obtained.

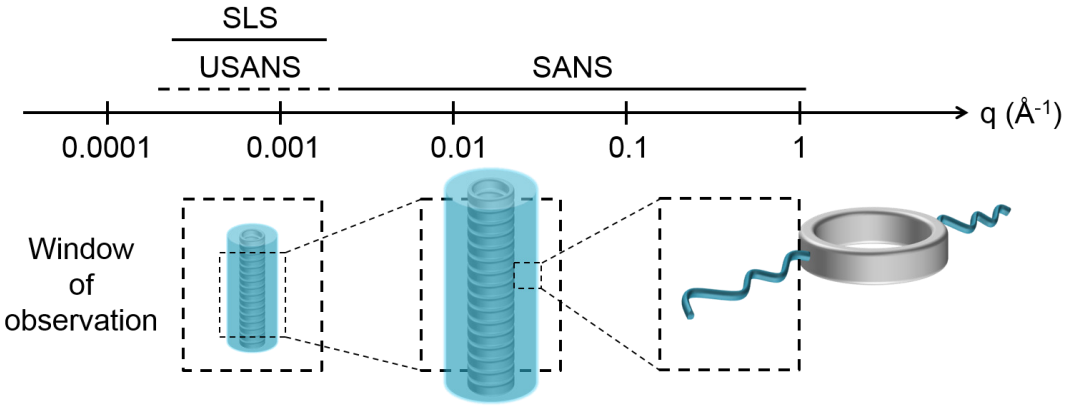

Figure 3.6: Relationship between q-range and size of the window of observation; complementarity of SLS and SANS.

SANS measurements were conducted on conjugates **C1-3** in solution in deuterated PBS in order to assess their self-assembly and elucidate key structural parameters including shape

(using the q-dependency of the scattered intensity) and dimensions (using the intensity at low q values).[45]

Interestingly, all three conjugates exhibit very different scattering profiles (Figure 3.7). Data for both homopolymer-based conjugates **C1** and **C2** show a plateau at low q values (q<0.02), indicative of a finite length, while a q^{-1} dependency is observed for **C3** in that q range, characteristic of a longer cylindrical structure.

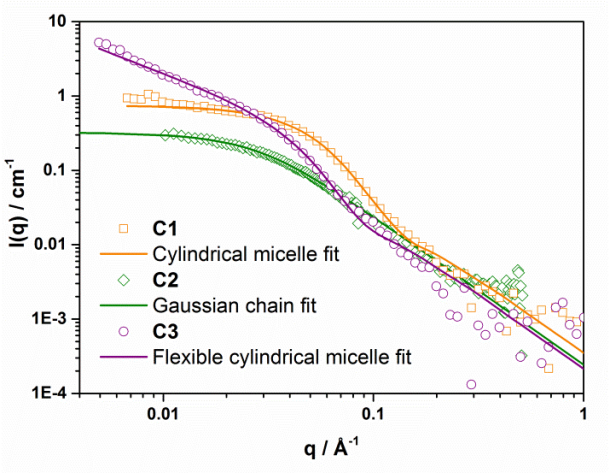

Figure 3.7: Small angle neutron scattering profiles of **C1** at 10 mg/mL (orange squares), **C2** at 5 mg/mL (green diamonds), **C3** at 5 mg/mL (purple circles) in PBS and their fits using cylindrical micelle (orange line), Gaussian chain (green line) and flexible cylindrical micelle (purple line) models, respectively.

In SANS of polymers, the scattered intensity $I_{(q)}$ can be described by the following equation:

$$I_{(q)} = (\eta_{solv} - \eta)^2 * \Phi * \frac{MW}{d*N_a} * P_{(q)} * S_{(q)} \quad \text{where} \quad \Phi = \frac{C}{d} \qquad (2)$$

N_a is Avogadro's constant, MW is the molecular weight of the polymer, d its density, C the concentration. η_{solv} and η are the scattering length densities corresponding to the solvent and the compound, respectively, and can be calculated from the chemical formulas. $S_{(q)}$ is the structure factor, describing interaction between species at high concentration. All following work was carried out in dilute conditions, in which $S_{(q)} \rightarrow 1$. $P_{(q)}$ is the form factor, which describes the morphology of the compound in solution.

In the case of **C2**, the data is best fitted with a Gaussian chain model, which represents non-assembled polymer chains in solution (Table 3.2).[46] The form factor for this model is described by equation (3):

$$P_{(q)\ Gaussian\ chain} = \frac{2[\exp(-x)-1+x]}{x^2} \text{ where } x = q^2R_g^2 \quad (3)$$

The fit was performed with the molecular weight (MW) and radius of gyration (R_g) as adjustable parameters, minimising the sum of the squared errors between the data and fit, and afforded MW = 12900 g/mol and R_g = 52 Å. The MW obtained from SANS is reasonable when compared to the theoretical value for the unimer (M_n = 16600 g/mol) which demonstrates that this conjugate does not assemble.

Table 3.2: Fitting parameters obtained for **C2** using a Gaussian chain form factor.

Parameter	Definition	Value	
MW (g.mol^{-1})	Molecular weight	12900	Fitting
R_g (Å)	Radius of gyration	52	
η_{solv} (Å^{-2})	Scattering length density of the solvent	6.39E-6	Calculated
η (Å^{-2})	Scattering length density of the compound	8.2742E-7	

In contrast, models corresponding to assembled structures were necessary to fit the data corresponding to the other two conjugates. More precisely, cylindrical micelle models (worm-like) were used to fit the data for **C1** and **C3**, as they take into account both the cylindrical shape provided by the cyclic peptide core when self-assembled into nanotubes (characteristic q^{-1} dependency at low q values: cylinder form factor), as well as the polymer arms (Gaussian chain form factor at high q values).[47] For these models, a radius of 5 Å was used for the peptide core, in accordance with previously reported results.[32] Using these parameters, values confirming the elongated shape of the structures were obtained. A cylindrical micelle model was best to fit the data corresponding to the conjugate **C1**, and the CYL+Chains(RW) model predefined on the scattering software SASfit was used (Table 3.3).[47]

Table 3.3: Fitting parameters obtained for **C1** using a cylindrical micelle form factor.

Parameter	Definition	Value	
N	Scale factor	0.578576	Fitting
n_agg	Grafting density	0.017755	
Rg (Å)	Radius of gyration of the polymer arms	11.31	
H (Å)	Length of the cylinder	51.72	
V_brush ($Å^3$)	Volume of the polymer arms[a]	6355	Calculated
eta_core ($Å^{-2}$)	Scattering length density of the core	8.5801E-7	
eta_brush ($Å^{-2}$)	Scattering length density of the polymer arms	8.5801E-7	
eta_solv ($Å^{-2}$)	Scattering length density of the solvent	6.39E-6	
R_core (Å)	Radius of the core	5	Fixed
xsolv_core	Fraction of solvent in the core, set to 0	0	
d	d = 1 mimics the non-penetration of the polymer chains in the core	1	

[a] *Calculated using* $V_{brush} = MW/(dxN_a).10^{24}$*, where MW is the molecular weight of the polymer, d its density and* N_a *Avogadro's number.*

In the case of **C1** a nanotube length of about 5.2 nm was obtained, which corresponds to a number of aggregation (N_{agg}) of 11, as calculated using the previously reported distance between adjacent peptides (L_c = 4.7 Å).[33,40]

$$N_{agg} = \frac{H}{L_c} = \frac{51.72}{4.7} = 11$$

To fit the data corresponding to the conjugate **C3**, we used the flexible cylindrical micelle model predefined on SASfit (WORM+Chains(RW)), which uses the the same form factor as the previously described model, with the Kuhn's length *l* as an additional parameter (Table 3.4).

Table 3.4: Fitting parameters obtained for **C3** using a flexible cylindrical micelle form factor.

Parameter	Definition	Value	
N	Scale factor	0.0258881	Fitting
n_agg	Grafting density	0.0064568	
Rg (Å)	Radius of gyration of the polymer arms	17.104	
l (Å)	Kuhn's length	1006.14	
V_brush (Å^3)	Volume of the polymer arms[a]	14100	Calculated
eta_core (Å^{-2})	Scattering length density of the core	9.0369E-7	
eta_brush (Å^{-2})	Scattering length density of the polymer arms	9.0369E-7	
eta_solv (Å^{-2})	Scattering length density of the solvent	6.39E-6	
R_core (Å)	Radius of the core	5	Fixed
xsolv_core	Fraction of solvent in the core, set to 0	0	
L (Å)	Length of the cylinder[b]	1000	

[a] *Calculated using* $V_{brush} = MW/(dxN_a).10^{24}$, *where MW is the molecular weight of the polymer, d its density and* N_a *Avogadro's number.* [b] *The length of the cylinder cannot be determined because of the absence of a roll-over at low q values, an arbitrary value of 100 nm was therefore used for the fit.*

For this conjugate, SLS measurements were carried out in parallel to SANS in order to widen the window of observation and obtain scattering intensity values at low q (Figure 3.8 A).

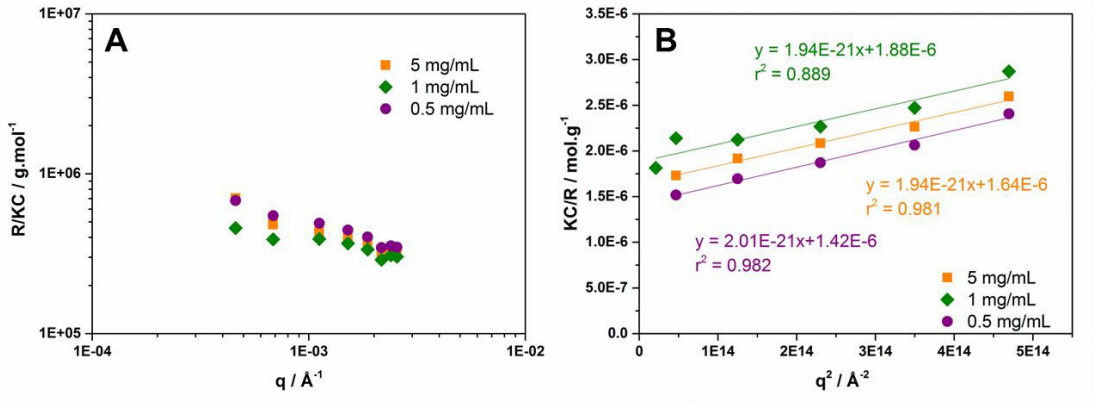

Figure 3.8: A) Evolution of R/KC of **C3** (CP-(p(HPMA-*co*-PUEMA))$_2$) in solution in PBS as a function of the scattering wave vector q and for different concentrations. B) Determination of the molecular weight of **C3** by SLS.

Multiple concentrations were measured at various angles and the Rayleigh ratio, R_θ, was determined using equation 4:[48]

$$R_\theta = \frac{I_{solution}(\theta) - I_{solvent}(\theta)}{I_{toluene}(\theta)} \cdot \left(\frac{n_{solvent}}{n_{toluene}}\right)^2 \cdot R_{toluene} \quad (4)$$

Where $I_{solution}$, $I_{solvent}$ and $I_{toluene}$ are the scattering intensities of the solution, solvent and reference (toluene), respectively. n is the refractive index (n_{water} = 1.333, $n_{toluene}$ = 1.496) and $R_{toluene}$ the Rayleigh ratio of toluene ($R_{toluene}$ = 1.35 x 10^{-5} cm^{-1} for λ = 632.8 nm).

The optical constant K is defined by equation 4, where N_a is the Avogadro number and dn/dC is the incremental refractive index.

$$K = \frac{4\pi^2 n_{solvent}^2}{\lambda^4 N_a}\left(\frac{dn}{dC}\right)^2 \quad (5)$$

At a given concentration, the Rayleigh ratio R_θ is related to the apparent molecular weight of the sample (equation 6). It is only at infinite dilutions, when the interactions between scattering particles are negligible, that the apparent molecular weight is equal to the true molecular weight. Linear regression analysis was used to determine the apparent molecular weight when conc. = 0 (Figure 3.8 B).

$$\frac{KC}{R_\theta} = \frac{1}{M_a} \cdot \left(1 + \frac{q^2.R_g^2}{3}\right) \quad (6)$$

Results showed that the molecular weight of the assemblies was independent of the concentration of the solution (within the tested range) with a value of $6.15.10^5 \pm 0.86.10^5$ $g.mol^{-1}$. Using these data, together with the molecular weight of the unimer and the distance between adjacent peptides, a number of aggregation of 34 ± 5, and an average length of 16.0 ± 2.3 nm was determined (Table 3.5).

Table 3.5: Determination of aggregates size by SLS for conjugate **C3**.

	Slope	Intercept	MW (g/mol)	N_{agg} [a]	L [b] (nm)	R_g (nm)
5 mg/mL	1.94E-21	1.64E-6	6.09E5	33.81	15.89	59.58
1 mg/mL	1.94E-21	1.88E-6	5.32E5	29.57	13.90	55.66
0.5 mg/mL	2.01 E-21	1.42E-6	7.04E5	39.13	18.39	65.16

[a] *N_{agg} = MW/M_unimer.* [b] *$L = N_{agg}$ x Lc, with Lc = 4.7 10^{-1} nm the distance between two adjacent cyclic peptides.*

Such a noticeable difference in the assembly of the three conjugates is likely due to the nature of the polymers attached to the cyclic peptide, with a combination of steric hindrance and hydrogen bonding capacity influencing the stacking of the conjugates. While comparing **C1** and **C2**, both based on homopolymers of HPMA (DP 25 and 53, respectively), it seems reasonable to conclude that longer polymer chains tend to hinder the self-assembly process more, with the conjugate **C1** forming short cylinders (N_{agg} = 11) while **C2** remains as unimers in solution. This result is in line with previously reported work, which showed decreasing tube length with increasing polymer molecular weight.[49,50] The difference between **C2** and **C3** is the most striking, since they have comparable molecular weights but contrasting morphologies in solution: the homopolymer-based **C2** does not assemble while **C3**, which contains 5% of the comonomer PUEMA, stacks into elongated tubes (N_{agg} = 34 ± 5). We attribute the differences of morphology to the presence of the urea and pyridine motifs in PUEMA, which provide additional hydrogen bonding and π-π stacking sites, respectively, thereby counterbalancing steric hindrance caused by the long polymer chains and strengthening the overall assembly. In addition, this effect might be enhanced by the blockiness of the copolymer (see section 3.2.1.2): the PUEMA units are on average located towards the α-chain end of the polymer, thus towards the core of the nanotube, and their proximity to each other is likely to result in secondary interactions despite the limited proportion of PUEMA within the copolymer.

3.2.3 *In vitro* studies

In view of these data, PUEMA-containing conjugate **C3** was selected as a suitable candidate for *in vitro* studies. Polymer **P4** was used as a non-self-assembling polymeric control (see section 3.2.1.2). In addition, rhodamine monomer (rhodamine methacrylate, RhMA) was copolymerised with HPMA and PUEMA, following similar synthetic procedures as described above (3.2.1.2), to afford rhodamine-labelled conjugate **C5** and polymer **P6** (Table 3.6 and Figure 3.9). The amount of RhMA was kept below 0.1% of the total monomer content, to prevent disruption of the self-assembly.

Table 3.6: Characterisation of rhodamine-labelled materials.

Entry	Material	$M_{n,\,th}$ [a] (g.mol^{-1})	$M_{n,\,GPC}$ [b] (g.mol^{-1})	$Đ$ [b]
P5	RhB-pHPMA$_{58}$-*co*-PUEMA$_4$	9700	14900	1.10
C5	CP-(RhB-pHPMA$_{58}$-*co*-PUEMA$_4$)$_2$	20400	28300	1.13
P6	RhB-pHPMA$_{98}$-*co*-PUEMA$_8$	15700	20500	1.20

[a] Determined by ^{1}H NMR. [b] Determined by SEC using DMF (0.1% LiBr) as eluent, calibrated with pMMA standards.

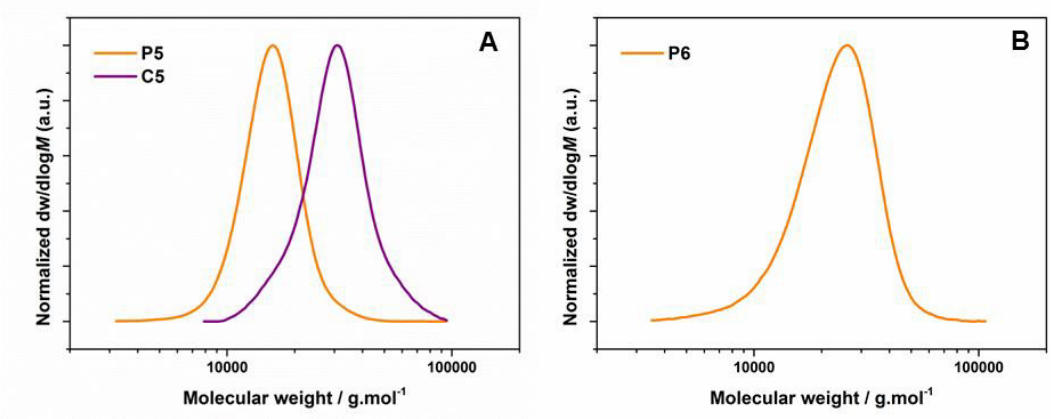

Figure 3.9: SEC chromatograms of A) RhB-pHPMA$_{58}$-*co*-PUEMA$_4$ (**P5**) and CP-(RhB-pHPMA$_{58}$-*co*-PUEMA$_4$)$_2$ (**C5**) B) RhB-pHPMA$_{98}$-*co*-PUEMA$_8$ (**P6**).

Since the polymer **P6** and the conjugate **C5** are not necessarily labelled to the same extent, correction factors were used to enable quantitative comparison between the two compounds: fluorescence was determined for solutions of both **C5** and **P6** at different concentrations. The slope of the obtained linear fit was used to calculate the correction factor (Figure 3.10 and Table 3.7).

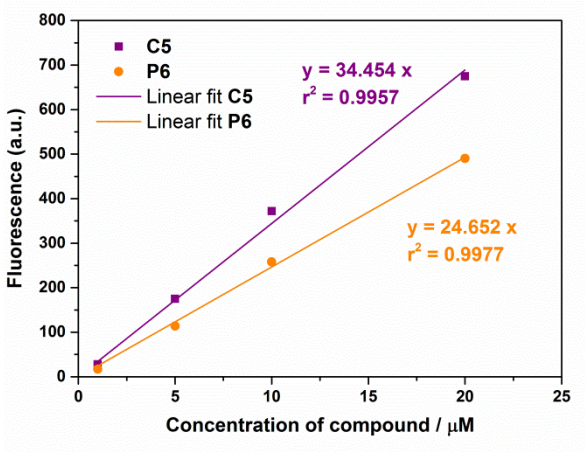

Figure 3.10: Fluorescence calibration curves for **C5** and **P6**.

Table 3.7: Calculation of fluorescence correction factors for **C5** and **P6**.

	C5	**P6**	Average
Slope	34.454	24.652	29.553
Correction factor	**1.166**	**0.834**	1

The biocompatibility of the compounds was tested *in vitro* on three cell lines (A2780 human ovarian carcinoma, PC3 human prostate carcinoma and MDA-MB-231 breast cancer) by performing cell growth inhibition assays for 72 h. Although it should be acknowledged that these cell lines are all cancerous and they therefore generally exhibit a higher tolerance to challenge than healthy cells, they provide a good indication of potential toxicity in healthy cells. In all three cell lines, incubation with up to 500 $\mu g.mL^{-1}$ of the non-labelled compounds, **C3** and **P4,** did not result in any noticeable reduction of the cell viability (Figure 3.11 A-C).

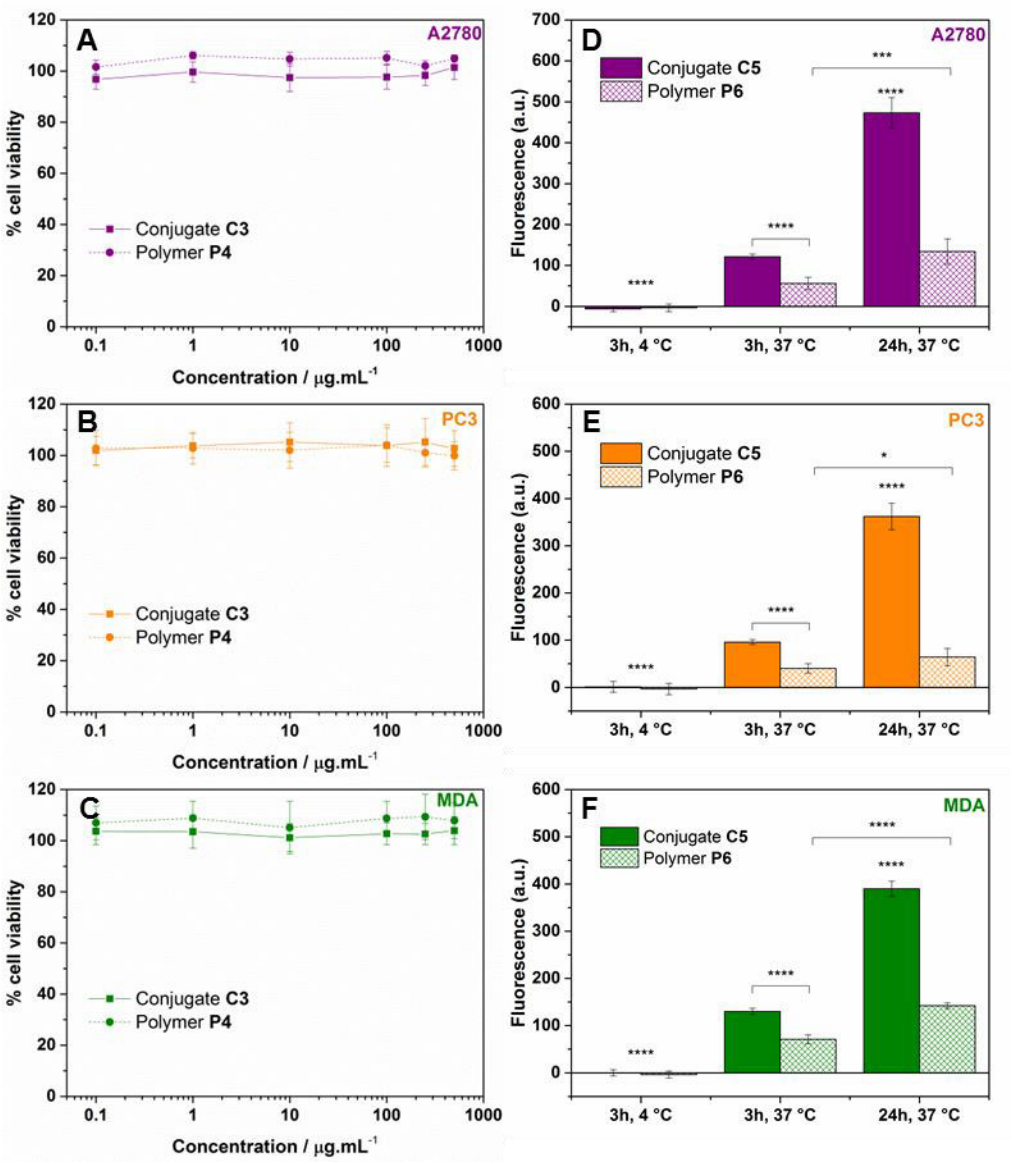

Figure 3.11: Antiproliferative activity of the compounds (continuous: conjugate, dashed: polymer) in A) A2780 B) PC3 and C) MDA cells, and cellular fluorescence intensity associated with rhodamine as determined by flow cytometry after incubation of the compounds for 3 h at 4 °C, 3 h at 37 °C and 24 h at 37 °C in D) A2780 E) PC3 and F) MDA cells. Data represents geometric mean of fluorescence ± SD for two independent experiments done in triplicates: *$p < 0.05$, ***$p < 0.001$, ****$p < 0.0001$.

The amount of compound associated with the cells was then quantified using flow cytometry (Figure 3.11 D-F). Cells were incubated in presence of the labelled compounds **C5** and **P6** for 3 h and 24 h at 37 °C. For both incubation times, and in all three cell lines, the polymer control associated significantly less than the conjugate ($p < 0.0001$). For example in A2780, the amount of conjugate **C5** measured in the cells was nearly double that of polymer **P6** after

3 h; the discrepancy increased to 3.5 times more conjugate after 24 h incubation. This result is attributed to the difference in size and aspect ratio between the two compounds. In these conditions, the conjugates self-assemble to form a cylindrical assembly with an average number of aggregation of 34 (see SLS results, section 3.2.2), whereas polymer **P6** remains as a single unit. Particle shape[51] and size[52-54] are thought to play a non-negligible role in cellular uptake, with larger particles exhibiting increased uptake up to a certain size, above which the uptake generally decreases. Depending on the study, percentage of uptake tends to peak with particles between 20 and 100 nm, and particles with a diameter of either less than 10 nm or more than 100 nm entering the cells to a lesser degree. This effect is found across particles of different compositions, including coated iron oxide,[52] silica[53] and polymeric[54] nanoparticles. The present results are in line with these findings, with 16 nm-long nanotubes entering the cells to a higher extent than the single polymer chains.

It is also interesting to note that cellular association increases with time, indicating uptake occurs to a higher extent than excretion. In the case of the conjugates, a 3-fold increase of fluorescence in MDA cells was observed when varying the incubation time from 3 h to 24 h. Similar increases were found in other cell lines, with 3.8x in PC3 and 3.9x in A2780. This effect was also observed for the polymer, although to a lesser extent: increases in fluorescence between 3 h and 24 h incubation of 2.4x in A2780, 1.6x in PC3 and 2.0x in MDA were recorded. In summary, these results indicate that the compounds accumulate in the cells over time (uptake > exocytosis), which is commonly observed for nanosized objects.[55,56]

In order to probe whether the mechanism of internalisation was energy-dependent, the experiment was performed at 4 °C, whereby these pathways are not activated. In all three cell lines, both compounds showed no accumulation after 3 h in these conditions, indicating that the mechanism of cellular entry relies on endocytosis or other energy-dependent pathways.

Intracellular localisation of the conjugate was confirmed by confocal imaging, using the rhodamine-labelled compound **C5** (Figure 3.12). Following PC3 cells incubation with the conjugate at 20 μM (400 $\mu g.mL^{-1}$) for 24 h, rhodamine staining inside the cells confirmed that the compound was readily taken up by the cells and not simply associated with the membrane. Lysotracker ® green was added together with the conjugate to assess organelle localisation. The merged images of the red and green channels clearly demonstrate a

noticeable amount of colour coincidence of the conjugates with the lysosomal compartments, which is in agreement with the flow cytometry data, indicating energy-dependent entry pathways.

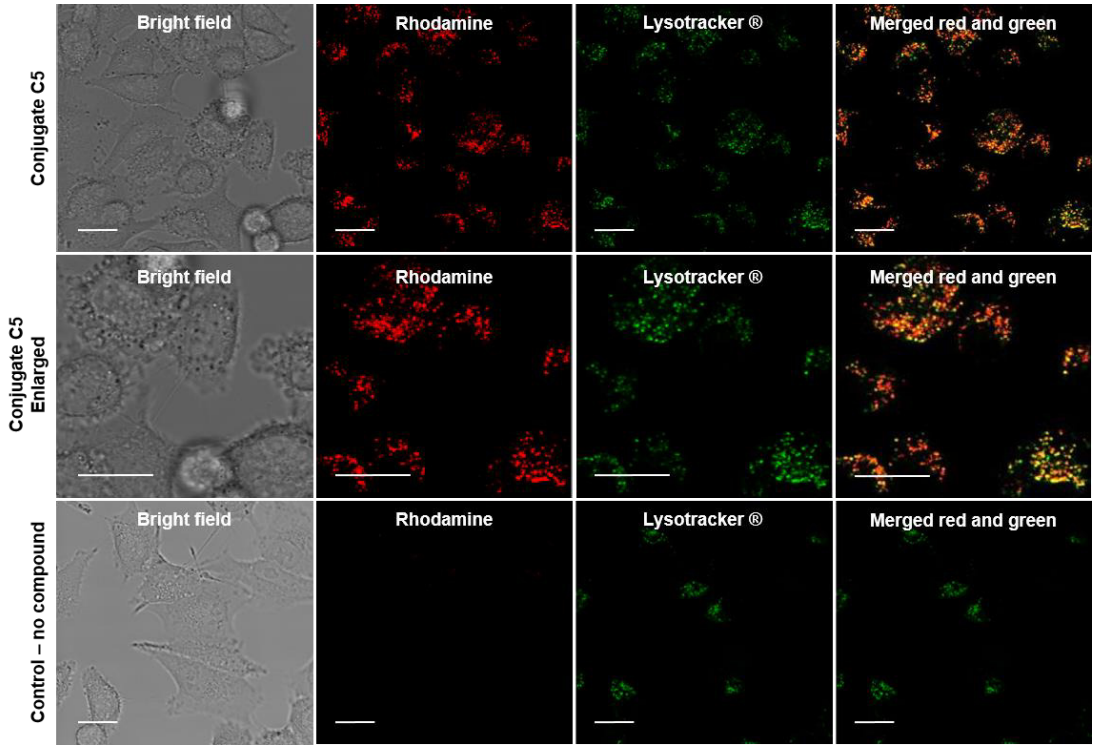

Figure 3.12: Confocal images of PC3 human prostate carcinoma cells treated with rhodamine-labelled conjugates **C5** for 24 h at 37 °C at a concentration of 20 μM. Lysosomes were stained using Lysotracker ® Green DND-26. Scale bar 20 μm.

3.2.4 Plasma pharmacokinetics and organ biodistribution

In order to characterise the *in vivo* behaviour of these compounds, both the conjugate and control polymer were radiolabelled, taking advantage of the hydroxyl groups present on pHPMA to attach ^{14}C-ethanolamine (Scheme 3.4). Carbonyldiimidazole (CDI) was used as the coupling reagent. This compound reacts with alcohols and amines, and when reacted with alcohols the stability of the formed imidazole carboxylic ester depends on the nature of the starting alcohol. If the parent alcohol is secondary (such as in HPMA), further reaction is limited to primary alcohols or amines, leading to the formation of carbonates or carbamates, respectively.[57,58] When translated to post-polymerisation modification of polymers, the reaction of CDI onto pendant chains containing primary alcohols would lead to crosslinking, but in the present case it allows for the attachment of functional primary amines such as radiolabelled ethanolamine.

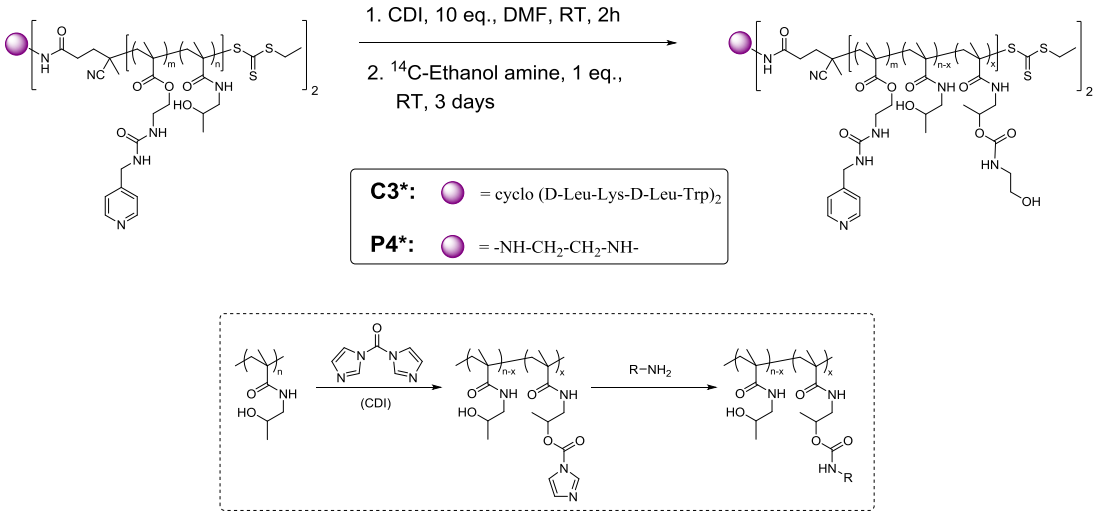

Scheme 3.4: Radiolabelling of **C3** and **P4** using carbonyldiimidazole coupling agent.

The obtained compounds **C3*** and **P4*** were purified by size exclusion chromatography (SEC) and extensively dialysed to remove any radiolabel excess. Effective labelling was confirmed by scintillation counting of SEC fractions and HPLC analysis (Figure 3.13).

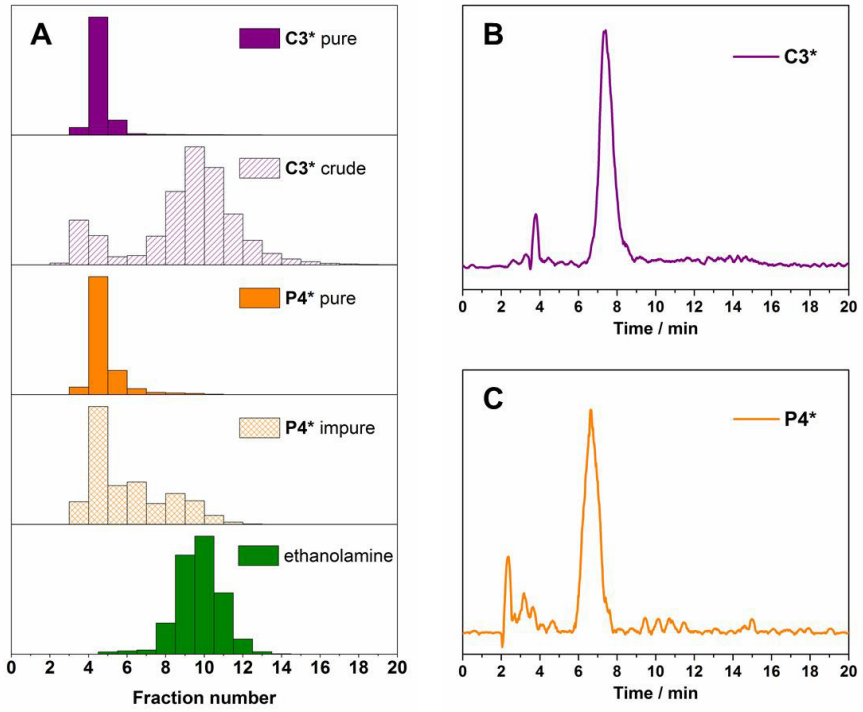

Figure 3.13: A) Scintillation counting of size exclusion chromatography fractions of conjugate **C3*** and polymer **P4*** before and after purification. B) Radiometric detector traces of HPLC of the ^{14}C labelled conjugate **C3*** and polymer **P4***. In both cases, free radiolabel represents less than 10% of the total counts.

The radiolabelled polymer **P4*** and conjugate **C3*** were injected intravenously to male Sprague-Dawley rats at 12 mg/kg and blood samples were taken at regular intervals for 24 h to determine the plasma concentration *vs* time profiles (Figure 3.14).

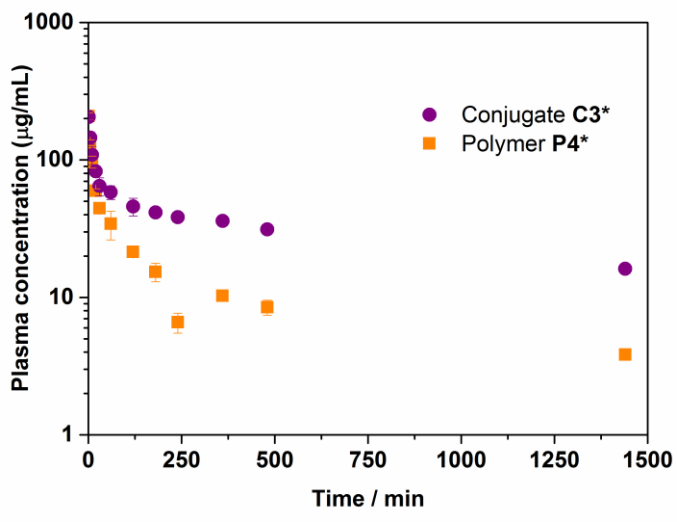

Figure 3.14: Plasma concentration *vs* time profiles of ^{14}C-labelled polymer **P4*** (orange squares) and conjugate **C3*** (purple circles) following intravenous administration to rats at 12 mg/kg (mean ± SD, n = 4-5 rats).

The obtained profiles present the two phases characteristic of IV injections: the distribution phase (rapid dispersion or dissemination of substances throughout the fluids and tissues of the body until equilibrium is reached) and the elimination phase (metabolism and excretion of the injected substance). Non-compartmental analysis was performed and the pharmacokinetic parameters are summarised in Table 3.8. The initial volume of the central compartment (V_c) was close to blood volume, which is typical of IV injections. The non-assembling polymer, **P4***, showed rapid elimination from systemic circulation, in accordance with previously reported results on HPMA copolymers.[59-61] The elimination half-life ($t_{1/2}$, obtained from the slope of the elimination phase in the plasma concentration *vs* time profile) of the nanotubes was only slightly longer than that of the polymer control, indicating a similar rate of elimination from the system after the distribution phase. However, total exposure, in the case of the nanotubes, was significantly higher than for the polymer ($p < 0.0001$), as shown by the difference in the AUC (area under the curve), which was found to be more than three times higher for the conjugates. We attribute this discrepancy to the larger size of the nanotubes, which allows them to partially avoid immediate renal clearance. The increased exposure is in agreement with the reduced clearance (Cl, 3 ± 0.2 mL/h for the

nanotubes *vs* 12 ± 0.4 mL/h for the polymer) and reduced terminal volume of distribution ($V_{d,\beta}$, 70 ± 2 mL for the nanotubes *vs* 225 ± 35 mL for the polymer). The clearance of a chemical is the volume of plasma from which the chemical is apparently completely removed, per unit time. As such, it gives a measure of the speed of elimination. The volume of distribution (V_d) represents the volume in which the compound seems to be distributed with a concentration equal to the plasma concentration: a low V_d that remains close to blood volume means that the compound mostly stays in the plasma, whilst a high V_d indicates that the compound is distributed outside of the central compartment (either excreted or distributed to other tissues). The observed volume of distribution of the nanotubes is lower than for small molecular weight linear polymers, but higher than reported values for PEGylated dendrimers (as low as 25 mL after 30 h),[62] stars (approximately 60 mL after 7 days)[63] or small brushes (60 mL after 24 h),[22] suggesting an intermediate performance in terms of circulation.

Table 3.8: Calculated pharmacokinetic parameters and urine recovery after intravenous administration of conjugate **C3*** and polymer **P4*** to rats at 12 mg/kg (mean ± SD, n = 4-5 rats). $^{**}p < 0.01$, $^{****}p < 0.0001$.

	Conjugate (C3*)	**Polymer (P4*)**
$t_{1/2}$ (h)	16.1 ± 1.3	13.4 ± 2.0
AUC (µg/mL.h)	1120 ± 62	331 ± 10****
V_c (mL)	15.0 ± 1.0	16.6 ± 1.0
$V_{d,\beta}$ (mL)	70 ± 2	225 ± 35**
Cl (mL/h)	3 ± 0.2	12 ± 0.4****
Urine (% dose)	62 ± 7	72 ± 8

The percentage of dose recovery in urine was high for both the polymer (72 ± 8 %) and the conjugates (62 ± 7 %), indicating that the majority of both compounds is ultimately excreted from the body. The molecular weight cut-off for renal filtration is generally estimated to be around 50 kDa,[24] which is well below the molecular weight of the nanotubes (estimated to be 615 kDa by SLS) but above the mass of the polymer and the unimers. Hence, this result suggests that the labelled compounds found in the urine are fragments of the initial nanotubes, either degraded chemically (free radiolabel), or physically (unimeric conjugates or very short tubes).

To understand the fate of both compounds after administration, specifically to verify that they are both largely excreted from the body within 24 h, their accumulation in major organs (liver, spleen, pancreas, kidneys, heart, lungs, and brain) was quantified by measuring the residual ^{14}C present in the tissues harvested 24 h after IV injection. Figure 3.15 shows the percentage of injected ^{14}C recovered in each organ. Levels of accumulation were very low in all examined organs, with the highest amount found in the liver (3.1 ± 0.4 % for the conjugate, 1.3 ± 0.3 % for the polymer). Such low levels of organ accumulation are typical of small molecular weight HPMA copolymers.[61]

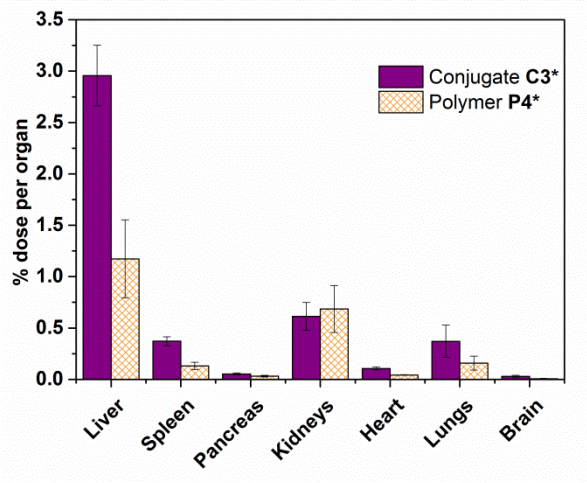

Figure 3.15: Distribution of ^{14}C in organs, 24 h after intravenous administration of conjugate (purple) and polymer (orange) at 12 mg/kg (mean ± SD, n = 4-5 rats).

The very low organ uptake, together with the high urine excretion, and the intermediate value of $V_{d,\beta}$ (lower than for a small molecular weight polymer but higher than for dendrimers or stars or small brushes) may indicate that the nanotubes are in fact constituted of a mixture of slowly disassembling structures. A more advanced study is required to fully elucidate the mechanism of clearance, but one hypothesis is that the initially assembled structures exhibit prolonged circulation (as evidenced by the higher exposure of the nanotubes compared to the non-assembling polymer) and the resulting unimeric conjugates are ultimately cleared out of the body without organ accumulation.

3.3 Conclusions

Peptide-polymer conjugates consisting of self-assembling cyclic peptides functionalised with HPMA (co)polymers were synthesised, and a study of their assembly in solution showed the formation of nanotubes. Interestingly, a small fraction of a comonomer prone to non-covalent interactions greatly helped the self-assembly process. The comonomer-containing conjugate was tested against a non-assembling control and clear differences in their cell uptake behaviour *in vitro* and their pharmacokinetics *in vivo* were observed. Cellular accumulation studies demonstrated a time and temperature dependent internalisation of the compounds, with larger sized nanotubes increasing the uptake by a factor 3 to 4 compared to that of the polymer. Colour coincidence studies confirmed accumulation of the conjugates in the lysosomal compartments of the cells, further indicating an endosomotropic uptake pathway. After intravenous injection to rats, conjugates were found to circulate for a reasonable amount of time, and exhibit a higher exposure than the control polymer. Such characteristics are beneficial when attempting passive tumour targeting though the EPR effect. Most importantly, conjugates were ultimately cleared out, which might be related to a slow disintegration of the self-assembled nanotubes into smaller structures or unimers. This feature certainly helps to avoid undesired long-term accumulation in organs such as the liver and spleen which is essential for future applications in drug delivery. Considering all the observed results, these cyclic peptide-polymer nanotubes represent a novel and promising class of materials for application as carrier material for the transport of pharmaceutically active compounds.

3.4 Experimental

3.4.1 Materials

N-methylmorpholine (NMM, 99 %) was purchased from Alfa Aesar. 2,2'-Azobis[2-(2-imidazolin-2-yl)propane]dihydrochloride (VA-044) was purchased from Wako Chemicals. *O*-(Benzotriazole-1-yl)-*N,N,N',N'*-tetramethyluronium hexafluorophosphate (HBTU) was purchased from Iris Biotech. Methacryloxyethyl thiocarbamoyl rhodamine B (Rhodamine methacrylate, RhMA) was purchased from Polysciences. Ethanolamine [1-14C] (55 mCi/mmol, 0.1 mCi/mL) was obtained from ARC (American Radio Chemicals). Deuterated solvents for NMR were purchased from Sigma-Aldrich. All solvents were bought from

commercial sources and used as received. The cyclic peptide and chain transfer agent CPAETC were synthesised as described in Chapter 2. $E(CPAETC)_2$ was synthesised according to previously reported protocols.[64]

3.4.2 Characterisation methods

NMR spectra were recorded on a Bruker DPX-300 instrument. Molecular weights and dispersities of polymers were assessed by size exclusion chromatography (SEC) on a Polymer Laboratories PL-GPC 50 Plus system in DMF with 0.1% LiBr, using a poly(methyl methacrylate) calibration as described in Chapter 2.

SANS was carried out either on the Sans2d small angle diffractometer at the ISIS Pulsed Neutron Source (STFC Rutherford Appleton Laboratory, Didcot, UK)[65,66] or on SANS Instrument D11 at Institut Laue-Langevin in Grenoble, France.

On the Sans2d instrument, a collimation length of 4 m and incident wavelength range of 1.75 – 16.5 Å was employed. Data were measured simultaneously on two 1 m^2 detectors to give a q-range of 0.0045 – 1.00 $Å^{-1}$. The small-angle detector was positioned 4 m from the sample and offset vertically 60 mm and sideways 100 mm. The wide-angle detector was positioned 2.4 m from the sample, offset sideways by 980 mm and rotated to face the sample. The wave vector, q, is defined as:

$$q = \frac{4\pi \sin\frac{\theta}{2}}{\lambda}$$

where θ is the scattered angle and λ is the incident neutron wavelength. The beam diameter was 8 mm. Samples were prepared at a concentration of 5 mg/mL in deuterated phosphate buffer saline (PBS, pH 7.4), and were contained in 2 mm path length quartz cells. Each raw scattering dataset was corrected for the detectors efficiencies, sample transmission and background scattering and converted to scattering cross-section data ($\partial\Sigma/\partial\Omega$ *vs.* q) using the instrument software.[67] These data were placed on an absolute scale (cm^{-1}) using the scattering from a standard sample (a solid blend of hydrogenous and perdeuterated polystyrene) in accordance with established procedures.[68]

On the D11 instrument, scattering intensities were recorded by a two-dimensional position-sensitive ^3He detector. Three different instrument settings were used corresponding to a q range of $0.01 < q < 0.5$. H_2O was used for instrumental calibration. The data were placed on

an absolute scale (cm^{-1}) using the scattering from a standard sample in accordance with established procedures.[69] The obtained reduced data was analysed with the open access software SASfit.[70]

Light scattering measurements were obtained using an ALV-CGS3 system operating with a vertically polarised laser with a wavelength of 632 nm. The measurements were taken at 20 °C, at different degree intervals, corresponding to a wider range of scattering vectors. The incremental refractive index, d*n*/d*C*, was determined by measuring the refractive index of the polymer in water at various concentrations ranging from 0.25 to 2 mg/mL, using a Shodex RI detector operating at a wavelength of 632 nm.

3.4.3 Synthetic procedures

3.4.3.1 Synthesis of 2-hydroxypropyl methacrylamide (HPMA)

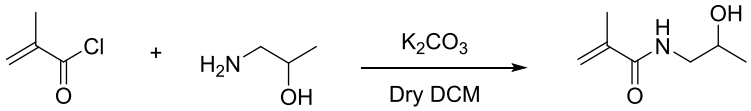

Potassium carbonate (29 g, 1.1 eq., 0.21 mol) was dispersed in 120 mL of dry DCM. The mixture was cooled to -10 °C with an ice-ethanol bath and 1-amino-2-propanol (14.5 mL, 1 eq., 0.19 mol) was added. Methacryloyl chloride (18.5 mL, 1 eq., 0.91 mol) was diluted with 20 mL of dry DCM, and added dropwise to the previous mixture, while maintaining the temperature at -10 °C. Once the addition was complete, the reaction was left to warm up to room temperature and stirred overnight. After filtration and drying over $MgSO_4$, the DCM was evaporated and a white solid was obtained. The product was dissolved in methanol and washed with hexane, and the methanol phase was evaporated. The obtained solid was recrystallised from acetone. Yield: 45% (10.2 g). ^{1}H-NMR (d_6-DMSO, 300 MHz, ppm): δ = 7.82 (broad s, 1H, N*H*) , 5.65 (s, 1H, C*H* vinyl), 5.31 (s, 1H, C*H* vinyl), 4.71 (s, 1H, O*H*), 3.69 (m, 1H, C*H*), 3.05 (m, 2H, CH_2), 1.85 (s, 3H, CH_2=C(CH_3)), 1.00 (d, *J* = 6 Hz, 3H, CH-CH_3). ^{13}C-DEPT-NMR (d_6-DMSO, 75 MHz, ppm): δ = 167.7, 139.9, 118.9, 85.1, 46.7, 21.1, 18.6. MP: 69-72 ºC.

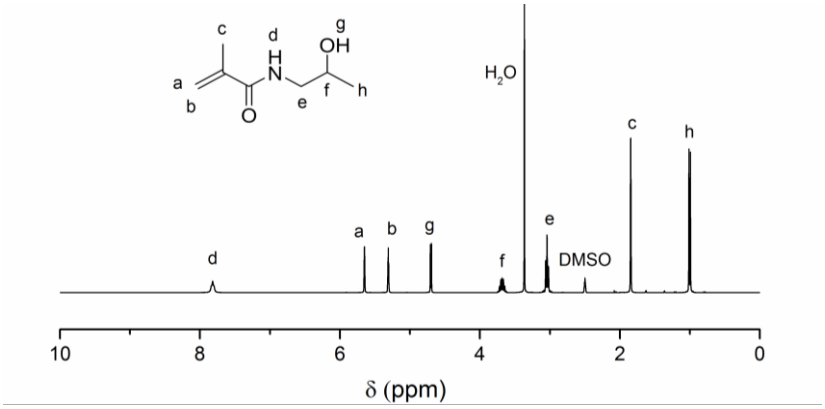

Figure 3.16: ^{1}H NMR spectrum (d_6-DMSO, 300 MHz) of 2-hydroxypropyl methacrylamide (HPMA).

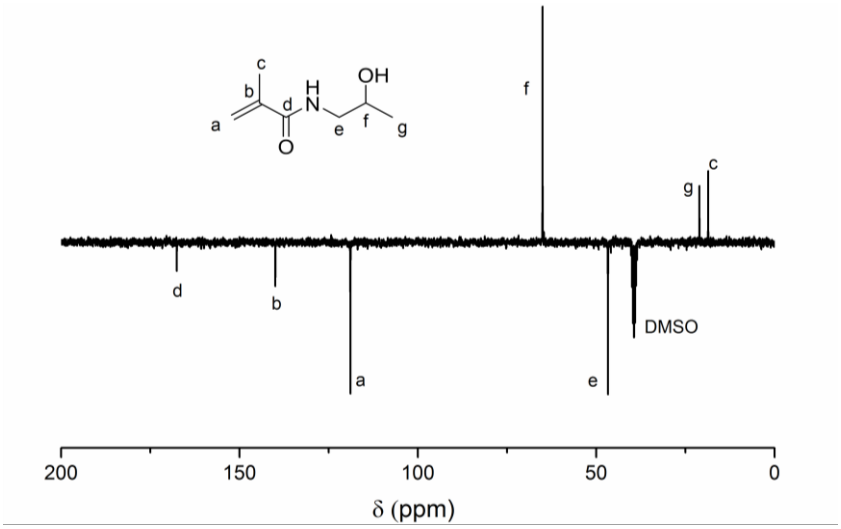

Figure 3.17: ^{13}C-APT NMR spectrum (d_6-DMSO, 75 MHz) of 2-hydroxypropyl methacrylamide (HPMA).

3.4.3.2 Synthesis of 2-(3-(pyridin-4-ylmethyl)ureido)ethyl)methacrylate (PUEMA)

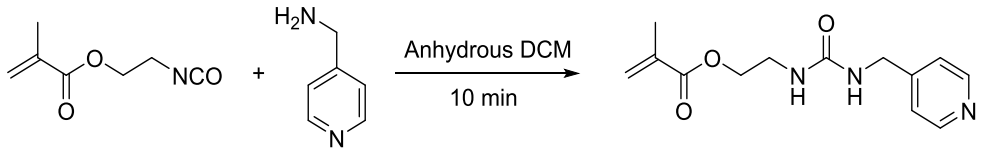

2-Isocyanatoethyl methacrylate (2.2 g, 14.15 mmol) and 4-aminomethyl pyridine (1.53 g, 1 eq., 14.15 mmol) were mixed in dry DCM (10 mL) and left to stir at room temperature for 10 min. The solvent was evaporated under reduced pressure and PUEMA was collected as a white powder. Yield: 95% (3.53 g). ^{1}H-NMR ($CDCl_3$, 300 MHz, ppm): δ = 8.52 (d, 2H, C*H*-N-C*H* pyridine), 7.19 (d, 2H, C*H*-C-C*H* pyridine), 6.09 (s, 1H, C*H* vinyl), 5.59 (s, 1H, C*H*

vinyl), 5.13 (broad t, 1H, N*H* urea), 4.97 (broad t, 1H, N*H* urea), 4.38 (d, 2H, NH-C*H*$_2$-pyridine), 4.25 (t, 2H, O-C*H*$_2$), 3.53 (q, 2H, O-CH$_2$-C*H*$_2$), 1.93 (s, 3H, C*H*$_3$). ^{13}C-DEPT-NMR ($CDCl_3$, 75 MHz, ppm): 166.9, 157.5, 149.2, 148.3, 135.3, 125.5, 121.4, 63.4, 42.4, 39.0, 17.6. FTIR: (ν, cm^{-1}): 3313 (N-H stretch, urea), 1720 (C=O stretch, methacrylate), 1623 (C=C stretch, alkene), 1585 (C=O stretch, urea). MS (ESI): $[M+Na]^+$ calculated: 286.1, found: 285.9. MP: 109-112 ºC.

3.4.3.3 RAFT polymer synthesis

Chain transfer agent (CTA, here CPAETC or E(CPAETC)$_2$), monomers (HPMA, PUEMA, RhMA), initiator (VA 044) and solvent (70/30 DMSO/H_2O) were introduced into a flask equipped with a magnetic stirrer and sealed with a rubber septum (see Table 3.9 for detailed conditions). The solution was degassed by bubbling through with nitrogen for 15 min, and then put in an oil bath at 44 °C. Kinetic experiments were conducted over 24 hours and reactions times for subsequent polymerisations are indicated in Table 3.9. Conversions were determined by ^{1}H NMR. For polymers **P5** and **P6**, conversion of RhMA could not be determined because the extremely low amounts did not allow visualisation of the corresponding signals. The polymers were precipitated in ice-cold acetone and dried under vacuum. The rhodamine-labelled polymers **P5** and **P6** were further dialysed to remove any excess dye.

Table 3.9: Summary of polymerisation conditions. All reactions were performed with $[HPMA]_0 = 2$ mol.L^{-1}.

	CTA	Time (hours)	$\frac{[HPMA]_0}{[CTA]_0}$	$\frac{[PUEMA]_0}{[CTA]_0}$	$\frac{[RhMA]_0}{[CTA]_0}$	$\frac{[CTA]_0}{[I]_0}$	Conversion (%)	
							HPMA	PUEMA
P1	CPAETC	8	50	-	-	20	50	-
P2	CPAETC	18	70	-	-	20	75	-
P3	CPAETC	18	66.5	3.5	-	20	82	>99
P4	E(CPAETC)$_2$	18	137	7	-	10	68	>99
P5	CPAETC	20	66	3.5	0.07	20	75	>99
P6	E(CPAETC)$_2$	20	133	7	0.13	10	68	>99

3.4.3.4 Conjugation of polymers to the cyclic peptide

The cyclic peptide, polymer (2.5 eq.) and HBTU (3.75 eq.) were solubilised in DMSO (1.5 mL). NMM (6 eq.) was added to the reaction mixture and was left to stir at room temperature for 2 hours. After the reaction, DMSO was removed using a stream of N_2 and the conjugates were dissolved in water and purified from the excess polymer using centrifugal ultrafiltration, with a molecular weight cut off of 30 kDa (Amicon® Ultra centrifugal filter). The isolated conjugates were freeze-dried.

3.4.3.5 Radiolabelling of compounds

Conjugate (or polymer) was introduced in a vial, together with CDI (10 eq.) and anhydrous DMF (1 mL) and the mixture was stirred for 4 hours. An aliquot of ^{14}C-labelled ethanolamine in ethanol was withdrawn from the bottle (1 eq.) and the ethanol evaporated using a steam of nitrogen. The radiolabel was redissolved in DMF and added to the mixture, which was then stirred for 4 days. The solvent was removed using a stream of nitrogen and the dried-up mixture was solubilised in water, and passed over a size exclusion column (PD10, GE Healthcare Life Sciences) to remove most of the remaining free radiolabel prior to dialysis. The purity of the compound was assessed by HPLC and size exclusion chromatography using PD10 columns (pre-packed cartridges). Briefly, 0.7 mL fractions were collected and the activity of each fraction was determined by scintillation counting.

3.4.4 *In vitro* testing

3.4.4.1 Cells

A2780 (human ovarian carcinoma), PC3 (human prostate carcinoma) and MDA-MB-231 (human breast cancer) cells were obtained either from the European Collection of Cell Cultures (ECACC) or Sigma-Aldrich. A2780 were grown in Roswell Park Memorial Institute medium (RPMI-1640), and PC3 and MDA-MB-231 in Dulbecco's Modified Eagle Medium (DMEM). Both media were supplemented with 10% v/v of foetal calf serum, 1% v/v of 2 mM glutamine and 1% v/v penicillin/streptomycin. Cells were grown as adherent monolayers at 37 °C in a 5% CO_2 humidified atmosphere and passaged at approximately 70-80% confluence.

3.4.4.2 Growth inhibition assay

Briefly, 5000 cells were seeded per well in 96-well plates and allowed to grow for 24 h before adding different concentrations of the compounds to be tested. Compounds were dissolved directly in cell culture medium at concentrations ranging from 0.1 to 500 μg/mL. Culture medium was replaced by dilutions of the compounds and cells further incubated for 72 h. After this, supernatant was removed and replaced by fresh medium. The XTT assay was used to determine cell metabolic activity as a measure of viability. Absorbance measurements of the plate at 475 nm were carried out using a Synergy HTX (Biotek) plate reader. Degree of viable treated cells was determined by comparison to untreated controls. Two independent sets of experiments in triplicates were carried out and standard deviations were used for error bars.

3.4.4.3 Microscopy

Cells were seeded in an 8-chamber imaging plate (Eppendorf) at 15 000 cells per well and incubated overnight at 37 °C with 5% CO_2. Rhodamine-labelled conjugate dissolved in PBS was added to the wells to a final concentration of 20 μM and incubated for 24 h. Colocalisation studies were carried out after lysosome staining using Lysotracker ® Green DND-26. Labelling was achieved by incubating cells in the presence of Lysotracker (100 nM) for 2 hours. The cells were washed 2 times with fresh media and images were recorded using a confocal microscope (SP5, Leica, Gmbh).

3.4.4.4 Flow cytometry

Cells were seeded in 24-well plates at 100 000 cells per well and incubated in 500 μL of compound-free media overnight at 37 °C with 5% CO_2. Rhodamine-labelled compounds were then added to cells in triplicate, achieving a final concentration of 20 μM. Three sets of conditions were tested: incubation at 37 °C for 24 h, incubation at 37 °C for 3 h, and incubation at 4 °C for 3 h. For incubation at 4 °C, the cells were placed on ice for 10 min prior to addition of the compound, and subsequently in the fridge. After incubation, the culture medium was removed and the cells were washed with PBS, harvested with trypsin, transferred to Eppendorf tubes and spun at 1500 g for 5 min. The supernatant was discarded and cell pellets were resuspended in PBS, transferred into flow cytometry tubes and stocked on ice until measurement. Samples were analysed on a BD FACScan flow cytometer using the FL2 channel (585/42 nm). Cells were analysed using forward and side scatter gates to exclude debris and cell aggregates. Fluorescence intensity corresponding to untreated cells

was subtracted, the data were processed using Flowing software 2® and reported values correspond to the average of the means of fluorescence for a population of 10000 cells.

3.4.5 Pharmacokinetics and Biodistribution studies

3.4.5.1 Activity Determination and Scintillation Counting

The specific activity of the compounds was determined by dilution of known amounts of material into PBS. Aliquots were mixed with 4 mL of Ultima Gold and scintillation counted on a Packard Tri-Carb 2000CA liquid scintillation analyzer (Meriden, CT).

3.4.5.2 Animals

All animal experimental protocols were approved by the Monash Institute of Pharmaceutical Sciences Animal Ethics Committee, Monash University, Parkville, VIC, Australia. Male Sprague-Dawley rats (250-350 g) were used in these experiments. Animals were maintained on a 12 h light/dark cycle at all times.

3.4.5.3 Intravenous Pharmacokinetic Studies

A day prior to compound administration, each rat was anaesthetised under isoflurane (2-5% v/v) and cannulas (polyethylene tubing 0.96 x 0.58 mm, Paton Scientific, Victor Harbour, Australia) were surgically inserted into the right jugular vein and carotid artery (to facilitate IV administration and blood collection respectively) as previously described.[71] The rats were transferred to individual metabolic cages (to permit separate collection of urine and faeces) and allowed to recover overnight prior to dosing. Each animal was fasted up to 14 h prior to and up to 8 h after administration of the IV dose with water provided *ad libitum*. Prior to injection, blood samples (0.2 mL) were obtained from the carotid artery. The compounds were dissolved in phosphate buffered saline (PBS) and 0.5 mL was administered at a dose of 12 mg/kg as a slow bolus intravenous injection (1 mL/min) *via* the jugular cannula. The cannula was then flushed with 0.5 mL of heparinised saline to ensure complete infusion of the dose. Subsequent blood samples (0.2 mL) were taken at 1, 5, 10, 20, 30, 60, 120, 180, 240, 360, 480, and 1440 min after dose administration. Blood samples were placed immediately into tubes containing 10 IU of heparin and centrifuged for 5 min at 3500 *g*. Plasma (0.1 mL) was collected, transferred to a separate vial and mixed with 4 mL of Ultima Gold scintillation cocktail prior to scintillation counting.

3.4.5.4 Biodistribution Studies

At the end of the pharmacokinetic studies (24 h), animals were humanely killed by injection of a lethal dose of sodium pentobarbital (*via* the jugular vein cannula) and the following tissues removed: liver, spleen, pancreas, kidneys, heart, lungs and brain. The tissues were frozen (-20 °C) and stored in pre-weighed polypropylene tubes until processing and analysis. The samples were homogenised using a gentleMACS Dissociator (Miltenyi Biotech) with 5 mL of MilliQ water. Triplicate samples from each tissue homogenate (typically 50-100 mg of tissue) were mixed with 2 mL of tissue solubiliser (Solvable, Perkin Elmer) and the samples stored at 60 °C overnight to facilitate tissue digestion. The samples were cooled to room temperature and 200 µL hydrogen peroxide (30% w/v) was added to each vial. Samples were left open at room temperature until bubbling had ceased. Ultima Gold (10 mL) was then added and the mixture vortexed before the samples were stored at 4 °C in the dark, without agitation, for at least 3 days prior to scintillation counting. Blank organs also were treated as above to provide for background correction. In order to correct for any reduction in radioactivity counting efficacy due to the processing of the tissues, an identical second set of samples was processed in the same way but the tissue homogenate aliquots were spiked with a known quantity of radiolabel prior to addition of Solvable. The samples were then scintillation counted at 12 °C.

A processing efficiency was calculated, using the following equation:

$$efficiency = \frac{spiked\ tissue_{dpm} - tissue_{dpm,uncorr}}{spiked\ solution_{dpm}}$$

Where spiked $tissue_{dpm}$ is the mass-corrected radioactivity measured in the spiked samples, $tissue_{dpm,uncorr}$ is the mass-corrected radioactivity in the non-spiked tissue samples, and spiked $soln_{dpm}$ is the known amount of radioactivity added to the spiked sample. Effectively, the calculation provides an indication of the efficiency of counting, using the known (spiked) amount of radioactivity in each tissue as a reference. This value for efficiency was used to correct the ^{14}C content in the processed sample using the following equation:

$$tissue_{dpm,corr} = \frac{tissue_{dpm,uncorr}}{efficiency}$$

The activity in the whole organ was then calculated knowing the mass fraction of the entire organ present in the processed sample. The results are expressed as percentage of injected dose in the organ at sacrifice.

3.4.5.5 Urine

Urine, pooled from immediately after dose administration till 24 h, was collected at the end of the study. A blank urine sample was also collected to provide for background correction. After accounting for the volume of urine collected a 100 μL aliquot was taken and mixed with 4 mL of Ultima Gold and scintillation counted. After background subtraction, the radiolabel content of the sample was corrected for the total volume of urine collected and converted to a percentage of the total administered dose.

3.4.5.6 Calculation of Pharmacokinetic Parameters

The concentrations of radiolabel in plasma/whole blood samples were converted to microgram equivalent concentrations using the specific activity of the radiolabeled compounds. Non-compartmental pharmacokinetic parameters were calculated with Excel using the PK solver add-in.[72] The NCA IV Bolus model was used, in which the $AUC_{0-\infty}$ was calculated using the linear trapezoidal method. The elimination half-life ($t_{1/2}$), volume of distribution (V_d) and clearance (Cl) were also determined from the model. An estimate of initial distribution volume, or volume of central compartment (V_c) was calculated from the dose/Cp^0, where Cp^0 was the extrapolated concentration in plasma at the moment of completion of the injection. Two-tailed t-tests were performed assuming unequal variance.

3.5 References

1. A. S. Hoffman, *J. Controlled Release* **2008,** *132* (3), 153-163.
2. K. Cho, X. Wang, S. Nie, Z. Chen, D. M. Shin, *Clinical Cancer Research* **2008,** *14* (5), 1310-1316.
3. H. Maeda, *Bioconjugate Chem.* **2010,** *21* (5), 797-802.
4. H. Maeda, H. Nakamura, J. Fang, *Adv. Drug Delivery Rev.* **2013,** *65* (1), 71-79.
5. G. Pasut, F. M. Veronese, *J. Controlled Release* **2012,** *161* (2), 461-472.
6. J. Nicolas, S. Mura, D. Brambilla, N. Mackiewicz, P. Couvreur, *Chem. Soc. Rev.* **2013,** *42* (3), 1147-1235.
7. L. Y. T. Chou, K. Ming, W. C. W. Chan, *Chem. Soc. Rev.* **2011,** *40* (1), 233-245.
8. N. Kamaly, Z. Y. Xiao, P. M. Valencia, A. F. Radovic-Moreno, O. C. Farokhzad, *Chem. Soc. Rev.* **2012,** *41* (7), 2971-3010.
9. P. Ghosh, G. Han, M. De, C. K. Kim, V. M. Rotello, *Adv. Drug Delivery Rev.* **2008,** *60* (11), 1307-1315.
10. C. Argyo, V. Weiss, C. Bräuchle, T. Bein, *Chem. Mater.* **2014,** *26* (1), 435-451.
11. C. E. Probst, P. Zrazhevskiy, V. Bagalkot, X. Gao, *Adv. Drug Delivery Rev.* **2013,** *65* (5), 703-718.
12. Y. Kaneda, T. Nakajima, T. Nishikawa, S. Yamamoto, H. Ikegami, N. Suzuki, H. Nakamura, R. Morishita, H. Kotani, *Molecular Therapy* **2002,** *6* (2), 219-226.

13. Z. Liu, K. Chen, C. Davis, S. Sherlock, Q. Cao, X. Chen, H. Dai, *Cancer Research* **2008,** *68* (16), 6652-6660.
14. W. B. Liechty, D. R. Kryscio, B. V. Slaughter, N. A. Peppas, *Annu. Rev. Chem. Biomol. Eng.* **2010,** *1*, 149-173.
15. S. Venkataraman, J. L. Hedrick, Z. Y. Ong, C. Yang, P. L. R. Ee, P. T. Hammond, Y. Y. Yang, *Adv. Drug Delivery Rev.* **2011,** *63* (14–15), 1228-1246.
16. N. P. Truong, M. R. Whittaker, C. W. Mak, T. P. Davis, *Expert Opin. Drug Delivery* **2015,** *12* (1), 129-142.
17. Y. Geng, P. Dalhaimer, S. S. Cai, R. Tsai, M. Tewari, T. Minko, D. E. Discher, *Nat. Nanotechnol.* **2007,** *2* (4), 249-255.
18. M. Müllner, *Macromol. Chem. Phys.* **2016,** *217* (20), 2209-2222.
19. T. L. Schlick, Z. Ding, E. W. Kovacs, M. B. Francis, *J. Am. Chem. Soc.* **2005,** *127* (11), 3718-3723.
20. M. A. Bruckman, L. N. Randolph, A. VanMeter, S. Hern, A. J. Shoffstall, R. E. Taurog, N. F. Steinmetz, *Virology* **2014,** *449*, 163-173.
21. D. A. Christian, S. Cai, O. B. Garbuzenko, T. Harada, A. L. Zajac, T. Minko, D. E. Discher, *Mol. Pharmaceutics* **2009,** *6* (5), 1343-1352.
22. M. Müllner, S. J. Dodds, T.-H. Nguyen, D. Senyschyn, C. J. H. Porter, B. J. Boyd, F. Caruso, *ACS Nano* **2015,** *9* (2), 1294-1304.
23. M. Mullner, D. Mehta, C. J. Nowell, C. J. H. Porter, *Chem. Commun.* **2016,** *52* (58), 9121-9124.
24. M. Elsabahy, K. L. Wooley, *Chem. Soc. Rev.* **2012,** *41* (7), 2545-2561.
25. M. C. Branco, J. P. Schneider, *Acta Biomaterialia* **2009,** *5* (3), 817-831.
26. T. Aida, E. W. Meijer, S. I. Stupp, *Science* **2012,** *335* (6070), 813.
27. E. Krieg, M. M. C. Bastings, P. Besenius, B. Rybtchinski, *Chem. Rev.* **2016,** *116* (4), 2414-2477.
28. J. Zhang, P. X. Ma, *Adv. Drug Delivery Rev.* **2013,** *65* (9), 1215-1233.
29. J. D. Hartgerink, E. Beniash, S. I. Stupp, *Science* **2001,** *294* (5547), 1684-1688.
30. J. B. Matson, S. I. Stupp, *Chem. Commun.* **2011,** *47* (28), 7962-7964.
31. S. Soukasene, D. J. Toft, T. J. Moyer, H. Lu, H.-K. Lee, S. M. Standley, V. L. Cryns, S. I. Stupp, *ACS Nano* **2011,** *5* (11), 9113-9121.
32. R. Chapman, M. Danial, M. L. Koh, K. A. Jolliffe, S. Perrier, *Chem. Soc. Rev.* **2012,** *41* (18), 6023-6041.
33. M. R. Ghadiri, J. R. Granja, R. A. Milligan, D. E. McRee, N. Khazanovich, *Nature* **1993,** *366* (6453), 324-327.
34. B. M. Blunden, R. Chapman, M. Danial, H. X. Lu, K. A. Jolliffe, S. Perrier, M. H. Stenzel, *Chem. Eur. J.* **2014,** *20* (40), 12745-12749.
35. Y. Wang, S. Yi, L. Sun, Y. Huang, S. C. Lenaghan, M. Zhang, *J. Biomed. Nanotechnol.* **2014,** *10* (3), 445-454.
36. J. Kopeček, P. Kopečková, *Adv. Drug Delivery Rev.* **2010,** *62* (2), 122-149.
37. R. Duncan, *Nat Rev Cancer* **2006,** *6* (9), 688-701.
38. J. Sanchis, F. Canal, R. Lucas, M. J. Vicent, *Nanomedicine* **2010,** *5* (6), 915-935.
39. G. Moad, E. Rizzardo, S. H. Thang, *Aust. J. Chem.* **2012,** *65* (8), 985-1076.
40. C. W. Scales, Y. A. Vasilieva, A. J. Convertine, A. B. Lowe, C. L. McCormick, *Biomacromolecules* **2005,** *6* (4), 1846-1850.
41. C.-Y. Hong, C.-Y. Pan, *Macromolecules* **2006,** *39* (10), 3517-3524.
42. M. Danial, C. M. N. Tran, K. A. Jolliffe, S. Perrier, *J. Am. Chem. Soc.* **2014,** *136* (22), 8018-8026.
43. M. Danial, C. M. N. Tran, P. G. Young, S. Perrier, K. A. Jolliffe, *Nat. Commun.* **2013,** *4*, 2780.

44. S. C. Larnaudie, J. C. Brendel, K. A. Jolliffe, S. Perrier, *J. Polym. Sci., Part A: Polym. Chem.* **2016,** *54* (7), 1003-1011.
45. S. Perrier, T. Barlow, S. Catrouillet, P. Gurnani, A. Kerr, M. L. Koh, S. Larnaudie, J. Rho, R. Schweins, P. Lindner, G. Warr, *Institut Laue-Langevin (ILL), doi:10.5291/ILL-DATA.9-10-1412* **2015**.
46. P. Debye, *The Journal of Chemical Physics* **1946,** *14* (10), 636-639.
47. J. S. Pedersen, *J. Appl. Crystallogr.* **2000,** *33* (1), 637-640.
48. B. Chu, *Laser Light Scattering: Basic Principles and Practice*. Acad. Press: 1991.
49. J. Couet, M. Biesalski, *Small* **2008,** *4* (7), 1008-1016.
50. R. Chapman, K. A. Jolliffe, S. Perrier, *Polym. Chem.* **2011,** *2* (9), 1956-1963.
51. X. Huang, X. Teng, D. Chen, F. Tang, J. He, *Biomaterials* **2010,** *31* (3), 438-448.
52. J. Huang, L. Bu, J. Xie, K. Chen, Z. Cheng, X. Li, X. Chen, *ACS Nano* **2010,** *4* (12), 7151-7160.
53. F. Lu, S.-H. Wu, Y. Hung, C.-Y. Mou, *Small* **2009,** *5* (12), 1408-1413.
54. K. Yin Win, S.-S. Feng, *Biomaterials* **2005,** *26* (15), 2713-2722.
55. S. A. Kulkarni, S.-S. Feng, *Pharm. Res.* **2013,** *30* (10), 2512-2522.
56. E. Hinde, K. Thammasiraphop, H. T. T. Duong, J. Yeow, B. Karagoz, C. Boyer, J. J. Gooding, K. Gaus, *Nat. Nano.* **2017**, *12* (1), 81-89.
57. S. P. Rannard, N. J. Davis, *Org. Lett.* **1999,** *1* (6), 933-936.
58. S. P. Rannard, N. J. Davis, *Org. Lett.* **2000,** *2* (14), 2117-2120.
59. T. Etrych, L. Kovář, J. Strohalm, P. Chytil, B. Říhová, K. Ulbrich, *J. Controlled Release* **2011,** *154* (3), 241-248.
60. T. Etrych, V. Šubr, J. Strohalm, M. Šírová, B. Říhová, K. Ulbrich, *J. Controlled Release* **2012,** *164* (3), 346-354.
61. S. Sadekar, A. Ray, M. Janàt-Amsbury, C. M. Peterson, H. Ghandehari, *Biomacromolecules* **2011,** *12* (1), 88-96.
62. L. M. Kaminskas, B. D. Kelly, V. M. McLeod, B. J. Boyd, G. Y. Krippner, E. D. Williams, C. J. H. Porter, *Mol. Pharmaceutics* **2009,** *6* (4), 1190-1204.
63. S. Y. Khor, J. Hu, V. M. McLeod, J. F. Quinn, M. Williamson, C. J. H. Porter, M. R. Whittaker, L. M. Kaminskas, T. P. Davis, *Nanomed. Nanotechnol. Biol. Med.* **2015,** *11* (8), 2099-2108.
64. S. Catrouillet, J. C. Brendel, S. Larnaudie, T. Barlow, K. A. Jolliffe, S. Perrier, *ACS Macro Letters* **2016,** *5* (10), 1119-1123.
65. http://www.isis.stfc.ac.uk.
66. R. K. Heenan, S. E. Rogers, D. Turner, A. E. Terry, J. Treadgold, S. M. King, *Neutron News* **2011,** *22* (2), 19-21.
67. http://www.mantidproject.org.
68. G. D. Wignall, F. S. Bates, *J. Appl. Crystallogr.* **1987,** *20*, 28-40.
69. T. Zemb, P. Lindner, *Neutrons, X-rays and light: scattering methods applied to soft condensed matter*. North-Holland: 2002.
70. I. Bressler, J. Kohlbrecher, A. F. Thunemann, *J. Appl. Crystallogr.* **2015,** *48* (5), 1587-1598.
71. B. J. Boyd, L. M. Kaminskas, P. Karellas, G. Krippner, R. Lessene, C. J. H. Porter, *Mol. Pharmaceutics* **2006,** *3* (5), 614-627.
72. Y. Zhang, M. Huo, J. Zhou, S. Xie, *Computer Methods and Programs in Biomedicine 99* (3), 306-314.

Chapter 4

Cyclic peptide-polymer nanotubes as efficient and highly potent drug delivery systems for organometallic anticancer complexes

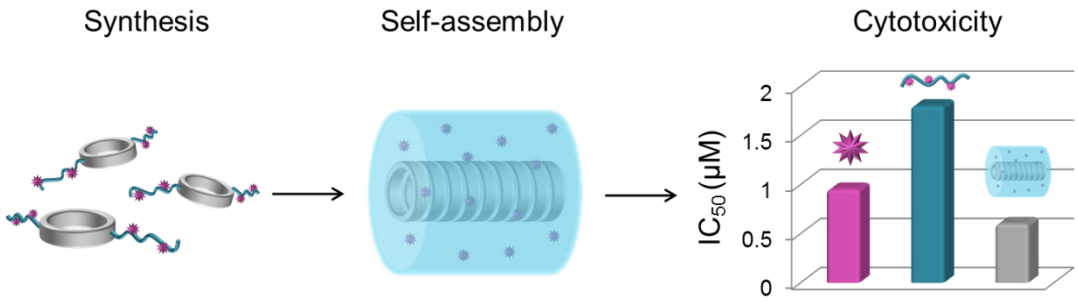

Functional drug carrier systems have potential for increasing solubility and potency of drugs while reducing side effects. Complex polymeric materials, particularly anisotropic structures, are especially attractive due to their long circulation times. In this chapter, cyclic peptides were conjugated to the biocompatible polymer poly(2-hydroxypropyl methacrylamide) (pHPMA). The resulting conjugates were further functionalised with organoiridium anticancer complexes. Small angle neutron scattering and static light scattering confirmed their self-assembly and elongated cylindrical shape. Drug-loaded nanotubes exhibited more potent antiproliferative activity towards human cancer cells than either the free drug or the drug-loaded polymers, whilst the nanotubes themselves were non-toxic. Cellular accumulation studies revealed that the increased potency of the conjugate appears to be related to a more efficient mode of action rather than a higher cellular accumulation of iridium.

4.1 Introduction

Small molecules designed as highly potent anticancer drugs often face limitations related to their poor solubility, rapid elimination, and limited stability in the body.[1,2] The use of drug carriers may address these challenges by providing a protective shell that enhances solubility and retards clearance from the blood stream. Moreover, drug delivery vectors possess additional means of introducing functionality and increasing the selective accumulation at the specific target.[3] Tuneable in size, the devices can be optimized for passive targeting to tumours via the enhanced permeability and retention (EPR) effect.[4] In addition, most carriers can be functionalized by a variety of ligands (carbohydrates, peptides, proteins, antibodies, aptamers etc.) to allow for active targeting towards specific cells.[5] Overall, drug carrier systems offer potential for improving the therapeutic efficiency of drugs and reducing their side effects.

It is therefore not surprising that a plethora of potential drug delivery systems has been reported, including spherical polymer micelles or vesicles.[6] So far neglected, but particularly interesting, are organic nanotubes (NTs) formed by cyclic peptide-polymer conjugates. Cylindrical objects exhibit a longer residence time in the body than spheres of comparable size,[7] and also can show higher activity than spherical particles[8] when loaded, for example, with active peptides,[9] antibodies,[10] or proteins.[11] The high aspect ratio and functionality of these organic nanotubes are potentially valuable design features for drug delivery.

Despite all the above mentioned advantages of these cyclic peptide nanotubes and the advances in the synthesis of functional materials, so far only a few examples of their use as drug delivery vehicles has been reported.[12-14] Blunden *et al.* have described the synthesis of such nanotubes bearing RAPTA-C, a moderately active ruthenium anticancer drug. They demonstrated that the attachment of the drug helped to increase its activity against cancer cells.[12]

Here, we present a specifically designed system comprising a self-assembling cyclic peptide core, a functional polymer shell, and a highly potent organoiridium drug candidate. Particular attention was paid to the use of biocompatible components in the synthesis and the effective attachment of the metallodrug through efficient drug conjugation suitable for cancer therapy. In this context, poly(2-hydroxypropyl methacrylamide) (pHPMA) was chosen, since it has attracted particular interest for drug delivery applications over the past

few decades.[15,16] Several systems derived from pHPMA have been studied in detail and are currently undergoing clinical trial.[17,18]

In addition to comprehensive optimisation of the delivery vector, the choice of a compatible and potent drug is critical for designing effective therapeutics. Recently, organoiridium complexes have been shown to exhibit high potency towards a wide range of cancer cells[19] and, through careful choice of ligands, the efficiency of these complexes can be improved by three orders of magnitude, reaching sub-micromolar values.[20] Depending on the cell line and the complex, activity was shown to be *ca.* 5 to 10 times higher than that of the clinical drug cisplatin, and more than 200 times higher than RAPTA-C. The attachment of this type of complex to a polymeric carrier can be achieved through incorporation of a suitable metal-binding ligand on the polymer chains, as mentioned in Chapter 3.

Based on these considerations, a cyclic peptide-pHPMA conjugate was synthesised and loaded with an organoiridium anticancer complex. The organoiridium fragment was attached through ligation to a pyridine-containing comonomer in the polymer shell. The ability of the drug-loaded conjugates to self-assemble into nanotubes in solution was thoroughly established by scattering techniques, and their cytotoxicity *in vitro* was assessed and compared to that of the free drug. For the first time, this supramolecular system was also tested alongside a drug-loaded polymer control that does not contain the cyclic peptide core, in order to clearly assess the impact of the self-assembly on the cytotoxicity. Finally, cellular accumulation of the three compounds was studied both qualitatively and quantitatively and the mechanism of action was explored.

4.2 Results and discussion

4.2.1 Synthesis of the polymer and conjugate carriers

The well-studied monomer building block 2-hydroxypropyl methacrylamide (HPMA) was chosen as the main monomer for designing the polymeric drug used in this work. In order to provide a binding site for the ligation of anticancer iridium complexes, PUEMA was introduced as a comonomer (see Chapter 3). Pyridine was chosen as the binding ligand, as it can readily replace the chloride ligand present on the selected organoiridium precursor. Moreover, organoiridium pyridine complexes themselves exhibit good anticancer activity.[21]

The cyclic peptide-polymer conjugate **2** containing pHPMA-*co*-PUEMA was synthesised using Reversible Addition Fragmentation Chain Transfer (RAFT) polymerisation followed by coupling of the polymer to the chosen cyclic peptide, cyclo(D-Leu-Lys-D-Leu-Trp)$_2$ (Scheme 4.1 and Table 4.1).

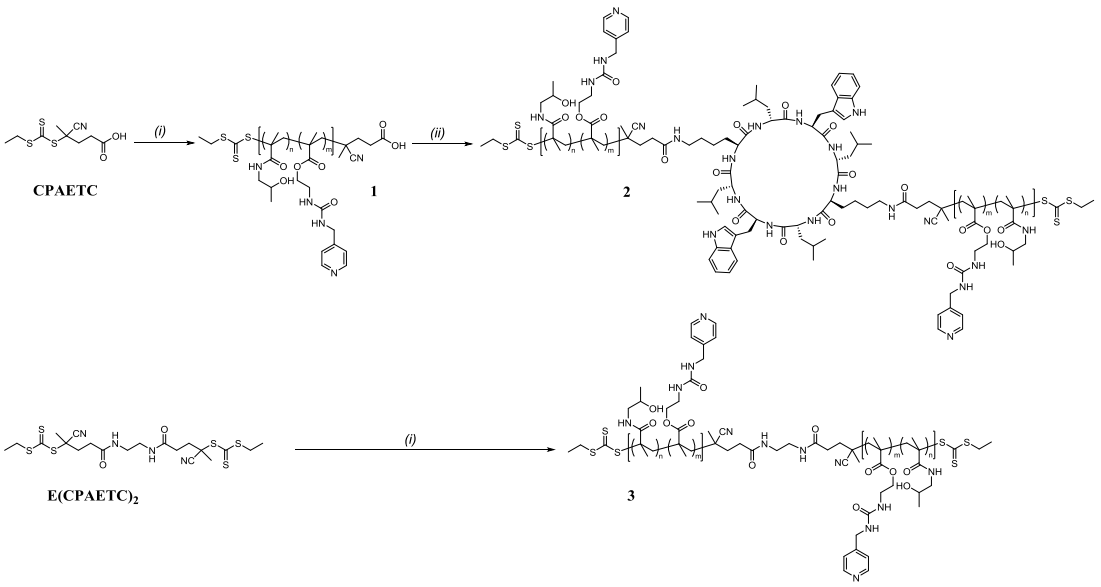

Scheme 4.1: Synthesis of conjugate **2**: CP-(pHPMA-*co*-PUEMA)$_2$ and polymer **3**: pHPMA-*co*-PUEMA. *(i)* HPMA, PUEMA, VA 044, DMSO/H_2O. *(ii)* cyclo(D-Leu-Lys-D-Leu-Trp)$_2$, HBTU, NMM, DMSO.

The bifunctional CTA E(CPAETC)$_2$ was used to provide a non self-assembling polymeric control (**3,** Scheme 4.1). The obtained polymers **1** and **3** were well defined, with narrow dispersities of 1.16 and 1.12, respectively (Figure 4.1 A and Table 4.1), and the final content of PUEMA in polymer **1** was estimated to be 6.5 %, due to the slightly lower conversion of HPMA compared to PUEMA. This value was confirmed by ^{1}H NMR of the precipitated polymer (Figure 4.1 B). As detailed in the previous chapter, kinetic measurements of the copolymerisation showed that PUEMA was consumed significantly faster than HPMA. The direct consequence of this observation is that the functional monomer tends to be incorporated first, meaning that most of the pyridine ligands for metallodrug attachment will ultimately be located towards the α-chain end of polymer **1**.

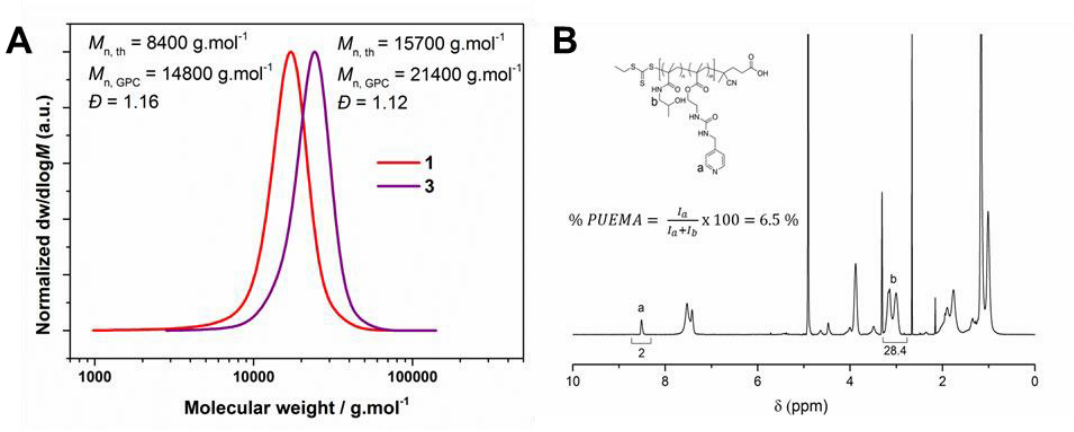

Figure 4.1: A) Molecular weight distribution of polymers **1** and **3**. B) Determination of PUEMA content in polymer **1**.

Copolymer **1** was attached to the cyclic peptide by reacting the amine groups present on the cyclic peptide with the carboxylic acid end-group of **1**, using *O*-(benzotriazol-1-yl)-*N,N,N′,N′*-tetramethyluronium hexafluorophosphate (HBTU) as a coupling reagent. The coupling was complete after 1 h and the water-soluble nature of these conjugates enabled for straightforward purification by dialysis. The purified conjugate **2** was well-defined, with a dispersity of 1.19. Interestingly, since attachment occurs at the α-chain end of the polymer, the pyridine units used for organoiridium attachment are located on average close to the cyclic peptide core, allowing the HPMA-richer shell to provide shielding of the drug from the environment.

Table 4.1: Summary of polymers used in this work.

Entry	Material	$M_{n, th}$ [a] (g.mol^{-1})	$M_{n, GPC}$ [b] (g.mol^{-1})	Đ[b]
1	p(HPMA$_{51}$-*co*-PUEMA$_{3.5}$)	8400	14 800	1.16
2	CP-(p(HPMA$_{51}$-*co*-PUEMA$_{3.5}$))$_2$	17800	29200	1.19
3	pHPMA$_{93}$-*co*-PUEMA$_7$	15700	21400	1.12

[a] Determined by ^{1}H NMR. [b] Determined by SEC using DMF (0.1% LiBr) as eluent, calibrated with pMMA standards.

4.2.2 Complexation of organoiridium anticancer drugs

Attachment of the selected iridium complexes to polymer **3** and cyclic peptide-polymer conjugate **2** was achieved following a ligand exchange procedure, previously used to synthesise pyridine analogues of the chloride-containing drugs.[21] The complexes used in this work were the [(Cp*)Ir(phpy)Cl] (abbreviated as Ir-Cp*, **4a**), which contains pentamethylcyclopentadienyl (Cp*) and *C,N*-chelated phenylpyridine (phpy) as ligands,[22] as well as the more hydrophobic [(Cp^{xph})Ir(phpy)Cl] (Ir-Cp^{xph}, **4b**), in which the Cp* is replaced by an extended phenyltetramethylcyclopentadienyl (Cp^{xph}) ligand.[23] Organoiridium drug complexes were synthesised by Dr. Abraha Abtemariam. The chloride ligand of the iridium complexes **4a** and **4b** was first removed using silver nitrate, followed by complexation to pyridine units in the polymer chains (Scheme 4.2).

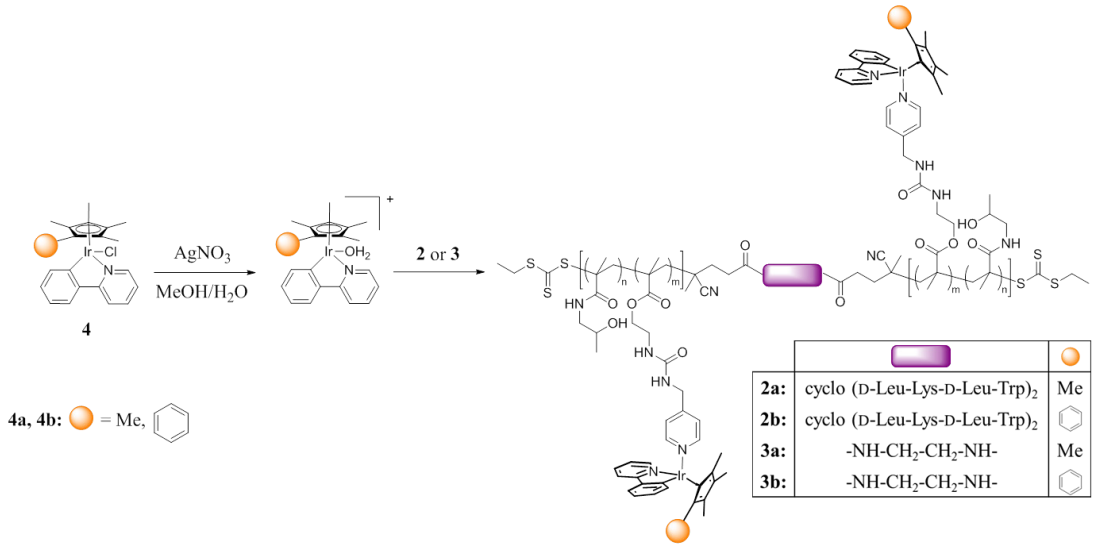

Scheme 4.2: Complexation of organoiridium complexes **4a** and **4b** to conjugate **2** and polymer **3**.

An excess of the iridium complex **4a** or **4b** (3 mol equiv per pyridine site) was used to maximise the drug loading onto the polymer and peptide-polymer conjugate. After purification by size exclusion chromatography, the drug-bearing compounds (conjugates **2a** and **2b**, and polymers **3a** and **3b**) were characterised by ^{1}H NMR spectroscopy (Figure 4.2). When substituting the Cl ligand by pyridine in [(Cp^{xph})Ir(phpy)Cl], the signal corresponding to proton a in Figure 4.2 is shifted downfield from 8.60 to 8.88 ppm in MeOD.[21-22] In the present case, this characteristic shift was also observed, as well as the broadening of the

signals associated with the complex, demonstrating full complexation of the drug to the polymer.

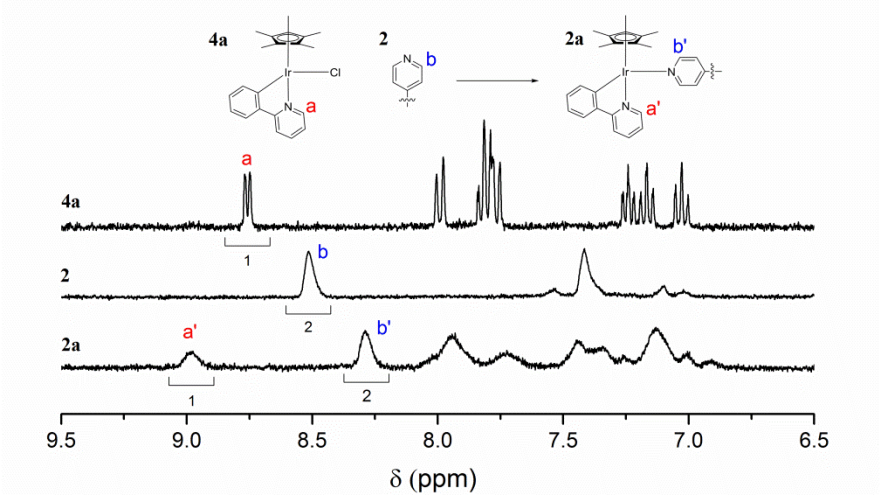

Figure 4.2: ^{1}H NMR characterisation of the attachment of complex **4a** onto conjugate **2**, affording conjugate **2a.** The spectra corresponding to the other three reactions can be found in Appendix B.

4.2.3 Characterisation of supramolecular nanotubes

In order to confirm the self-assembly of the conjugates into tubular structures, small angle neutron scattering (SANS) measurements were performed on the drug-bearing conjugate **2a** (Figure 4.3) in solution in deuterated PBS.

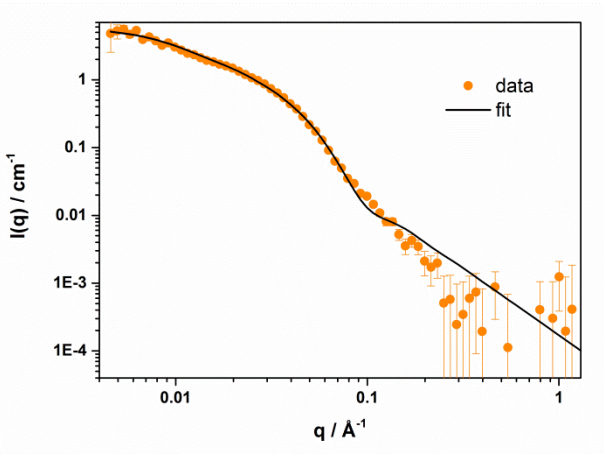

Figure 4.3: Small angle neutron scattering profile of conjugate **2a** (orange dots) and its fit using a cylindrical micelle model (black line).

The SANS data were fitted with a cylindrical micelle model (Figure 4.3), which accounts for both the overall elongated shape provided by the self-assembled cyclic peptide core (a characteristic q^{-1} dependency at low q values: cylinder form factor) and the polymer arms (Gaussian chain form factor at high q values), as was used in Chapter 3.[24] The fit was performed using the CYL+Chains(RW) model on SASfit, and reasonable values were obtained starting from a radius of 5 Å for the peptide core, in accordance with previously reported results (Table 4.2).[25,26]

Table 4.2: Fitting parameters obtained for the fit of the SANS data corresponding to conjugate **2a** using a hairy rod form factor.

Parameter	Definition	Value	
R_core (Å)	Radius of the core	3.9486	Fitting
N	Scale factor	0.0050795	
n_agg	Grafting density	0.0206747	
Rg (Å)	Radius of gyration of the polymer arms	16.664	
V_brush ($Å^3$)	Volume of the polymer arms[a]	17000	Calculated
eta_core ($Å^{-2}$)	Scattering length density of the core	9.06E-07	
eta_brush ($Å^{-2}$)	Scattering length density of the polymer arms	9.06E-07	
eta_solv ($Å^{-2}$)	Scattering length density of the solvent	6.39E-06	
d	d = 1 mimics the non-penetration of the polymer chains in the core	1	Fixed
xsolv_core	Fraction of solvent in the core, set to 0	0	
L (Å)	Length of the cylinder[b]	1000	

[a] *Calculated using* $V_{brush} = MW/(dxN_a).10^{24}$*, where MW is the molecular weight of the polymer, d its density and* N_a *Avogadro's number.* [b] *The length of the cylinder cannot be determined because of the absence of a roll-over at low q values, an arbitrary value of 100 nm was therefore used for the fit.*

However, the maximum length of these tubes cannot be fully determined by these SANS measurements, as the scattering intensity is still increasing at the lowest measured q values, and does not show the formation of a plateau which is indicative of a finite length.

As such, static light scattering (SLS) measurements were then recorded, as this technique allows access to a larger window of observation (Figure 4.4 A). Following the method

described in Chapter 3, a plot of linear regression was used to determine the apparent molecular weight at conc. = 0 (Figure 4.4 B).

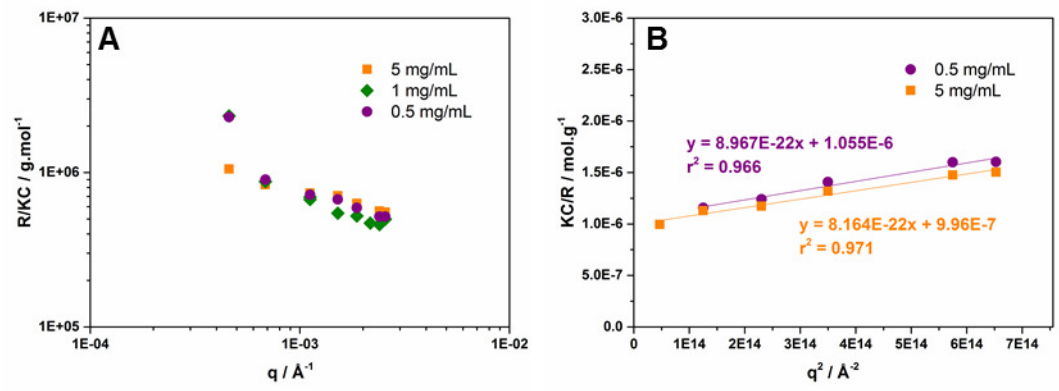

Figure 4.4: A) Static light scattering profile of conjugate **2a** (CP-(p(HPMA-*co*-PUEMA))$_2$) in solution in PBS at different concentrations. B) Determination of the molecular weight of **2a** by SLS.

SLS experiments showed that the molecular weight of the assemblies was not affected by the concentration of the solution (within the tested range), and the molecular weight was determined to be $9.74.10^5 \pm 0.37.10^5$ g.mol^{-1} for the drug-bearing conjugate (Table 4.3). Using the molecular weight of the unimer and the previously reported distance between adjacent peptides,[26,27] the average length of the objects can be determined as 21.8 ± 0.9 nm, corresponding to 46 assembled conjugates.

Table 4.3: Determination of aggregates size by SLS for conjugate **2a**.

	Slope	Intercept	MW (g/mol)	N_{agg} [a]	L [b] (nm)	R_g (nm)
5 mg/mL	8.16E-22	9.96E-7	1.00E6	47.80	22.47	49.6
0.5 mg/mL	8.97E-22	1.05E-6	9.48E5	45.14	21.22	50.5

[a] *N_{agg} = MW/M_unimer.* [b] *L = N_{agg} x Lc, with Lc = 4.7 10^{-1} nm the distance between two adjacent cyclic peptides.*

4.2.4 Anticancer activity and cellular accumulation

The antiproliferative activity of the polymers and conjugates was initially determined using A2780 human ovarian cancer cells, and presented as IC_{50} values, the concentration at which 50% of cell growth is inhibited. The drug-free control samples (polymer alone and cyclic

peptide-polymer conjugates) were non-toxic in the tested range of concentrations (Figure 4.5 A). However, the organoiridium-containing samples showed high activity (Figure 4.5 B).

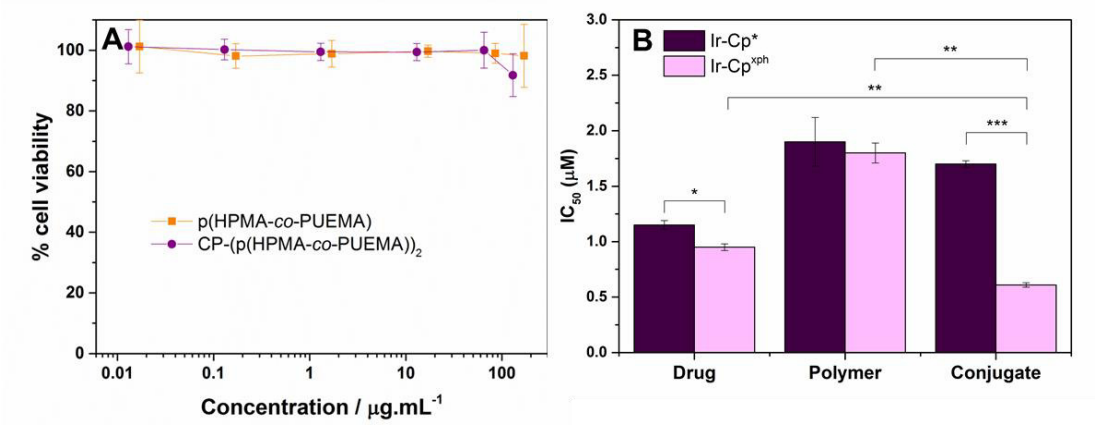

Figure 4.5: Antiproliferative activity in A2780 cells. A) Non-toxicity of drug-free compounds. B) IC_{50} values for free organoiridium complexes, drug-bearing polymers, and drug-bearing conjugates using Ir-Cp* (dark) and Ir-Cp^{xph} (light) as the drug. *$p < 0.05$, **$p < 0.01$, ***$p < 0.001$.

For both drugs, the IC_{50} values of the loaded polymers were slightly higher (however still in the same order of magnitude) compared to that of the free drug: 1.90 ± 0.22 µM for the polymer **3a** compared to 1.15 ± 0.04 µM for Ir-Cp*, and 1.80 ± 0.09 µM for the polymer **3b** compared to 0.95 ± 0.03 µM for Ir-Cp^{xph}. For Ir-Cp*, no major difference was observed between the polymer and the conjugate (1.90 ± 0.22 µM for the polymer **3a** compared to 1.70 ± 0.03 µM for the conjugate **2a**). However the IC_{50} of the conjugate **2b** (0.61 ± 0.02 µM) in A2780 was 3x lower than that of the drug-loaded polymer **3b** (1.8 ± 0.09 µM). This substantial increase in activity between the polymer and the nanotubes suggests that the self-assembly has a noticeable impact on the behaviour of the carrier. Furthermore, the conjugate **2b** was twice as potent as the free drug Ir-Cp^{xph}. For all the studied compounds, the IC_{50} values were lower for Ir-Cp^{xph}, which is a more hydrophobic complex than for Ir-Cp*. This result shows the same trend as previously reported data for the complexes themselves.[22,23] These organoiridium complexes have not been previously conjugated to delivery systems, but it is clear from previous studies that increasing the hydrophobicity of the cyclopentadienyl ligand enhances their antiproliferative activity.[20,23,28] The present report suggests that this is also the case when the complexes are conjugated to polymers and cyclic peptide-polymer conjugates. For this reason, further studies focused on the more potent compounds bearing Ir-Cp^{xph}.

The antiproliferative activity of the three compounds (Ir-Cp^{xph} as free drug, loaded onto the polymer (**3b**), and the conjugate (**2b**)) was then determined against human ovarian fibroblasts (HOF), a model for healthy, non-cancerous cells (Figure 4.6), and compared to that against A2780 ovarian cancer cells.

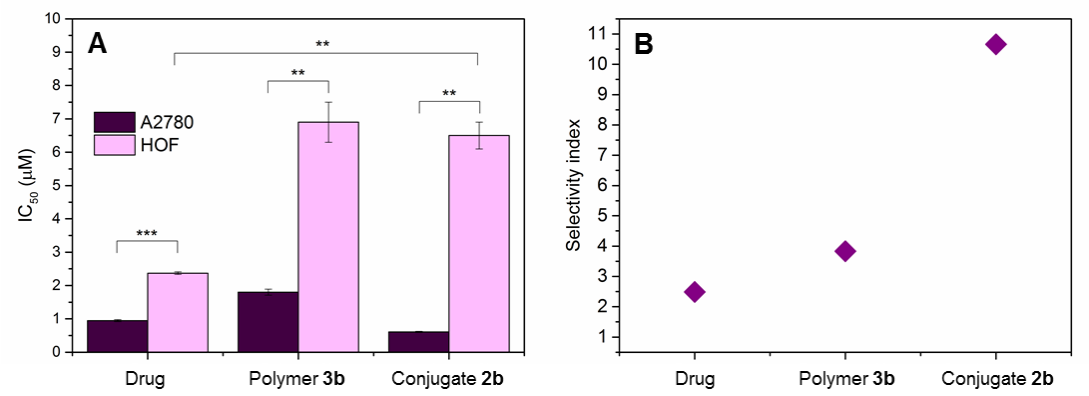

Figure 4.6: Comparison of antiproliferative activity between healthy and cancerous cells. A) Antiproliferative activity of free drug Ir-Cp^{xph}, drug-bearing polymer **3b** and drug-bearing conjugate **2b** in A2780 (cancer, dark) and HOF (healthy, light) ovarian cells. B) Selectivity index of the Ir-Cp^{xph} compounds, determined between A2780 and HOF. $^{**}p < 0.01$, $^{***}p < 0.001$.

All compounds are less toxic in normal HOF cells than in A2780 (Figure 4.6 A). The observed selectivity is likely attributable to the nature of the drug. This class of iridium anticancer complexes has previously been shown to exhibit selectivity towards cancer cells, which is believed to derive from interference of the complexes with cellular redox homeostasis (the ability of the cells to regulate their levels of reactive oxygen species) in cancer cells specifically.[19] In addition, the selectivity index (SI, the ratio between the IC_{50} in HOF and the IC_{50} in A2780) is 2.5 and 3.8 for the free drug and the polymer, respectively (Figure 4.6 B). Interestingly, it is significantly higher for the conjugate (10.7), suggesting that an additional degree of selectivity towards cancer cells is provided by the carrier, highlighting an advantage of using these new materials as delivery vectors.

The increased activity of the conjugate **2b** compared to the polymer **3b** and the free drug in A2780 cells may be related either to enhanced cellular accumulation or to a more efficient mode of action, for example through a different partitioning of the drug amongst the cell organelles. The possibility of enhanced accumulation (the balance of the uptake and efflux equilibrium), was investigated by exposing A2780 cells to the Ir-Cp^{xph} compounds (free

drug, polymer and conjugate) at their respective IC_{50} values: 0.95 µM for the free drug, 1.8 µM for polymer **3b** and 0.6 µM for conjugate **2b**. At regular intervals over 24 h, cells were collected and digested in nitric acid to determine the amount of iridium accumulated using inductively coupled plasma mass spectrometry (ICP-MS) (Figure 4.7).

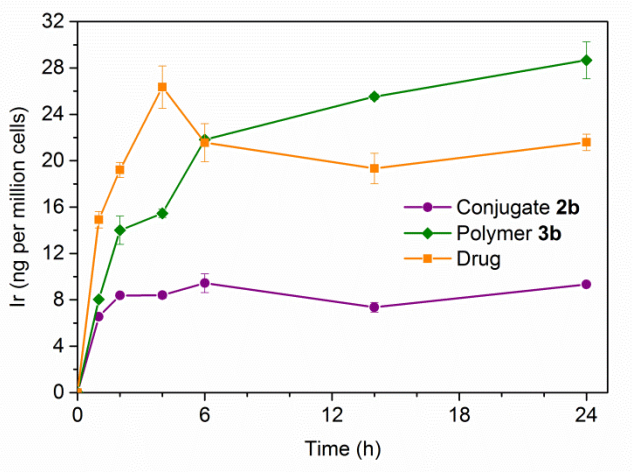

Figure 4.7: Iridium accumulated in A2780 cells after 24 h of exposure to the free drug Ir-Cp^{xph} (orange squares), the drug bearing polymer **3b** (green diamonds) and the drug bearing conjugate **2b** (purple circles) at equipotent IC_{50} conditions.

Figure 4.7 shows that the kinetics of uptake are different for the three compounds: the maximum amount of accumulated iridium is reached after 2 h in the case of the conjugate **2b**, after which it remains the constant; while for the polymer **3b**, the amount is still increasing after 24 h. In the case of the free drug, the amount of iridium reaches maximum at 4 h, before decreasing slightly. Such cellular efflux is common for organometallic complexes.[29,30] These differences in the rate and profile of uptake suggest that the conjugate interacts differently with the cells. After 24 h of exposure to the free drug, the drug-bearing polymer and the drug-bearing conjugate under equipotent conditions, each at their IC_{50} concentrations (0.95 µM, 1.80 µM and 0.6 µM, respectively), 21.6 ± 0.7 ng, 28.7 ± 1.6 ng and 9.3 ± 0.2 ng of iridium per million cells were accumulated, respectively. Taking the differences in IC_{50} values into account, similar percentages of the total amount of iridium administered are retained: 7.7 ± 0.2 % of the initial amount was accumulated for the drug, 6.5 ± 0.4 % for the polymer, and 6.5 ± 0.1 % in the case of the conjugate. These values are similar to those observed previously for organometallic drugs.[21,30]

The results of the equipotent iridium accumulation study suggest that the increased cytotoxicity of the conjugate **2b** compared to the other compounds is not due to enhanced

uptake of iridium by the cells. These results are further supported by the amount of iridium accumulated after exposure under equimolar conditions, when incubating the cells in the presence of the three compounds at the lowest concentration (corresponding to the IC_{50} of conjugate **2b**, 0.6 μM). Under these conditions, similar amounts of iridium were accumulated for the three compounds (10.1 ± 0.1 ng per million cells for the free drug, 10.5 ± 0.2 ng for the polymer, and 9.3 ± 0.8 ng for the conjugate). It can be concluded that attachment of the drug to the polymer or the conjugate does not affect the extent of the accumulation of iridium in the cells. This result suggests that the nanotubes exhibit a more effective mode of action, for example through a different partitioning of the drug amongst the cell organelles.

In order to evaluate this partitioning, equipotent uptake experiments were repeated and the cell pellets collected after 24 h. The iridium content of the membrane, cytosol, cytoskeleton and nucleus fractions was determined by fractionation of the cell compartments, and the results are shown in Figure 4.8 A. The total amount of iridium in each fraction follows the trend previously observed for whole cells: the amount of iridium increases in the order conjugate < drug < polymer. The percentage of total recovered iridium in the membrane fraction increases slightly in the order drug (56 %) < polymer (65 %) ≈ conjugate (69 %), which may indicate that the polymer-conjugated drugs favour an endocytosis-mediated pathway, since endosomes and lysosomes are collected in the membrane fraction. To confirm that the polymer and conjugate follow an energy-dependent mechanism, accumulation experiments were undertaken at 4 °C, conditions known to block endocytosis processes (as used in Chapter 3).[31] At 4 °C the free drug accumulated to an extent of 3.8 ± 0.2 ng Ir per 10^6 cells, which corresponds to about 15% of the amount accumulated at 37 °C, suggesting that energy-independent pathways (such as passive diffusion) play at least a partial role in the cellular accumulation of the free drug, in accordance with previous reports (Figure 4.8 B).[30] The polymer **3b** accumulated to a lesser extent, with 1.9 ± 0.3 ng Ir per 10^6 cells. In contrast the conjugate **2b** did not accumulate significantly in these conditions, supporting the hypothesis that cell entry involves energy-dependent mechanisms.

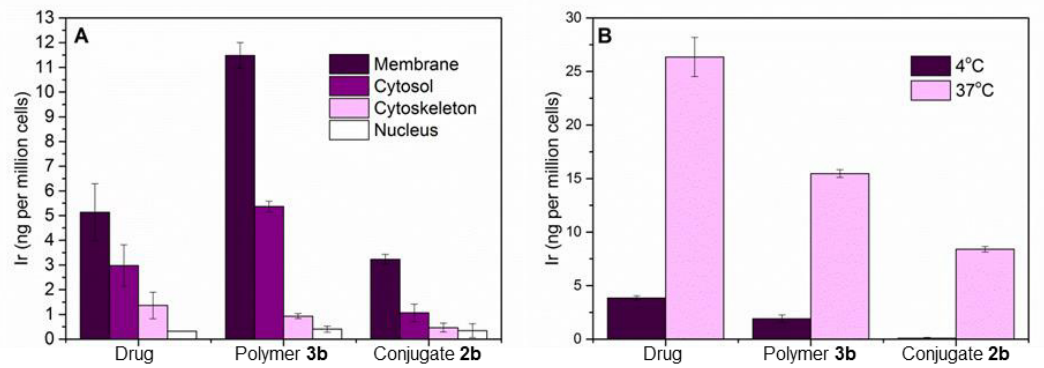

Figure 4.8: Investigation of mechanism of cellular entry. A) Iridium content of the membrane, cytosol, cytoskeleton and nucleus fractions of A2780 cells after 24 hours of exposure to the Ir-Cp^{xph} compounds at equipotent IC_{50} concentrations. B) Cellular accumulation of Ir after 4 h of exposure to the Ir-Cp^{xph} compounds at equipotent IC_{50} concentrations at 4°C and 37°C.

4.3 Conclusions

This chapter discusses the synthesis of novel cyclic peptide-polymer conjugates able to carry organoiridium anticancer complexes. 2-Hydroxypropyl methacrylamide (HPMA) was copolymerised with a pyridine-containing monomer which provides a specific binding site for the complexation of highly potent anticancer complexes [(Cp*)Ir(phpy)Cl] and [(Cp^{xph})Ir(phpy)Cl]. The copolymer was then conjugated to self-assembling cyclic peptides using HBTU coupling. The self-assembly of these conjugates was studied by static light scattering and small angle neutron scattering, which revealed that the building blocks form short cylinders about 20 nm in length on average. These drug-bearing nanotubes exhibited comparable or increased toxicity towards human ovarian cancer cells compared to the free drug. Remarkably, their toxicity towards a healthy cell model was lower than the free drug, suggesting a degree of selectivity towards cancer cells. Interestingly, the nanotubes also showed higher toxicity as well as higher selectivity towards cancer cells when compared to the drug-bearing polymers used as a non-assembling control and more conventional example of a drug carrier. The analysis of the amount of iridium accumulated in the cells after equipotent and equimolar uptakes revealed that a similar percentage of iridium enters the cells in each case, indicating that the drug-bearing conjugates do not enhance the iridium uptake, but rather exhibit a more efficient mode of action. Investigations into the mechanisms of entry and partitioning profile of the drug into different organelles revealed

that energy-dependent mechanisms of cell uptake account for a higher fraction of the accumulated iridium in the case of the polymer and conjugate than for the free drug.

4.4 Experimental

4.4.1 Materials

N-methylmorpholine (NMM, 99 %) was purchased from Alfa Aesar. 2,2'-Azobis[2-(2-imidazolin-2-yl)propane]dihydrochloride (VA-044) was purchased from Wako Chemicals. *O*-(Benzotriazole-1-yl)-*N,N,N',N'*-tetramethyluronium hexafluorophosphate (HBTU) was purchased from Iris Biotech. All solvents were bought from commercial sources and used as received. The cyclic peptide and chain transfer agent CPAETC were synthesised as described in Chapter 2. Monomers (HPMA and PUEMA) were synthesised as described in Chapter 3. $E(CPAETC)_2$ was synthesised according to previously reported protocols.[32] [(Cp*)-Ir-(phpy)(Cl)] and [(Cp^{xph})-Ir(phpy)(Cl)] were synthesised and characterised by Abraha Abtemariam as previously described.[22,23]

4.4.2 Characterisation methods

NMR spectra were recorded on a Bruker DPX-300 instrument. Mass spectra were obtained on an Agilent 6130B Single Quad. Molecular weights and dispersities of the polymers were assessed by size exclusion chromatography (SEC) on a Polymer Laboratories PL-GPC 50 Plus system in DMF with 0.1% LiBr, using a poly(methyl methacrylate) calibration, as described in Chapter 2. Infrared absorption experiments were performed on a Bruker VECTOR-22 FTIR spectrometer. The incremental refractive index, d*n*/d*C*, was determined by measuring the refractive index of the polymer in water at various concentrations ranging from 0.25 to 2 mg/mL, using a Shodex RI detector operating at a wavelength of 632 nm.

SANS and SLS experiments were carried out as discussed in Chapter 3.

4.4.3 Synthetic procedures

4.4.3.1 Copolymerisation of HPMA and PUEMA

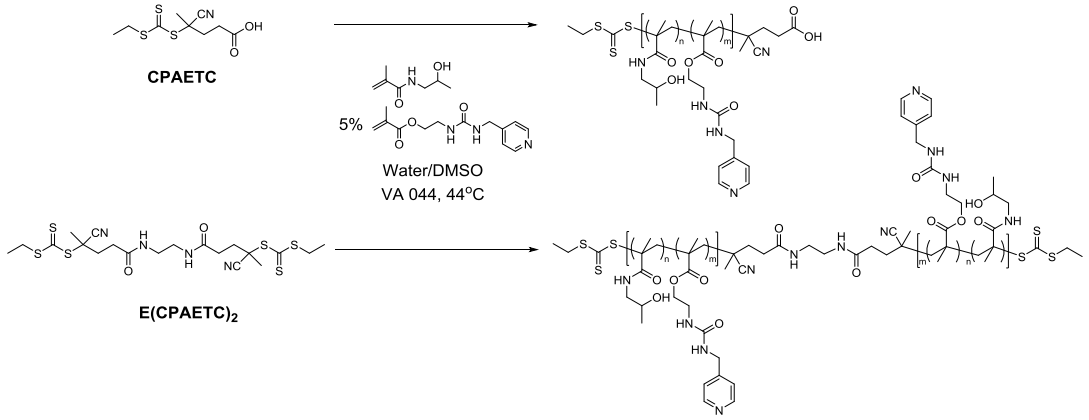

Chain transfer agent (CTA), monomers, initiator (VA 044) and solvent (30 % water in DMSO) were introduced into a flask equipped with a magnetic stirrer and sealed with a rubber septum. (See Table 4.4 for detailed conditions). The solution was degassed by bubbling nitrogen through it for 15 min, and then put in an oil bath at 44 °C. The polymerisation was stopped after 18 hours, when the conversion of PUEMA and HPMA reached > 99% and 75%, respectively. The polymers were precipitated in ice-cold acetone and dried under vacuum.

Table 4.4: Summary of polymerisation conditions.

Polymer	$[HPMA]_0$ ($mol.L^{-1}$)	$[PUEMA]_0$ ($mol.L^{-1}$)	$[HPMA]_0/[CTA]_0$	$[PUEMA]_0/[CTA]_0$	$[CTA]_0/[I]_0$
1	2	0.1	66.5	3.5	20
3	2	0.1	137	7	10

4.4.3.2 Conjugation of polymers to CP

See section 3.4.3.2.

4.4.3.3 Complexation of the iridium complexes to the conjugates

[(Cp*)-Ir-(phpy)(Cl)] (15.6 mg, $3.02.10^{-5}$ mol) was dissolved in water/methanol 1/1 (12 mL) in a vial wrapped in aluminium foil, and silver nitrate (5.12 mg, 1 eq., $3.02.10^{-5}$ mol) was

added. The mixture was stirred at room temperature overnight, and centrifuged to remove the silver chloride salts. The supernatant was decanted in a round bottomed flask and CP-(p($HPMA_{51}$-*co*-$PUEMA_{3.5}$))$_2$ (25.7 mg, 3 mol eq. of Ir per pyridine unit, $1.44.10^{-6}$ mol) was added. The reaction was left to stir for 2 days, after which most of the solvent was evaporated, keeping ~ 1 mL. The drug-loaded conjugates were purified from the excess complex on a disposable size exclusion column (PD10, Sephadex G25, GE Healthcare) and freeze dried. The drug loading was determined by ^{1}H-NMR in MeOD. The same protocol was used for the complexation of [(Cp*)-Ir-(phpy)(Cl)] to p$HPMA_{93}$-*co*-$PUEMA_7$ and of [(Cp^{xph})-Ir-(phpy)(Cl)] to CP-(p($HPMA_{51}$-*co*-$PUEMA_{3.5}$))$_2$ and p$HPMA_{93}$-*co*-$PUEMA_7$.

4.4.4 Inductively coupled plasma (ICP)

Measurements of trace Ir in biological samples were determined using ICP techniques. These measurements were carried out by James Coverdale. Ir standard solution (iridium chloride, 995 ± 4 µg/mL in 10% v/v hydrochloric acid) was purchased from Inorganic Ventures. Ultra-pure nitric acid (72%) was freshly distilled and diluted using milliQ water to achieve 3.6% v/v working concentration.

For iridium-containing solutions in culture medium, iridium concentration was determined using a Perkin Elmer Optima 5300 DV Optical Emission Spectrophotometer (ICP-OES) with standard addition of sodium chloride (TraceSELECT) to freshly prepared calibration standards (50-700 ppb) to match the sample matrix. Data were processed using WinLab32 V3.4.1 for Windows (Perkin Elmer).

For cell digest samples, iridium concentrations (ng × 10^6 cells) were determined using a Agilent Technologies 7500 series ICP-MS in no-gas and He-gas mode. Calibration standards for ^{193}Ir were freshly prepared (0.1-1000 ppb) and an internal standard (^{167}Er, 50 ppb) was used. Data were processed using ChemStation version B.03.05 (Agilent Technologies, Inc.).

4.4.5 *In vitro* testing

Experiments in this section were performed with the help of Dr Isolda Romero-Canelon, Dr Carlos Sanchez-Cano and James Coverdale.

4.4.5.1 Cell Culture

Human A2780 ovarian carcinoma cells were obtained from the European Collection of Cell Cultures (ECACC) used between passages 5 and 18 and were grown in Roswell Park Memorial Institute medium (RPMI-1640) or Dulbecco's Modified Eagle's Medium (DMEM) supplemented with 10% v/v of foetal calf serum, 1% v/v of 2 mM glutamine and 1% v/v penicillin/streptomycin. HOF human ovarian fibroblasts were obtained from ScienCell Research Laboratories, and maintained in fibroblast medium supplemented with 2% v/v of foetal calf serum, 1% v/v of penicillin/streptomycin and 1% v/v of growth factor serum. They were grown as adherent monolayers at 37 °C in a 5% CO_2 humidified atmosphere and passaged at approximately 70-80% confluence.

4.4.5.2 Growth Inhibition Assay

5000 cells were seeded per well in 96-well plates. The cells were pre-incubated in the corresponding drug-free media at 37 °C for 48 h before adding different concentrations of the compounds to be tested. Stock solutions of the Ir(III) complexes themselves were firstly prepared in 5% v/v DMSO, and either 95% v/v PBS or cell culture medium. For the 'conjugated complexes' or polymer/conjugate controls the use of DMSO was omitted. The concentration of Ir solutions was determined by ICP-OES before drug administration. In all cases, stock solutions were further diluted in cell culture medium until working concentrations were achieved, maintaining the total amount of DMSO below 1%. The drug exposure period was 24 h. After this, supernatants were removed by suction and each well was washed with PBS. A further 72 h was allowed for the cells to recover in drug-free medium at 37 °C. The SRB assay was used to determine cell viability. Absorbance measurements of the solubilised dye (on a BioRad iMark microplate reader using a 470 nm filter) allowed the determination of viable treated cells compared to untreated controls. IC_{50} values (concentrations which caused 50% of cell growth inhibition), were determined as duplicates of triplicates in two independent sets of experiments and their standard deviations were calculated. Two-tailed t-tests were performed assuming equal variance.

4.4.5.3 Equipotent metal accumulation in cancer cells

Cell accumulation studies of Iridium complexes were conducted on A2780 ovarian cells. Briefly, 3 x 10^6 cells were seeded on a Petri dish. After 24 h of pre-incubation time in drug-free medium at 37 °C, the compounds were added to give final concentrations equal to the IC_{50} (the concentration of Ir solutions was determined by ICP-OES before drug administration), and 24 h of drug exposure was allowed. After this time, cells were washed,

treated with trypsin, counted, and cell pellets were collected. Each sample was digested in Wheaton v-vials using 200 µL of 72% v/v nitric acid at 80 °C overnight (72%) and then diluted with milliQ water to achieve final concentration of 3.6% v/v acid. ^{193}Ir concentration was determined by ICP-MS in both no-gas and He-gas mode. These experiments were all carried out in triplicate and the standard deviations were calculated.

4.4.5.4 Equimolar metal accumulation in cancer cells

Experiments were carried out as described above with the following modifications: drug concentrations were equimolar and equal to 0.60 µM. Drug exposure times were kept unchanged (24 h).

4.4.5.5 Time-dependent metal accumulation in cancer cells

Experiments were carried out as described above with the following modifications: drug exposure times were: 1 h, 2 h, 4 h, 6 h, 14 h and 24 h at equipotent concentrations equal to IC_{50} values.

4.4.5.6 Metal accumulation in cancer cells at 4 °C

Experiments were carried out as described above with the following modifications: plates were placed at 4 °C 20 min prior to dosing at IC_{50} values, and drug exposure was limited to 4 h.

4.4.5.7 Cellular metal distribution

Cell pellets were obtained as described above, and were fractionated using the FractionPREP kit from BioVision according to the supplier's instructions. Each sample was digested in Wheaton v-vials using 200 µL of 72% v/v nitric acid at 80°C overnight (72%) and then diluted with milliQ water to achieve final concentration of 3.6% v/v acid. ^{193}Ir concentration was determined by ICP-MS in both no-gas and He-gas mode. These experiments were all carried out in triplicate and the standard deviations were calculated.

4.5 References

1. A. Z. Wang, R. Langer, O. C. Farokhzad, *Annu. Rev. Med.* **2012,** *63* (1), 185-198.
2. R. A. Petros, J. M. DeSimone, *Nat. Rev. Drug Discov.* **2010,** *9* (8), 615-627.
3. T. Lammers, F. Kiessling, W. E. Hennink, G. Storm, *J. Controlled Release* **2012,** *161* (2), 175-187.

4. H. Maeda, J. Wu, T. Sawa, Y. Matsumura, K. Hori, *J. Controlled Release* **2000,** *65* (1–2), 271-284.
5. J. Nicolas, S. Mura, D. Brambilla, N. Mackiewicz, P. Couvreur, *Chem. Soc. Rev.* **2013,** *42* (3), 1147-1235.
6. L. Y. T. Chou, K. Ming, W. C. W. Chan, *Chem. Soc. Rev.* **2011,** *40* (1), 233-245.
7. Y. Geng, P. Dalhaimer, S. S. Cai, R. Tsai, M. Tewari, T. Minko, D. E. Discher, *Nat. Nanotechnol.* **2007,** *2* (4), 249-255.
8. N. P. Truong, J. F. Quinn, M. R. Whittaker, T. P. Davis, *Polym. Chem.* **2016,** *7* (26), 4295-4312.
9. T. Muraoka, C. Y. Koh, H. G. Cui, S. I. Stupp, *Angew. Chem. Int. Ed.* **2009,** *48* (32), 5946-5949.
10. S. Mandal, Z. H. Eksteen-Akeroyd, M. J. Jacobs, R. Hammink, M. Koepf, A. J. A. Lambeck, J. C. M. van Hest, C. J. Wilson, K. Blank, C. G. Figdor, A. E. Rowan, *Chem. Sci.* **2013,** *4* (11), 4168-4174.
11. S. Kumar, A. C. Anselmo, A. Banerjee, M. Zakrewsky, S. Mitragotri, *J. Controlled Release* **2015,** *220, Part A*, 141-148.
12. B. M. Blunden, R. Chapman, M. Danial, H. X. Lu, K. A. Jolliffe, S. Perrier, M. H. Stenzel, *Chem. Eur. J.* **2014,** *20* (40), 12745-12749.
13. Y. Wang, S. Yi, L. Sun, Y. Huang, S. C. Lenaghan, M. Zhang, *J. Biomed. Nanotechnol.* **2014,** *10* (3), 445-454.
14. J. Chen, B. Zhang, F. Xia, Y. Xie, S. Jiang, R. Su, Y. Lu, W. Wu, *Nanoscale* **2016,** *8* (13), 7127-7136.
15. J. Strohalm, J. Kopeček, *Angew. Makromol. Chem.* **1978,** *70* (1), 109-118.
16. J. Kopeček, P. Kopečková, *Adv. Drug Delivery Rev.* **2010,** *62* (2), 122-149.
17. J. Sanchis, F. Canal, R. Lucas, M. J. Vicent, *Nanomedicine* **2010,** *5* (6), 915-935.
18. R. Duncan, *Nat. Rev. Cancer* **2006,** *6* (9), 688-701.
19. Z. Liu, I. Romero-Canelon, B. Qamar, J. M. Hearn, A. Habtemariam, N. P. E. Barry, A. M. Pizarro, G. J. Clarkson, P. J. Sadler, *Angew. Chem. Int. Ed.* **2014,** *53* (15), 3941-3946.
20. Z. Liu, P. J. Sadler, *Acc. Chem. Res.* **2014,** *47* (4), 1174-1185.
21. Z. Liu, I. Romero-Canelón, A. Habtemariam, G. J. Clarkson, P. J. Sadler, *Organometallics* **2014,** *33* (19), 5324-5333.
22. Z. Liu, L. Salassa, A. Habtemariam, A. M. Pizarro, G. J. Clarkson, P. J. Sadler, *Inorg. Chem.* **2011,** *50* (12), 5777-5783.
23. Z. Liu, A. Habtemariam, A. M. Pizarro, G. J. Clarkson, P. J. Sadler, *Organometallics* **2011,** *30* (17), 4702-4710.
24. J. S. Pedersen, *J. Appl. Crystallogr.* **2000,** *33* (1), 637-640.
25. R. Chapman, M. Danial, M. L. Koh, K. A. Jolliffe, S. Perrier, *Chem. Soc. Rev.* **2012,** *41* (18), 6023-6041.
26. R. Chapman, M. L. Koh, G. G. Warr, K. A. Jolliffe, S. Perrier, *Chem. Sci.* **2013,** *4* (6), 2581-2589.
27. M. R. Ghadiri, J. R. Granja, R. A. Milligan, D. E. McRee, N. Khazanovich, *Nature* **1993,** *366* (6453), 324-327.
28. Z. Liu, A. Habtemariam, A. M. Pizarro, S. A. Fletcher, A. Kisova, O. Vrana, L. Salassa, P. C. A. Bruijnincx, G. J. Clarkson, V. Brabec, P. J. Sadler, *J. Med. Chem.* **2011,** *54* (8), 3011-3026.
29. S. H. van Rijt, I. Romero-Canelon, Y. Fu, S. D. Shnyder, P. J. Sadler, *Metallomics* **2014,** *6* (5), 1014-1022.
30. V. Novohradsky, Z. Liu, M. Vojtiskova, P. J. Sadler, V. Brabec, J. Kasparkova, *Metallomics* **2014,** *6* (3), 682-690.
31. C. A. Puckett, R. J. Ernst, J. K. Barton, *Dalton Trans.* **2010,** *39* (5), 1159-1170.

32. S. Catrouillet, J. C. Brendel, S. Larnaudie, T. Barlow, K. A. Jolliffe, S. Perrier, *ACS Macro Lett.* **2016,** *5* (10), 1119-1123.

Chapter 5

pH-Responsive, amphiphilic core-shell supramolecular polymer brushes from cyclic peptide-polymer conjugates

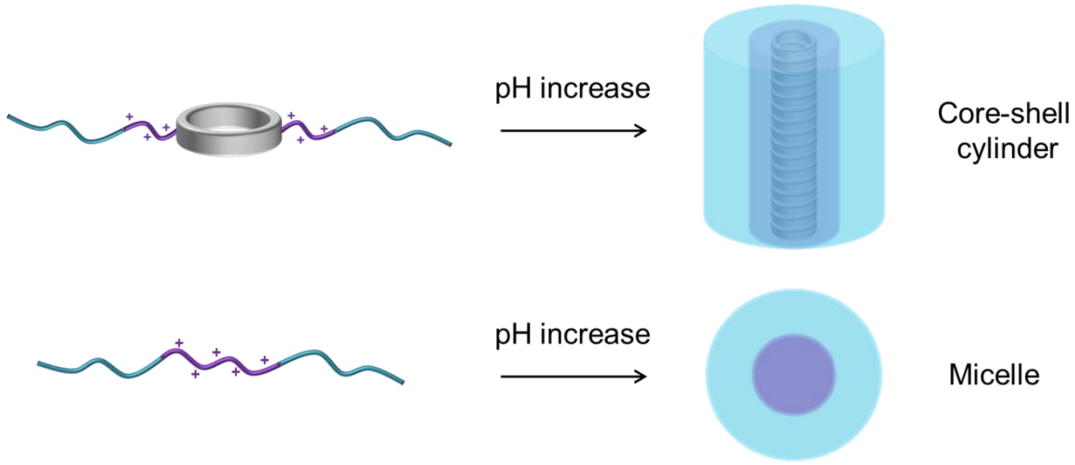

This chapter explores an alternative drug loading method, through encapsulation in a switchable hydrophobic domain. As such, the synthesis of pH-responsive, amphiphilic cyclic peptide-polymer conjugates is described. The design relies on the introduction of a poly(2-(diisopropylamino)ethyl methacrylate) (pDPA) block between the cyclic peptide and a pHPMA block. These conjugates are disassembled and protonated at low pH but assemble at physiological pH, when the DPA units are deprotonated, as determined by combining titration experiments with scattering techniques. The fitting of SANS profiles establishes that their self-assembly is controlled by the strong hydrogen bonding of cyclic peptides, leading to core-shell nanotubes. Investigations into their mode of self-assembly using UV-Vis indicate that the presence of the hydrophobic core renders the assembly more cooperative than in the case of purely hydrophilic conjugates, thereby providing additional stability to the system.

5.1 Introduction

Organic nanotubes have recently attracted considerable attention, with applications ranging from (bio)sensing to nanomedicine and electronics.[1] They can be accessed through a variety of synthetic methods but supramolecular approaches are particularly interesting thanks to their versatility and the ease in synthesis of the small building blocks.[2] More recent developments within self-assembled organic nanotubes look at the use of supramolecular polymer brushes, which are composed of a rigid supramolecular core, dictating the cylindrical shape, and flexible polymer arms.[3,4] For the core molecules to interact and self-assemble, the interactions need to be strong enough to overcome the steric repulsion of the polymer arms, and to date only a few systems have been reported to be suitable for that kind of assembly. One of the first examples relied on π-π stacking of highly unsaturated shape persistent macrocycles.[5] However in most cases, strong hydrogen bonding, sometimes used together with π-π stacking,[6] is utilised to create such elongated structures, as reported for the self-assembly of bis-[4] or tris-ureas[7] or the β-sheet stacking of peptides, and specifically cyclic D,L-α-peptides. The combination of cyclic peptides with reversible-deactivation radical polymerisation (RDRP) techniques,[8] in particular, has enabled the synthesis of a variety of well-defined polymer-peptide conjugates which assemble into the desired supramolecular polymer brushes.[9] Very recently, such systems have demonstrated beneficial properties for the transport of drugs such as cytotoxic metal complexes[10] in comparison to the pure, linear polymers. In particular when combined with stealth polymers such as 2-hydroxypropyl methacrylamide (HPMA), circulation time could be enhanced, which is certainly related to the size and shape of the nanostructures, and also indicates the excellent stability of the assembly *in vivo* (see Chapters 3 and 4).

In addition, the use of specific monomers permits the introduction of a stimuli-responsiveness,[11,12] which is triggered upon a change of temperature,[13] light,[14] or pH,[15] allowing the materials to change shape or size as a result. The variation of pH values in different biological environments has widely been recognised as a useful trigger for directed and selective drug delivery.[15] Polymers such as poly(acrylic acid),[16] poly(ethylene imine)[17] or poly(2-(dimethylamino)ethyl methacrylate) (pDMAEMA)[18] have attracted particular attention due to their ability to become reversibly charged within physiologically relevant pH ranges.[19] The increase in electrostatic repulsions, due to the protonation of some

polymers in more acidic environments such as tumour tissues, has been shown to trigger disassembly of self-assembled structures made with pH responsive materials.[20,21]

To demonstrate the ability of supramolecular polymer brushes to reversibly assemble upon a change in pH, cyclic peptide-polymer nanotubes were recently made with pDMAEMA. These conjugates can be protonated and disassembled upon a decrease of pH.[22] Despite the ability to control the size of the assembly, the relatively high pK_a of pDMAEMA makes this system disassemble below pH 8, which drastically limits its possible applications in biological systems. The challenge, therefore, remains to create a system comprising a suitable responsive material which leads to a rapid disintegration, hence release of encapsulated drugs, in physiologically relevant conditions.

Therefore, a cyclic peptide-polymer conjugate based on poly(2-(diisopropylamino)ethyl methacrylate) (pDPA), whose pK_a is better suited to drug delivery applications, is discussed in this chapter. DPA exhibits a pK_a of 6.8, and the pK_a of pDPA polymers tends to be lower, ranging between 6 and 7, due to the increased difficulty of protonating adjacents units. Particles made with pDPA have been exploited for pH-triggered endosomal drug release, as pDPA is deprotonated and hydrophobic at physiological pH (7.4), and can therefore encapsulate drugs, but becomes protonated and hydrophilic at endosomal and lysosomal pH (4.0 - 6.0), which cause particles to disassemble and the drug to be released.[23-25] To ensure the solubility of the nanotubes and provide stealth properties to the conjugates, pHPMA was introduced as a second block.[26-29] The system described here is composed of a cyclic peptide core from which two pDPA-*b*-HPMA diblock copolymers arms are grown by reversible addition fragmentation chain transfer (RAFT) polymerisation.[30,31] The self-assembly of the obtained amphiphilic peptide-polymer conjugates in solution at different pH values was studied using a variety of scattering techniques to determine whether the presence of the cyclic peptide core is sufficient to enable the assembly to be governed by the β-sheet formation, leading to core-shell cylindrical structures. In addition, an appropriate triblock copolymer pHPMA-*b*-pDPA-*b*-HPMA was synthesised and analysed for comparison. The biocompatibility of both compounds as well as their ability to encapsulate hydrophobic molecules was investigated.

5.2 Results and discussion

5.2.1 Design and synthesis

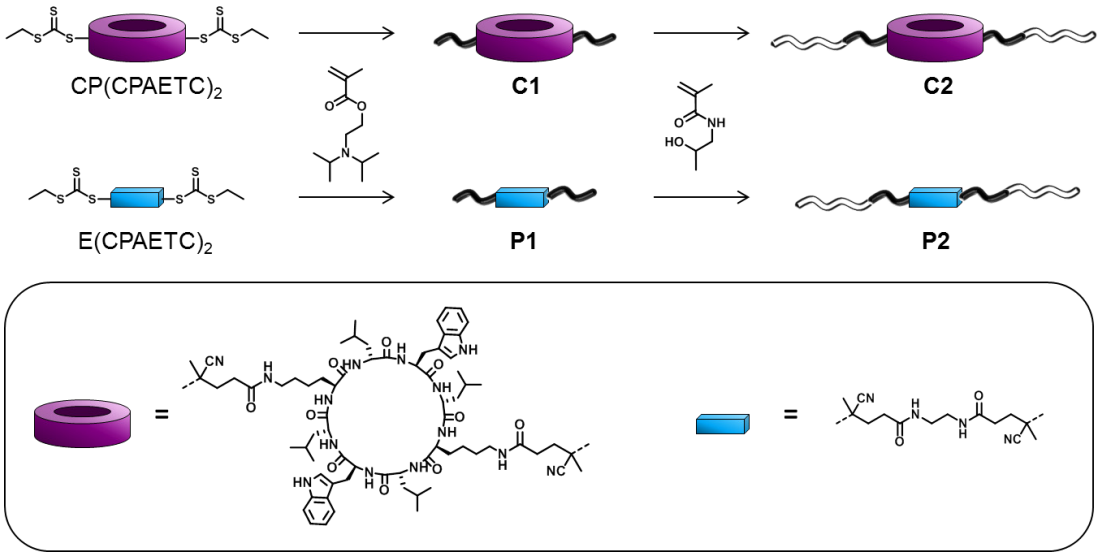

Scheme 5.1: Synthetic route yielding the amphiphilic compounds: polymer **P2** and conjugate **C2**.

The two main synthetic routes yielding peptide-polymer conjugates are grafting-to and grafting-from (see Chapter 2).[32] Various factors typically influence the choice of method, including the solubility of the different components. The cyclic peptide selected for this study is only soluble in solvents that are strong hydrogen-bond competitors, such as DMSO and DMF, in which the solubility of pDPA is limited, making the grafting-to method very challenging. For this reason, the grafting-from approach was chosen, and the CP-$(pDPA)_2$ conjugate **C1** was obtained by polymerising DPA from the CTA-modified cyclic peptide $CP(CPAETC)_2$ by RAFT polymerisation in a chloroform/DMSO mixture (Scheme 5.1). The use of these conditions enabled the initial solubilisation of $CP(CPAETC)_2$ while avoiding polymerisation-induced precipitation of pDPA, affording **C1** with reasonable control over the polymerisation (Table 5.1).

Table 5.1: Summary of polymers used in this work.

Entry	Material	$M_{n,th}$ [a] (g.mol^{-1})	$M_{n,GPC}$ [b] (g.mol^{-1})	$Đ$ [b]
C1	CP-(pDPA$_{24}$)$_2$	11800	13900	1.27
P1	(pDPA$_{21}$)$_2$	9600	7800	1.09
C2	CP-(pDPA$_{24}$-*b*-HPMA$_{55}$)$_2$	27600	26800	1.26
P2	p(DPA$_{21}$-*b*-HPMA$_{56}$)$_2$	25600	28500	1.12

[a] *Determined by ^{1}H NMR.* [b] *Determined by SEC using DMF (0.1% LiBr) as eluent, calibrated with pMMA standards.*

The control polymer **P1,** that does not contain the cyclic peptide, was obtained using the bifunctional CTA E(CPAETC)$_2$ in dioxane. It has been previously demonstrated that the physical characteristics of the polymer (degree of polymerisation (DP), and size of the monomer units) have a tremendous influence on the ability of the conjugates to self-assemble into nanotubes. Therefore, a DP of 25 was targeted for the DPA blocks, to provide enough protonation sites while limiting the possible steric hindrance from the bulky monomer. **C1** and **P1** were purified and used as macro-CTAs for the subsequent polymerisation of the hydrophilic block. The polymerisation of HPMA is best achieved in aqueous conditions in order to reach high conversions while maintaining good control over the polymerisation.[33] Aqueous 1 M HCl was used as the solvent in the second step, conditions in which the protonation of the DPA units of **C1** and **P1** enables the solubilisation of the macro-CTAs. A DP of 55 was targeted for the HPMA block, in order to provide sufficient hydrophilic shielding of the pDPA core. The size exclusion chromatograms of all compounds are shown in Figure 5.1.

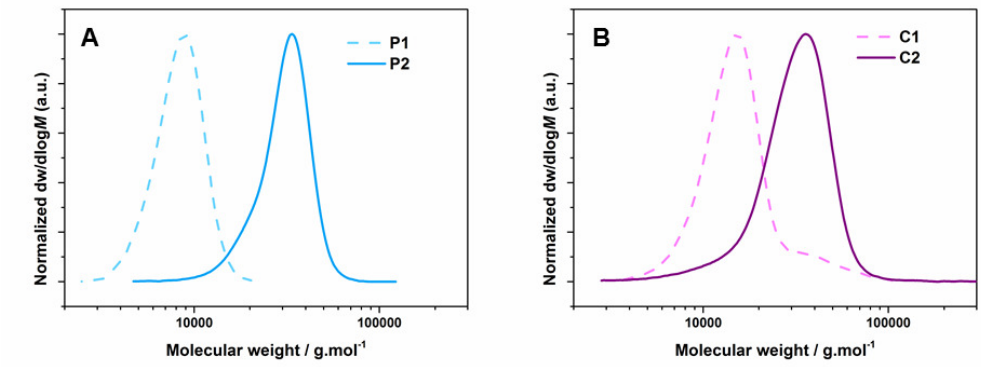

Figure 5.1: Size exclusion chromatograms of synthesised materials.

5.2.2 Cell viability assay

The biocompatibility of the amphiphilic systems **C2** and **P2** was tested by performing cell growth inhibition assays in three different cell lines (MDA, A2780 and PC3). After incubation with up to 500 µg/mL of the compounds, no noticeable loss of cell viability was observed, indicating the non-toxicity of both the conjugate and the polymer (Figure 5.2).

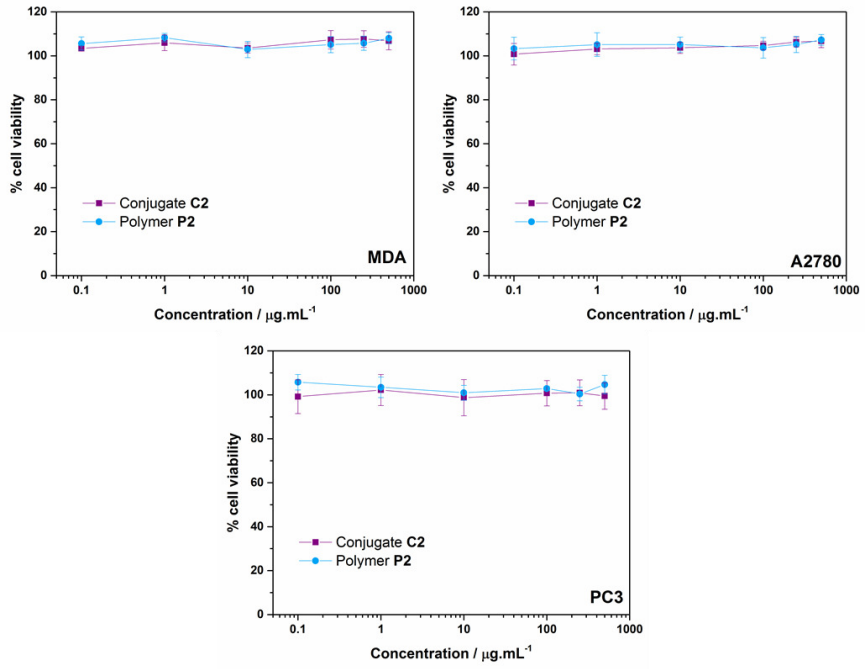

Figure 5.2: Cell viability in the presence of **C2** and **P2** in MDA, A2780 and PC3 cells.

5.2.3 Potentiometric titration

The pK_a of the conjugate **C2** and the polymer **P2** was then determined by potentiometric titrations of acidified solutions of the compounds using sodium hydroxide (Figure 5.3). Both **C2** and **P2** exhibit a distinct buffer range as can be seen on the figure, which is likely due to the fact that the charge loss resulting from the deprotonation of the DPA units triggers self-assembly of the compounds, thereby shielding the remaining charged pDPA units and making further charge loss more difficult. This observation is indicative of a very sharp transition from free chains to assembly. The pH value at which the compounds exhibit a buffer capacity is similar for the polymer and the conjugate, however the plateau is broader for **C2**, which may indicate an additional effect of the cyclic peptide on the assembly. The degree of ionisation β (which is the ratio between the amount of protonated DPA units to the total amount of DPA units in a given compound) was determined for each value of pH using

equation 1, where $[DPA^+]$ is the concentration of charged DPA units and $[DPA]_{tot}$ is the total concentration of DPA units:

$$\beta = \frac{[DPA^+]}{[DPA]_{tot}} \quad (1)$$

These concentrations can be calculated from the pH value and the amount of titrant added. The apparent pK_a of the compounds was obtained as the pH at which β = 0.5.[34] Both pK_a values are around 7 (7.05 for **C2** and 7.10 for **P2**, respectively), which is within the expected range for pDPA polymers.

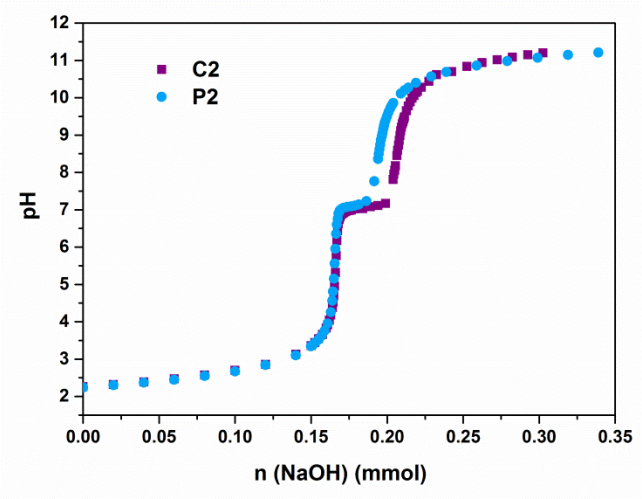

Figure 5.3: Potentiometric titration of **P2** (blue circles) and **C2** (purple squares).

5.2.4 Study of the pH-dependent aggregation

The behaviour of the compounds in solution at pH 5.0 and 7.4 was then studied by a combination of scattering techniques. To prepare the solutions, the protonated polymers were dissolved in a given amount of water, and the same amount of 2-fold acetate or phosphate buffer was added dropwise to adjust the pH to 5.0 or 7.4, respectively. Dynamic light scattering (DLS) measurements first showed an increase in size of the compounds for both conjugate **C2** (the diameter varies from 6.5 to 14 nm) and polymer **P2** (the diameter varies from 7.7 to 11.8 nm) when increasing the pH, indicating self-assembly is taking place (Figure 5.4 C). Interestingly, the size difference upon pH increase is higher for conjugate **C2**, which may indicate formation of bigger assemblies. However, due to the nature of the technique, which assumes spherical shapes, this result alone was not sufficient to define the assembled structures.

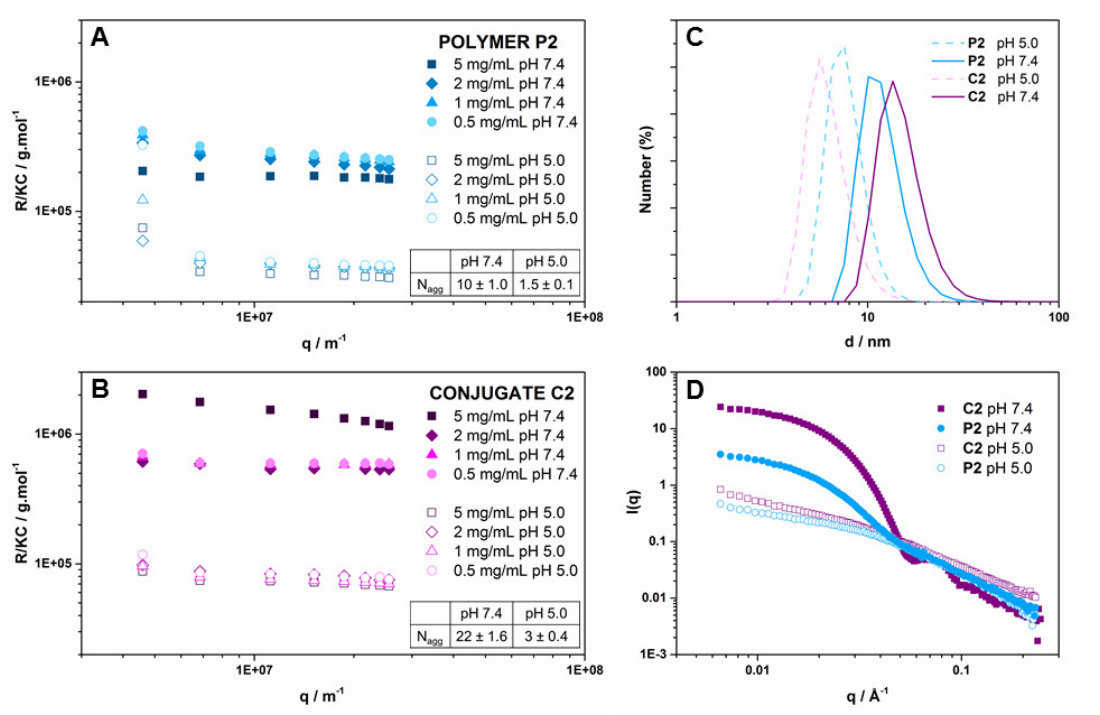

Figure 5.4: Characterisation of self-assembly using scattering techniques. A) Static light scattering profile of polymer **P2** in solution at different concentrations and different pH values. B) Static light scattering profile of conjugate **C2** in solution at different concentrations and different pH values. C) Number size distribution of **P2** (blue) and **C2** (purple) at pH 5 (dotted lines) and pH 7.4 (solid lines). D) Small angle neutron scattering profiles of **P2** (blue circles) and **C2** (purple squares) in at pH 5 (empty symbols) and pH 7.4 (full symbols).

In addition, static light scattering (SLS) experiments were performed, which allow for the determination of molecular weight. A study looking at different concentrations was carried out for both compounds at pH 5.0 and 7.4 (Figure 5.4 A-B). A clear increase in size was observed for both **C2** and **P2** upon increase of pH, confirming self-assembly triggered by deprotonation of the pDPA units. At pH 5.0, where the DPA units are protonated, all concentrations result in similar scattering profiles for each compound. Moreover, a plateau is observed in both cases, allowing for direct molecular weight determination of the assemblies.

As detailed in chapter 3, at a given concentration the Rayleigh ratio R_θ is related to the apparent molecular weight of the sample, given by equation (2).

$$\frac{KC}{R_\theta} = \frac{1}{M_a} \cdot \left(1 + \frac{q^2.R_g^2}{3}\right) \quad (2)$$

It is only at infinite dilutions, when the interactions between scattering particles are negligible, that the apparent molecular weight is equal to the true molecular weight of the molecule. As such, different concentrations of sample were measured; 0.5, 1, 2 and 5 mg/mL. At pH 5.0, all the measured concentrations result in similar profiles, allowing for the assumption that interactions are negligible. Equation (2) can therefore be simplified to equation (3):

$$\frac{KC}{R_\theta} = \frac{1}{M_a} \quad (3)$$

Using this equation, molecular weights of 79.9 ± 7.2 kg/mol and 38.7 ± 2.3 kg/mol were obtained for **C2** and **P2** at pH 5.0, corresponding to a number of aggregation (N_{agg}) of about 3 and 1.5, respectively (Table 5.2). These values confirm the fact that the electrostatic interactions are strongly hindering the self-assembly. At pH 7.4, the data sets also form an overlapping plateau for the three lowest tested concentrations (2, 1 and 0.5 mg/mL) for both the conjugate and the polymer, indicating that interactions are negligible in this range of concentrations. Molecular weights of 590 ± 42 kg/mol and 273 ± 50 kg/mol were obtained for **C2** and **P2**, corresponding to N_{agg} = 22.0 ± 1.6 and 10.0 ± 1.0, respectively. These results confirm the aggregation of conjugates **C2** into bigger structures than those formed upon assembly of **P2**. Assuming the formation of hydrogen bonding between peptides, and using the previously reported distance between two adjacent cyclic peptides,[35,36] the length of the cylinders formed by cyclic peptide-directed assembly of **C2** would be 10.4 ± 0.7 nm (L = Nagg x L_c, with L_c = 4.7 10^{-1} nm the distance between two adjacent cyclic peptides[9,35]).

Table 5.2: Determination of aggregates size by SLS.

Compound	pH	MW (kg/mol)	N_{agg} [a]
C2	7.4	590 ± 42	22.0 ± 1.6
	5.0	79.9 ± 7.2	2.9 ± 0.3
P2	7.4	273 ± 50	10.0 ± 1.0
	5.0	38.7 ± 2.3	1.5 ± 0.1

[a] *N_{agg} = MW/M_unimer.*

Complementary small angle neutron scattering (SANS) experiments were conducted (Figure 5.4 D). Both compounds were measured at each pH, and the SANS profiles at low q values clearly confirmed the size increase upon pH change, as well as the formation of bigger

structures for **C2** than for **P2** at pH 7.4. In addition, the fitting of SANS profiles at pH 7.4 provides information on the shape of the assemblies (see below, section 5.2.5).

Fluorescence measurements were also conducted on conjugate **C2** at pH 5.0 and 7.4, and the shift of the emission peak corresponding to the tryptophan present on the cyclic peptide core clearly indicates a change in local environment polarity,[37] coherent with the self-assembly of **C2** and the formation of a hydrophobic pDPA domain at the centre of the nanotubes (Figure 5.5). The significant decrease of the fluorescence intensity can be attributed to self-quenching of the tryptophan groups in the assembled state.

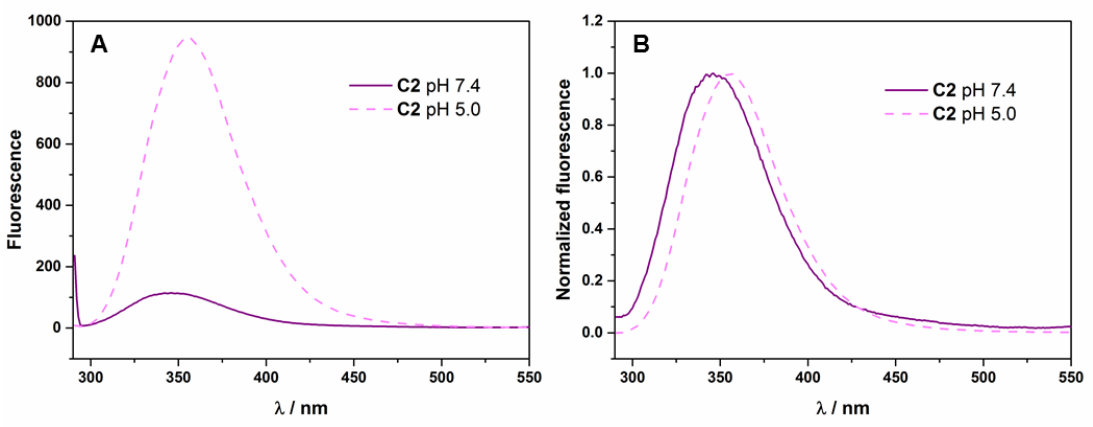

Figure 5.5: Fluorescence emission spectra for **C2** at pH 5.0 (dotted lines) and pH 7.4 (plain lines).

To assess the ability of the compounds to encapsulate hydrophobic molecules, Nile red was used as a model compound. The dye was mixed with varying amounts of **P2** and **C2** in methanol, before dropwise addition of PBS. Being non-water soluble, Nile red was forced into the hydrophobic core of the self-assembled structures. Subsequently, the methanol was slowly evaporated; the solutions were filtered to remove any excess fluorophore and freeze-dried. The solids were redissolved in methanol and fluorescence emission spectra were recorded for each sample (Figure 5.6 A-B).

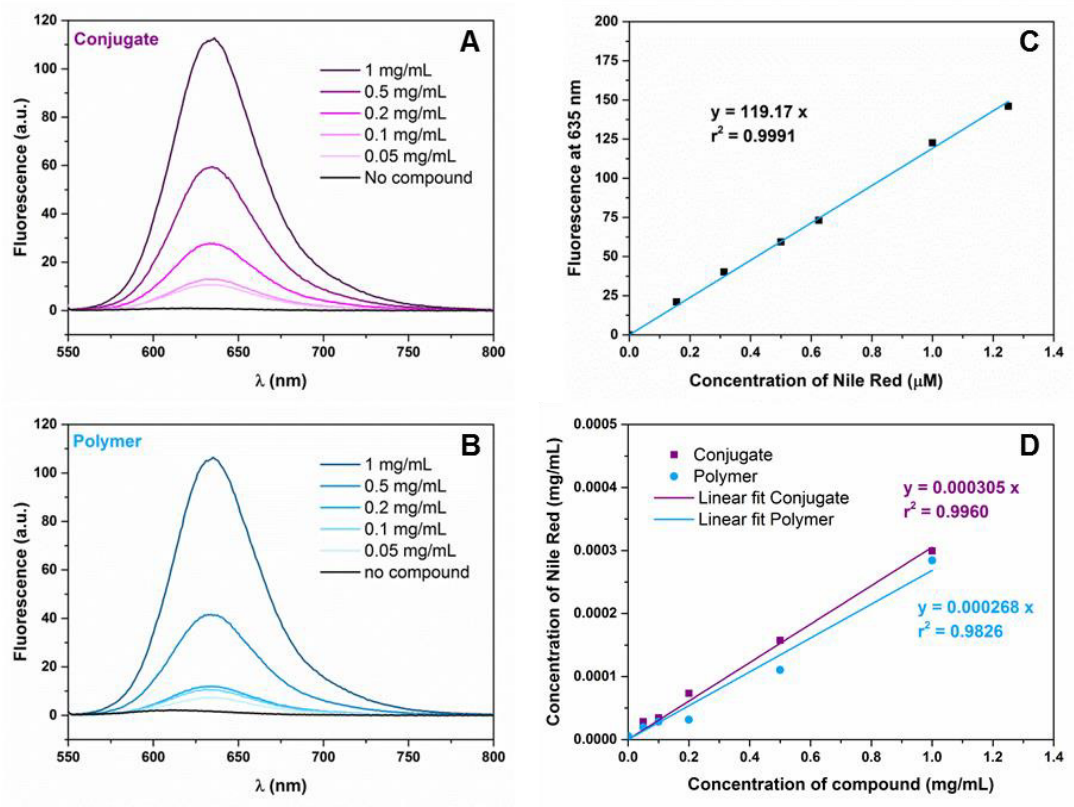

Figure 5.6: Quantification of Nile Red encapsulation. A) Fluorescence emission spectra of Nile red solubilised by varying amounts of conjugate **C2**. B) Fluorescence emission spectra of Nile red solubilised by varying amounts of polymer **P2**. C) Fluorescence calibration curve of Nile red in methanol. D) Determination of Nile red loading by weight concentration using the fluorescence intensity at 635 nm.

In order to quantify the encapsulation, the maximum intensity in each case was compared to a calibration of Nile red alone in methanol (Figure 5.6 C). Loading efficiencies are generally determined using absorbance, which is linear in a broader range of concentrations. However, low intensities were recorded (still in the linear range of fluorescence), and this technique provided better resolution than absorbance in this specific case. By plotting the weight concentration of Nile red *vs* the weight concentration of the compounds a loading capacity can be determined using the slope of the linear fit (Figure 5.6 D). Loading capacities of 0.031 % and 0.027 % were obtained for **C2** and **P2**, respectively. These values are very low (loading capacities are usually 0.1-2 % in literature) but these results constitute a proof of concept that encapsulation of hydrophobic molecules in constructs formed by amphiphilic cyclic peptide-polymer conjugates is possible.

5.2.5 Determination of the shape of the assemblies

To gain information on the shape of the assemblies in solution, the SANS profiles at pH 7.4 were fitted using different models. For the data corresponding to polymer **P2**, the best suited model is the one of a spherical micelle, which takes into account both the spherical shape of the core and the Gaussian chains forming the corona (Figure 5.7 A).[38] The model SPHERE+Chains(RW) on SASfit was used for this form factor, and the results are shown in Table 5.3. The scattering length densities were calculated using the tool provided by SASfit, assuming the core is constituted of the pDPA block and the brush of the pHPMA block.

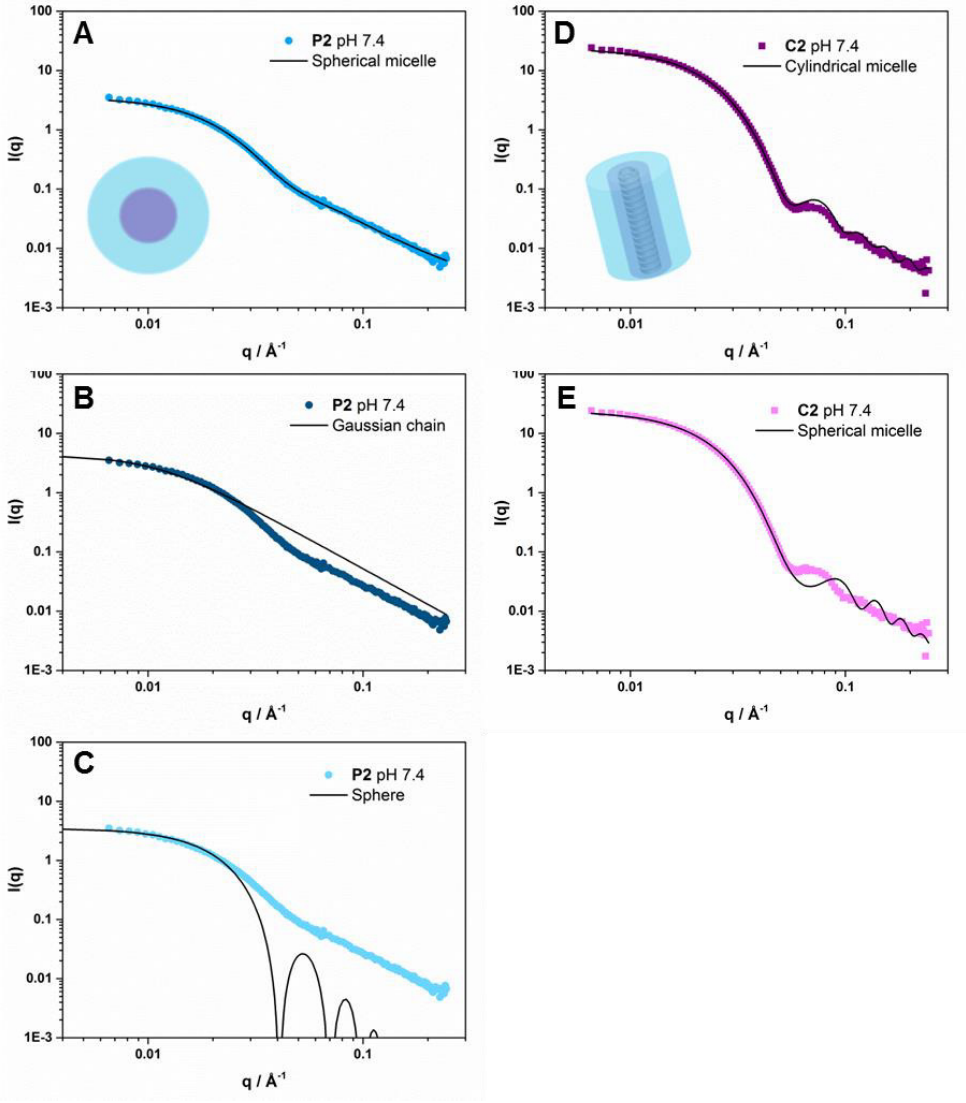

Figure 5.7: SANS profile of **P2** and its fit using models corresponding to A) a spherical micelle, B) a Gaussian chain C) a solid sphere; SANS profile of **C2** and its fit using models corresponding to D) a cylindrical micelle and E) a spherical micelle in solution at pH 7.4.

Table 5.3: Fitting parameters obtained for **P2** using a spherical micelle form factor.

Parameter	Definition	Value	
N	Scale factor	4.3896	Fitting
n_agg	Grafting density	0.0276	
R_core (Å)	Radius of the core	5.889	
Rg (Å)	Radius of gyration of the polymer arms	49.41	
xsolv_core	Fraction of solvent in the core	2.55	
d	d = 1 mimics the non-penetration of the polymer chains in the core	0.80	
V_brush (Å^3)	Volume of the polymer arms[a]	13500	Calculated
eta_core (Å^{-2})	Scattering length density of the core	4.40E-7	
eta_brush (Å^{-2})	Scattering length density of the polymer arms	7.83E-7	
eta_solv (Å^{-2})	Scattering length density of the solvent	6.39E-6	

[a] *Calculated using* $V_{brush} = MW/(dxN_a).10^{24}$*, where MW is the molecular weight of the pHPMA block, d its density and* N_a *Avogadro's number.*

To further confirm the solution morphology of **P2**, other models were also attempted, and showed to be inadequate. First, a Gaussian chain model was used (Table 5.4 and Figure 5.7 B).[39] The fit was performed with R_g and MW as adjustable parameters and afforded R_g = 132 Å and MW = 166300 g/mol. The obtained molecular weight is very different from the molecular weight of the unimer (M_n = 25600 g/mol), demonstrating individual chains are not representative of the morphology of **P2** at pH 7.4.

Table 5.4: Fitting parameters obtained for **P2** using a Gaussian chain form factor.

Parameter	Definition	Value	
MW (g/mol)	Molecular weight	166300	Fitting
R_g (Å)	Radius of gyration	132	
η_{solv} (Å^{-2})	Scattering length density of the solvent	6.39E-6	Calculated
η (Å^{-2})	Scattering length density of the compound	6.647E-7	

A rigid sphere model was also attempted (Table 5.5 and Figure 5.7 C), for which the form factor is defined by:[40]

$$I_{(q)} = (\eta_{solv} - \eta)^2 * \Phi * \frac{MW}{d*N_a} * P_{(q)} \quad (3)$$

where $\Phi = \frac{C}{d}$

$$P_{(q)\,Sphere} = \frac{9}{X^6}(sinX - XcosX)^2 \qquad \text{with} \qquad X = qR \quad (4)$$

N_a is Avogadro's constant, d is the density of the polymer and was set to 1, C is the concentration. η_{solv} and η are the scattering length densities corresponding to the solvent and the compound, respectively. The fit was performed with MW and R as adjustable parameters. As can be seen on Figure 5.7 C, this form factor was not adapted to the data, as it does not account for the hydrophilic blocks present on the outside of the micelle.

Table 5.5: Fitting parameters obtained for **P2** using a solid sphere form factor.

Parameter	Definition	Value	
MW (g/mol)	Molecular weight	126900	Fitting
R (Å)	Radius	106	
η_{solv} (Å^{-2})	Scattering length density of the solvent	6.39E-6	Calculated
η (Å^{-2})	Scattering length density of the compound	6.647E-7	

For conjugate **C2**, both cylindrical micelle (Table 5.6 and Figure 5.7 D) and spherical micelle (Table 5.7 and Figure 5.7 E) fits were attempted.

Table 5.6: Fitting parameters obtained for **C2** using a cylindrical micelle form factor.

Parameter	Definition	Value	
N	Scale factor	0.0714026	Fitting
R_core (Å)	Radius of the core	75.36	
n_agg	Grafting density	9.46E-4	
Rg (Å)	Radius of gyration of the polymer arms	24.44	
H (Å)	Length of the cylinder	113.9	
V_brush ($Å^3$)	Volume of the polymer arms[a]	13300	Calculated
eta_core ($Å^{-2}$)	Scattering length density of the core	5.091E-7	
eta_brush ($Å^{-2}$)	Scattering length density of the polymer arms	7.829E-7	
eta_solv ($Å^{-2}$)	Scattering length density of the solvent	6.39E-6	
xsolv_core	Fraction of solvent in the core, set to 0	0	Fixed
d	d = 1 mimics the non-penetration of the polymer chains in the core	1	

[a] *Calculated using* $V_{brush} = MW/(dxN_a).10^{24}$, *where MW is the molecular weight of the pHPMA block, d its density and* N_a *Avogadro's number.*

Table 5.7: Fitting parameters obtained for **C2** using a spherical micelle form factor.

Parameter	Definition	Value	
N	Scale factor	0.08411	Fitting
R_core (Å)	Radius of the core	67.83	
n_agg	Grafting density	2.13E-3	
Rg (Å)	Radius of gyration of the polymer arms	26.079	
V_brush ($Å^3$)	Volume of the polymer arms[a]	13300	Calculated
eta_core ($Å^{-2}$)	Scattering length density of the core	5.091E-7	
eta_brush ($Å^{-2}$)	Scattering length density of the polymer arms	7.829E-7	
eta_solv ($Å^{-2}$)	Scattering length density of the solvent	6.39E-6	
xsolv_core	Fraction of solvent in the core, set to 0	0	Fixed
d	d = 1 mimics the non-penetration of the polymer chains in the core	1	

[a] *Calculated using* $V_{brush} = MW/(dxN_a).10^{24}$, *where MW is the molecular weight of the pHPMA block, d its density and* N_a *Avogadro's number.*

The data is best fitted with the cylindrical micelle model, demonstrating the formation of the expected core-shell like cylindrical structures. Moreover the value obtained for the height of the cylinder is in excellent agreement with the value obtained with SLS (11.4 nm by SANS *vs* 10.4 nm by SLS, N_{agg} 24 *vs* 22, respectively). Finally, N_{agg} can also be determined from the number of aggregation per surface area n_agg provided by the fit. By multiplying this value by the surface of the core S ($S_{sphere} = 4\pi R\_core^2$ and $S_{cylinder} = 2\pi HR\_core$), N_{agg} values of 123 and 51 are obtained for the spherical and cylindrical micelle fits, respectively. This value corresponds to the total number of chains and needs to be divided by two since each peptide contains two polymer chains. The N_{agg} values calculated by this method are therefore 63 and 26 for the spherical and cylindrical micelle fits, respectively. The N_{agg} value afforded by the cylindrical fit is in much better agreement with the values obtained by SLS and by using the height of the cylinder in SANS, providing further evidence that this fit is best suited, and hence confirming that the presence of the cyclic peptide core dictates the assembly of **C2** into nanotubes instead of simple micelles.

5.2.6 Evaluation of the assembly mechanism

The stability in water of supramolecular polymers relying on hydrogen bonding interactions has previously been shown to be improved by the introduction of hydrophobic interactions close to the hydrogen bonding sites.[41] Following this principle, it can be hypothesised that the amphiphilic system described here would lead to more stable assemblies than a cyclic peptide conjugated to purely hydrophilic polymers.

In an attempt to assess the hypothesis that the presence of a hydrophobic pDPA block at the core of the nanotubes formed by **C2** would help to stabilise the structures, a study on the mode of assembly was carried out. To this end, UV-Vis measurements were recorded in PBS, using solutions of **C2** at different temperatures (Figure 5.8) and concentrations (Figure 5.9). The variation of these parameters enables the transition from unimeric (disassembled) state to assembled structures. From these measurements, calculations can give information on the isodesmic or cooperative nature of the assembly. During an isodesmic supramolecular polymerisation, the reactivity of the end group does not change as the polymerisation progresses, and the assembly process is characterised by a single binding constant for the addition of each monomer unit. In contrast, a cooperative supramolecular polymerisation begins by a nucleation phase, followed by an elongation phase. It is therefore characterised by two distinct association constants, each corresponding to a phase of the assembly.[42] A

hydrophilic conjugate made with a copolymer of HPMA and PUEMA (CP-(pHPMA$_{55}$-*co*-PUEMA$_{3.5}$)$_2$, see Chapter 3) was used for comparison.

Initially, a study in temperature was carried out: UV-Vis spectra were recorded for both **C2** and the hydrophilic control conjugate CP-(pHPMA$_{55}$-*co*-PUEMA$_{3.5}$)$_2$ at temperatures varying from 20 to 80 °C (Figure 5.8 A-B). The temperature-dependent degree of aggregation α can be calculated from the normalisation of the extinction coefficient ε at a specific wavelength, calculated using the Beer-Lambert law.[43] Values of ε at 330 nm and 269 nm were used in the determination of α for **C2** and the control conjugate, respectively. The data was plotted against the temperature T and fitted using non-linear least square analyses (Figure 5.8 C-D). The obtained curve displays a sigmoidal shape in the case of the control conjugate (Figure 5.8 D), indicating a more isodesmic self-assembly mechanism. The much sharper curve in the case of conjugate **C2** suggests a higher degree of cooperativity in the case of the core-shell structure (Figure 5.8 C). From the values of α, the equilibrium constant K_{eq} can be determined for each temperature, according to the following equation:

$$K_{eq} = \frac{DP_n^2}{C} - \frac{DP_n}{C} \quad (5)$$

where C is the concentration of the sample and DP_n the number averaged degree of polymerisation, defined by:

$$DP_n = \frac{1}{\sqrt{1-\alpha}} \quad (6)$$

The Van't Hoff plot, representing $\ln(K_{eq})$ *vs* T^{-1} can then be obtained (Figure 5.8 E-F), and thermodynamic parameters can be extracted using the linear fit of the data by the Van't Hoff equation:

$$\ln(K_{eq}) = -\frac{\Delta H}{RT} + \frac{\Delta S}{R} \quad (7)$$

where ΔH is the molar enthalpy release related to the formation of intermolecular supramolecular interactions, ΔS the change in entropy and R the gas constant. The variation of Gibbs free energy at a given temperature can be deduced using equation 8:

$$\Delta G = \Delta H - T\Delta S \quad (8)$$

The obtained thermodynamic parameters are summarised in Table 5.8.

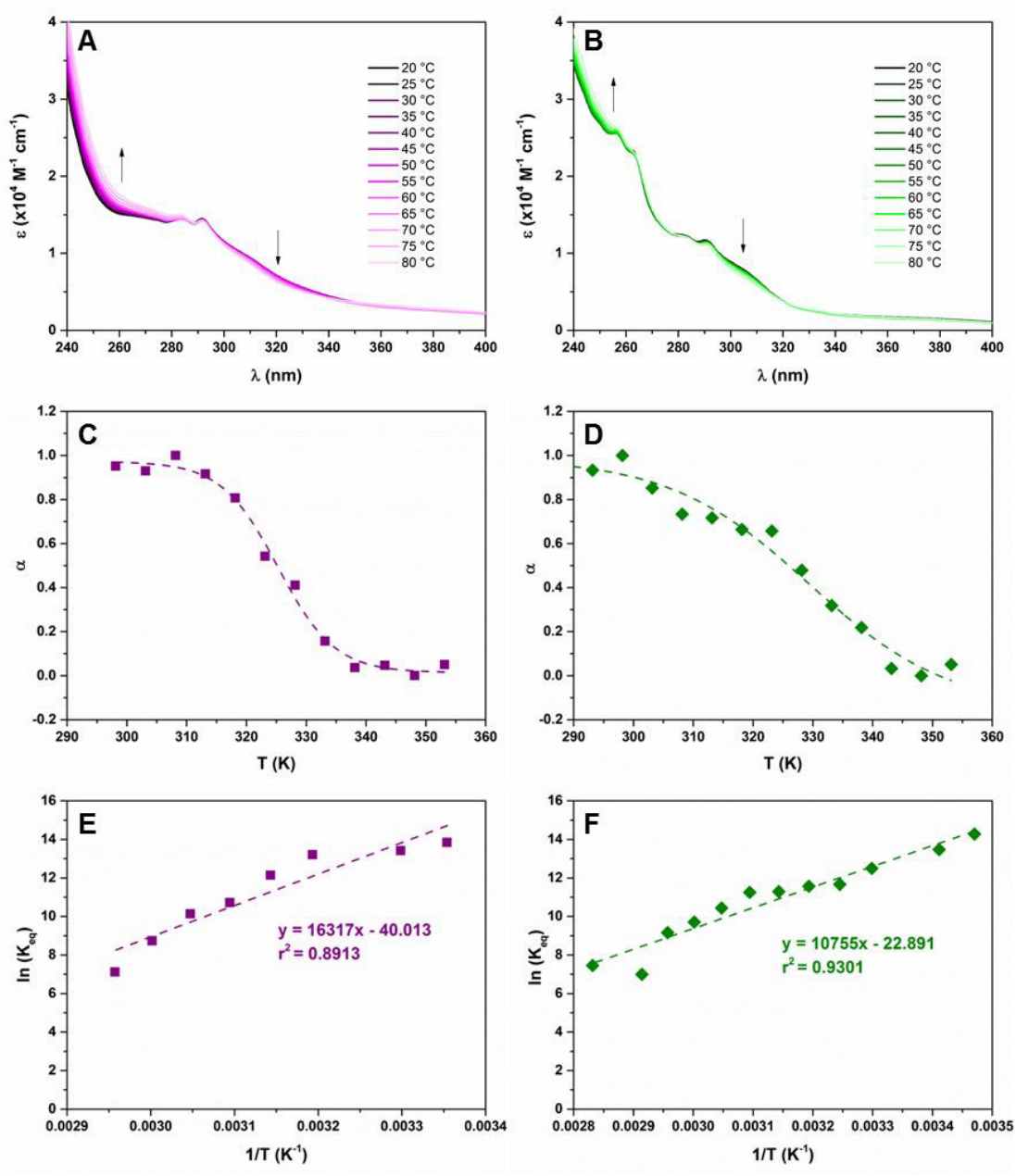

Figure 5.8: Study in temperature of **C2** (left) and the hydrophilic control conjugate CP-(pHPMA$_{55}$-*co*-PUEMA$_{3.5}$)$_2$ (right). A-B) UV-Vis spectra recorded at 20-80 °C at 5 °C intervals. C-D) Temperature-dependent degree of aggregation α. E-F) Van't Hoff plots.

Table 5.8: Thermodynamic parameters describing the self-assembly of **C2** and the hydrophilic control conjugate CP-(pHPMA$_{55}$-*co*-PUEMA$_{3.5}$)$_2$.

Compound	ΔH (kJ.mol^{-1})	ΔS (J.mol^{-1}.K^{-1})	ΔG^{a} (kJ.mol^{-1})	$K_{eq}{}^{a}$ (10^5 M^{-1})
C2	-136	-333	-35	6.7
Control	-89	-190	-32	2.7

[a] *Determined at 303K.*

The large and negative values of ΔH (-136 and -89 kJ.mol^{-1}) indicate that the process is exothermically driven. This study in temperature suggests that the self-assembly of **C2** is more cooperative than that of the control conjugate. Next, a study in concentration was carried out, since it allows for the determination of the degree of cooperativity σ.

To this end, UV-Vis spectra were recorded for both compounds at concentrations varying from 0.24 to 125 μM at 25 °C (Figure 5.9 A-B). In a similar manner as for the temperature study, the degree of aggregation α was calculated at a given wavelength (245 nm, and 250 nm for **C2** and the control, respectively). Each data set can be fitted with two Hill plots,[44] each corresponding to a phase of the self-assembly (nucleation at low concentrations, elongation at higher concentrations) (Figure 5.9 C-D). These fits provide the dissociation constants for each phase, from which the association constants corresponding to the nucleation (K_n) and elongation phase (K_e) can be calculated. The ratio K_n/K_e gives the degree of cooperativity σ. This parameter equals 1 for an isodesmic system, and tends to 0 for a fully cooperative system.[45] σ-values of 0.0098 and 0.21 were obtained for **C2** and the control conjugate, respectively. These results show that the assembly is more cooperative in the case of the diblock conjugate **C2**, indicating that the core-shell structures formed by this amphiphilic conjugate are less dynamic and more stable than the ones formed by the hydrophilic conjugate used in previous chapters. This finding provides a very good insight into ways the self-assembly process could eventually be controlled.

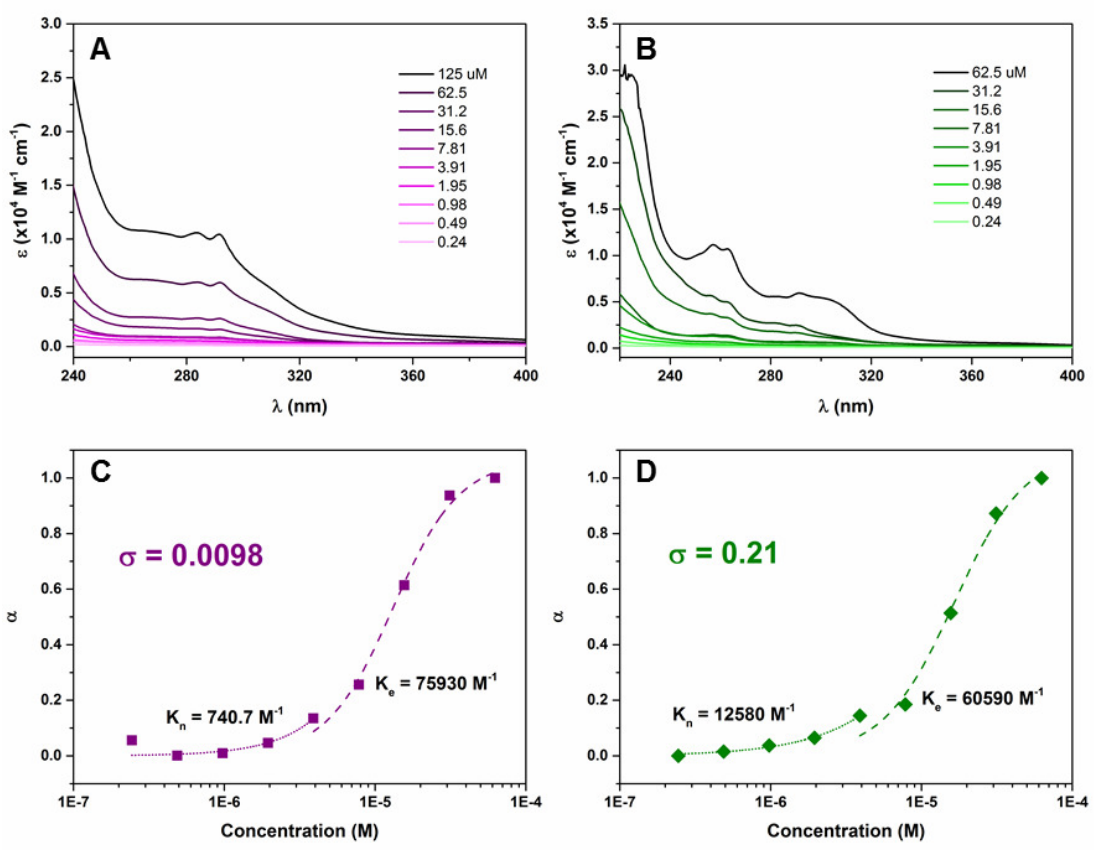

Figure 5.9: Study in concentration of **C2** (left) and the hydrophilic control conjugate CP-(pHPMA$_{55}$-*co*-PUEMA$_{3.5}$)$_2$ (right). A-B) UV-Vis spectra of varying concentrations recorded at 25 °C. C-D) Concentration-dependent degree of aggregation α and their fits using Hill plots.

5.3 Conclusions

Amphiphilic, pH-responsive cyclic peptide-polymer conjugates were synthesised and their supramolecular assembly in aqueous solution was thoroughly characterised. The combined use of DPA and HPMA afforded stabilised water soluble core-shell nanotubes at physiological pH, able to disassemble due to the protonation of the pDPA core in more acidic environments. A triblock copolymer which does not contain the cyclic peptide core was also synthesised for comparison purposes. Both compounds were found to be non-toxic, and their pK_a was determined to be around 7.0, which is within the desired range to trigger disassembly in endosomes following cellular uptake, revealing potential to facilitate endosomal release. Proof of concept studies highlighted the potential of these systems to encapsulate a hydrophobic dye, which was used as a model drug compound. The structures formed by their assembly were characterised by scattering techniques at pH 7.4 and 5.0. SLS

showed a distinct change in size between the different pH values in both cases, with the cyclic peptide-conjugates forming larger assemblies. Moreover, SANS demonstrated the cylindrical shape of the peptide-containing structures in contrast to the spherical micelles formed by the control polymer. This finding confirms that the supramolecular stacking of the cyclic peptide core, and not the block copolymer self-assembly, governs the formation of the obtained core-shell structures. In addition, the system described here constitutes the first report on the self-assembly of amphiphilic cyclic peptide-polymer conjugates in water. Investigations on its mechanism of self-assembly revealed that the presence of a hydrophobic block around the supramolecular core of the cylinder helps to enhance its stability compared to hydrophilic polymers alone. This chapter presents promising preliminary data for the development of alternative drug carriers.

5.4 Experimental

5.4.1 Materials

2-(Diisopropylamino)ethyl methacrylate (DPA), 1,1′-Azobis(cyclohexanecarbonitrile) (vazo 88), Nile red and deuterated solvents for NMR were purchased from Sigma-Aldrich. 2,2'-Azobis[2-(2-imidazolin-2-yl)propane]dihydrochloride (VA-044) was purchased from Wako Chemicals. Sodium hydroxide pellets were obtained from Fisher scientific. All solvents were bought from commercial sources and used as received. Cyclic peptide, chain transfer agents $(CP(CPAETC)_2$ and $E(CPAETC)_2)$, the monomer HPMA, and the control conjugate $(CP-(pHPMA_{55}$-*co*-$PUEMA_{3.5})_2$ used in section 5.2.3.2 were synthesised as described in previous chapters.

5.4.2 Characterisation methods

NMR spectra were recorded on a Bruker DPX-300 instrument. Molecular weights and dispersities of the polymers were assessed by size exclusion chromatography (SEC) on a Polymer Laboratories PL-GPC 50 Plus system in DMF with 0.1% LiBr, using a poly(methyl methacrylate) calibration, as described in Chapter 2.

DLS measurements were taken using a Malvern instruments Zetasizer Nano at 25 °C with a 4 mW He-Ne 633 nm laser at a scattering angle of 173 (back scattering).

Static light scattering measurements were obtained using an ALV-CGS3 system operating with a vertically polarised laser with a wavelength of 632 nm. The measurements were taken at 20 °C over a range of scattering wave vectors.

SANS was carried out on SANS Instrument D11 at Institut Laue-Langevin in Grenoble, France as described in previous chapters. UV measurements were recorded on an Agilent Cary 60 UV-Vis and fluorescence on an Agilent Cary eclipse Fluorescence spectrophotometer.

5.4.3 Polymer synthesis

For the first block, the chain transfer agent (CTA), monomer (DPA), initiator (vazo 88) and solvent were introduced into a flask equipped with a magnetic stirrer and sealed with a rubber septum (see Table 5.9 for detailed conditions). The solution was degassed by bubbling nitrogen through it for 15 min, and then put in an oil bath at 90 °C for 8h. Conversions were determined by ^{1}H NMR. The polymers were precipitated in ice-cold H_2O/MeOH 1/2 and dried under vacuum.

For the second block, the previously synthesised polymer **P1** and conjugate **C1** were used as macro CTAs. They were mixed in a flask with HPMA, initiator (VA 044) and HCl 1M. The flask was sealed and the mixture degassed for 15 min before placing it in an oil bath at 44 °C for the indicated time. Conversions were determined by ^{1}H NMR, the polymers were precipitated in ice-cold acetone and dried under vacuum.

Table 5.9: Summary of polymerisation conditions.

	(macro)CTA	Solvent	Time (hours)	$[M]_0$	$\frac{[M]_0}{[CTA]_0}$	$\frac{[CTA]_0}{[I]_0}$	Conversion (%)
P1	$E(CPAETC)_2$	Dioxane	8	2	58	20	73
C1	$CP(CPAETC)_2$	DMSO/$CHCl_3$ 6/4	8	1	56	20	85
P2	**P1** $(pDPA_{21})_2$	HCl 1M	13	2	152	10	73
C2	**C1** CP-$(pDPA_{24})_2$	HCl 1M	19	2	200	10	55

5.4.4 *In vitro* testing

5.4.4.1 Cells

A2780 (human ovarian carcinoma), PC3 (human prostate carcinoma) and MDA-MB-231 (human breast cancer) cells were obtained either from the European Collection of Cell Cultures (ECACC) or Sigma-Aldrich. A2780 were grown in Roswell Park Memorial Institute medium (RPMI-1640), and PC3 and MDA-MB-231 in Dulbecco's Modified Eagle Medium (DMEM). Both media were supplemented with 10% v/v of foetal calf serum, 1% v/v of 2 mM glutamine and 1% v/v penicillin/streptomycin. Cells were grown as adherent monolayers at 37 °C in a 5% CO_2 humidified atmosphere and passaged at approximately 70-80% confluence.

5.4.4.2 Growth inhibition assay

Briefly, 5000 cells were seeded per well in 96-well plates and allowed to grow for 24 h before adding different concentrations of the compounds to be tested. Stock solutions (5 $mg.mL^{-1}$) were prepared by dissolution in water followed by dropwise addition of PBS (20% water), and diluted in cell culture medium at concentrations ranging from 0.1 to 500 $\mu g.mL^{-1}$. Culture medium was replaced by dilutions of the compounds and cells further incubated for 72 h. After this, supernatant was removed and replaced by fresh medium. XTT assay was used to determine cell metabolic activity as a measure of viability. Absorbance measurements of the plate at 475 nm were carried out using a Synergy HTX (Biotek) plate reader. Determination of viable treated cells was done in comparison to untreated controls. Two independent sets of experiments in triplicates were carried out and standard deviations were used for error bars.

5.4.5 Methods

5.4.5.1 Potentiometric titration

40 mL of solution at 0.5 $mg.mL^{-1}$ was used for each potentiometric titration experiment. Potentiometric titrations were performed manually at room temperature with a syringe pump to control the added volume and a pH meter (HI2211 Hanna Intruments) was used to determine the pH. The addition of titrant (NaOH at 0.05, 0.1 or 0.2 $mol.L^{-1}$) was done with various added volumes (from 0.01 mL to 0.2 mL) in order to obtain a steady increase of pH between each addition. Raw titration data yielded the evolution of the pH of the solution as a

function of the amount of titrant. The degree of ionisation β was calculated and plotted as a function of pH. From these data, the apparent pK_a of the polymers was determined as the value of pH for which β = 0.5. The data were treated according to published procedures with some minor modifications to fit for polybases instead of polyacids.[34]

5.4.5.2 Nile red encapsulation

To probe the encapsulation ability of both compounds, Nile red was dissolved in methanol at a concentration of 0.796 mg/mL. 40 μL of this solution (100 nmol) were added to vials containing compounds in methanol (500 μL) at varying concentrations. 2 mL of PBS was added dropwise to each vial, using a syringe pump over one hour. Methanol was left to evaporate overnight. The solutions were filtered using 0.2 μm syringe filters, and 1.5 mL of each solution was freeze dried. The resulting solid was dissolved in methanol and the fluorescence was recorded (the samples were excited at a wavelength of 543 nm and emission was recorded between 550 and 800 nm). Nile red calibration was performed using solutions of the dye in methanol at various concentrations.

5.4.5.3 UV-Vis study

To investigate the mechanism of self-assembly, UV-Vis experiments were carried out. A stock solution of **C2** in PBS was prepared by dissolving 27.6 mg of compound in H_2O (0.5 mL). PBS (1.5 mL) was added dropwise, until a concentration of 1 mmol.L^{-1} was reached. Serial dilutions in PBS were performed to achieve working concentrations ranging from 0.24 to 125 μmol.L^{-1}. The stock solution for the control conjugate CP-(pHPMA$_{55}$-*co*-PUEMA$_{3.5}$)$_2$ was prepared in a similar manner, without the dropwise addition. Spectra were recorded at 25 °C in a 10 mm path length quartz cuvette. The temperature dependent experiments were carried out using the solutions of **C2** and control conjugate at 15.6 μmol.L^{-1}. Spectra were recorded at every 5 °C at temperatures varying from 20 to 80 °C (with 30 min equilibration time). Measurements were obtained by Dr. Edward Mansfield.

5.5 References

1. C. R. Martin, P. Kohli, *Nat. Rev. Drug Discovery* **2003,** *2* (1), 29-37.
2. D. T. Bong, T. D. Clark, J. R. Granja, M. R. Ghadiri, *Angew. Chem. Int. Ed.* **2001,** *40* (6), 988-1011.
3. M. Fritzsche, S.-S. Jester, S. Höger, C. Klaus, N. Dingenouts, P. Linder, M. Drechsler, S. Rosenfeldt, *Macromolecules* **2010,** *43* (20), 8379-8388.

4. S. Pensec, N. Nouvel, A. Guilleman, C. Creton, F. Boué, L. Bouteiller, *Macromolecules* **2010,** *43* (5), 2529-2534.
5. S. Rosselli, A. D. Ramminger, T. Wagner, B. Silier, S. Wiegand, W. Häußler, G. Lieser, V. Scheumann, S. Höger, *Angew. Chem. Int. Ed.* **2001,** *40* (17), 3137-3141.
6. L. Tian, R. Szilluweit, R. Marty, L. Bertschi, M. Zerson, E.-C. Spitzner, R. Magerle, H. Frauenrath, *Chem. Sci.* **2012,** *3* (5), 1512-1521.
7. S. Catrouillet, C. Fonteneau, L. Bouteiller, N. Delorme, E. Nicol, T. Nicolai, S. Pensec, O. Colombani, *Macromolecules* **2013,** *46* (19), 7911-7919.
8. D. A. Shipp, *Polym. Rev.* **2011,** *51* (2), 99-103.
9. R. Chapman, M. Danial, M. L. Koh, K. A. Jolliffe, S. Perrier, *Chem. Soc. Rev.* **2012,** *41* (18), 6023-6041.
10. B. M. Blunden, R. Chapman, M. Danial, H. X. Lu, K. A. Jolliffe, S. Perrier, M. H. Stenzel, *Chem. Eur. J.* **2014,** *20* (40), 12745-12749.
11. P. Theato, B. S. Sumerlin, R. K. O'Reilly, T. H. Epps, *Chem. Soc. Rev.* **2013,** *42* (17), 7055-7056.
12. C. d. l. H. Alarcon, S. Pennadam, C. Alexander, *Chem. Soc. Rev.* **2005,** *34* (3), 276-285.
13. H. J. Moon, D. Y. Ko, M. H. Park, M. K. Joo, B. Jeong, *Chem. Soc. Rev.* **2012,** *41* (14), 4860-4883.
14. F. D. Jochum, P. Theato, *Chem. Soc. Rev.* **2013,** *42* (17), 7468-7483.
15. S. Dai, P. Ravi, K. C. Tam, *Soft Matter* **2008,** *4* (3), 435-449.
16. H. Mori, A. H. E. Müller, *Prog. Polym. Sci.* **2003,** *28* (10), 1403-1439.
17. M. Jager, S. Schubert, S. Ochrimenko, D. Fischer, U. S. Schubert, *Chem. Soc. Rev.* **2012,** *41* (13), 4755-4767.
18. S. Agarwal, Y. Zhang, S. Maji, A. Greiner, *Mater. Today* **2012,** *15* (9), 388-393.
19. D. Schmaljohann, *Adv. Drug Delivery Rev.* **2006,** *58* (15), 1655-1670.
20. D. M. Lynn, M. M. Amiji, R. Langer, *Angew. Chem. Int. Ed.* **2001,** *40* (9), 1707-1710.
21. Y. Bae, S. Fukushima, A. Harada, K. Kataoka, *Angew. Chem.* **2003,** *115* (38), 4788-4791.
22. S. Catrouillet, J. C. Brendel, S. Larnaudie, T. Barlow, K. A. Jolliffe, S. Perrier, *ACS Macro Letters* **2016,** *5* (10), 1119-1123.
23. C. Pegoraro, D. Cecchin, L. S. Gracia, N. Warren, J. Madsen, S. P. Armes, A. Lewis, S. MacNeil, G. Battaglia, *Cancer Letters* **2013,** *334* (2), 328-337.
24. K. Liang, G. K. Such, Z. Zhu, Y. Yan, H. Lomas, F. Caruso, *Adv. Mater.* **2011,** *23* (36), H273-H277.
25. H. Yu, Z. Xu, D. Wang, X. Chen, Z. Zhang, Q. Yin, Y. Li, *Polym. Chem.* **2013,** *4* (19), 5052-5055.
26. A. Jäger, E. Jäger, F. Surman, A. Höcherl, B. Angelov, K. Ulbrich, M. Drechsler, V. M. Garamus, C. Rodriguez-Emmenegger, F. Nallet, P. Štěpánek, *Polym. Chem.* **2015,** *6* (27), 4946-4954.
27. C.-M. J. Hu, R. H. Fang, B. T. Luk, L. Zhang, *Nanoscale* **2014,** *6* (1), 65-75.
28. J. Kopeček, P. Kopečková, *Adv. Drug Delivery Rev.* **2010,** *62* (2), 122-149.
29. A. Wicki, D. Witzigmann, V. Balasubramanian, J. Huwyler, *J. Controlled Release* **2015,** *200*, 138-157.
30. J. Chiefari, Y. K. Chong, F. Ercole, J. Krstina, J. Jeffery, T. P. T. Le, R. T. A. Mayadunne, G. F. Meijs, C. L. Moad, G. Moad, E. Rizzardo, S. H. Thang, *Macromolecules* **1998,** *31* (16), 5559-5562.
31. G. Moad, E. Rizzardo, S. H. Thang, *Aust. J. Chem.* **2012,** *65* (8), 985-1076.
32. S. C. Larnaudie, J. C. Brendel, K. A. Jolliffe, S. Perrier, *J. Polym. Sci., Part A: Polym. Chem.* **2016,** *54* (7), 1003-1011.

33. C. W. Scales, Y. A. Vasilieva, A. J. Convertine, A. B. Lowe, C. L. McCormick, *Biomacromolecules* **2005,** *6* (4), 1846-1850.
34. O. Colombani, E. Lejeune, C. Charbonneau, C. Chassenieux, T. Nicolai, *J. Phys. Chem. B* **2012,** *116* (25), 7560-7565.
35. M. R. Ghadiri, J. R. Granja, R. A. Milligan, D. E. McRee, N. Khazanovich, *Nature* **1993,** *366* (6453), 324-327.
36. R. Chapman, M. L. Koh, G. G. Warr, K. A. Jolliffe, S. Perrier, *Chem. Sci.* **2013,** *4* (6), 2581-2589.
37. J. T. Vivian, P. R. Callis, *Biophys. J.* **2001,** *80* (5), 2093-2109.
38. J. S. Pedersen, *J. Appl. Crystallogr.* **2000,** *33* (1), 637-640.
39. P. Debye, *J. Chem. Phys.* **1946,** *14* (10), 636-639.
40. A. Guinier, G. Fournet, C. Walker, Small angle scattering of X-rays. *J. Wiley & Sons, New York* **1955**.
41. E. Obert, M. Bellot, L. Bouteiller, F. Andrioletti, C. Lehen-Ferrenbach, F. Boué, *J. Am. Chem. Soc.* **2007,** *129* (50), 15601-15605.
42. T. F. A. De Greef, M. M. J. Smulders, M. Wolffs, A. P. H. J. Schenning, R. P. Sijbesma, E. W. Meijer, *Chem. Rev.* **2009,** *109* (11), 5687-5754.
43. M. M. J. Smulders, M. M. L. Nieuwenhuizen, T. F. A. de Greef, P. van der Schoot, A. P. H. J. Schenning, E. W. Meijer, *Chem. Eur. J.* **2010,** *16* (1), 362-367.
44. J. L. Garcés, L. Acerenza, E. Mizraji, F. Mas, *J. Biol. Phys.* **2008,** *34* (1-2), 213-235.
45. U. Mayerhoffer, F. Wurthner, *Chem. Sci.* **2012,** *3* (4), 1215-1220.

Conclusions and perspectives

The aims of this thesis were to design polymeric nanotubes based on self-assembling cyclic peptides that can be used as drug delivery vectors, to thoroughly characterise their assembly in solution and to investigate their behaviour *in vitro* and *in vivo*.

Chapter 2 describes the two synthetic pathways leading to cyclic peptide-polymer conjugates, which were critically compared. A range of functional monomers was polymerised from and grafted to, a cyclic peptide, using an active ester ligation strategy. Initial kinetic studies using a cyclic peptide modified with CTA groups clearly revealed excellent control over the polymerisation without the appearance of any detectable termination reaction. With the exception of PEGA, where polymerisation from the peptide was not controlled due to steric hindrance, all the tested monomers led to well defined conjugates in under twelve hours (and under two hours for acrylic monomers). Their grafting-to counterparts were obtained after polymerisation using an NHS-functionalised CTA, followed by an active ester coupling to the cyclic peptide. Conjugation was found to proceed efficiently across a wide range of monomers. Generally comparing the two investigated synthetic routes, the grafting-from approach achieves pure conjugate synthesis (no unreacted polymeric chains remain in the sample) in faster reaction times. This approach is, however, dependant on the availability of a solvent that can solubilise the peptide, the monomer and resulting conjugate. It is also unfavourable when attempting to control the polymerisation of bulky monomers such as PEGA. On the other hand, the grafting-to strategy remains more flexible in terms of choice of solvent and scalability, and also enables a modular approach to design peptide conjugates, using different combinations of peptides and polymers. Nevertheless, purification to remove excess or unreacted polymer remains a challenge, and the reactivity of some monomers can be an obstacle for efficient conjugation. In summary, both techniques carry advantages and disadvantages, but are complementary in nature. Their combination gives access to a large variety of well-defined cyclic peptide-polymer conjugates.

Chapter 3 introduced cyclic peptide-based nanotubes specifically designed for drug delivery applications. Self-assembling cyclic peptides functionalised with HPMA (co)polymers were synthesised, and a study of their assembly in solution showed the formation of nanotubes.

Interestingly, a small fraction of a comonomer prone to non-covalent interactions greatly helped the self-assembly process. The comonomer-containing conjugate was tested against a non-assembling control, and clear differences in their cell uptake behaviour *in vitro* as well as their pharmacokinetics *in vivo* were observed. Cellular accumulation studies demonstrated a time and temperature dependent internalisation of the compounds, with larger sized nanotubes increasing the uptake by a factor 3 to 4 compared to that of the polymer. Colour coincidence studies confirmed accumulation of the conjugates in the lysosomal compartments of the cells, further indicating endosomal uptake as the main pathway. After intravenous injection to rats, conjugates were found to circulate for a reasonable amount of time ($t_{1/2}$ = 16 h) , and exhibit a higher exposure than the control polymer. Such characteristics are beneficial when attempting passive tumour targeting though the EPR effect. Most importantly, conjugates were ultimately cleared out, which might be related to a slow disintegration of the self-assembled nanotubes into smaller structures or even unimers. This feature makes it possible to potentially avoid undesired long-term accumulation and side-effect toxicity in organs such as the liver and spleen. Considering all the observed results, these cyclic peptide-polymer nanotubes certainly represent a novel and promising class of materials, especially for applications as delivery systems for the transport of pharmaceutically active compounds.

Based on these findings, chapter 4 discussed the attachment of organoiridium anticancer complexes to the pHPMA-based polymeric cyclic peptide nanotubes presented in chapter 3. The pyridine-containing comonomer provides a specific binding site for the complexation of highly potent anticancer complexes. [(Cp*)Ir(phpy)Cl] and [(Cp^{xph})Ir(phpy)Cl] were used in this study. The self-assembly of these conjugates was confirmed by static light scattering and small angle neutron scattering, which revealed that the building blocks form short cylinders about 20 nm in length. These drug-bearing nanotubes exhibited comparable or increased toxicity towards human ovarian cancer cells compared to the free drug. Remarkably, their toxicity towards a healthy cell model was lower than the free drug, suggesting a degree of selectivity towards cancer cells. Interestingly, the nanotubes also showed higher toxicity, as well as higher selectivity, towards cancer cells when compared to the drug-bearing polymers used as a non-assembling control. Analysis of the amount of iridium accumulated in the cells after equipotent and equimolar uptake studies revealed that a similar percentage of drug enters the cells in each case, indicating that the drug-bearing conjugates do not enhance the iridium uptake, but rather exhibit a more efficient mode of action. Investigations into the mechanisms of entry and partitioning profile into different

organelles revealed that energy-dependent mechanisms of cell uptake account for a higher fraction of the accumulated drug, in the case of the polymer and conjugate when compared to the free drug.

Finally, chapter 5 explored the early stages of the development of an alternative delivery system designed for drug encapsulation and subsequent pH-triggered release. Amphiphilic, pH-responsive cyclic peptide-polymer conjugates were synthesised and their supramolecular assembly in aqueous solution was thoroughly characterised. The combined use of DPA and HPMA afforded stabilised water soluble core-shell nanotubes at physiological pH, able to disassemble due to the protonation of the pDPA core in more acidic environments. A triblock copolymer which does not contain the cyclic peptide core was also synthesised for comparison purposes. Both compounds were found to be non-toxic, and their pK_a was determined to be around 7.0, which is within the desired range to trigger disassembly in endosomes following cellular uptake, revealing potential to facilitate endosomal release. Proof of concept studies highlighted the potential of these systems to encapsulate a hydrophobic dye, which was used as a model drug compound. The structures formed by their assembly were characterised by scattering techniques at pH 7.4 and 5.0. SLS showed a distinct change in size between the different pH values in both cases, with the cyclic peptide-conjugates forming larger assemblies. Moreover, SANS demonstrated the cylindrical shape of the peptide-containing structures in contrast to the spherical micelles formed by the control polymer. This finding confirms that the supramolecular stacking of the cyclic peptide core, and not the block copolymer self-assembly, governs the formation of the obtained core-shell structures. In addition, the system described here constitutes the first report on the self-assembly of amphiphilic cyclic peptide-polymer conjugates in water. Investigations on its mechanism of self-assembly revealed that the presence of a hydrophobic block around the supramolecular core of the cylinder helps to enhance its stability compared to hydrophilic polymers alone.

In summary, this thesis demonstrates that supramolecular nanotubes based on self-assembling cyclic peptides present sufficient advantages compared to other nanoscale systems, and should be considered suitable candidates in the search for new drug delivery systems. The influence of the self-assembly on cellular uptake and pharmacokinetic parameters was demonstrated by comparing nanotubes with a non-assembling control polymer. However, different aspects of this work could be pursued further.

Chapter 2 demonstrated that both the grafting-to and grafting-from methods lead to identical conjugates in most cases, but a comparison of their self-assembly would be ideal to confirm the formation of similar materials. In addition, it would be worthwhile to explore other ligations techniques such as CuAAC coupling, or the HBTU coupling used in the following chapters.

The *in vivo* studies on the drug-free conjugate presented in chapter 3 could be expanded, particularly in order to verify the hypothesis that the enhanced performance of the nanotubes compared to the polymers is related to their ability to slowly disassemble into smaller structures that can be cleared out. For example, looking at covalently cross-linked nanotubes would provide pharmacokinetic parameters for a system of similar dimensions which is unable to disintegrate. Moreover, to confirm that the observed difference between conjugate and polymer is not due to the sole presence of the cyclic peptide, a non-assembling conjugate could be used as an additional control. Additionally, histology analyses could reveal organ localisation.

Further *in vitro* evaluation of the iridium loaded nanotubes, presented in chapter 4, could also be pursued. A precise understanding of the separate fate of the conjugates and the iridium drug is currently lacking. In order to investigate this aspect, fluorophores need to be attached to both the polymers and the drug. While fluorescent labelling of polymers is widely established, attachment of fluorophores to the iridium complexes is problematic. The properties of such organometallic complexes are highly dependent on the ligands and modifying or replacing a ligand with a dye molecule would certainly have an impact on their potency. This limitation could be circumvented by using a different drug, such as the fluorescent anticancer agent doxorubicin (DOX). However DOX is not an organometallic complex; as such this approach would require modification of the synthetic strategy. An *in vivo* study focusing on drug-loaded systems would also be highly desirable. Ideally tumour animal models should be used, and the accumulation of drug in the tumours should be assessed. Preliminary studies looking at the penetration of an iridium drug, and drug-loaded polymer and nanotube into spheroids are currently being carried out. The attachment of tumour-targeting ligands such an RGD peptide (arginine-glycine-aspartic acid) to the nanotubes could be investigated, and their influence on tumour accumulation determined. Eventually, attachment of different drugs could be explored.

The amphiphilic system introduced in chapter 5 is currently in the early stages of development and could be highly improved. The first issue to address would be

encapsulation efficiency of the material, which should be greatly enhanced to provide a more realistic therapeutic dose. In order to do this, the core of the assembly needs to be made more hydrophobic. One way of achieving this goal would be to vary the DPs of the respective blocks, and/or of the overall polymer. A longer DPA block might help creating a more hydrophobic environment towards the core of the assemblies. Another possibility would be to work with fully deprotonated polymers and a solvent switch method instead of progressive deprotonation using the slow addition of PBS. The method used in chapter 5 does not guarantee the complete absence of charges, and the presence of even a small amount of charges would limit the degree of hydrophobicity and therefore hinder the encapsulation of hydrophobic molecules. After improvement of the loading capacity, encapsulation of more relevant molecules, such as active drugs, could be explored. Following on, the materials should be tested for their expected ability to facilitate endosomal release.

Appendix A

NMR spectra from Chapter 2

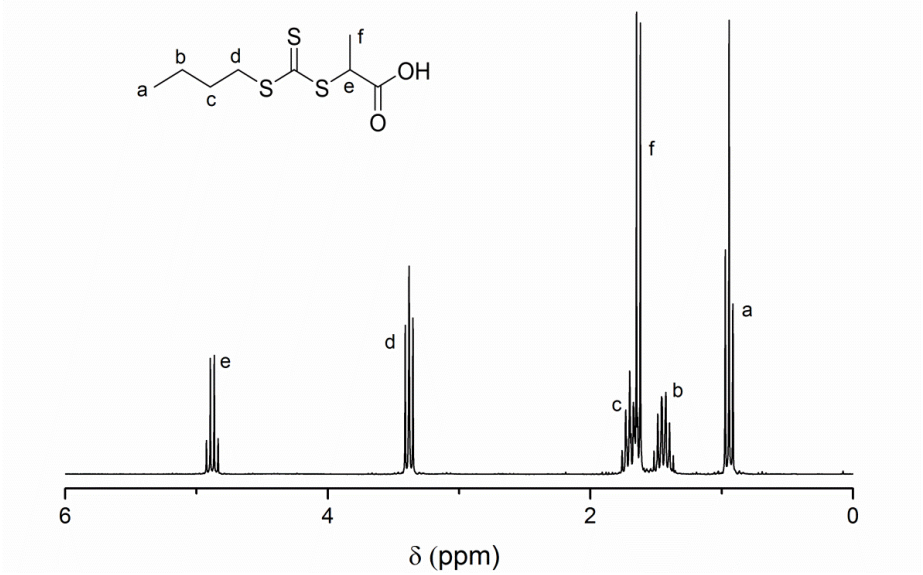

Figure A.1: ^{1}H NMR spectrum ($CDCl_3$, 300 MHz) of (propanoic acid)yl butyl trithiocarbonate (PABTC).

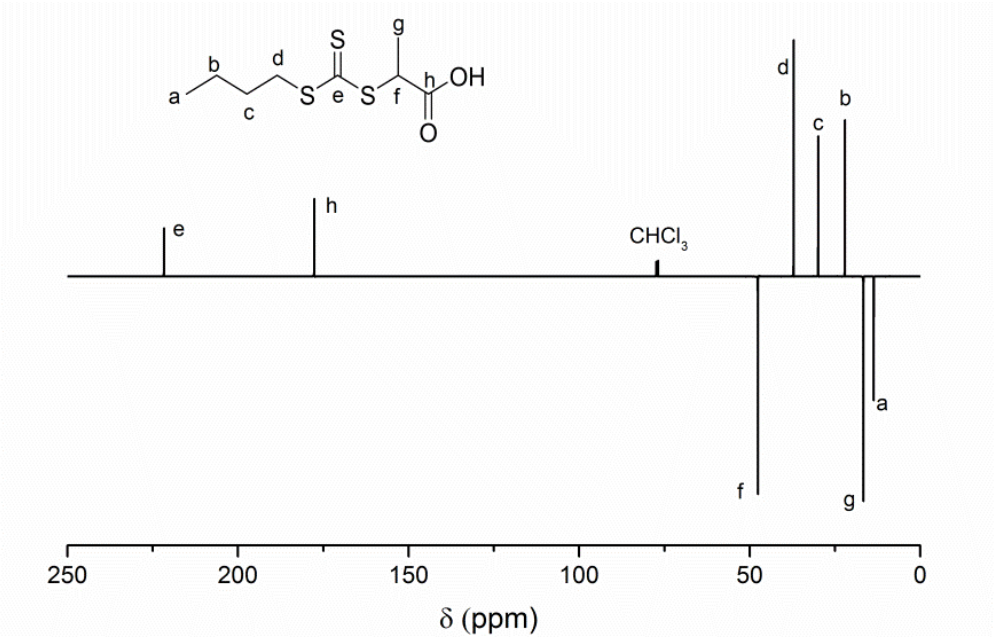

Figure A.2: ^{13}C-APT NMR spectrum ($CDCl_3$, 125 MHz) of (propanoic acid)yl butyl trithiocarbonate (PABTC).

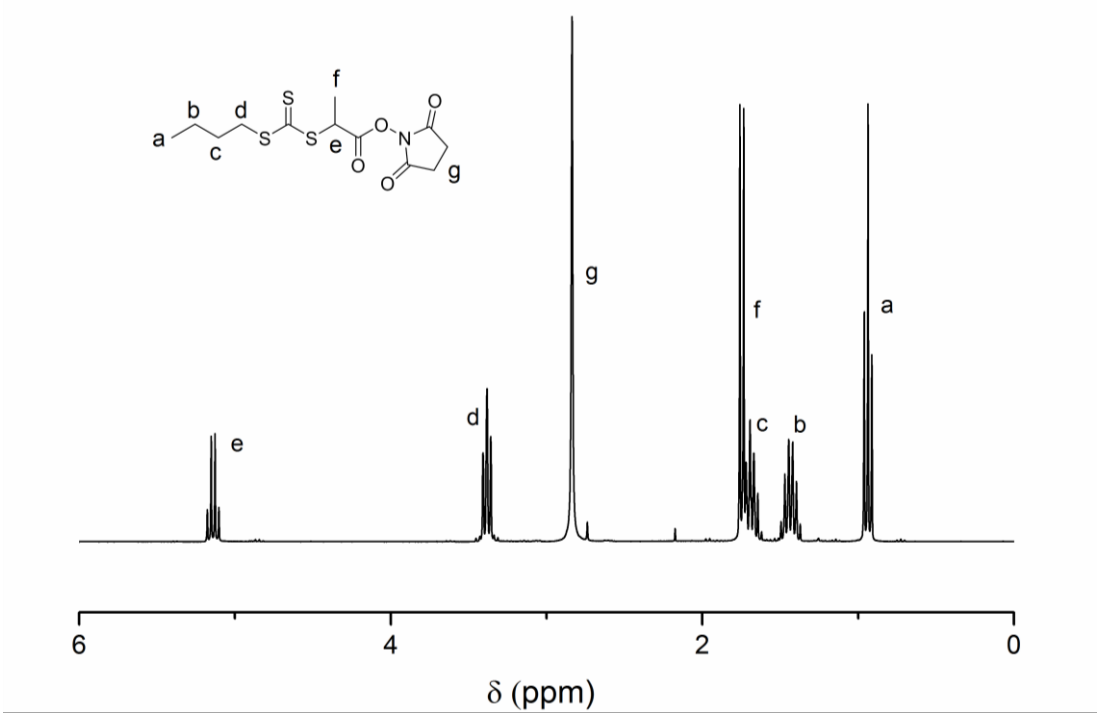

Figure A.3: ^{1}H NMR spectrum ($CDCl_3$, 300 MHz) of *N*-hydroxysuccinimide-(propanoic acid)yl butyl trithiocarbonate (NHS-PABTC).

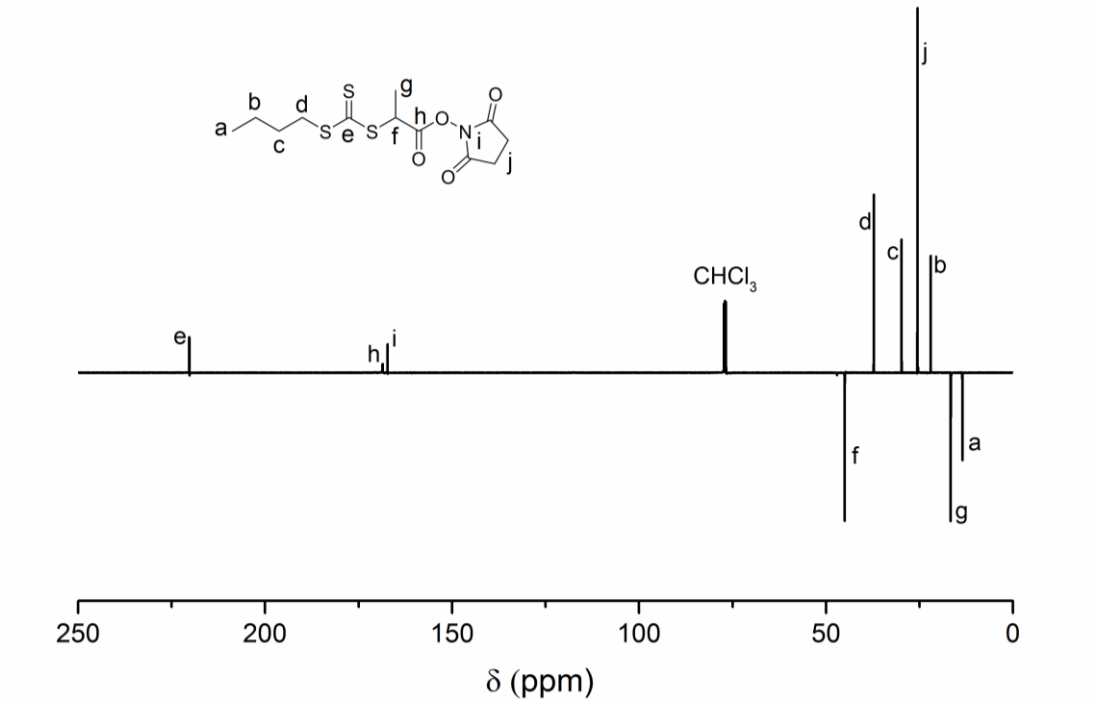

Figure A.4: ^{13}C-APT NMR spectrum ($CDCl_3$, 125 MHz) of *N*-hydroxysuccinimide-(propanoic acid)yl butyl trithiocarbonate (NHS-PABTC).

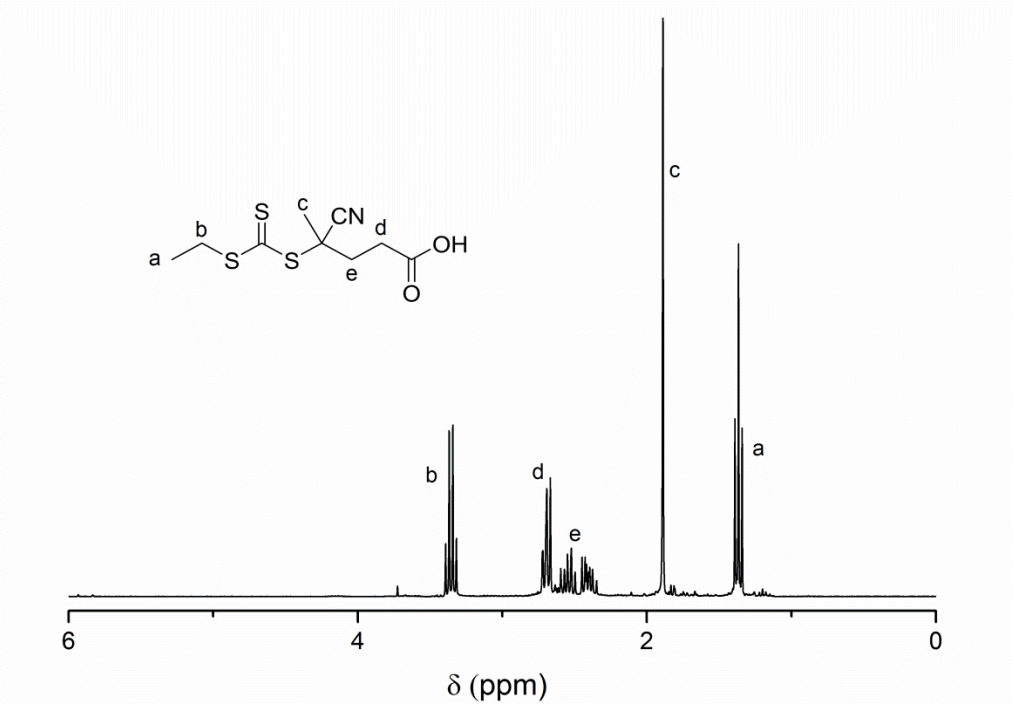

Figure A.5: ^{1}H NMR spectrum ($CDCl_3$, 300 MHz) of (4-cyano pentanoic acid)yl ethyl trithiocarbonate (CPAETC).

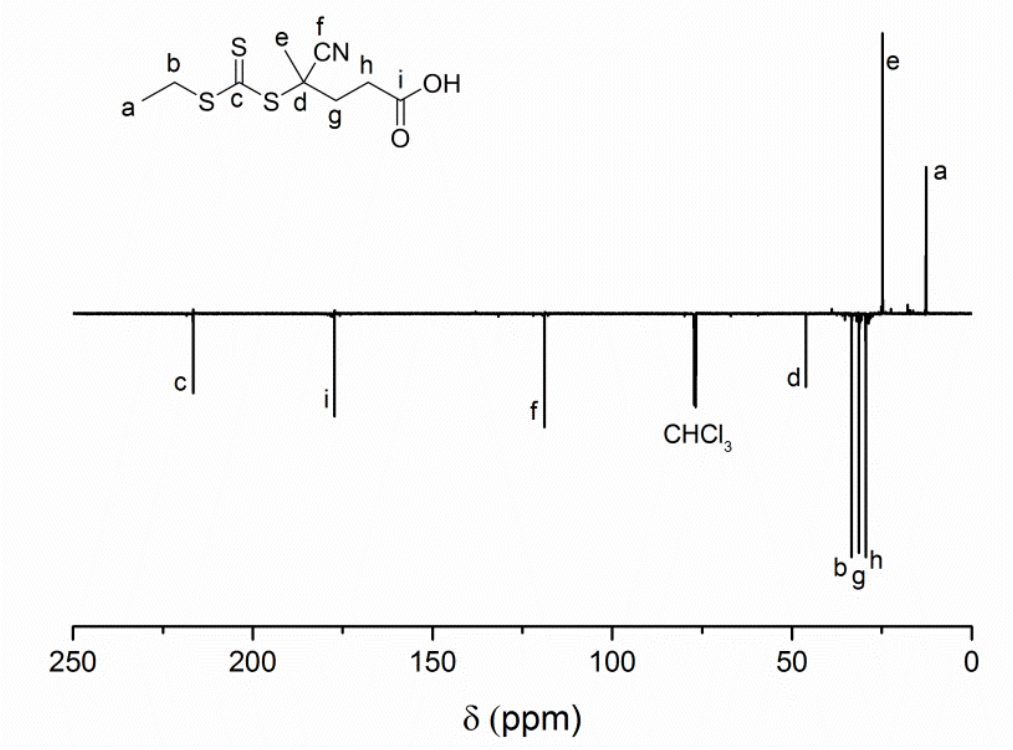

Figure A.6: ^{13}C-APT NMR spectrum ($CDCl_3$, 125 MHz) of (4-cyano pentanoic acid)yl ethyl trithiocarbonate (CPAETC).

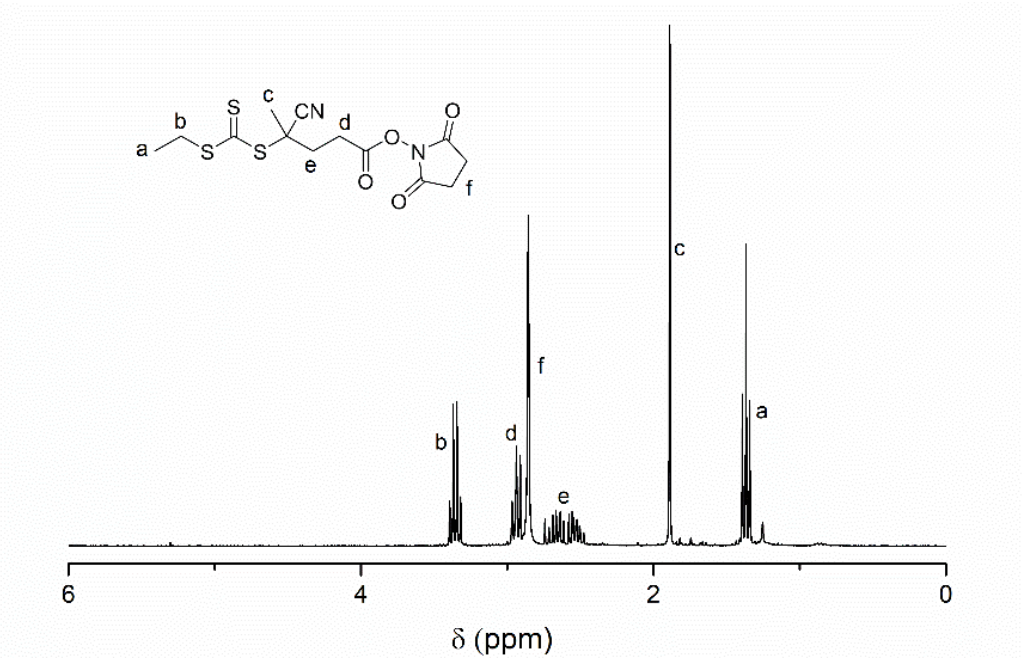

Figure A.7: ^{1}H NMR spectrum ($CDCl_3$, 300 MHz) of *N*-hydroxysuccinimide-(4-cyano pentanoic acid)yl ethyl trithiocarbonate (NHS-CPAETC).

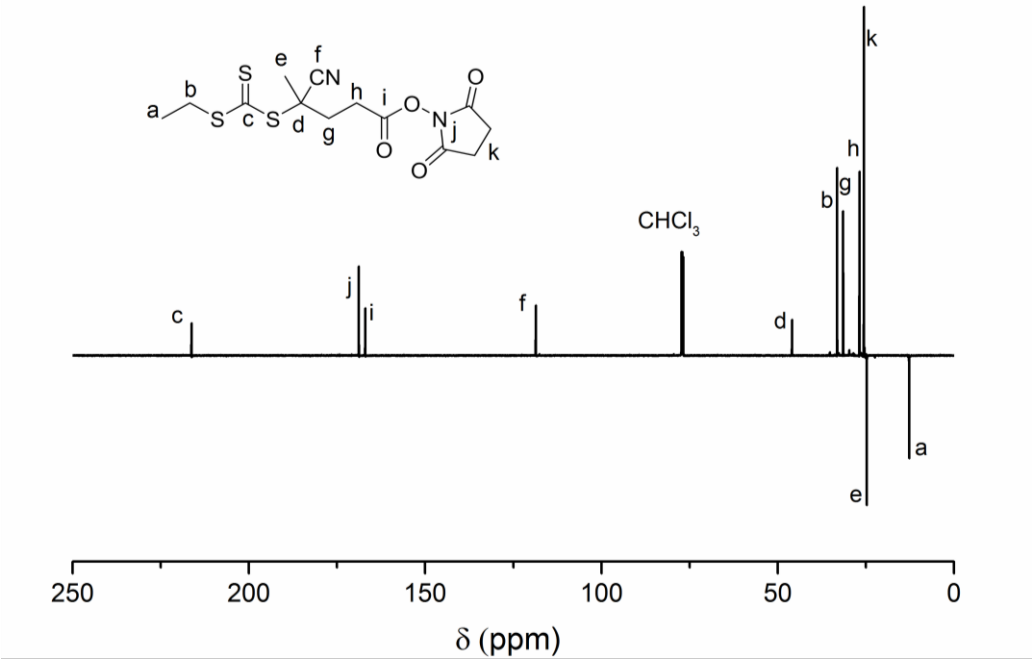

Figure A.8: ^{13}C-APT NMR spectrum ($CDCl_3$, 125 MHz) of *N*-hydroxysuccinimide-(4-cyano pentanoic acid)yl ethyl trithiocarbonate (NHS-CPAETC).

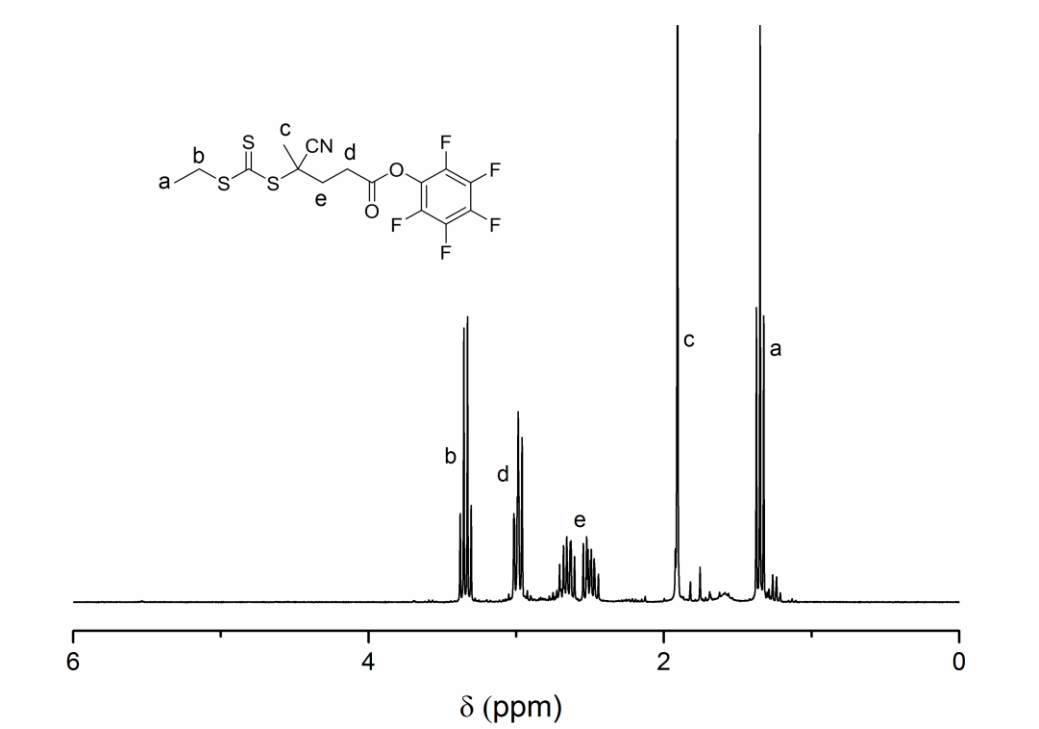

Figure A.9: ^{1}H NMR spectrum ($CDCl_3$, 300 MHz) of pentafluorophenol-(4-cyano pentanoic acid)yl ethyl trithiocarbonate (PFP-CPAETC).

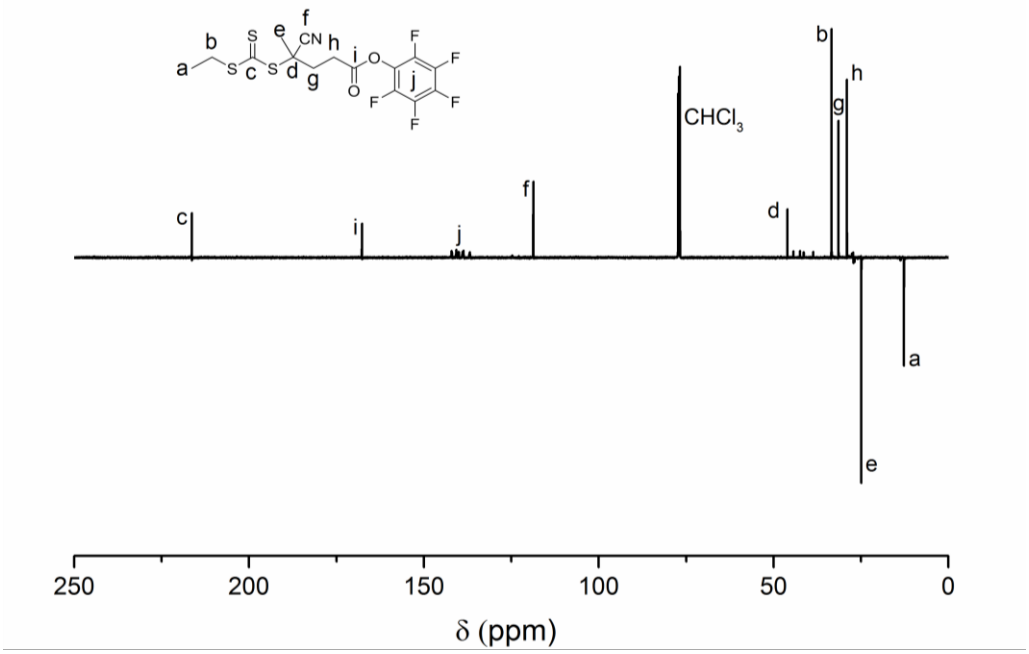

Figure A.10: ^{13}C-APT NMR spectrum ($CDCl_3$, 125 MHz) of pentafluorophenol-(4-cyano pentanoic acid)yl ethyl trithiocarbonate (PFP-CPAETC).

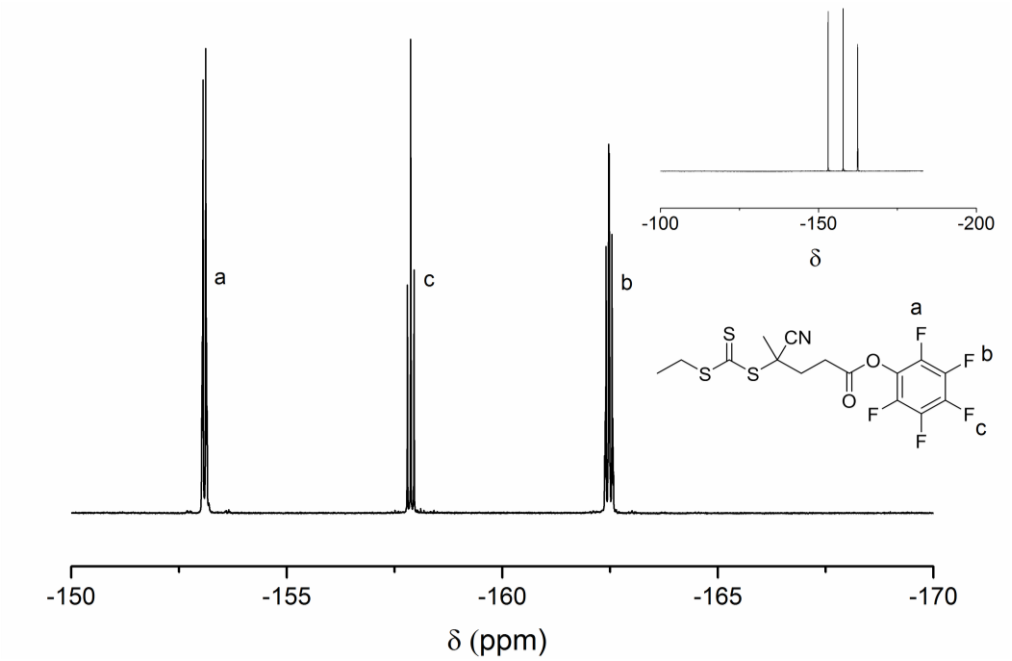

Figure A.11: ^{19}F NMR spectrum ($CDCl_3$, 300 MHz) of pentafluorophenol-(4-cyano pentanoic acid)yl ethyl trithiocarbonate (PFP-CPAETC).

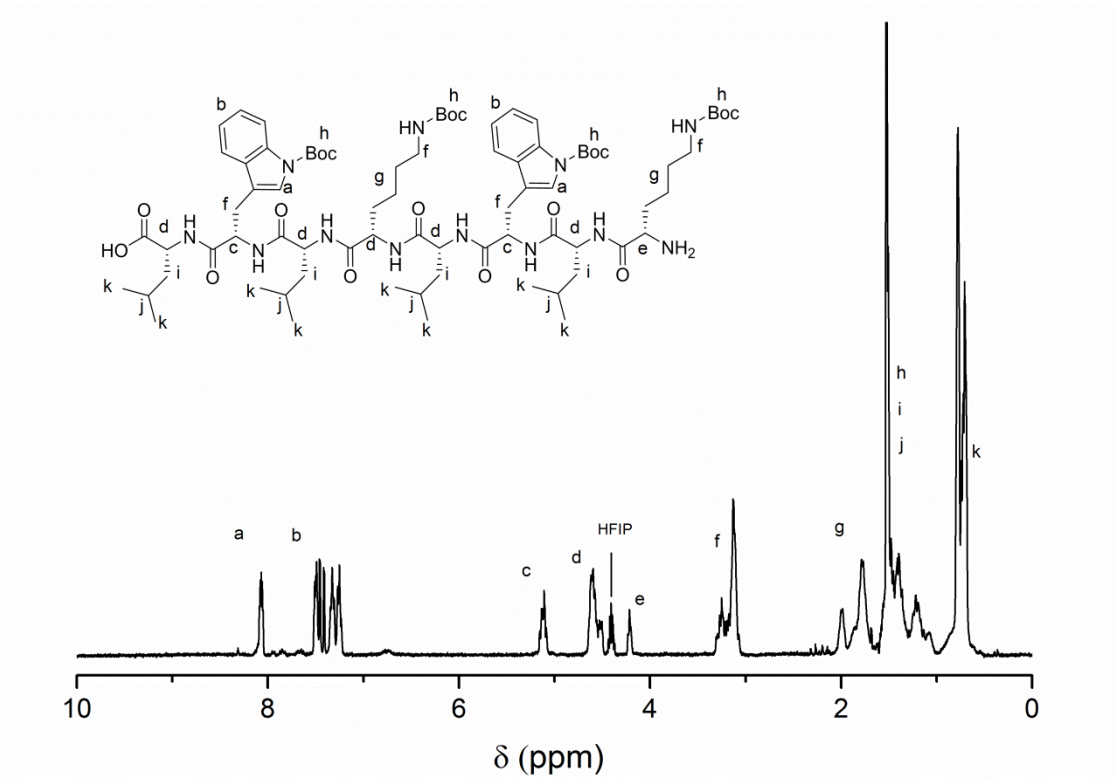

Figure A.12: ^{1}H NMR spectrum (TFA-*d*, 400 MHz) of linear peptide H_2N-L-Lys(Boc)-D-Leu-L-Trp(Boc)-D-Leu-L-Lys(Boc)-D-Leu-L-Trp(Boc)-D-Leu-COOH.

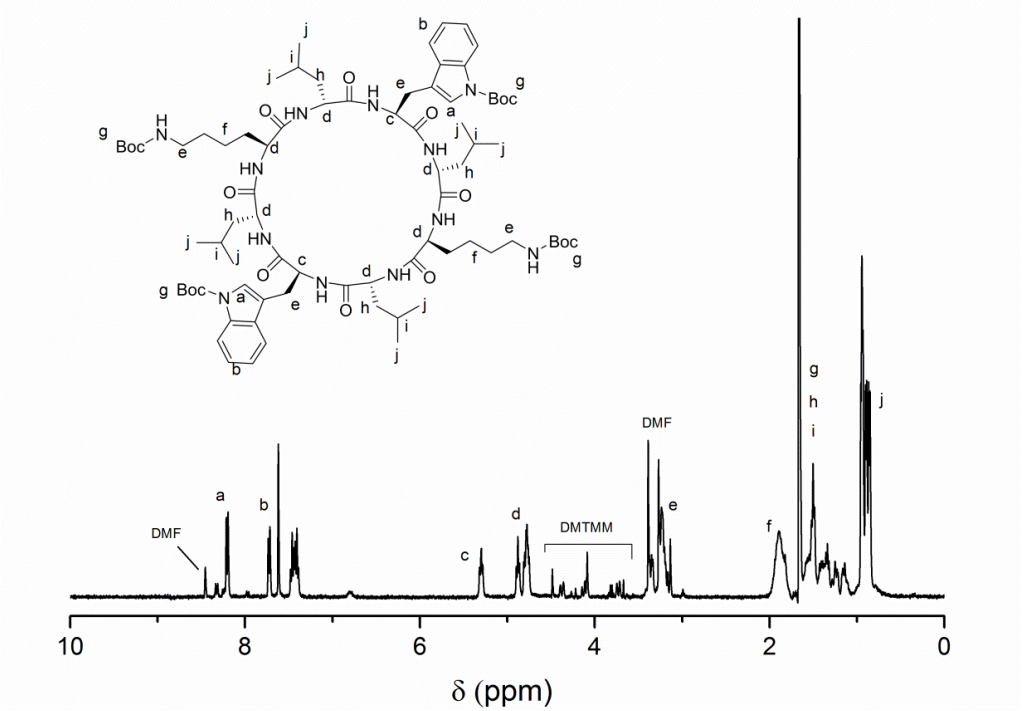

Figure A.13: ^{1}H NMR spectrum (TFA-*d*, 400 MHz) of cyclic peptide (L-Lys(Boc)-D-Leu-L-Trp(Boc)-D-Leu)$_2$.

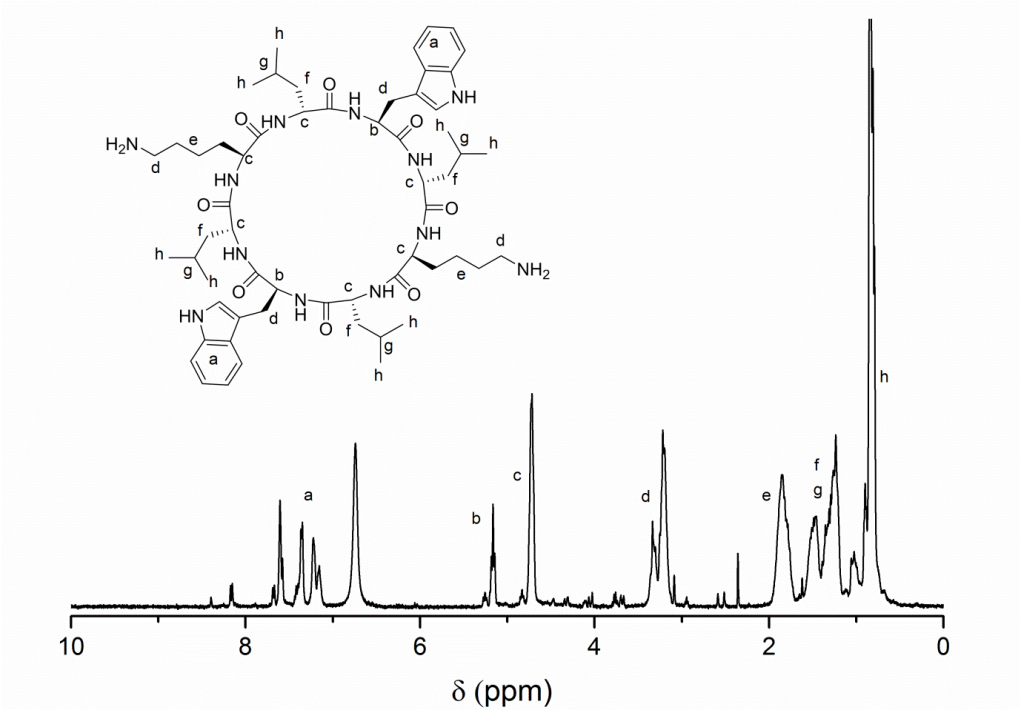

Figure A.14: ^{1}H NMR spectrum (TFA-*d*, 400 MHz) of cyclic peptide (L-Lys-D-Leu-L-Trp-D-Leu)$_2$.

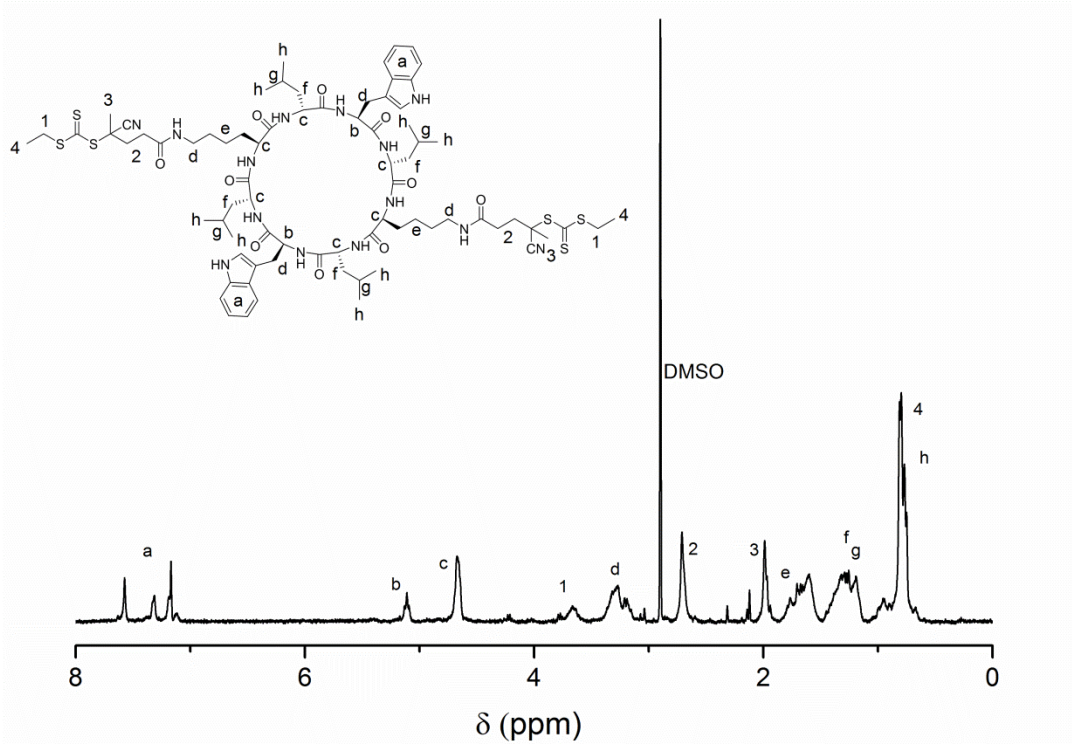

Figure A.15: ^{1}H NMR spectrum (TFA-*d*, 400 MHz) of cyclic peptide (cyano pentanoic acid)yl ethyl trithiocarbonate (CP(CPAETC)$_2$).

Appendix B

NMR spectra corresponding to attachment of Iridium complexes

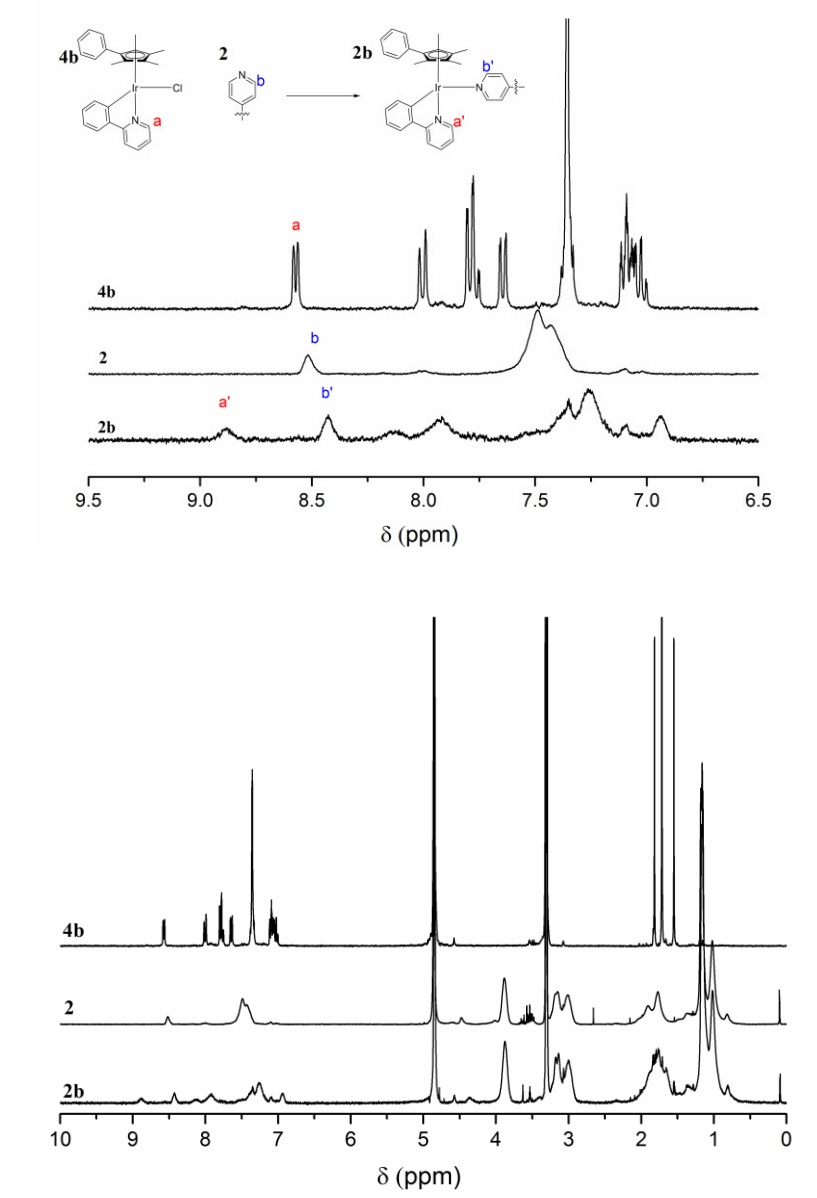

Figure B.1: ^{1}H NMR characterisation of the attachment of complex **4b** onto conjugate **2**, affording conjugate **2b**.

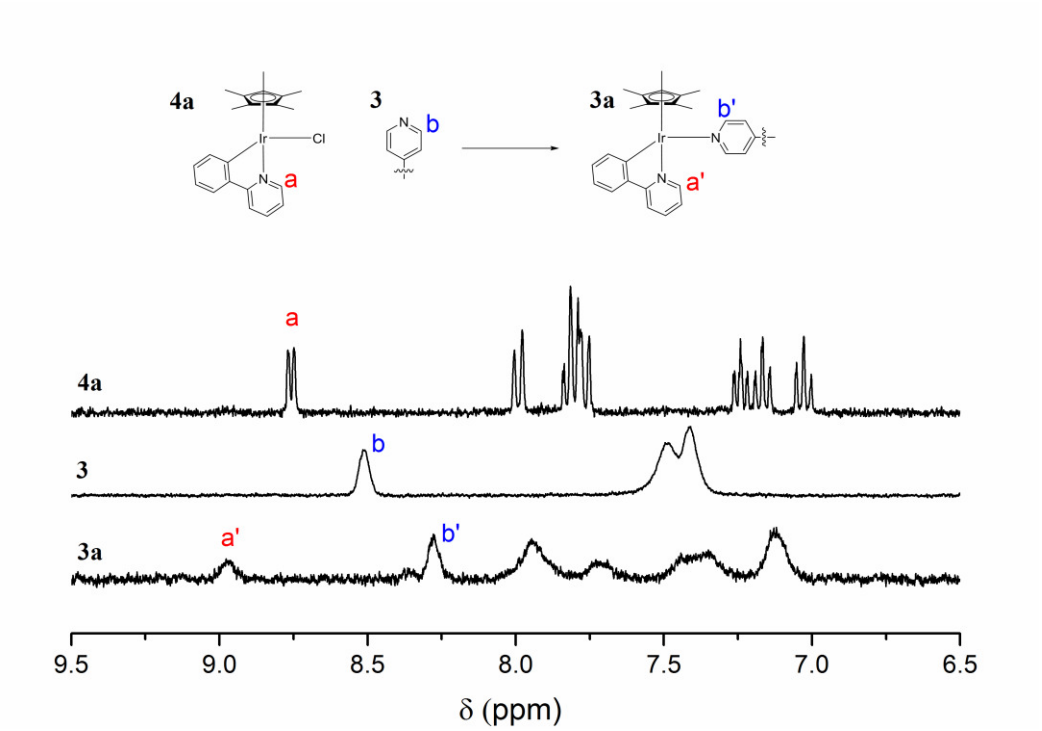

Figure B.2: ^{1}H NMR characterisation of the attachment of complex **4a** onto polymer **3**, affording polymer **3a**.

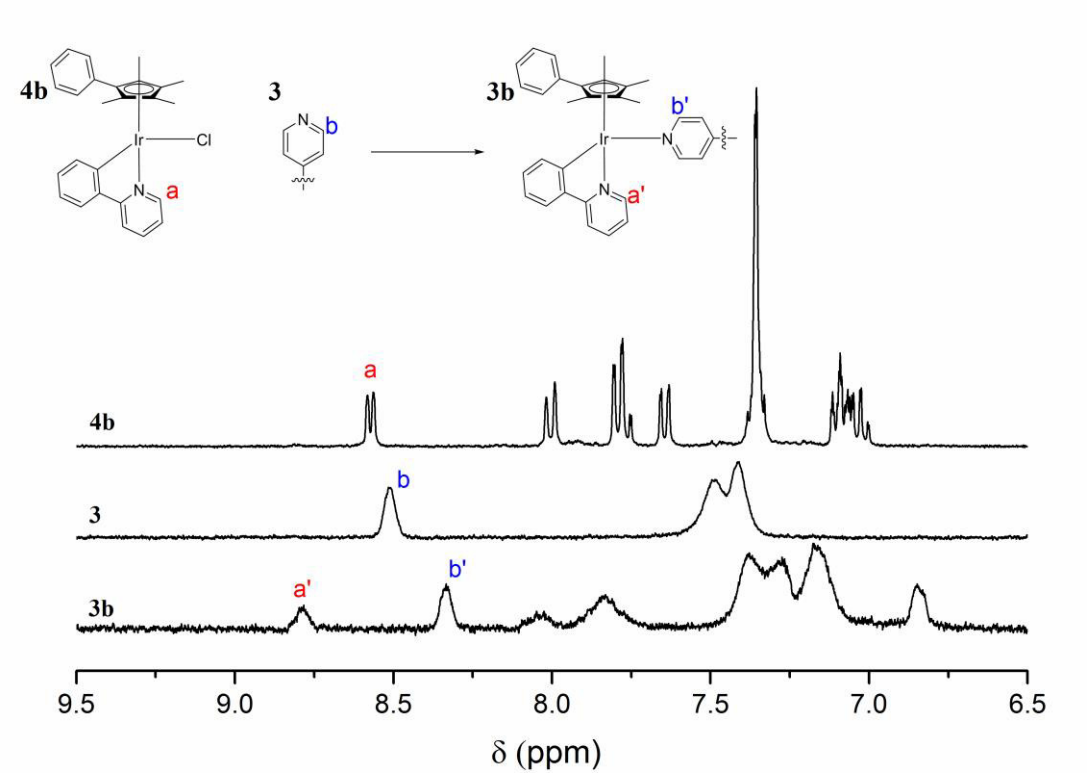

Figure B.3: ^{1}H NMR characterisation of the attachment of complex **4b** onto polymer **3**, affording polymer **3b**.

Appendix C

List of publications

1. Cyclic peptide-polymer conjugates: Grafting-to vs grafting-from. **S. C. Larnaudie**, J. C. Brendel, K. A. Jolliffe, S. Perrier, *J. Polym. Sci., Part A: Polym. Chem.* **2016,** *54* (7), 1003-1011.

2. Tunable length of cyclic peptide-polymer conjugate self-assemblies in water. S. Catrouillet, J. C. Brendel, **S. C. Larnaudie**, T. Barlow, K. A. Jolliffe, S. Perrier, *ACS Macro Letters* **2016,** *5* (10), 1119-1123.

3. Cyclic peptide-polymer nanotubes as efficient and highly potent drug delivery systems for organometallic anticancer complexes. **S. C. Larnaudie**, J. C. Brendel, I. Romero-Canelón, C. Sanchez-Cano, S. Catrouillet, J. Sanchis, J. P. C. Coverdale, J.-I. Song, A. Habtemariam, P. J. Sadler, K. A. Jolliffe, S. Perrier. *Submitted for publication.*

4. Cyclic peptide-poly(HPMA) nanotubes as drug delivery vectors : *in vitro* assessment, pharmacokinetics and biodistribution. **S. C. Larnaudie**, J. Sanchis, T.-H. Nguyen, R. Peltier, J. C. Brendel, S. Catrouillet, C. J. H. Porter, K. A. Jolliffe, S. Perrier. *Submitted for publication.*

5. pH-Responsive, amphiphilic core-shell supramolecular polymer brushes from cyclic peptide-polymer conjugates. **S. C. Larnaudie**, J. C. Brendel, E. Mansfield, K. A. Jolliffe, S. Perrier. *Submitted for publication.*